Vibration Transmission and Support Loss in MEMS Sensors

Benjamin Chouvion

Ingénieur INSA Lyon

Thesis submitted to The University of Nottingham
for the degree of Doctor of Philosophy

January 2010

Abstract

Micro-Electro-Mechanical Systems (MEMS) inertial sensors that are based on a resonating structure are used in a wide range of applications including inertial guidance and automotive safety systems. Damping has a significant and negative effect on sensor performance and there is an increasing need to accurately predict and control damping levels, particularly for high performance guidance and navigation applications. Support loss, which governs the losses from the resonator to its foundation through the supporting structure, is an important source of damping in MEMS resonators. This thesis focuses on improving the understanding of this particular damping mechanism and on developing efficient models to predict support loss at the design stage.

The coupling between resonator and support is of primary interest when evaluating the interaction and energy transmission between them. To quantify the stresses acting on the support, a model that predicts vibration transmission through common MEMS structures is first developed. A general wave propagation approach for the vibration analysis of networks consisting of slender, straight and curved beam elements, and a complete ring is presented. The analysis is based on a ray tracing method and a procedure to predict the natural frequencies and mode shapes of complex ring/beam structures is demonstrated, for both in-plane and out-of-plane vibration. Furthermore, a simplification of the analysis for cyclically symmetric structure is presented. An analytical method is then used to model the support, approximated as a semi-infinite domain, and to quantify support losses, again for both in-plane and out-of-plane vibration.

To illustrate the effectiveness of the models, several numerical examples are presented, ranging from simple beam-like structures to ring/beam structures of increasing complexity. A parametric study on the design of particular ring-based resonators, and general strategies for improving the quality factor of common MEMS sensors by reducing support losses, are also considered.

Acknowledgements

I would particularly like to thank my supervisors Colin Fox, Stewart McWilliam and Atanas Popov for their support over the past few years. Your comments have always been insightful. Colin, I hope you can finally fully enjoy your retirement and thanks again for coming back so often especially for me. Stewart, despite the long distance that now separates us, I still enjoy our meetings and your help. Thanks both of you for allowing me to have a break when I needed most. And finally Atanas, thank you for being always so easily available and I sincerely think it is a shame that I did not work with you since the beginning of my course.

In addition, I would like to extend my acknowledgement to Atlantic Inertial Systems (AIS) for making my studies possible via their funding.

Pour finir, merci à toi, Céline, d'avoir été là depuis le début. Merci pour tes encouragements et ton soutien dans les moments difficiles, surtout vers la fin (et au milieu aussi...).

Je dédie cette thèse à mon père.

Contents

Abstract i

Acknowledgements iii

Nomenclature ix

Abbreviations xiii

1 Introduction and literature review 1

1.1 General introduction and energy damping 1
1.1.1 Gyroscopes 1
1.1.2 Damping in MEMS resonators 3
1.2 Theory of vibrating gyroscopes 5
1.2.1 Gyroscope operating principles 5
1.2.2 Motion equations 7
1.2.3 Special case of the ring-based rate sensor 8
1.3 MEMS damping mechanisms 11
1.3.1 The quality factor 11
1.3.2 Air damping 14
1.3.3 Thermoelastic damping 16
1.3.4 Material losses 18
1.4 Support loss 19
1.4.1 Computational approach 20
1.4.2 Analytical approach 22
1.5 Vibration transmission and propagation 25
1.5.1 Finite element analysis 25
1.5.2 Statistical energy analysis 26
1.5.3 Wave approach 28
1.6 Summary of the literature review 30

1.7 Aims and objectives of the thesis 31
1.8 Outline of the thesis 32
Figures 34

2 In-plane vibration analysis using a wave approach 38
2.1 Introduction 38
2.2 Wave propagation in beams 41
2.2.1 Curved beams 41
2.2.2 Simplification to straight beams 45
2.3 The ray tracing method 47
2.3.1 Simplified development for a two-beam example 47
2.3.2 Procedure development for a more complex example 51
2.3.3 Forced response 53
2.4 Transmission coefficients 55
2.4.1 Ring/beam transmission 56
2.4.2 Transmission at an abrupt change in direction 59
2.4.3 Wave reflection at common boundaries 61
2.5 Validation of the ray tracing method for simple structures 61
2.5.1 Free response of a perfect ring 62
2.5.2 Forced response of a beam structure 62
2.6 Conclusion 68
Figures 70

3 Model simplifications for symmetric structures 76
3.1 Introduction 76
3.2 Structures showing periodic properties 78
3.2.1 Substructuring method 79
3.2.2 Simplifications for periodic structures 81
3.3 Structures showing cyclic symmetry properties 83
3.3.1 Cyclic symmetry theory 84
3.3.2 Simplifications for cyclically symmetric structures 87
3.3.3 Obtaining the mode shape of the entire structure 91
3.4 Applications 92
3.4.1 Beam with identical uniformly-spaced point masses 92
3.4.2 Ring with identical uniformly-spaced point masses 94
3.4.3 Regular polygons 96

3.4.4 Ring-based rate sensor . . . 96
3.5 Conclusion . . . 98
Figures and tables . . . 100

4 Modelling the support loss for in-plane vibrations 110
4.1 Introduction . . . 110
4.1.1 Analytical model . . . 110
4.1.2 High-fidelity multiphysics simulations . . . 112
4.1.3 Truncated domain FEA approaches . . . 113
4.2 Analytical model . . . 113
4.2.1 Physical modelling and main assumptions . . . 113
4.2.2 Model of the support structure . . . 115
4.2.3 Introducing the boundary conditions . . . 118
4.2.4 Solution procedure . . . 120
4.2.5 Derivation of the Q-factor . . . 122
4.3 Perfectly matched layer . . . 124
4.3.1 Indroduction . . . 124
4.3.2 Definition of the PML for a one-dimensional case . . . 126
4.3.3 Difficulties with the convergence . . . 129
4.4 Infinite elements . . . 131
4.4.1 Introduction . . . 131
4.4.2 Infinite element characteristics . . . 131
4.4.3 Convergence analysis . . . 133
4.5 Results for some simple test cases . . . 135
4.5.1 Cantilever beam . . . 135
4.5.2 Two-beam system . . . 137
4.6 Conclusion . . . 139
Figures . . . 141

5 Influence of leg design on the Q-factor 149
5.1 Introduction . . . 149
5.2 Original study . . . 152
5.2.1 Main steps for calculating Q . . . 152
5.2.2 Results from the original analysis . . . 154
5.3 Influence of leg dimension . . . 155
5.3.1 Change of the leg geometry . . . 155

5.3.2 Change of leg width 158
5.4 Addition of blocking masses 160
5.4.1 Mass added to a beam portion within the leg 160
5.4.2 Mass added to a corner of the leg 163
5.5 Sensitivity study by modifying one leg only 167
5.6 Conclusion 168
Figures and tables 171

6 Support loss prediction for out-of-plane vibrations 187
6.1 Introduction 187
6.2 The ray tracing method applied to out-of-plane vibrations 190
6.2.1 Wave propagation in straight and curved beams 190
6.2.2 Development of the ray tracing method for out-of-plane vibrations 195
6.2.3 Transmission coefficients 196
6.2.4 Possible simplifications 201
6.3 Modelling the support losses for out-of-plane vibrations 203
6.3.1 Introduction 203
6.3.2 Admittance of the support 204
6.3.3 Power flow and support loss 206
6.4 Applications 208
6.4.1 Natural frequencies and mode shapes 209
6.4.2 Support loss 213
6.5 Conclusion 221
Figures and tables 223

7 Conclusions and future work 234
7.1 Introduction 234
7.2 Chapter reviews and conclusions 235
7.3 Suggestions for future work 239
7.3.1 Vibration transmission analysis 239
7.3.2 Support loss model 241

References 244

Appendices

A Analytical support model **256**

A.1 Three dimensional model of the support 256

A.2 In-plane reduction 257

A.2.1 Reduction 257

A.2.2 Wave propagation velocities 258

A.2.3 Elastic wave equation 260

A.3 Simplification and Fourier transform 260

A.3.1 Simplification with the introduction of new operators 260

A.3.2 Introduction of the shear and normal stresses 262

A.3.3 Fourier Transform of the main equations 263

A.4 Solution procedure 264

A.4.1 Differential equation solution 264

A.4.2 Derivation of constants 265

A.4.3 Displacements arising from stress sources 267

A.5 Inverse Fourier transform 268

A.5.1 Inverse Fourier transform of the displacements 268

A.5.2 Derivation of the mean displacement over the source region 271

A.6 Energy loss calculation 272

A.7 Proof 1: The indirect stress has no contribution to the mean displacement 274

A.8 Proof 2: The bending moment effect is negligible 276

A.8.1 Change of w due to a bending moment 277

A.8.2 Change of u due to a bending moment 278

A.8.3 Energy loss due to a bending moment 279

References 281

B Geometry constraints **282**

B.1 Original dimensions 283

B.2 Coupling between parameters 284

Figures and tables 286

Nomenclature

Roman Symbols

$\mathbf{a}$	Wave amplitude vector
A	Cross-sectional area ..... (m^2)
$\mathbf{B}^{(j)}$	$[3 \times 3]$ reflection coefficients matrix at discontinuity j
b	In-plane width ..... (m)
C	Coefficient of damping ..... (Ns/m)
c	One-dimensional wave speed ..... (m/s)
c_L	Propagation velocity for longitudinal wave ..... (m/s)
c_T	Propagation velocity for transverse wave ..... (m/s)
$\mathbf{D}$	Diagonal dispersion matrix
D	Plate bending stiffness ..... (Nm)
d_j	Diameter of a rigid joint ..... (m)
E	Young's modulus ..... (Pa)
f	Natural frequency ..... (Hz)
G	Shear modulus ..... (Pa)
h, h_p	Thickness of the resonator and the support in the out-of-plane (or axial) direction ..... (m)
i	Unit imaginary number such that $\mathrm{i} = \sqrt{-1}$
$\mathbf{I}$	Identity matrix
i	Positive integer
I_x, I_y	Second moment of area of the cross-section ..... (m^4)
I_{x_j}, I_{y_j}, I_{z_j}	Moment of inertia of a rigid joint ..... (kg m^2)
I_{zz}	Polar moment of inertia of the cross-section (for twisting along the z-axis) ..... (m^4)
J	Torsion constant ..... (m^4)

j	Positive integer
K	Stiffness (N/m)
k, k_o	In-plane and out-of-plane wavenumbers (m^{-1})
k_1, k_2, k_3	Principal extensional, flexural and decaying wavenumber in curved beams (m^{-1})
k_L	Longitudinal wavenumber in straight beams (m^{-1})
k_T	Torsional wavenumber in straight beams (m^{-1})
k_{Fx}, k_{Fy}	Flexural wavenumber in straight beams for out-of- and in-plane vibration (m^{-1})
L, $L^{(j)}$	Length, length of the $(j)^{\mathrm{th}}$ component (m)
L_0	Distance between two substructures, or length of one side of a regular polygon (m)
M	Mass (kg)
M_1, M_2	In-plane and out-of-plane bending moments (Nm)
m_j	Mass of a rigid joint (kg)
M_T	Twisting moment (Nm)
N	Number of sectors in the cyclic symmetry simplification, number of point masses, number of sides in regular polygons
n	Positive integer
$\hat{o}$	Torsional wave amplitude (rad)
P	Out-of-plane shear force (N)
Q	Quality factor (-)
$\mathbf{R}^{(j)}$	$[3 \times 3]$ reflection coefficients matrix at boundary j
R	Mean radius of curvature, radius of regular polygons (m)
r	Ratio of wave speeds (-)
S	In-plane shear force (N)
s	Circumferential coordinate along a curved beam or ring component (m)
$\mathbf{T}$	Shear stress tensor
$\mathbf{T}$	Transmission coefficients matrix
T	Normal, tensile force (N)
t	Time (s)
$\hat{u}$	In-plane flexural wave amplitude (m)
$\mathbf{u}$	Wave amplitude row-vector containing three components: extensional, flexural and decaying waves
u	In-plane radial, flexural displacement (m)
U_0	Amplitude of vibration (m)

$\hat{v}$	Out-of-plane flexural wave amplitude (m)
v	Out-of-plane (axial) flexural displacement (m)
$\hat{w}$	Extensional wave amplitude (m)
W	Total energy stored (J)
w	Tangential, longitudinal displacement (m)
w	Width (m)
W_0	Amplitude of vibration (m)
X	Amplitude of vibration (m)
x	Displacement along the x-axis (m)
X_i, X_{oi}	Amplitude ratio between radial and flexural waves in curved beams for in-plane vibration, and between axial and torsional waves for out-of-plane vibration (-)
$\mathbf{Y}$	Point mobility matrix
Y	Amplitude of vibration (m)
y	Displacement along the y-axis (m)
z	Coordinate along the beam centreline (z-axis) (m)

Greek Symbols

α	Angle (rad)
ΔW	Energy loss per cycle (J)
$\mathbf{\Delta}_{L^{(j)}}$	$[3 \times 3]$ dispersion matrix along the length $L^{(j)}$
κ	Cyclic mode number (-)
Λ	Substructure name
λ	Lamé constant (-)
λ_T	Transverse elastic waves wavelength (m)
μ	Lamé constant (-)
ν	Poisson's ratio (-)
Ω	Angular motion of the cross-section (rad)
Ω	Circular frequency of vibration (rad/s)
ω	Circular frequency of vibration (rad/s)
$\mathbf{\Pi}^{(i)\rightarrow(j)}$	$[3 \times 3]$ transmission matrix from (i) to (j)
Π	Power transmitted to the support (W)
ψ	Rotational motion of the cross-section (rad)
ρ	Mass density (kg/m^3)
$\mathbf{\Sigma}$	Strain tensor

Σ	Strain ..... (-)
σ	Normal stress ..... (Pa)
$\sigma(s)$	PML absorbing function
τ	Shear stress ..... (Pa)
Θ	Dilatation ..... (-)
θ	Angle ..... (rad)
$\boldsymbol{\Upsilon}$	$[3 \times 3]$ change of phase matrix
ξ	Fourier transform variable ..... (-)
ζ	Viscous damping ratio ..... (-)

Superscripts

$+$, $-$	Denotes positive- and negative-going direction in s or z axis
(j)	Index of the component considered
(l), (r)	Left or right component considered
*	Denotes the complex conjugate
T	Matrix transpose

Subscripts

1, 2, 3	Denotes the wave type (mainly extensional, flexural and decaying)
b	Straight beam related
F	Denotes a function expressed in the Fourier domain
initial	First wave taken into account in the ray tracing approach
o	Related to out-of-plane vibration
r	Ring component related

Other Symbols

Im	Denotes the imaginary part of a complex entity
Re	Denotes the real part of a complex entity

Abbreviations

AIS	Atlantic Inertial Systems
EFA	Energy Flow Analysis
FE	Finite Element
FEA	Finite Element Analysis
HRG	Hemispherical Resonating Gyroscope
MEMS	Micro-Electro-Mechanical Systems
PML	Perfectly Matched Layer
SEA	Statistical Energy Analysis

Chapter 1

Introduction and literature review

1.1 General introduction and energy damping

The research reported in this thesis relates to the understanding, modelling and quantification of a specific damping mechanism, called support loss, encountered notably in Micro-Electro-Mechanical Systems (MEMS) sensors. The research is focused on applications in the area of miniaturised vibrating resonators that are manufactured using recently developed MEMS technology processes and, in particular, resonators in the form of rings used for angular rate measurements (gyroscopes).

1.1.1 Gyroscopes

Gyroscopes are inertial devices used to measure angular velocity, and are often referred to as rate sensors. The Foucault pendulum which was first used in about 1850 to demonstrate the Earth's rotation may be thought of as the earliest man-made vibrating gyroscope. It was observed that the plane of the swing of the pendulum appeared to rotate at the same rate as the local vertical component of the Earth's rate, as the angular momentum vector of the pendulum was fixed in inertial space. The gyroscopic effect was there first experimentally proved. This effect has then be used to manufacture rate sensor devices.

The basic design for conventional mechanical gyroscopes consists of one gimbal supported on a frame that is usually constrained by some elastic restraints, see Figure 1.1. The coupling gyroscopic effects of the high speed rotor would provide means of measuring the rate. However the need for acute precision bearings to support a very high speed rotor (typically between 20 000 and 30 000 rev/min) and their general complexity have kept their size quite large. The cost of production of such devices remains very high. These factors have limited the range of applications for such gyroscopes to the naval, aerospace and military industries.

Recent technological advances have made possible the emergence of new generations of rate sensors that do not rely on a spinning rotor to measure the rate. The first category, namely "optical gyroscopes", relies on the properties of light. The second group includes all devices that rely on the mechanical resonance of two or more modes of vibrations of a resonating structure. These sensors are known as vibrating structure rate sensors. They consist of a mass supported in the sensor, a means to excite the mass along a primary mode, and a means to measure the resulting response along the coupled secondary mode. They make use of Coriolis forces to determine the rate at which it is rotating about one or more axes. Their main advantage is that they have no rotating parts that require bearings, and hence they can be easily miniaturised and batch-fabricated using micro-machining techniques.

The latest generation of vibrating gyroscopes are micro-engineered from silicon and have dimensions and feature sizes ranging from a few millimetres to a few micrometres. They are manufactured using the MEMS technology. By taking advantage of the wafer processing technology developed for the electronics industry where many devices can be created per wafer (see for instance Figure 1.2(a)), a high volume, low cost and robust manufacturing process can be designed. This yields very small devices that take full advantage of the excellent mechanical and electrical properties of crystalline silicon.

This new generation of gyroscopes has widened the range of applications for rate sensors. In addition to the classic field of applications already stated – mainly military, rate sensors are now used in automotive safety and navigation, robotics,

biomechanics and prosthetic aids. An example of practical application is to measure how quickly a car turns by mounting a set of gyroscopes inside the vehicle. If the gyroscopes sense that the car is spinning out of control, differential braking engages to bring it back into control. This application is known as the Electronic Stability Control or Program (ESC or ESP) and is now mounted in most high standard cars. The angular rate can also be integrated over time to determine angular position – particularly useful for maintaining continuity of GPS-based navigation when the satellite signal is lost for short periods of time. Other possible applications can be found in the aerospace or military domain with platform stabilisation of avionics.

The potential of gyroscope sensors is quickly expanding with the constant improvement in miniaturisation and performance. The thesis focuses on the MEMS vibrating ring-based rate sensor developed by Atlantic Inertial Systems (AIS), (previously BAE Systems). Figure 1.2 shows photographs and a schematic representation of the sensor. It consists of a silicon ring structure supported on eight thin, nominally identical external legs [1]. Ring/beam structures of this form will be used as the main focus of the thesis.

The sensitivity of the sensor depends on the natural frequencies of the primary and secondary modes of vibration. For a perfect ring the natural frequencies are identical and the sensitivity is maximised. However, the presence of manufacturing variations introduces frequency splits that can significantly degrade performance. The sensitivity of the sensor is also degraded by the presence of damping. This project aims to gain improved understanding of the damping caused by support losses, so that sensors with increased sensitivity can be designed. The following section provides an overview of damping in MEMS resonators.

1.1.2 Damping in MEMS resonators

Energy is dissipated from MEMS resonators through a number of different damping mechanisms. Systems contained in a fluid medium (gas or liquid) lose energy through viscous forces in the fluid, and by radiating sound into the fluid. For ex-

ample in the Foucault pendulum mentioned in Section 1.1.1, air resistance damps the oscillation of the mass, so Foucault pendulums in museums often incorporate an electromagnetic or other drive to keep the mass swinging; others are restarted and re-launched regularly. By removing the fluid that surrounds the resonator, the effects of fluid damping can be made negligible.

Energy can also be dissipated by intrinsic damping mechanisms. These are damping mechanisms that originate within the material itself. One of them is thermoelastic damping which is caused by the interaction between mechanical strain and thermal effects in the resonator. Thermoelastic damping in ring resonators has been investigated in previous research work [2]. Brief reviews of gas damping, thermoelastic damping and other intrinsic damping mechanisms are presented in Section 1.3. Energy can also be lost by transmission of vibrations from the resonator to its foundation through the supporting structure; this loss mechanism is known as support loss, see Section 1.4. This form of damping is less well known than the other damping mechanisms, and relatively little work has been performed in this area. This topic forms the main focus of the research project.

The optimum level of damping depends of course on applications. In some cases, such as mechanical machinery and civil engineering structures, a lack of damping may lead to excessive vibrations, especially at resonance, leading to fatigue and fracture. In these cases, there is a need to design the structure such that the damping is over some minimum level to give safe operation. In vibro-acoustic applications, the goal is usually to reduce the sound transmitted to another environment and a sufficient amount of damping is consciously introduced (with the use of visco-elastic materials for example). On the other hand, there are applications in sensors and instrumentation where it is necessary to minimise the damping, or to control it at some relatively low level, in order to obtain good performance. The consideration of damping is therefore important in the design of mechanical systems that contain vibrating structures. An application where minimising energy losses by damping becomes very important is when micro-mechanical resonators are used as filtering elements in electronics using their vibrational transfer function. When a vibrating beam is under-damped, its vibration will have a bigger amplitude at its natural

frequency than at any other frequency, giving rise to a resonant peak. Maximum efficiency will be obtained when this peak is as high as possible.

The work presented in this thesis is motivated by the general need to gain an improved understanding of the energy dissipation mechanisms in vibrating microstructures used in vibrating gyroscopes, and to develop models to quantify and predict damping levels at the design stage. Within the main damping mechanisms occurring in such devices, support loss is one of the most complex and least well understood.

To set the scene for the rest of Chapter 1, a brief theory of the principles of operation of gyroscopes will be presented in Section 1.2. A detailed review of the various sources of damping mechanisms that exist in MEMS structures will follow, in Section 1.3. The ring-based resonator on which the research is focused is supported on complexly-shaped, folded beam legs, and one may easily understand that the vibration and energy propagation from the ring to the support are of particular interest. A review of wave transmission and propagation will therefore be presented in Section 1.5. Subsequently, the aims and objectives of the research will be stated in Section 1.7.

1.2 Theory of vibrating gyroscopes

1.2.1 Gyroscope operating principles

All vibrating rate sensors are based upon the phenomenon of Coriolis acceleration [3]. This acceleration is experienced by a particle undergoing linear motion in a frame of reference which is rotating about an axis perpendicular to that of the linear motion. The resulting acceleration, which is directly proportional to the rate of turn, occurs in the third axis which is perpendicular to the plane containing the other two axes. Thus, in a rate sensor, vibrating motion is coupled from a primary vibrating mode into a secondary mode, when the sensor experiences angular

rate. The Coriolis acceleration couples two fundamental modes of vibration of the resonator structure. In most micro-mechanical vibrating gyroscopes, the sensitive element can be represented as an inertia element and elastic suspensions with two prevalent degrees of freedom. A generic example is presented in Figure 1.3.

The sensitive element is driven to oscillate at one of its modes with prescribed amplitude. This mode is usually called primary mode. When the sensitive element rotates about a particular fixed-body axis, which is called sensitive axis, the resulting Coriolis force causes the proof mass to move in a different mode. Excited oscillations are referred to as primary oscillations and drive mode, whereas oscillations caused by angular rate are referred to as secondary oscillations, secondary mode or companion mode.

In effect, the operation of Coriolis-based vibrating rate sensors can be summarised as follows. One mode of vibration of a resonator possessing two orthogonal modes is excited at a frequency matching its natural frequency in order to minimise the drive force required to achieve a given amplitude of vibration. Due to the Coriolis acceleration, energy is transferred from this excited drive mode to a companion mode that in turn experiences linear motion. The steady state motion of the companion mode is a direct measure of the rotational rate that the resonator is experiencing (see theory in Section 1.2.2). If both modes have the same frequency of vibration, the coupling is maximised and the sensitivity reached is maximum.

In general, it is possible to design gyroscopes with different types of primary and secondary oscillations. For example, a combination of translation as primary oscillations and rotation as secondary oscillations was implemented in a so-called tuning-fork gyroscope [4]. It is worth mentioning that the nature of the primary motion does not necessarily have to be translatory but could be rotary as well. Such gyroscopes are called rotary vibrating gyroscopes. However, it is typically more convenient for the vibrating gyroscopes to be implemented with the same type and nature of primary and secondary oscillations.

Nowadays, there are many practical designs which can be used as a gyroscope. With respect to the number of inertia elements used, the nature of primary and secondary

motions of the sensitive element, it is convenient to subdivide these into three groups as follows: simple oscillators (mass on a string, beam), balanced oscillators (tuning fork), shell resonators (wine glass, cylinder, ring); see [5] for details and principle of operation for each of these groups.

One of the most well known examples of oscillatory gyroscope with continuous vibrating media is the Hemispherical Resonating Gyroscope (HRG). Its sensitive element design is based on the resonating shell that has a hemispheric or so-called "wine-glass" shape. Primary oscillations are provided by exciting vibrations in the rim of the shell. In case of no external angular rate, the nodes of vibration do not move. If the sensitive element rotates around its sensitive axis, which is orthogonal to the plane of vibration, the secondary oscillations can be detected at the nodes. Despite the HRG itself has never been referred to as a micro-mechanical gyroscope, its operation principle has been widely used in numbers of micro-mechanical designs. The hemispherical shape of the shell has in particular been replaced with a thin cylinder or a ring.

By correct design of a shell resonator it is possible to overcome problems associated with resonator mount sensitivity experienced by simple oscillators and thus improve bias performance, and greatly reduce sensitivity to shock and vibration [1].

1.2.2 Motion equations

To illustrate the principle of a vibrating gyroscope, consider a point mass M attached to a rigid frame by four springs of stiffness K and four dampers with damping coefficient C as shown in Figure 1.4. The mass is constrained to move in the (x, y) plane. In operation, the mass is forced to vibrate at the frequency ω in the x-direction by some external mechanism which maintains a constant amplitude X_0 of oscillation such that $x = X_0\, e^{\mathrm{i}\omega t}$. Assuming that there are no linear accelerations experienced by the device along the x- and y-axes, but that the frame is rotated about the z-axis at an angular velocity Ω, the response y of the mass along the

y-axis is governed by [5]:

$$M\ddot{y} + 2C\dot{y} + 2Ky = -2\mathrm{i}M\omega X_0\Omega\, e^{\mathrm{i}\omega t}. \tag{1.1}$$

The angular velocity Ω is assumed to be constant in the following discussion. Provided that the vibration along the x-axis is maintained, it can be deduced from Equation (1.1) that vibrations along the y-axis exist only when the angular velocity Ω is non zero. In other terms, when a constant angular rate of turn is applied, the Coriolis force causes the mass to vibrate in the perpendicular direction. For steady state response, $y = Y_0\, e^{\mathrm{i}\omega t}$ is substituted into Equation (1.1) and the motion of the mass becomes [5]:

$$y = -\left(\frac{2\mathrm{i}M\omega X_0\Omega}{-M\omega^2 + 2\mathrm{i}C\omega + 2K}\right) e^{\mathrm{i}\omega t}. \tag{1.2}$$

Equation (1.2) shows that the steady state amplitude of the response in the y-direction is directly proportional to the applied angular velocity Ω. Thus the amplitude of the response in the y-direction provides a measure of the applied angular velocity Ω.

1.2.3 Special case of the ring-based rate sensor

Operating principle

For the purposes of discussing the basic operation of a ring-based vibrating gyroscope, it is convenient to neglect the supporting legs and consider the ring in isolation. For a perfectly circular ring with an uniform rectangular cross-section, it is well known [5] that the in-plane flexural modes of vibration occur in degenerate pairs with equal natural frequencies. Figure 1.5 shows the mode shapes for the so-called 2θ and 3θ pairs of modes. The modes in a degenerate pair of flexural modes have identical natural frequencies, are asymmetric, have the same deformed shape and are separated from each other by an angle $\dfrac{\pi}{2n}$, n being the flexural mode number ($n = 2$ for the 2θ mode and $n = 3$ for the 3θ mode).

To operate as a sensor, one of the 2θ modes, which is normally referred to as the

primary mode, is driven at constant amplitude at its natural frequency via inductive, capacitive or piezoelectric actuation. Figure 1.2(c) illustrates an inductive excitation where a magnet is present within the ring. When there is no angular velocity applied to the ring (*i.e.* the ring is stationary), the motion of the ring is described by the primary mode only (see Figure 1.5). However, when the ring is rotated about its polar axis, Coriolis acceleration occurs and the complementary secondary mode of vibration is excited (see Figure 1.5). By placing transducers at the nodal points of the primary mode, the radial component of vibration of the secondary mode can be measured. Given that the amplitude of this vibration is proportional to the rate of turn, the angular velocity of the sensor about the polar axis can be determined.

In the new generation of ring gyroscopes, out-of-plane modes are excited and measured [6]. Even though this design is more complex and difficulties occur in matching each vibrating mode with a particular resonant frequency [7], the operating principles are the same as for in-plane vibrations.

Existing model

The inductive sensor that vibrates in-plane is shown in Figure 1.2. Electrical current travels around segments of the ring. It provides inductive drive forces on the sensor that excite its primary mode of vibration. Similar inductive means are used to monitor the vibration of its secondary mode [1]. This sensor is composed of a thin ring supported on eight external, nominally identical legs attached to a surrounding structure. The supporting legs consist of three straight beams with curved sections between them, each beam having a rectangular cross-section area. The geometry of the supporting legs and the point at which they are attached to the ring critically affect the performance of the sensor. The chosen design ensures that the displaced shape of the resonator is not significantly different from that of a free ring when the sensor is in operation. This ensures that the ring is the dominant resonant structure, and prevents frequency splitting [8].

The tangential $w_n(\theta, t)$ and radial $u_n(\theta, t)$ modal displacements for the in-plane

flexural vibrations of a thin ring vibrating at the frequency ω are given by [9]:

$$w_n(\theta, t) = W_0 \sin(n\theta)\, e^{\mathrm{i}\omega t} \qquad \text{and} \qquad u_n(\theta, t) = U_0 \cos(n\theta)\, e^{\mathrm{i}\omega t}, \tag{1.3}$$

where θ is the circumferential location relative to a pre-defined datum. In practical applications, the ring is never perfect and small imperfections are always present. Imperfections due to manufacturing variations and material non-uniformity fix the positions of the modes relative to the ring and yield small frequency splits [10].

In order to model the complete sensor (ring and legs) it is necessary to combine the above ring model with an appropriate leg model. In previous work [11], the leg was modelled as point masses with three discrete springs (two translational and one rotational). This lumped parameter model was used to determine the governing equation of motion and natural frequencies for the complete sensor. The principal stiffness values were obtained by using an analytical approach to deduce the compliance matrix. The effective masses were then obtained by using a frequency response method in conjunction with finite elements. In this model, the leg deformation was assumed to be determined by the ring displacement at the point of attachment of the leg to the ring. It was also assumed that the mode shapes of the ring were identical to those of a free ring. This model was then re-used to calculate the quantity of energy lost by thermoelastic damping in the legs [2]. But again, the vibrations of the legs were assumed not to have any influence on the ring and were not modelled in detail.

In order to study the support losses, it is necessary to fully understand the displacements of the leg at the end attached to the supporting structure, referred to as the anchor end (see Section 1.4). To achieve this, an improved model of the supporting leg is required that properly takes account of the vibrations in the different leg sections. Techniques capable of achieving this are discussed in Section 1.5.

1.3 MEMS damping mechanisms

Characterisation and quantification of the different damping mechanisms are important steps in the design of MEMS resonators. A variety of damping mechanisms can lower the quality in resonant MEMS, including gas damping, material losses, thermoelastic damping, and support losses. Which loss mechanism matters most to a particular design depends on the device geometry, the material used, the environment, and the operating frequency range. All of these damping mechanisms have been studied experimentally for different types of cantilever beam resonators [12–14]. The work reported in [15] gives a more general review. Each of the different energy loss mechanisms is discussed in this section. Before doing this the quantity used to define energy loss, namely the quality factor, is defined.

1.3.1 The quality factor

Damping cannot be measured directly but instead is deduced from the response characteristics of selected vibrating systems. The steady state response of a single degree of freedom system, excited by a harmonic force of constant amplitude, can be used to determine damping through the observation of several characteristics, including the bandwidth of the frequency response, the amplitude of the response at resonance, Nyquist plots, hysteresis loops, and dynamic stiffness [16].

For sufficiently small values of damping, the quality factor Q (or Q-factor) can be experimentally measured from the amplitude-frequency curve and defined as:

$$Q = \frac{\omega_0}{\omega_2 - \omega_1}, \tag{1.4}$$

where ω_0 is the natural resonant frequency; ω_1 and ω_2 are situated around the resonant frequency such that the amplitude of response X_1 at frequency ω_1 and X_2 at frequency ω_2 are equal to $\frac{1}{\sqrt{2}}$ times the peak amplitude X_0 (amplitude at ω_0):

$$X_1 = X_2 = \frac{X_0}{\sqrt{2}}. \tag{1.5}$$

It can be shown [17] that the energies dissipated at the frequencies ω_1 and ω_2 are then equal to one-half of the energy dissipated at resonance. For this reason, the above bandwidth $(\omega_2 - \omega_1)$ is often called the half-power bandwidth. Noting that:

$$\begin{aligned} 20 \log_{10} \frac{X_{1,2}}{X_0} &= 20 \log_{10} \frac{1}{\sqrt{2}}, \\ &\simeq -3 \end{aligned} \tag{1.6}$$

justifies the frequently practical used technique of determining the half-power bandwidth by locating the frequencies on either side of resonance peak for which the response has decreased by three decibels, see Figure 1.6.

The Q-factor is a measure of the sharpness of the resonance peak of the system response curve. Systems with high Q-factor have a sharp, large magnitude and well-defined resonance, and equivalently low levels of energy loss.

The Q-factor can also be introduced with the simple viscous damping model that is usually presented in vibration textbooks. Consider the free vibration of a linear mass-spring-damper system whose equation of motion can be written as:

$$M\ddot{x} + C\dot{x} + Kx = 0, \tag{1.7}$$

with M the mass, C the damping coefficient, K the stiffness and x the displacement. The form of the solution to Equation (1.7) depends on the amount of damping. If the damping is small enough, the system will still vibrate, but eventually, over time, will stop vibrating. This case is called under-damping – this is of most interest in vibration analysis. If the damping is increased just to the point where the system no longer oscillates, the point of critical damping is reached. After this point, the system is over-damped. The value that the damping coefficient needs to reach for critical damping in the mass-spring-damper model is: $C_c = 2\sqrt{KM}$. When ζ, the viscous damping ratio defined as $\zeta = C/C_c$, is small, *i.e.* $\zeta < 0.1$, the Q-factor can be approximated as [17]:

$$Q \simeq \frac{1}{2\zeta}. \tag{1.8}$$

The damping ratio ζ characterises the amount of damping in the system. The

form of the solution of the differential equation (1.7) depends on the value of the parameter ζ.

This mechanical quality factor Q is a key performance factor in MEMS resonators. Just like the damping ratio ζ, the Q-factor is a non-dimensional parameter that quantifies the level of damping in the system. Whilst the damping ratio is widely used in the vibration literature to quantify damping, the Q-factor is widely used in the MEMS literature, and will also be used in this thesis. Q can also be seen as a measure of the ratio of the total energy stored in the system W to the energy dissipated per cycle of vibration ΔW (energy lost per cycle). It is defined as [18]:

$$Q = 2\pi \frac{W_{\text{total}}}{\Delta W_{\text{loss}}}. \tag{1.9}$$

The presence of damping causes a reduction in vibration amplitude and can seriously affect sensor performance. Generally damping forces can depend on many quantities and in practical systems, such as MEMS resonators, different energy loss mechanisms occur. There are three main ways for the energy of vibrating systems to be dissipated. First of all, the interaction of vibrating structure with its ambient fluid causes energy dissipation either via local viscous effect or radiation away into the fluid. This is called air (or gas) damping. Secondly, energy can be dissipated throughout the entire bulk material used to manufacture the structure. This is often referred to as intrinsic material damping which includes thermoelastic damping and energy losses as a result of dislocation and grain boundaries relaxation in the material, called material losses. Lastly, vibrational energy can be dissipated through transmission of elastic waves away from the resonator during vibration. These vibrations usually propagate and dissipate in the support structure. This mechanism is known as support loss. It can be shown that the overall Q-factor, Q_{total}, due to a set of n distinct independent loss mechanisms with individual Q-factors Q_1, Q_2, ..., Q_n can be calculated as [19]:

$$\frac{1}{Q_{\text{total}}} = \frac{1}{Q_1} + \frac{1}{Q_2} + \ldots + \frac{1}{Q_n}. \tag{1.10}$$

This relationship indicates that it is the lowest Q-factor of the different mecha-

nisms which limits the total Q. The several known sources of damping in MEMS resonators will be discussed in the following section.

1.3.2 Air damping

Air damping can occur in a number of different ways. A body that travels through a fluid collides with the molecules of that fluid and transmits some of its energy to those molecules. This process causes viscous damping by displacing some of the fluid around the body, commonly referred to as viscous drag, and acoustic radiation by exciting the fluid in a direction parallel to the motion. The source of damping is the resulting shear force and drag force acting on the resonator as it cuts through the gas during motion. Analysis of this problem is not trivial because of the large volume of gas interacting with the resonator.

One common situation of air damping in MEMS applications is a body moving near a stationary body or surface. If the vibrating structure oscillates parallel to the base structure separated by a thin gap, the gas in the gap and ambient to the microstructure is sheared which in turn, imposes viscous damping on the system. This phenomenon is often modelled as Couette flow. In the case where the vibrating structure has a perpendicular motion towards the stationary surface, squeezed gas damping is present as the surfaces move towards each other. This is particularly the case for devices relying on capacitive sensing and actuation, such as the one described in [6]. Generally, smaller gap thickness will increase the level of electrostatic excitation but gas film forces also increase rapidly as the gap thickness reduces. Consequently, the viscous forces in the gas can cause a significant amount of damping to the motion.

Modelling the flow of real gas mathematically is never simple. The gas flow can be represented either as a continuum or as a collection of molecules. Its modelling depends on the flow regime. A dimensionless parameter that is commonly used to determine the flow regime in a particular case is the Knudsen number [20], which is the ratio of the mean free-path length of molecules within the gas to a characteristic

dimension of geometry.

When the Knudsen number is small, gas behaviour is described by differential equations in terms of spatial and temporal variations of density, velocity, pressure, temperature and other macroscopic quantities [20]. The well-known continuum model is the Navier-Stokes equations. This is the most commonly applicable mathematical model. When the continuum model is valid, local gas properties such as density or velocity can be defined as averages over a volume that is large compared to the microscopic structure of the gas [20]. However, continuum models based on the incompressible Navier-Stokes equations do not cover the cases where MEMS devices operate in a low pressure environment or when the devices are designed with gaps in the order of a micron.

When the Knudsen number is not small, sub-continuum deviations from the Navier-Stokes model begin to play a role. For Knudsen numbers greater that 0.01, slip flow along walls starts to become important; for Knudsen numbers between 0.1 and 10 the flow is in the transitional regime, where the bulk of the fluid no longer conforms to the incompressible constant-viscosity assumptions of the Navier-Stokes equation; and for Knudsen numbers greater than 10, one enters the regime of free molecular flow, where interactions between gas molecules are much less frequent than interactions between a gas molecule and the solid boundary [20].

When the Knudsen number is not small, the flow is modelled using the second approach: as a collection of molecules. In this approach, the gas is regarded as a very large number of discrete particles. The model is derived from statistical mechanics in which a distribution of gas molecule velocities is used to compute the momentum transferred from the vibrating device into the gas [20, 21]. In other words, the flow is in this case studied using deterministic or probabilistic methods. For structures with simple geometry, the continuum model is often tractable.

Gas damping was recognised early as a major energy loss mechanisms for micro-resonators, as it is for macroscopic resonator. Consequently the role of gas damping in micro-resonators has been widely studied using both theoretical models and experiments. A recent review on the subject can be found in [22]. With the advances

in MEMS packaging technology, resonators are now often designed to be contained in a vacuum encapsulation. Assuming that the gas pressure is sufficiently low, gas damping of the vibration of the resonator is eliminated, but other damping mechanisms are still present and limit the Q-factor. One of these is thermoelastic damping, which is discussed in the next section.

1.3.3 Thermoelastic damping

Thermoelasticity describes the coupling between the elastic field in the structure caused by deformation and the temperature field. When a beam bends, it produces a stress gradient in the direction of the bending, which is accompanied by a strain gradient. One side of the beam will be in compression and the other in tension. Volume changes will exist that are opposite on each side of the beam. The strain field causes a change in the internal energy such that the compressed region becomes hotter and the extended region becomes cooler. This volume change creates a temperature gradient. When this temperature gradient is created, the body tends to move back to thermal equilibrium, and dissipative heat flow will ensue. Energy is dissipated within this irreversible heat flow.

The earliest study of thermoelastic damping can be found in Zener's classical work starting in 1937 [23–25]. In these papers, Zener described the mechanism of thermoelastic damping, derived approximate formulae of the damping effects in beams and other simple geometries, and compared his predictions to experimental measurements. The formula he derived for evaluation of thermoelastic damping for beam structures in bending has been widely accepted due to its closed form, simplicity, and applicability. It has been verified to be accurate, but is only applicable to beams or thin structures vibrating in low order flexural modes. Many of the following works on thermoelastic damping are extensions of Zener's studies.

Lifshitz and Roukes [26] presented a refined mathematical analysis of the same thermoelastic problem in which the governing equations were solved in a more exact manner. Instead of using a sine series to approximate the temperature profile

(method used by Zener), the differential equation for temperature was solved analytically. The results from [24] and [26] analyses agreed well. Unfortunately, their model was still restricted to beams.

Wong [2] performed a detailed study on thermoelastic damping in MEMS resonator. He took two existing analyses for simple beam structures [24, 26] and extended them to deal with the in-plane and out-of-plane flexural vibrations of thin perfect rings, developing analytical formulae for their Q-factors. This work also extended Zener's theory [24] to a multi-component structure composed of a ring supported on eight beam-like legs. During his research, analytical models for thermoelastic damping were developed which provided improved understanding of how resonator geometry, dimensions and material properties affect thermoelastic damping in ring resonators. Further work extended the models to consider bi-layer beams and slotted rings.

As designers explore different geometries which are no longer simple beam-like structures, more general methods based on numerical simulations have been developed. Some recent studies have used finite element simulations to numerically solve the coupled equations of elasticity [27–29]. The finite element approaches are based on the discretisation of the coupled equations of thermoelasticity. They have been shown to be valid and verified against experimental data for beam-type geometries. However, they have an important drawback which is that solving coupled equations increases the degrees of freedom of the problem and increases the computational cost. Koyama [30] presented a finite element based numerical method to efficiently evaluate the transfer function for the coupled equations of thermoelasticity. From this transfer function, the Q-factors of MEMS resonators including the effect of thermoelastic damping were computed. Finite element analysis allows Q-evaluation of devices irrespective of fabrication material or geometry, liberating designers from the contemporary beam-like structures. To enable a fast transfer function evaluation, Koyama used the projection of the large finite element discretised system of equations onto a smaller subspace of solutions. This method based on transfer function evaluation of a reduced-order model was proved to be up to 60 times faster than a full finite element discretisation, and as accurate [30].

In a recent work [31], a finite element analysis was used to validate predictions obtained with a modal approach. In this modal approach, the key was to represent mechanical vibration using pure structural modes and temperature distribution using a summation of pure thermal modes. The approach concentrated on understanding the interactions between the mechanical strain and the thermal gradients. It was applied to simple beams and to more complicated slotted structures and showed good agreement with the finite element method.

It is important to note that thermoelastic damping is one of the most dominant damping mechanisms in structures with sizes in the range of a few microns to a few hundred microns. Sub-micron-sized structures have natural frequencies that are comparable to that of the lattice vibration of the material, and it is not possible to consider the system as an elastic continuum. Moreover, it is not possible to define the temperature locally and the definition of the thermal expansion coefficient is not valid [26]. For this range of sub-micron resonators, a transition from thermoelastic damping loss to surface-related loss (or material loss) is suggested [14].

1.3.4 Material losses

An ever-present source of energy loss in MEMS resonators is internal friction [14, 32]. This source is the most difficult to quantify, because it is dependent on the imperfections in the structure of the materials used and it is also highly dependent on fabrication methods.

Internal friction is the dissipation in the form of heat occurring when chemical bonds are made and broken. In a single-crystal beam, point defects and dislocations are the cause of internal friction. The quantity of point defects and dislocations in the beam can be estimated using probabilities. The energy loss due to a single defect or dislocation can be modelled and the overall internal friction derived using the total number of defects and dislocations estimated. In a polycrystalline material, the dominant cause of internal friction is grain boundaries. In an amorphous material, the friction is a bulk property, and is greater than the other two cases. The

irreversible energy lost in the relaxation phenomena when defects and chemical impurities in the material try to relax back to equilibrium, is the basis of the so-called material losses.

In addition, the surface state of a material can cause energy loss due to the fact that bonds are dangling at the edge of a crystal. Composite materials also have energy lost at the boundary between two layers.

Surface-related loss is an important damping mechanism for structures with high surface to volume ratio [33]. The surface to volume ratio increases as the thickness reduces. It is common for micro-structures to have a thin layer with different material properties on their surfaces due to the different fabrication processes and surface contamination. This layer of material with properties different from those of the bulk material can affect the achievable Q-factor significantly. There is no clear explanation on how surface treatments processes modify the surface property but it is expected to change the crystallographic orientation of the bulk material [34].

A thorough review of support loss, which is the mechanism of main interest in the thesis, is given in the next section.

1.4 Support loss

An essential energy loss mechanism is support loss – also referred to as anchor loss. Every resonator is attached to the surrounding structure, and this attachment creates a path for the radiation of vibrational energy away from the resonator. Elastic waves are created when the anchor moves, sending internal pressure waves out into the bulk material. These waves can be longitudinal or transverse, depending on the vibrational mode of the resonator and anchor attachment.

Innovative designs potentially allow the coupling between the resonator and its anchor to be removed [35], reducing energy loss by reducing anchor motion. Such systems may involve a mounting mechanism which isolates shear and moment reactions from the support. Support loss can also be reduced by properly designing the

resonator so that the vibrating structure is symmetric and vibrations do not result in motion of the centre of mass [19]. If resonators were unbalanced, energy loss would occur at the mounts. It is recommended that resonators should have a fixed centre of mass and zero total moments resulting from vibration. Stemme [19] reported examples of balanced structures including a dual-diaphragm resonant pressure sensor where the vibrating structure was suspended at the two nodal lines.

Another efficient design in the support loss point of view can be exemplified by the keys of a xylophone. When the free bar flexes in the fundamental mode, there are two places that have no translational motion – otherwise known as the nodal points. The vibrating elements are suspended not at the ends, but at these nodal points. By simply supporting the bar at those points, the coupling is minimised, resulting in reduced energy radiation through the support. In addition, it is worth noting that the higher modes tend to have nodal points at different places, meaning that the support will damp these modes quickly. This allows the xylophone to have a sustained, pure tonal sound. A similar design can minimise energy loss due to energy radiation through the anchor in MEMS resonators, although creating a simple support for a micro-mechanical beam is difficult. A perfect simple support has infinitesimally small width and exact position at the nodes. With very narrow resonators, it is difficult to make the support beams sufficiently small, and manufacturing errors ensure that the position of the support will not be exact.

Energy propagation into the supporting structure has received only limited attention. A variety of different computational approaches have been proposed by Park and Park [36, 37] and Bindel *et al.* [38, 39] but the most relevant analytic treatments appear to be those by Jimbo and Itao [40], Cross and Lifshitz [41], Hao *et al.* [42, 43] and Photiadis *et al.* [44, 45]. These approaches are reviewed below.

1.4.1 Computational approach

In 2004, Park and Park [36, 37] proposed a computational model for predicting the propagation of waves from a vibrating beam to the substrate. They developed a

multi-physics model consisting of a resonating beam model, a spatially distributed electrostatic model and a substrate model. They assumed that the wave propagation in the substrate was caused by external forces at the anchors. The substrate motion was then treated as a classical wave propagation problem into an elastic half-space foundation. This assumption is analogous to the one made in references [41, 42], in which, sinusoidal excitations were applied at the anchor area of the resonator beam to obtain the mechanical force-displacement relation at the anchor. The resulting coupled model was then used to evaluate the resonator performance, in particular, the Q-factor degradation due to the anchor loss.

The assumption that the substrate can be modelled as a semi-infinite elastic half-space has often been used. By considering the resonator to be much smaller than the substrate, very little energy leaving the resonator is reflected back and therefore the substrate can be seen as being semi-infinite from the perspective of the resonator. To simulate the response of a semi-infinite domain, boundary dampers, infinite elements, boundary integrals or exact Dirichlet-to-Neumann boundary conditions can be used (see *e.g.* [46–49]). Each of these methods in some way truncates the simulation domain with an artificial boundary and attempts to absorb outgoing wave energy without reflection. However, all of these techniques have some failings that are mainly a "non-total" dissipation of energy when waves are impinging the exterior boundaries, and a high computational cost when using finite element methods.

In 2005, Bindel *et al.* [38, 39] developed an approach to implement a Perfectly Matched Layer (PML) applied on a radially driven centre-supported disk resonator. This approach was based on the fundamental work done by Bérenger [50]. Bindel *et al.* described how anchor losses can be computed accurately using an absorbing boundary based on a PML which reduces incoming waves over a wide frequency range. A PML is a finite domain that is attached to the outer boundary of a (finite element) model which incorporates the system of interest – the resonator, its anchors and part of the substrate. The extension of the PML technique fits naturally within the standard finite element code architecture. The PML is a continuum domain devised in such way that the mechanical impedance between the PML and the

model is perfectly matched. This essentially eliminates spurious reflections from the artificial interface. The PML is finite in extent and thus has an outer boundary. The presence of this outer boundary requires the PML to damp the out-going waves before they reflect and "pollute" the computation. The out-going waves go through the interface with the PML without being reflected; they are massively damped in the PML region; few of them are reflected on the outer boundary of the PML; the resulting in-coming waves are damped again in such a way that almost no in-coming waves come back into the model.

1.4.2 Analytical approach

In 1968, Jimbo and Itao [40] derived an expression for the energy loss from a cantilever vibrator of infinite out-of-plane thickness attached to a semi-infinite medium. They compared the vibration energy of the cantilever with the energy associated with strain induced in the elastic medium by the shear force and bending moment at the root of the cantilever. They suggested that the Q-factor (Q_{support}) given by the developed model was:

$$Q_{\text{support}} \simeq 2.17 \left(\frac{L}{b}\right)^3 \frac{E_{\text{sup.}}}{E}, \tag{1.11}$$

where b and L are the in-plane width and length of the cantilever, respectively, E is the Young's modulus of the cantilever, and $E_{\text{sup.}}$ is the Young's modulus of the supporting medium.

In 2003, Hao *et al.* [42] derived a closed-form expression for support loss in beam resonator. The beam resonator was vibrating in-plane and had the same out-of-plane thickness as its support. They modelled support losses in beams with clamped-free and clamped-clamped boundaries. The flexural vibrations of the beam were described using beam theory. Elastic waves excited by the shear stress of the beam resonator and propagating into the support structure were described using two-dimensional elastic wave theory. Proposed expressions for the Q-factor of in-plane bending vibrations are functions of the cube of length to in-plane width ratio $(L/b)^3$

and are mode shape dependent. The model suggested lower quality factor for higher order resonant modes compared to the fundamental mode of a beam resonator. Hao *et al.* calculated the Q-factor for the fundamental mode of in-plane vibration of cantilever beam to be:

$$Q_{\text{support}} \simeq 2.081 \left(\frac{L}{b}\right)^3. \tag{1.12}$$

Later, the work was extended to a centre-supported disk resonator [43]. The same method was used: separation and coupling between the three components (disk, support beam, and support structure). The disk was modelled by a free-edged circular thin-plate as the support beam was much smaller in size and had negligible effect on the mode considered. Hence, explicit expressions for its resonant frequencies, mode shapes and vibration energy were derived. The displacement at the disk end of the support beam was found from the mode shapes of the disk. Through the support beam, this displacement is further transferred to the stress on the support structure (substrate). The support structure was modelled as a semi-infinite medium, through which part of the vibration energy propagates to infinity (in the form of elastic waves) and cannot return to the resonator, leading to energy loss. The behaviour of the support structure was described by the elastic wave theory, giving rise to the displacement under varying stress. From these displacements and stresses, the quality factor could be evaluated.

The analytical closed form expressions obtained in [42, 43] are particularly attractive to designers due to their simplicity, but the drawback is that they are only valid under the assumptions that are made and available for restricted geometries. Thus if the geometry is special such that the mechanism of damping is not known, this method is inapplicable.

More recently, Cross and Lifshitz [41] considered elastic wave transmission across the junction between two plates of differing widths (having the same out-of-plane thickness), and calculated the associated energy loss. With both systems assumed to be small compared to a wavelength, they determined that Q was linearly proportional to L/b for the fundamental compression mode, the torsion mode and the out-of-plane flexural mode, and that Q was proportional to $(L/b)^3$ for the in-plane

bending mode. They suggested that thin-plate elasticity theory provides a useful and tractable approximation to the three-dimensional geometry. The results showed that when the resonator-support coupling is large, it is important to consider the dissipation properties of the support structures as well as the resonator.

The main difference between all these analytical studies is the way that they treat the support structure. The support is either considered to be of infinite out-of-plane thickness [40] or as a plate equal in thickness to the resonator [41, 42].

Photiadis *et al.* [44, 45] analysed these two different cases. They provided analytical expressions for the energy loss from vibrating mechanical resonators into their support structures for two limiting cases: supports that can be treated as plates with a thickness that needs not to be the same as that of the resonator itself, and supports that act as semi-infinite elastic media, with effectively infinite thickness. The support loss resulting from out-of-plane vibration of a cantilevered beam and radiation into a supporting medium, modelled as a semi-infinite plate, was found to be:

$$Q_{\text{support}} \simeq 1.053 \, \frac{L}{b} \left(\frac{h_{\text{sup.}}}{h} \right)^2 , \tag{1.13}$$

where b is the in-plane width of the cantilever beam, and h and $h_{\text{sup.}}$ are respectively the out-of-plane thickness of the cantilever beam and the support structure. The in-plane width of the support is supposed to be infinite as the support is modelled as a semi-infinite plate. One can see here the same proportionality in L/b expressed by Cross and Lifshitz [41]. As the in-plane stiffness of the plate is much greater than its out-of-plane stiffness, Photiadis *et al.* did not consider in-plane vibrations of the beam and assumed that the attachment loss due to in-plane displacement is negligible compared to loss due to out-of-plane displacements. When the support structure was sufficiently thick relative to the wavelength of the propagating waves, the base was approximated as a semi-infinite elastic medium (a half-space) and the Q-factor for out-of-plane vibration was found to be:

$$Q_{\text{support}} \simeq 3.226 \, \frac{L}{b} \left(\frac{L}{h} \right)^4 . \tag{1.14}$$

All these different studies use the displacements of the resonator at its anchor end to evaluate the support loss. In the case of a rate sensor consisting of a ring supported on legs, the derivation of these displacements is not straightforward. The vibration of the ring resonator is firstly transmitted to its anchor legs, then it travels along the first beam section of the leg to be partially transmitted to the second beam section. The same process occurs between the second and third beams constituting the leg. The resulting vibration in the third and last beam section impinges on the anchor end and gives the required displacements. From this description it is clear that the transmission and propagation of vibrations through the structure is of principal interest in this work. The following section discusses this topic.

1.5 Vibration transmission and propagation

This section reviews the current literature relating the prediction of vibration transmission and propagation through a structure. From this study it was concluded that the ray tracing method is well suited to analysing the vibration transmission through the rate sensor at a particular frequency. A brief description of this method is introduced later in this section, and a more detailed examination of the method is provided in Chapter 2. Before this, a brief description of other available techniques is provided, with the strengths and weaknesses of each approach highlighted. The approaches considered are the Finite Element Analysis (FEA), the Statistical Energy Analysis and (SEA) the Energy Flow Analysis (EFA) based on wave propagation.

1.5.1 Finite element analysis

Finite element analysis (FEA) is widely used in industry to model complex structures subjected to various loads and stresses. The technique can also be applied to vibration problems. This is usually done in two stages. The mesh of the structures is analysed to calculate the mode shapes and natural frequencies of the structure.

Using this data the response of the structure is evaluated using a modal superposition technique.

Gavric and Pavic [51] developed a superposition technique approach to model the vibrational energy response in a structure using FEA. The results presented showed that the response at low frequencies is affected by higher order modes. If these higher order modes are ignored then the predicted results can become misleading. Therefore a more dense mesh is required which is capable of including these higher modes, so an accurate prediction of the response of the structure is obtained for the lower frequency range, which also limits this approach to low frequencies. This is a common problem encountered in FEA. As the frequency increases, so does the number of modes in the structure, requiring more elements and hence increasing computing time. The mesh has to contain a large number of elements and makes even relatively simple cases, at low modes, very expensive and time-consuming to run. This factor limits the application of FEA. Even the most powerful computer has an upper limit to the problem size it can handle economically.

To study, understand and quantify support losses in MEMS resonators, it is important to know which parameters have strong influence on energy losses. From a single FEA, it is not possible to derive the significant parameters and to get a precise description of the behaviour at the anchor end.

1.5.2 Statistical energy analysis

In the early 1960's the existing FEA approach was found to be of limited practical use for modelling light weight aerospace structures, due to the restrictions imposed to the size and frequency range of the model and the computational cost, which are still limiting factors today. Statistical Energy Analysis (SEA), developed by Lyon [52], considers a greatly simplified structure compared to FEA. Instead of considering the variation of the response as a spatially dependent factor, the structure is split into subsystems and the average energy density of each subsystem is evaluated over a frequency band. Each subsystem is assumed to contain a uniform

energy density. Due to this, SEA produces a single statistically averaged prediction of the response in each subsystem, per frequency band, which is not sensitive to slight variations in the structure.

Criteria have been set which the structure should meet to provide some confidence in the predicted response. The main restrictions are that there should be more than five to seven resonant modes in a frequency band, in each subsystem [53]; and that there should be a weak coupling between subsystems. These criteria are likely to be satisfied at higher frequencies, which can be far above the reliable frequency of FEA, leaving a gap in mid-frequency range.

Confusion is often formed by the term "low", "mid" and "high" frequency. The predictive approaches, such as SEA and FEA, are concerned with the number of modes present in the structures. The exact number of modes is dependent upon the structure itself. If the frequency considered is low, there tends to be a low number of modes excited in the structure (which favours the FEA approach), as the frequency increases the number of modes increases (which favours the SEA approach). The term "mid" frequency represents the frequency range where there are too many modes to apply FEA with confidence and too few modes to satisfy the SEA assumptions. In some structures this band between FEA and SEA may not be present. However, in many structures the SEA approach is not appropriate (*i.e.* strongly coupled subsystems) and there is a void in the analysis for the "mid" and "high" frequencies.

There is therefore a possible gap between the applicability of the FEA and SEA approaches in the mid-frequency range and for structures where SEA cannot be reliably applied. Due to this, a different approach has been required which can be applied to structures which are strongly coupled in the mid- to high-frequency range. This approach is the energy flow analysis based on wave propagation, see Section 1.5.3. It is simple to apply to structures and can be implemented using existing FEA software, which reduces the development costs.

Moreover, SEA approach is not applicable to gyroscopes as they operate at particular frequencies and only these frequencies are of interest – not a frequency band

containing several modes. Furthermore, SEA is usually used for systems that are not precisely known and defined. It gives an approximate description of the energy contained in these systems. For the case of support losses in MEMS gyroscopes, a precise and detailed evaluation of the energy transmitted to the support is needed.

1.5.3 Wave approach

The vibrations of elastic structures, such as strings, beams, and rings, can be described in terms of waves that propagate and decay in waveguides. Such waves are reflected and transmitted when incident upon discontinuities [54, 55]. For the rate sensor under investigation, the different components (ring and legs) effectively form a waveguide and a wave approach seems to be a suitable approach.

Ray tracing

Mace [56, 57] was one of the first to use a wave approach to determine the power flow between two coupled Euler-Bernoulli beams and the distribution of energy within the system. In his model, each subsystem was essentially one-dimensional, supporting just one wave type. Mace showed that when the coupling between the two beams is weak, peaks in coupling power occur near the natural frequencies of the uncoupled subsystems. Expanding the work of Mace, Langley [58] developed a ray tracing method to evaluate the response of one-dimensional structures subjected to harmonic excitation. The application of this approach to the ring-based rate sensor is presented in Chapter 2.

Simple rod structures were first studied by Langley [58]. Ashby [59] incorporated near-field effects and validated the method for a simply supported beam. A similar approach was used recently [60] to describe wave propagation, transmission and reflection in Timoshenko beams under various conditions. In Timoshenko beams, the effect of transverse shear deformation and rotary inertia are no longer neglected. Propagation, reflection and transmission matrices were given for different discon-

tinuities such as general point supports, boundaries and change in section in Timoshenko beam. When Timoshenko beam theory is used, the vibration analysis becomes more complex and further difficulties arise from the increasing complexity of structures. However from these matrices, the vibration analysis becomes systematic and concise.

The application of the ray tracing method relies on having knowledge of the detailed propagation, reflection, and transmission characteristics of waves in different parts of the system. In particular, the precise detail of the waves at discontinuities is needed to predict their reflection and transmission. For the ring-based resonator considered here, the discontinuities occur between the ring and supporting legs, and between connected beams in the supporting legs.

As this approach is "exact", the precise detail of the structure, joint, material properties and frequency is required. A slight change in one of these terms can significantly alter the predicted response.

Energy flow analysis

The basic premise of Energy Flow Analysis (EFA) is that the state of vibration can be essentially represented by stored, dissipated, and transferred far-field energy densities. This method translates into differential terms the basic hypotheses of SEA, based on the thermal propagation principle. SEA considers a power balance among macro-structures or finite subsystems, while in EFA the same laws are written for element volumes. The energy flow analysis or power flow method is found to provide a reasonable space, time and frequency-averaged prediction.

In 1987, Nefske and Sung [61] presented the "power flow finite element method" and made the link between the modelling of heat conductivity and vibrational energy flow. Successively, Palmer [62] made a detailed study of the application of EFA to predict the flow of flexural vibration in one-dimensional structures. Bernhard *et al.* [63, 64] gave the partial differential equations that govern the propagation of energy-related quantities in simple structural elements such as rods, beams and

plates. They also derived the coupling relationships in terms of energy-related quantities that describe the transfer of energy for various joint. To couple simple structural elements together, they used the power transmission and reflections coefficients – that can be found in the literature, *e.g.* in [55].

Ashby [59] developed an EFA that can incorporate the near-field and phase coherence effects into the predicted response; and an alternative approach to apply EFA to structures containing more that one type of vibration.

1.6 Summary of the literature review

From the review of various damping mechanisms presented in Sections 1.3 and 1.4, it can be summarised that thermoelastic damping has already been thoroughly investigated and gas damping can be eliminated by packaging the resonators in sufficiently low pressure environment. Internal losses and surface-related losses are intrinsic damping mechanisms that occur at the microscopic level of the materials or when the surface to volume ratio is large, and are difficult to model and quantify. Also, they are not yet really relevant to devices which are not particularly "thin". Support loss, an ever present mechanism as the resonator will always be attached to a support, has not been widely investigated and its research mainly consisted of analytical models which derived parametric description of energy losses in simple cantilever beam structures. Regarding the complex design of the MEMS vibrating ring-based resonator, it has been seen that a vibration transmission and propagation model is needed.

The EFA – as the SEA, gives frequency-averaged predictions. Broadband excitation is always considered, which is not appropriate for studying the case of a vibrating resonator. For a resonator, the frequencies of interest are its resonant frequencies and the resonator does not operate over a frequency range. An "exact" model for a particular frequency is needed. Furthermore, the approach used by the FEA solution is a modal technique, which assumes that the total response of the structure is given by the sum of the responses of individual modes. An exact approach to

model the vibrations of structure at a particular frequency is to use waves to form the resulting response; this is the foundation of the ray tracing method. From this literature review, the ray tracing analysis seems the most appropriated method as it relies on an "exact" wave approach that gives the behaviour of complex structures at particular frequencies.

1.7 Aims and objectives of the thesis

The research presented in this thesis is motivated by the need to gain an improved understanding of the energy dissipation mechanisms in vibrating MEMS structures used in vibrating rate sensors, and to develop models to predict and quantify damping levels arising from support losses. It is anticipated that this work will provide improved understanding of the dynamical behaviour of MEMS sensors, so as to improve design and prediction capabilities, and hence aid the development of sensors with better mechanical performance characteristics.

The work will focus on a fundamental study of support loss in vibrating ring-based resonators in which energy flows from the ring through the supporting legs into the surrounding structure. The main themes of work to be considered include the two following steps:

1. Developing models to predict the vibrational energy flow through structures composed of ring/beam components is the first step to quantify the energy that impinges into the surrounding structure. The different methods presented in Section 1.5 have shown that a wave approach, and especially the ray tracing method is well suited to study the vibrations of complex structures at a particular frequency. The ring-based resonator, and the energy flow occurring from the ring to the supporting legs will be of principal interest.

2. Developing models to predict the vibration transmitted from a resonator to its surrounding structure represents the second important step in the support loss modelling. The existing analytical approach [42] is only applicable to

flexural vibrations of beam resonators. It is therefore necessary to consider an extension of this approach that can deal with more complex structures. A model that considers vibrations of complex resonators must be developed and must efficiently deal with various MEMS design.

Initially, the work will consider in-plane vibrations of the resonator, representing existing single-axis rate sensors. However, the presence of out-of-plane vibrations of the resonator and the associated support losses will be considered later in the thesis to investigate damping in novel multi-axis rate sensors [8].

It is also of high interest to understand and quantify the influence of different parameters on the support loss and on the particular vibrational motion of the sensor. The possibility of another ring-based rate sensor design with better performance with regard to support loss damping needs to be investigated.

The next section gives an overview of the organisation of the thesis.

1.8 Outline of the thesis

The content of the remaining chapters in the thesis is summarised below.

Chapter 2 presents the fundamental vibration analysis of ring/beam structures by the ray tracing method. A wave approach is used to model the free and forced vibrations of complex networks. It is intended to find the natural frequencies and mode shapes of the ring-based resonator by this method. A validation process of the method is carried out using known analytical solutions of simple beam systems. The approach relies on the knowledge of transmission coefficients and they are derived for the different discontinuities encountered in the ring-based rate sensor.

Chapter 3 shows simplification methods to analyse structures that exhibit symmetry properties. This is applied, in particular, to the ring-based resonator which is cyclically symmetric. The extension of a method firstly developed for finite element

analysis is presented. It allows a great reduction of the number of unknowns in the model. The model complexity and the computing time that is used to solve the equations of wave propagation and transmission are reduced. With this simplification, natural frequencies and mode shapes of different cyclic symmetric systems are derived and the vibrations of the ring-based rate sensor are modelled by what is proved to be a fast and efficient method.

Chapter 4 links the vibration analysis of the ring-based resonator with the overall research aim, which is to quantify support losses. In-plane vibrations are considered and a model for support loss is presented based on an analytical study that sees the support as a semi-infinite thin plate. This model is validated using two different finite element approaches that model in a different way the infinite length of the support. Simple test cases are studied and the results for the support losses obtained are compared with the different methods.

The previous model developed in Chapter 4 is a rapid and efficient technique to model support losses. By combining this model with the ray tracing method presented in Chapter 2, the support losses of the ring-based rate sensor can be calculated. Results for support losses for different ring-based rate sensors designs are presented in Chapter 5. A few parameters, such as material properties or leg dimensions are modified and their influence on the Q-factor is analysed. Chapter 5 also studies the possibility to add blocking masses in the sensor in order to reduce support loss.

Novel multi-axis rate sensors are designed to vibrate both in- and out-of-plane. The ray tracing method presented in Chapter 2 is extended to out-of-plane vibrations in Chapter 6 in order to study the vibrations of such sensors. A model for support loss when the resonator vibrates out-of-plane is presented. It is based on the particular out-of-plane bending characteristics of the support modelled as a semi-infinite thin plate. Numerical results and a detailed discussion of the proposed models are given.

Chapter 7 is the final chapter that summarises the key findings of all the work presented in this thesis and proposes suitable future work in this area of research.

Figures

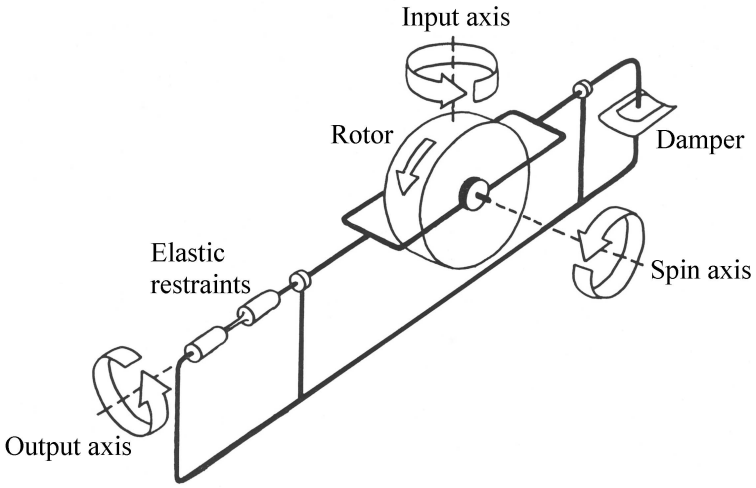

Figure 1.1: Traditional spinning rotor gyroscope.

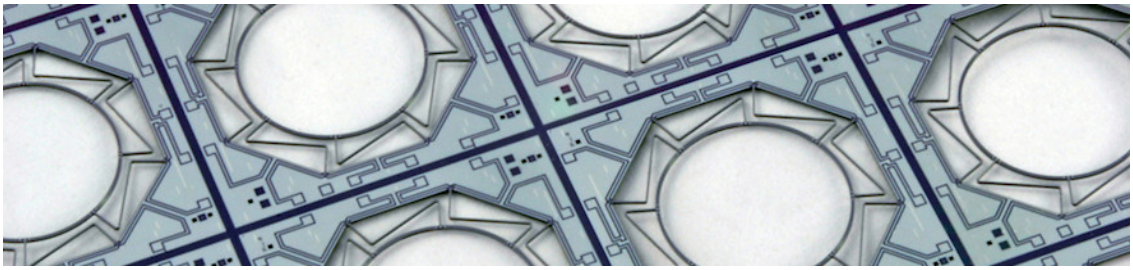

(a)

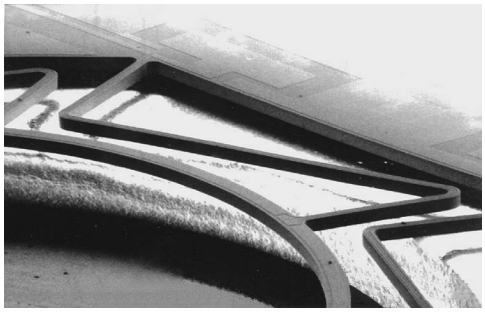

(b)

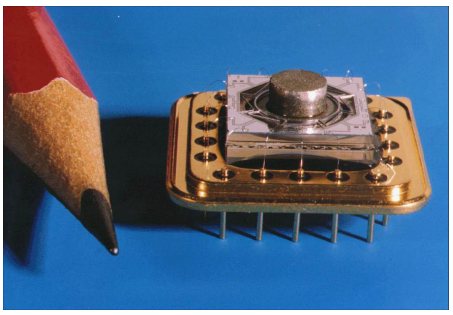

(c)

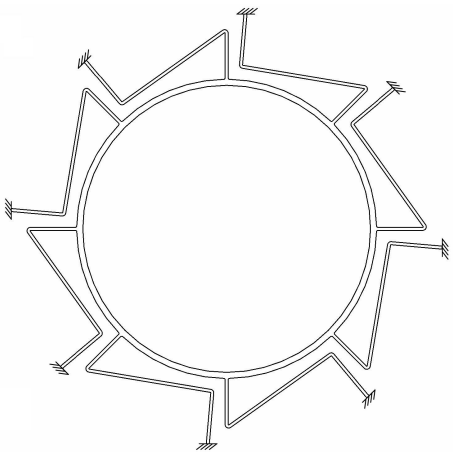

(d)

Figure 1.2: Photographs of the ring-based rate sensor: (a) on its silicon wafer, (b) details of the leg structure, and (c) mounted on its chip. (d) Schematic representation of the device.

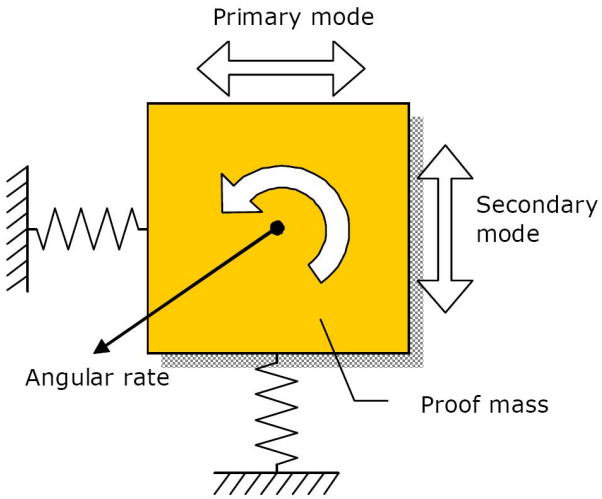

Figure 1.3: Schematic diagram of a simple mass-springs gyroscope.

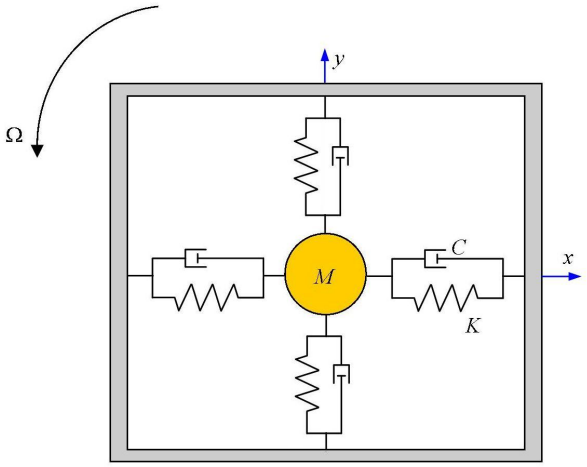

Figure 1.4: Schematic diagram of a vibrating gyroscope.

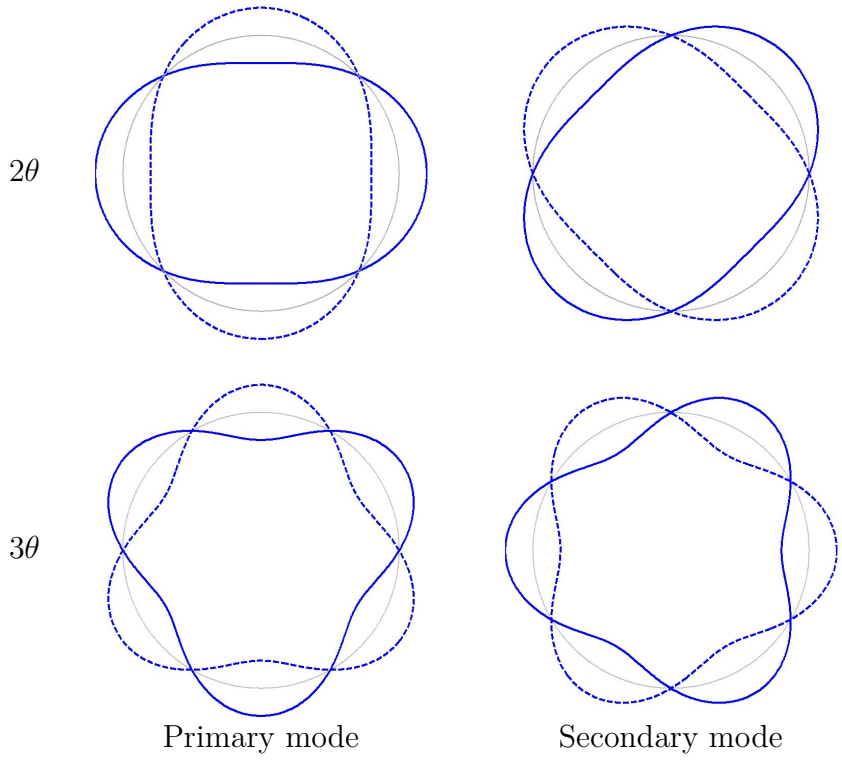

Figure 1.5: In-plane flexural modes of vibration of rings.

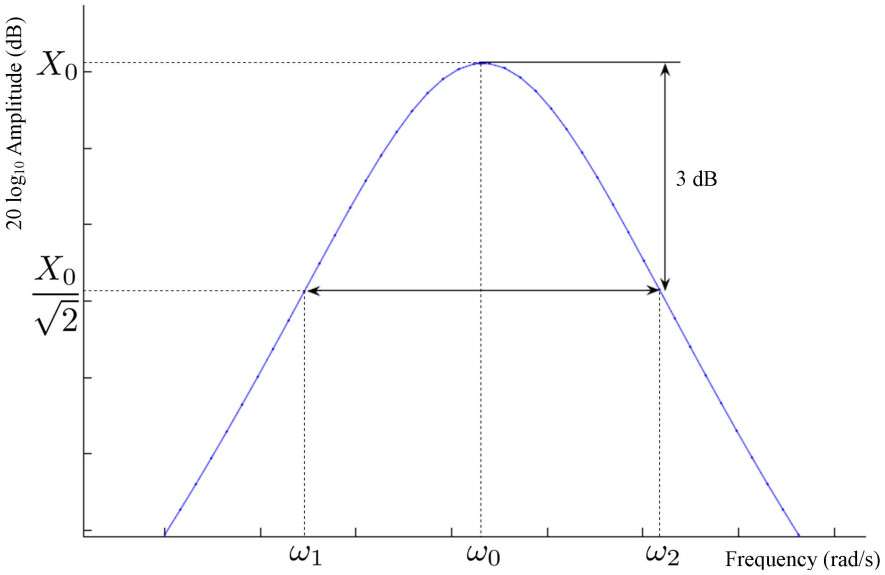

Figure 1.6: Various parameters shown on an amplitude-frequency response curve, used to calculate the Q-factor of a resonator.

Chapter 2

In-plane vibration analysis using a wave approach

2.1 Introduction

Engineering structures often consist of a number of components that can be modelled as straight and curved beams, and rings. Figure 2.1 shows a schematic representation of a MEMS ring-based rate sensor that is the main focus of interest in this thesis. The basic sensor structure is a resonator consisting of a slender circular ring, supported on slender legs as shown. Each leg consists of three straight beams. The design and optimisation of structures like these are aided greatly by the availability of efficient techniques to rapidly determine the effects of variations in geometry and dimensions on vibration characteristics, such as natural frequencies and mode shapes. The performance of MEMS sensors, like the one shown in Figure 2.1, is often highly dependent on the level of damping, see Chapter 1. One important damping mechanism is support loss or attachment loss [42, 44], which accounts for the transmission of vibration from the resonator into the supporting structure. The work reported in this chapter deals with the development of an efficient approach to analyse the vibrations of ring/beam structures that has the potential to be used to predict support losses. Chapters 4 and 5 will focus on predicting support losses

in ring-resonators.

The vibrational response of simple structures such as uncoupled beams or rings can be determined without difficulty [65] using the Rayleigh-Ritz or modal approaches. However, the analysis of complex systems containing several elements is more challenging. A possible method is the dynamic stiffness method [66, 67] that has been developed to analyse in-plane and out-of-plane vibrations of networks. Each component is modelled using an exact solution and matrices, coupling displacements and forces of each element with its neighbours, are considered. The Wittrick-Williams algorithm [68] is customarily applied to determine the natural frequencies of the system. An alternative method is the use of Finite Element (FE) packages that are employed widely to model complex structures, and can be used to calculate natural frequencies and mode shapes, and the vibration response. However, it is often computationally expensive if many different FE meshes need to be generated, when performing optimisation studies. In contrast, the wave-based approach considered in this chapter not only allows natural frequencies and mode shapes to be determined efficiently, but its formulation also allows the geometry and size of the structure to be varied easily and efficiently. The dynamic stiffness method, which is also based on an exact analysis, could have been applied at this point but wave approaches have proved to be powerful for analysing the energy transmission through structural networks [69], and their characteristics will be used in subsequent chapters to calculate support losses in MEMS structures.

As seen in Chapter 1, the vibrations of elastic structures, such as beams and rings, can be described in terms of waves that propagate and decay in waveguides. Such waves are reflected and transmitted when incident upon discontinuities [54, 55]. Expanding the work of Mace [56, 57], Langley [58] developed a ray tracing method to evaluate the response of one-dimensional structures subjected to harmonic excitation. This method was further exploited by Ashby [59] who incorporated near-field effects and validated the method for a simply supported beam. One of the earliest investigations of wave motion in curved beams was by Graff [54], who developed equations for a ring, accounting for extension, shear and rotary inertia. Dispersion curves were presented showing the effects of curvature, shear, and inertia on the

wave propagation. Kang *et al.* [70] extended the ray tracing method to planar circular curved beam structures including the effects of attenuating wave components. So far, the technique has not been used on complex structures, such as the one presented in Figure 2.1.

The principle behind the present approach is called phase closure [71] (also called wave-train closure [55]). This principle states that if the phase difference between incident and reflected waves is an integer multiple of 2π, then the waves propagate at a natural frequency and their motions constitute a vibration mode. The compact and systematic methodology of this approach allows complex structures, such as multi-span beams, trusses and aircraft panels with periodic supports to be analysed.

The application of the ray tracing method relies on having knowledge of the detailed propagation, reflection, and transmission characteristics of waves in different parts of the structure and particularly of their behaviour at discontinuities. The reflection and transmission of waves in Euler-Bernoulli beams at various discontinuities have been determined by Mace [72].

In the present chapter, the method has been extended to analyse the natural frequencies of a structure, such as that shown in Figure 2.1, which contains more complex discontinuities, like those arising between a ring and a straight beam. The method has also been extended to model the forced response of simple structures.

This chapter is organised as follows. Sections 2.2 and 2.3 provide a review of the basics of wave propagation in straight and curved beams, and show the development of the ray tracing method. Section 2.4 presents a derivation of the transmission coefficients for different discontinuities relevant to the structure of interest. Section 2.5 presents results for simple structures to validate the proposed ray tracing method for free and forced vibration analyses. Section 2.6 gives a summary and a statement of conclusions.

2.2 Wave propagation in beams

This section introduces the fundamental governing equations of motion of curved beams with constant radius, neglecting shear deformation and rotary inertia. A harmonic wave solution is used and the derivation of the corresponding wavenumbers is presented. By letting the radius of curvature tend to infinity, the equations and solutions are simplified to the case of straight beams. The equations obtained are well known [54] and are used extensively in later sections.

2.2.1 Curved beams

Consider a curved beam of constant radius of curvature as shown in Figure 2.2(a). The curved beam is characterised by the radius of curvature R, the cross-sectional area A, the second moment of area of the cross-section I_y, the Young's modulus E, and the mass density ρ. In Figure 2.2(a), S, T and M_1 are the resultant shear force, tensile force and bending moment, respectively, while u and w are the corresponding radial and tangential displacements. The circumferential coordinate along the centreline is denoted by s. For curved beams, the equations of motion can be expressed as [54]:

$$-EI_y\frac{\partial^3}{\partial s^3}\left(\frac{w}{R}+\frac{\partial u}{\partial s}\right)+\frac{EA}{R}\left(\frac{\partial w}{\partial s}-\frac{u}{R}\right)=\rho A\frac{\partial^2 u}{\partial t^2}, \tag{2.1}$$

$$\frac{EI_y}{R}\frac{\partial^2}{\partial s^2}\left(\frac{w}{R}+\frac{\partial u}{\partial s}\right)+EA\frac{\partial}{\partial s}\left(\frac{\partial w}{\partial s}-\frac{u}{R}\right)=\rho A\frac{\partial^2 w}{\partial t^2}. \tag{2.2}$$

In these coupled equations for u and w, the effect of rotary inertia and shear deformation are neglected. The equations of motion including these effects for circular rings and curved beams can be found in [65].

The axial force T, shear force S and bending moment M_1 are related to the dis-

placements by the relations:

$$T = EA\left(\frac{\partial w}{\partial s} - \frac{u}{R}\right), \tag{2.3}$$

$$M_1 = EI_y\frac{\partial}{\partial s}\left(\frac{\partial u}{\partial s} + \frac{w}{R}\right), \tag{2.4}$$

$$S = -EI_y\frac{\partial^2}{\partial s^2}\left(\frac{\partial u}{\partial s} + \frac{w}{R}\right). \tag{2.5}$$

The radial and tangential displacements satisfying Equations (2.1) and (2.2) are assumed to be time harmonic waves travelling in the positive s direction [55] and are expressed as:

$$u = \hat{u}\, e^{-\mathrm{i}(ks-\omega t)}, \tag{2.6a}$$

$$w = \hat{w}\, e^{-\mathrm{i}(ks-\omega t)}, \tag{2.6b}$$

where $\hat{u}$ and $\hat{w}$ are the amplitudes of the radial and tangential waves respectively, k is the associated wavenumber and ω is the circular frequency. Substituting Equations (2.6) into the equations of motion (2.1) and (2.2) gives:

$$\begin{bmatrix} -EI_yR^2k^4 + \rho R^2A\omega^2 - EA & -\mathrm{i}ERk\left(A + I_yk^2\right) \\ \mathrm{i}ERk\left(A + I_yk^2\right) & -Ek^2\left(AR^2 + I_y\right) + \rho R^2A\omega^2 \end{bmatrix} \begin{bmatrix} \hat{u} \\ \hat{w} \end{bmatrix} = \begin{bmatrix} 0 \\ 0 \end{bmatrix}. \tag{2.7}$$

Non-trivial solutions to Equation (2.7) give the characteristic (dispersion) equation for the wavenumber:

$$\left(E^2I_yR^4\right)k^6 - EI_yR^2\left(R^2\rho\omega^2 + 2E\right)k^4 - E\left(\rho R^2\omega^2\left(AR^2 + I_y\right) - EI_y\right)k^2 + A\rho R^2\omega^2\left(\rho R^2\omega^2 - E\right) = 0. \tag{2.8}$$

Equation (2.8) is a cubic equation in k^2 and has six complex roots $\pm k_i$ ($i = 1, 2, 3$) at any given frequency. If the wavenumber k_i is real and positive, then the displacement is given by:

$$u = \hat{u}\, e^{-\mathrm{i}k_is}. \tag{2.9}$$

This represents a wave travelling in the positive s direction. If the wavenumber is

complex, such that $k_i = \mathrm{Re}(k_i) + \mathrm{i}\,\mathrm{Im}(k_i)$, then:

$$u = \hat{u}\Big(e^{\,\mathrm{Im}(k_i)s}\, e^{-\mathrm{i}\,\mathrm{Re}(k_i)s} \Big). \tag{2.10}$$

To make this wave decay and propagate in the positive s direction, the basic rule applied to choose the appropriate wavenumbers among the six complex roots of (2.8) is: $\mathrm{Im}(k_i) \leq 0$ (that gives a wave decaying in the positive s direction) and $\mathrm{Re}(k_i) > 0$ (which makes the wave propagate in the positive s direction). A more detailed physical description of the complex wavenumbers in curved beams and the dispersion curves can be found in [73].

At a given frequency and as $R \to \infty$, the curved beam has an infinite radius and represents a straight beam. Alternatively, for a given radius, as $\omega \to \infty$, the curvature effect disappears and the wave travels as if the beam was straight. This ensures that straight and curved beams have a common limit as $R \to \infty$ and $\omega \to \infty$. This common limit provides a convenient way to characterise the resulting wavenumber, *i.e.*

- The root which tends to k_L (k_L being the wavenumber of longitudinal ("tangential") waves in a straight beam, see Section 2.2.2) when $R \to \infty$ or $\omega \to \infty$, is related to predominantly longitudinal waves and is denoted here by k_1.
- The roots which tend to k_{Fy} and $-\mathrm{i}k_{Fy}$ (k_{Fy} being the wavenumber of flexural ("radial") waves in a straight beam, see Section 2.2.2) when $R \to \infty$ or $\omega \to \infty$ are related to predominantly propagating far-field flexural waves and decaying near-field waves respectively. These roots will be denoted here by k_2 and k_3 respectively.

In any curved beam section, the radial and tangential displacements can be expressed as a sum of waves travelling in the right and left directions, *i.e.*:

$$u = \sum_{i=1}^{3} \left(\hat{u}_i^{+}\, e^{-\mathrm{i}k_i s} + \hat{u}_i^{-}\, e^{\mathrm{i}k_i(s-L)} \right) e^{\mathrm{i}\omega t}, \tag{2.11a}$$

$$w = \sum_{i=1}^{3} \left(\hat{w}_i^+ \, e^{-\mathrm{i}k_i s} + \hat{w}_i^- \, e^{\mathrm{i}k_i (s-L)} \right) e^{\mathrm{i}\omega t}. \tag{2.11b}$$

In these expressions, $\hat{u}_i^+$ and $\hat{w}_i^+$ are the complex amplitudes of the radial and tangential waves travelling in the positive s direction; while $\hat{u}_i^-$ and $\hat{w}_i^-$ are the complex amplitudes of the radial and tangential waves travelling in the negative s direction. The waves travelling in the positive s direction ($\hat{u}_i^+$, $\hat{w}_i^+$) originate from the location $s = 0$, whilst the waves travelling in the negative s direction ($\hat{u}_i^-$, $\hat{w}_i^-$) originate from the location $s = L$. In applications it is convenient to choose $s = 0$ and $s = L$ to be located at either end of the curved beam section.

From the analysis presented above it is clear that the radial and tangential displacements for a single curved section are defined by twelve unknown wave amplitudes. In general the amplitudes of these waves will depend on the waves propagating in other sections of the structure. However, for curved beams it can be shown that some of the radial and tangential wave amplitudes in a particular curved beam section are related to each other.

Substituting Equations (2.6) with appropriate wavenumbers into equation of motion (2.1), the following ratio X_i can be obtained:

$$X_i = \frac{\hat{u}_i^+}{\hat{w}_i^+} = -\frac{\hat{u}_i^-}{\hat{w}_i^-} = \frac{\mathrm{i}ERk_i\Big(I_y k_i^2 + A\Big)}{\rho R^2 A\omega^2 - \Big(EI_y R^2 k_i^4 + EA\Big)}. \tag{2.12}$$

The ratio X_i relates to the ratio of the radial to tangential wave amplitudes of waves travelling in the same direction that have the same wavenumber. Graphs of this coupling ratio as a function of the frequency can be found in [73]. Non-zero values of this ratio indicate that a radial wave of magnitude $\hat{u}_i^+$ is accompanied by a tangential wave of magnitude $X_i\hat{w}_i^+$ and a radial wave of magnitude $\hat{u}_i^-$ is accompanied by a tangential wave of magnitude $-X_i\hat{w}_i^-$. Thus for the wave amplitude pair ($\hat{u}_i^\pm$, $\hat{w}_i^\pm$) it is only necessary to determine one of the amplitudes, as the other is known implicitly from knowledge of the ratio X_i. As the amplitudes with subscript $i = 1$ are related to waves which are predominantly extensional, and those with subscript $i = 2$ and 3 to waves which are predominantly flexural (propagating and decaying

respectively), the six wave amplitudes $\left[\hat{w}_1^+, \hat{u}_2^+, \hat{u}_3^+, \hat{w}_1^-, \hat{u}_2^-, \hat{u}_3^-\right]$ are taken as primary unknowns. This coupling between the radial and tangential wave amplitudes indicates that six unknown wave amplitudes are needed to determine the radial and tangential displacements of each curved beam section – three travelling in the positive s direction, and three travelling in the negative s direction.

2.2.2 Simplification to straight beams

The equations derived for curved beams can be reduced to those for straight beams. The same notations are used and these are illustrated in Figure 2.2(b). By letting $R \to \infty$, the circumferential coordinate s is changed to a linear coordinate z, and Equations (2.1)-(2.5) give:

$$-EI\frac{\partial^4 u}{\partial z^4} = \rho A\frac{\partial^2 u}{\partial t^2}, \tag{2.13}$$

$$E\frac{\partial^2 w}{\partial z^2} = \rho\frac{\partial^2 w}{\partial t^2}, \tag{2.14}$$

$$T = EA\frac{\partial w}{\partial z}, \tag{2.15}$$

$$M_1 = EI_y\frac{\partial^2 u}{\partial z^2}, \tag{2.16}$$

$$S = -EI_y\frac{\partial^3 u}{\partial z^3}. \tag{2.17}$$

In these equations, u is the radial displacement, which is referred to as the flexural displacement for the straight beam case, and w is the tangential displacement, which is referred to as the longitudinal displacement for the straight beam case. It is important to note that for the straight beam case the equations governing the longitudinal and flexural displacements are uncoupled – this is in contrast to curved beams for which the tangential and radial equations are coupled. Following the same procedure to that followed for curved beams, the longitudinal and flexural displacements of straight beams are assumed to be time harmonic waves travelling in the positive z-direction, and are expressed in an identical form to Equations (2.6).

The dispersion equation for the straight beam case can be obtained easily by letting

$R \to \infty$ in Equation (2.8). This gives:

$$E^2 I_y k^6 - E I_y \rho \omega^2 k^4 - A E \rho \omega^2 k^2 + A \rho^2 \omega^4 = 0. \tag{2.18}$$

Since the longitudinal and flexural displacements are not coupled, Equation (2.18) can be factorised, such that:

$$\left(k^4 - \left(\omega \sqrt{\frac{\rho A}{EI}}\right)^2\right)\left(k^2 - \left(\omega \sqrt{\frac{\rho}{E}}\right)^2\right) = 0. \tag{2.19}$$

This equation has six roots $\pm k_i$ ($i = 1, 2, 3$), which are either purely real or purely imaginary, such that:

$$k_1 = k_L = \omega \sqrt{\frac{\rho}{E}}, \tag{2.20a}$$

$$k_2 = k_{Fy} = \sqrt{\omega \sqrt{\frac{\rho A}{EI}}}, \tag{2.20b}$$

$$k_3 = -\mathrm{i} k_{Fy} = -\mathrm{i} \sqrt{\omega \sqrt{\frac{\rho A}{EI}}}. \tag{2.20c}$$

Noting that the flexural and longitudinal displacements are not coupled, and that the ratios expressed in Equation (2.12) become $X_1 = 0$ and $X_2 = X_3 = \infty$ in a straight beam section, the flexural and longitudinal displacements can be described as the sum of waves travelling in the positive and negative z-directions, such that:

$$u = \left(\hat{u}_2^+ \, e^{-\mathrm{i} k_{Fy} z} + \hat{u}_3^+ \, e^{-k_{Fy} z} + \hat{u}_2^- \, e^{\mathrm{i} k_{Fy}(z-L)} + \hat{u}_3^- \, e^{k_{Fy}(z-L)}\right) e^{\mathrm{i}\omega t}, \tag{2.21a}$$

$$w = \left(\hat{w}_1^+ \, e^{-\mathrm{i} k_L z} + \hat{w}_1^- \, e^{\mathrm{i} k_L (z-L)}\right) e^{\mathrm{i}\omega t}. \tag{2.21b}$$

In these expressions, $\hat{w}_1^+$ and $\hat{w}_1^-$ are the complex amplitudes of the longitudinal waves propagating in the positive and negative z-directions respectively; $\hat{u}_2^+$ and $\hat{u}_2^-$ are the complex amplitudes of the flexural purely propagating waves in the positive and negative z-directions respectively; and $\hat{u}_3^+$ and $\hat{u}_3^-$ are the complex amplitudes of the flexural purely decaying (near field) waves in the positive and negative z-directions respectively. The waves travelling in the positive z-direction ($\hat{w}_1^+$, $\hat{u}_2^+$, $\hat{u}_3^+$) originate from the location $z = 0$, whilst the wave travelling in the negative

z-direction ($\hat{w}_1^-$, $\hat{u}_2^-$, $\hat{u}_3^-$) originate from the location $z = L$. In applications it is convenient to choose $z = 0$ and $z = L$ to be located at either end of the straight beam section.

The above equations indicate that six unknown wave amplitudes are needed to determine the longitudinal and flexural displacements – three travelling in the positive z-direction, and three travelling in the negative z-direction.

2.3 The ray tracing method

This section presents the development of the ray tracing method, which is an extension of the work carried out in [58]. It is based on a wave approach that is suitable for systems whose elements form waveguides. The technique, which is similar to the phase or wave-train closure principle [55] has been used previously for free vibration analysis of Timoshenko beams [60] or curved beams [70], but has not been used for complex networks such as the one presented in Figure 2.1. It provides a systematic approach to the free vibration analysis of complex waveguide structures, and is used here to analyse coupled curved/straight beam structures. An extension of the wave approach that deals with forced response of simple structures is also presented.

2.3.1 Simplified development for a two-beam example

To simplify the development and presentation, the case of a network composed of two straight beam components, coupled together at a discontinuity, and subjected to a harmonic vibration at frequency ω is considered, see Figure 2.3. The analysis is performed for this simple case and can be extended easily to more complex cases (see Section 2.3.2).

The longitudinal w and flexural u displacements in any component of the structure are defined as a sum of waves, see Section 2.2. The displacements at a location

having coordinate z in component (I) are expressed as:

$$w(z,t) = \left(\hat{w}_1^{(\mathrm{I})+}\, e^{-\mathrm{i}k_L z} + \hat{w}_1^{(\mathrm{I})-}\, e^{\mathrm{i}k_L (z-L^{(\mathrm{I})})}\right) e^{\mathrm{i}\omega t}, \tag{2.22}$$

$$u(z,t) = \left(\hat{u}_2^{(\mathrm{I})+}\, e^{-\mathrm{i}k_{Fy} z} + \hat{u}_3^{(\mathrm{I})+}\, e^{-k_{Fy} z} + \hat{u}_2^{(\mathrm{I})-}\, e^{\mathrm{i}k_{Fy} (z-L^{(\mathrm{I})})} + \hat{u}_3^{(\mathrm{I})-}\, e^{k_{Fy} (z-L^{(\mathrm{I})})}\right) e^{\mathrm{i}\omega t}, \tag{2.23}$$

where $L^{(\mathrm{I})}$ is the length of the component (I), $\hat{w}_1^{(\mathrm{I})\pm}$, $\hat{u}_2^{(\mathrm{I})\pm}$ and $\hat{u}_3^{(\mathrm{I})\pm}$ are the amplitudes of the longitudinal, flexural propagating and decaying waves, respectively in component (I). The amplitudes of waves travelling in the positive z-direction (with a superscript $+$) are defined at $z = 0$, while the ones corresponding to waves travelling in the negative z-direction (superscript $-$) are defined at $z = L^{(\mathrm{I})}$.

The ray tracing method considers an initial wave amplitude vector $\mathbf{a}_0$ which contains the initial waves amplitude sources in the "positive" and "negative" z-direction for each beam, see Figure 2.3. These waves start at any discontinuity and their amplitudes are maximum at the initial point. There are only non-zero terms in the excited beams. For the two-beam case considered, the initial wave amplitude vector has the form:

$$\mathbf{a}_{0_{[12\times 1]}} = \begin{bmatrix} \mathbf{u}_{initial}^{(\mathrm{I})+} & \mathbf{u}_{initial}^{(\mathrm{I})-} & \mathbf{u}_{initial}^{(\mathrm{II})+} & \mathbf{u}_{initial}^{(\mathrm{II})-} \end{bmatrix}^{\mathrm{T}}. \tag{2.24}$$

Each $\mathbf{u}_{initial}^{(j)\pm}$ represents the initial wave amplitude vector in component j ($j = \mathrm{I}$, II). $\mathbf{u}_{initial}^{(j)\pm}$ is a vector containing wave amplitudes corresponding to longitudinal, flexural and decaying waves and is defined as:

$$\mathbf{u}_{initial}^{(j)\pm} = \begin{bmatrix} \hat{w}1_{initial}^{(j)\pm} & \hat{u}2_{initial}^{(j)\pm} & \hat{u}3_{initial}^{(j)\pm} \end{bmatrix}. \tag{2.25}$$

While the waves travel from one end of the component to the other end, the propagating waves change phase and the decaying waves change amplitude. These effects depend on the wavenumber k_i ($k_i = k_L$, k_{Fy} or $-\mathrm{i}k_{Fy}$) and the length $L^{(j)}$ of the component. The complex amplitude of the waves changes from $\hat{u}_i^{(j)\pm}$ to $\hat{u}_i^{(j)\pm}\, e^{-\mathrm{i}k_i L^{(j)}}$. This phenomenon can be expressed using a diagonal matrix $\mathbf{D}$ called the dispersion matrix (or transfer matrix in [60]) whose diagonal elements have the form $\mathrm{D}_{ii} = e^{-\mathrm{i}k_i L^{(j)}}$, where k_i is the wavenumber associated with wave i and $L^{(j)}$ is

the corresponding beam length.

When a wave hits a discontinuity (boundary at the end of a component or discontinuity between two different elements), it can be either reflected back in the opposite direction or transmitted to another waveguide component. An incident wave of one type can induce reflected and transmitted waves of other types. For example, an incident flexural wave might induce reflected and transmitted flexural and longitudinal waves in all the components attached to the discontinuity. By considering the complex wave amplitude transmission and reflection coefficients, the amplitude of the waves leaving the discontinuity can be evaluated. This scattering at a discontinuity can be expressed in terms of a transmission matrix $\mathbf{T}$ of complex wave amplitude transmission/reflection coefficients, where $\hat{v}_i = \mathrm{T}_{ij}\hat{v}_j$ and T_{ij} is the transmission coefficient from a wave of amplitude $\hat{v}_j$ to a wave of amplitude $\hat{v}_i$.

The dispersion matrix has the form:

$$\mathbf{D}_{[12\times12]} = \begin{bmatrix} \boldsymbol{\Delta}_{L^{(\mathrm{I})}} & \mathbf{0} & \mathbf{0} & \mathbf{0} \\ \mathbf{0} & \boldsymbol{\Delta}_{L^{(\mathrm{I})}} & \mathbf{0} & \mathbf{0} \\ \mathbf{0} & \mathbf{0} & \boldsymbol{\Delta}_{L^{(\mathrm{II})}} & \mathbf{0} \\ \mathbf{0} & \mathbf{0} & \mathbf{0} & \boldsymbol{\Delta}_{L^{(\mathrm{II})}} \end{bmatrix}, \tag{2.26}$$

where $\boldsymbol{\Delta}_{L^{(j)}\,[3\times3]} = \begin{bmatrix} e^{-\mathrm{i}k_L L^{(j)}} & 0 & 0 \\ 0 & e^{-\mathrm{i}k_{Fy} L^{(j)}} & 0 \\ 0 & 0 & e^{-k_{Fy} L^{(j)}} \end{bmatrix}$, $j = \mathrm{I}, \mathrm{II}$. The transmission matrix has the form:

$$\mathbf{T}_{[12\times12]} = \begin{bmatrix} \mathbf{0} & \mathbf{R}^{(\mathrm{I})} & \mathbf{0} & \mathbf{0} \\ \mathbf{B}^{(\mathrm{I})+} & \mathbf{0} & \mathbf{0} & \boldsymbol{\Pi}^{(\mathrm{II})\to(\mathrm{I})} \\ \boldsymbol{\Pi}^{(\mathrm{I})\to(\mathrm{II})} & \mathbf{0} & \mathbf{0} & \mathbf{B}^{(\mathrm{II})-} \\ \mathbf{0} & \mathbf{0} & \mathbf{R}^{(\mathrm{II})} & \mathbf{0} \end{bmatrix}, \tag{2.27}$$

where $\mathbf{R}^{(\mathrm{I})}_{[3\times3]}$ and $\mathbf{R}^{(\mathrm{II})}_{[3\times3]}$ contain the reflection coefficients at the boundaries in beams (I) and (II) respectively; $\mathbf{B}^{(\mathrm{I})+}_{[3\times3]}$ and $\mathbf{B}^{(\mathrm{II})-}_{[3\times3]}$ contain the reflection coefficients at the discontinuity situated on the positive end of component (I) and the negative end

of component (II) respectively; $\mathbf{\Pi}_{[3\times3]}^{(i)\rightarrow(j)}$ contains the transmission coefficients from waves incident in beam (i) to beam (j).

After the waves have traversed along the length of the beam and one transmission has taken place, the new wave amplitude vector $\mathbf{a}_1$ can be written as:

$$\mathbf{a}_1 = \mathbf{TDa}_0. \tag{2.28}$$

This vector contains the wave amplitudes after one ray trace. This approach can be repeated to give the wave amplitudes after the next ray trace: $\mathbf{a}_2 = \mathbf{TDa}_1 = \Big(\mathbf{TD}\Big)^2\mathbf{a}_0$. The cycle of decay, propagation and transmission can be continued indefinitely. After an infinite number of ray traces, the total set of wave amplitudes $\mathbf{a}$ present in the structure is expressed as the sum of all the previous waves.

$$\mathbf{a} = \mathbf{a}_0 + \mathbf{a}_1 + \mathbf{a}_2 + \ldots + \mathbf{a}_\infty = \sum_{i=0}^{\infty}\Big(\mathbf{TD}\Big)^i\mathbf{a}_0. \tag{2.29}$$

Equation (2.29) is a geometric series with common ratio $\mathbf{TD}$ and first term $\mathbf{a}_0$. As $|\mathbf{TD}| < 1$, meaning that the amplitudes of the waves are attenuated from one trace to the next, it can be derived from Equation (2.29) that the final set of wave amplitudes $\mathbf{a}$ is governed by:

$$\Big(\mathbf{I} - \mathbf{TD}\Big)\mathbf{a} = \mathbf{a}_0, \tag{2.30}$$

where $\mathbf{I}$ is the identity matrix. In Equation (2.30), the term $\mathbf{a}$ represents the final set of wave amplitudes and defines the motion at any point in the system.

For the free vibration case, the initial wave amplitude vector is zero, and Equation (2.30) becomes:

$$\Big(\mathbf{I} - \mathbf{TD}\Big)\mathbf{a} = \mathbf{0}. \tag{2.31}$$

Non-trivial solutions to this equation occur when:

$$\Big|\mathbf{I} - \mathbf{TD}\Big| = 0. \tag{2.32}$$

This is the characteristic equation from which the natural frequencies of the system

can be found. This equation can be solved analytically for systems such as a simple beam with clamped, free or pinned boundary conditions or for a perfect ring (see Section 2.5.1). For more complex structures, a numerical solution is required.

The corresponding mode shape can be determined by back-substituting the frequency solutions ω_n in the **T** and **D** matrices, which are both frequency dependent, and calculating the corresponding wave amplitude vector **a** that is the solution to Equation (2.31). These wave amplitudes can be used in Equations (2.22) and (2.23) to determine the displacement mode shape.

2.3.2 Procedure development for a more complex example

The ray tracing method was presented above for a simple two-beam system, but can be extended easily to a more complex structure. Here it is applied to the ring-based rate sensor shown in Figure 2.1. In this example, the supporting legs consist of straight beams connected at different angles modelled as abrupt changes in direction, in contrast to real "radiused" angles as illustrated in Figure 1.2.

For simplification, the ray tracing method is applied here to only a single ring portion containing a single supporting leg. The set of initial wave amplitudes considered are presented in Figure 2.4. The system is divided into five different components: two ring portions (one on either side of the discontinuity ring/leg) and three straight beams. The initial wave amplitude vector is defined as:

$$\mathbf{a}_{0_{[30\times1]}} = \begin{bmatrix} \mathbf{u}_{initial}^{(\mathrm{I})+} & \mathbf{u}_{initial}^{(\mathrm{I})-} & \mathbf{u}_{initial}^{(\mathrm{II})+} & \mathbf{u}_{initial}^{(\mathrm{II})-} & \dots & \dots & \mathbf{u}_{initial}^{(\mathrm{V})+} & \mathbf{u}_{initial}^{(\mathrm{V})-} \end{bmatrix}^{\mathrm{T}}, \quad (2.33)$$

where $\mathbf{u}_{initial}^{(j)\pm} = \begin{bmatrix} \hat{w}1_{initial}^{(j)\pm} & \hat{u}2_{initial}^{(j)\pm} & \hat{u}3_{initial}^{(j)\pm} \end{bmatrix}$. Waves start at all discontinuities and in each direction. Their amplitude is taken to be maximum at their initial point. Equation (2.11) would imply the $\mathbf{u}_{initial}^{(j)\pm}$ to be of order six for the curved members; however, only three of these amplitudes are independent due to using the X_i ratio of Equation (2.12). In this example, $\mathbf{u}_{initial}^{(\mathrm{I})+}$ and $\mathbf{u}_{initial}^{(\mathrm{II})-}$ are evaluated at the joint with the neighbouring legs. The wavenumbers k_1, k_2 and k_3 (see Section 2.2) are associated with the amplitudes $\hat{w}_1^{(j)\pm}$, $\hat{u}_2^{(j)\pm}$ and $\hat{u}_3^{(j)\pm}$, respectively.

The transmission and dispersion matrices corresponding to Figure 2.4, with wave amplitude vector $\mathbf{a}$, defined in Equation (2.33), are as follows:

$$\mathbf{T}_{[30\times30]} = \begin{bmatrix} \mathbf{0} & \mathbf{R}^{(\mathrm{I})} & \mathbf{0} & \mathbf{0} & \mathbf{0} & \mathbf{0} \\ \mathbf{B}^{(\mathrm{I})+} & \mathbf{0} & \mathbf{0} & \mathbf{\Pi}^{(\mathrm{II})\to(\mathrm{I})} & \mathbf{0} & \mathbf{\Pi}^{(\mathrm{III})\to(\mathrm{I})} \\ \mathbf{\Pi}^{(\mathrm{I})\to(\mathrm{II})} & \mathbf{0} & \mathbf{0} & \mathbf{B}^{(\mathrm{II})-} & \mathbf{0} & \mathbf{\Pi}^{(\mathrm{III})\to(\mathrm{II})} \\ \mathbf{0} & \mathbf{0} & \mathbf{R}^{(\mathrm{II})} & \mathbf{0} & \mathbf{0} & \mathbf{0} \\ \mathbf{\Pi}^{(\mathrm{I})\to(\mathrm{III})} & \mathbf{0} & \mathbf{0} & \mathbf{\Pi}^{(\mathrm{II})\to(\mathrm{III})} & \mathbf{0} & \mathbf{B}^{(\mathrm{III})-} \\ \mathbf{0} & \mathbf{0} & \mathbf{0} & \mathbf{0} & \mathbf{B}^{(\mathrm{III})+} & \mathbf{0} \\ \mathbf{0} & \mathbf{0} & \mathbf{0} & \mathbf{0} & \mathbf{\Pi}^{(\mathrm{III})\to(\mathrm{IV})} & \mathbf{0} \\ \mathbf{0} & \mathbf{0} & \mathbf{0} & \mathbf{0} & \mathbf{0} & \mathbf{0} \\ \mathbf{0} & \mathbf{0} & \mathbf{0} & \mathbf{0} & \mathbf{0} & \mathbf{0} \\ \mathbf{0} & \mathbf{0} & \mathbf{0} & \mathbf{0} & \mathbf{0} & \mathbf{0} \end{bmatrix} \cdots \begin{bmatrix} \mathbf{0} & \mathbf{0} & \mathbf{0} & \mathbf{0} \\ \mathbf{0} & \mathbf{0} & \mathbf{0} & \mathbf{0} \\ \mathbf{0} & \mathbf{0} & \mathbf{0} & \mathbf{0} \\ \mathbf{0} & \mathbf{0} & \mathbf{0} & \mathbf{0} \\ \mathbf{0} & \mathbf{0} & \mathbf{0} & \mathbf{0} \\ \mathbf{0} & \mathbf{0} & \mathbf{0} & \mathbf{0} \\ \mathbf{0} & \mathbf{\Pi}^{(\mathrm{IV})\to(\mathrm{III})} & \mathbf{0} & \mathbf{0} \\ \mathbf{0} & \mathbf{B}^{(\mathrm{IV})-} & \mathbf{0} & \mathbf{0} \\ \mathbf{B}^{(\mathrm{IV})+} & \mathbf{0} & \mathbf{0} & \mathbf{\Pi}^{(\mathrm{V})\to(\mathrm{IV})} \\ \mathbf{\Pi}^{(\mathrm{IV})\to(\mathrm{V})} & \mathbf{0} & \mathbf{0} & \mathbf{B}^{(\mathrm{V})-} \\ \mathbf{0} & \mathbf{0} & \mathbf{R}^{(\mathrm{V})} & \mathbf{0} \end{bmatrix}, \tag{2.34}$$

$$\mathbf{D}_{[30\times30]} = \begin{bmatrix} \mathbf{\Delta}_{L^{(\mathrm{I})}} & \mathbf{0} & \mathbf{0} & \mathbf{0} & \dots & \mathbf{0} & \mathbf{0} \\ \mathbf{0} & \mathbf{\Delta}_{L^{(\mathrm{I})}} & \mathbf{0} & \mathbf{0} & \dots & \mathbf{0} & \mathbf{0} \\ \mathbf{0} & \mathbf{0} & \mathbf{\Delta}_{L^{(\mathrm{II})}} & \mathbf{0} & \dots & \mathbf{0} & \mathbf{0} \\ \mathbf{0} & \mathbf{0} & \mathbf{0} & \mathbf{\Delta}_{L^{(\mathrm{II})}} & \dots & \mathbf{0} & \mathbf{0} \\ \vdots & \vdots & \vdots & \vdots & \ddots & \mathbf{0} & \mathbf{0} \\ \mathbf{0} & \mathbf{0} & \mathbf{0} & \mathbf{0} & \mathbf{0} & \mathbf{\Delta}_{L^{(\mathrm{V})}} & \mathbf{0} \\ \mathbf{0} & \mathbf{0} & \mathbf{0} & \mathbf{0} & \mathbf{0} & \mathbf{0} & \mathbf{\Delta}_{L^{(\mathrm{V})}} \end{bmatrix}. \tag{2.35}$$

All matrix entities present in $\mathbf{T}$ and $\mathbf{D}$ are $[3 \times 3]$ matrices. The matrices $\mathbf{R}^{(j)}$

(j = I, II, V) contain the reflection coefficients at the boundaries. The boundaries in component (I) and (II) are not "real" boundaries in the ring-based rate sensor. They have been introduced here to demonstrate how the $\mathbf{T}$ matrix is formed. The wave amplitudes $\mathbf{u}^{(\mathrm{I})+}$ and $\mathbf{u}^{(\mathrm{II})-}$ are functions of the waves incident from the neighbouring legs and ring portions. The matrices $\mathbf{B}^{(j)+}$ and $\mathbf{B}^{(j)-}$ contain the reflection coefficients at the discontinuity situated at the positive or negative end of component (j). The matrices $\mathbf{\Pi}^{(i)\to(j)}$ contain the transmission coefficient from waves incident from component (i) to component (j). The $\mathbf{\Delta}_{L^{(j)}}$ matrices are defined as:

$$\mathbf{\Delta}_{L^{(j)}} = \begin{bmatrix} e^{-\mathrm{i}k_1 L^{(j)}} & 0 & 0 \\ 0 & e^{-\mathrm{i}k_2 L^{(j)}} & 0 \\ 0 & 0 & e^{-\mathrm{i}k_3 L^{(j)}} \end{bmatrix}. \tag{2.36}$$

For the straight beam sections (III), (IV) and (V), $k_1 = k_L$, $k_2 = k_{Fy}$ and $k_3 = -\mathrm{i}k_{Fy}$. The analysis performed is similar to the simple case considered in Section 2.3.1. However the matrices involved are much larger.

The transmission coefficients for discontinuities such as the ones encountered in the ring-based rate sensor are derived in Section 2.4. In a complex structure where the same discontinuity is encountered several times, the transmission coefficients only need to be calculated once. These coefficients will then be placed in the overall $\mathbf{T}$ matrix containing all transmission coefficients of the system. For example, for the entire ring-based rate sensor studied in Chapter 3, the overall matrices involved in the ray tracing method ($\mathbf{T}$ and $\mathbf{D}$) have a size of $[192 \times 192]$. But there are no more transmission coefficients needed than the ones presented in Equation (2.34). By solving Equation (2.32), the natural frequencies of the system can be calculated.

2.3.3 Forced response

The application of a force acts as a discontinuity in the structure. Applied harmonic point forces and moments have the effect of injecting waves on both sides of the disturbance. To simplify the analysis, the case of a straight beam is presented here but the same approach can be used to model the forced response of curved beams.

Consider a straight beam that is split in two components by the application of an external tensile force T_{ext}, a shear force S_{ext} and a bending moment M_{ext}, see Figure 2.5. The variables $\mathbf{u}^{(\text{I})+}$, $\mathbf{u}^{(\text{I})-}$, $\mathbf{u}^{(\text{II})+}$ and $\mathbf{u}^{(\text{II})-}$ model the waves impinging and leaving the discontinuity created by the applied forces. Each of them represents a set of wave amplitudes consisting of an extensional wave, a flexural propagating wave and a decaying wave:

$$\mathbf{u}^{(j)\pm} = \begin{bmatrix} \hat{w}_1^{(j)\pm} & \hat{u}_2^{(j)\pm} & \hat{u}_3^{(j)\pm} \end{bmatrix}. \tag{2.37}$$

The sets of wave amplitudes $\mathbf{u}_{\text{F}}^{\pm}$ introduced by the external forces are defined as:

$$\mathbf{u}_{\text{F}}^{+} = \mathbf{u}^{(\text{II})+} - \mathbf{u}^{(\text{I})+}, \tag{2.38}$$

$$\mathbf{u}_{\text{F}}^{-} = \mathbf{u}^{(\text{I})-} - \mathbf{u}^{(\text{II})-}. \tag{2.39}$$

By suppressing the temporal terms in the wave solutions (2.21), the longitudinal $w^{(j)}$ and flexural $u^{(j)}$ displacements in the component (j) ($j = \text{I, II}$) can be expressed in terms of wave amplitudes:

$$w^{(j)} = \hat{w}_1^{(j)+}\, e^{-\mathrm{i}k_L z} + \hat{w}_1^{(j)-}\, e^{\mathrm{i}k_L z}, \tag{2.40}$$

$$u^{(j)} = \hat{u}_2^{(j)+}\, e^{-\mathrm{i}k_{Fy} z} + \hat{u}_3^{(j)+}\, e^{-k_{Fy} z} + \hat{u}_2^{(j)-}\, e^{\mathrm{i}k_{Fy} z} + \hat{u}_3^{(j)-}\, e^{k_{Fy} z}. \tag{2.41}$$

Forces and moment equilibrium evaluated at the point of applied forces ($z = 0$) give:

$$T_{\text{ext}} = T^{(\text{I})} - T^{(\text{II})}, \tag{2.42}$$

$$S_{\text{ext}} = S^{(\text{I})} - S^{(\text{II})}, \tag{2.43}$$

$$M_{\text{ext}} = M_1^{(\text{I})} - M_1^{(\text{II})}, \tag{2.44}$$

where $T^{(j)}$, $S^{(j)}$ and $M_1^{(j)}$ are the internal tensile force, shear force and bending moment of the component (j) ($j = \text{I, II}$), and are defined in Equations (2.15)-(2.17). Using the displacement and slope continuity (at $z = 0$) between the two

components and Equations (2.37)-(2.44), one can derive that:

$$\mathbf{u}_{\mathrm{F}}^{+} = \begin{bmatrix} -\mathrm{i} & 0 & 0 \end{bmatrix} \frac{T_{\mathrm{ext}}}{2EAk_L} + \begin{bmatrix} 0 & -\mathrm{i} & -1 \end{bmatrix} \frac{S_{\mathrm{ext}}}{4EI_y k_{Fy}^3} + \begin{bmatrix} 0 & 1 & -1 \end{bmatrix} \frac{M_{\mathrm{ext}}}{4EI_y k_{Fy}^2}, \quad (2.45)$$

$$\mathbf{u}_{\mathrm{F}}^{-} = \begin{bmatrix} -\mathrm{i} & 0 & 0 \end{bmatrix} \frac{T_{\mathrm{ext}}}{2EAk_L} + \begin{bmatrix} 0 & -\mathrm{i} & -1 \end{bmatrix} \frac{S_{\mathrm{ext}}}{4EI_y k_{Fy}^3} - \begin{bmatrix} 0 & 1 & -1 \end{bmatrix} \frac{M_{\mathrm{ext}}}{4EI_y k_{Fy}^2}. \quad (2.46)$$

These are the amplitudes of the waves created by the applied forces, waves leaving the point of application of these forces.

For a forced response analysis, the ray tracing method presented in Section 2.3.1 takes into account the force terms $\mathbf{u}_{\mathrm{F}}^{+}$ and $\mathbf{u}_{\mathrm{F}}^{-}$ in the $\mathbf{a}_0$ term of Equation (2.30). Equation (2.30) can then be solved. It gives the set of wave amplitudes $\mathbf{a}$, which govern the displacement at any point of the structure. Application of this method on different beam systems is presented in Section 2.5.2.

As seen in Section 2.3, the ray tracing method requires several transmission coefficients matrices, and these are considered next.

2.4 Transmission coefficients

Transmission coefficients are used to quantify the reflection and transmission of waves when incident upon discontinuities [54, 55]. They are calculated by considering the continuity and force equilibrium equations at discontinuities taken in isolation from the rest of the structure. This section presents a derivation of the principal transmission coefficients encountered in common MEMS structures, such as the one presented in Figure 2.1. This includes reflection at beam boundaries, transmission through connected beams at abrupt junction, and transmission between a ring and an attached beam.

2.4.1 Ring/beam transmission

The general case for the transmission between a ring and an attached beam is investigated first. The configuration considered is shown in Figure 2.6. The beam forms an angle α with the ring. The discontinuity is modelled as a rigid joint (cylindrical mass) connecting two ring portions and a beam. This joint has been introduced to study the influence on the transmission coefficients of an added mass or inertia at the discontinuity. This analysis is an extension of the work carried out in [59] that studied the energy transmission between straight beams.

In Figure 2.6, the subscripts r and b relate to the ring and the beam respectively, the superscript (j) (j = I, II, III) corresponds to the component considered (two ring parts and one beam part), the superscript k ($k = +, -$) corresponds to the direction of propagation of the waves (positive and negative direction respectively). Each of the variables $\mathbf{u}_r^{(\mathrm{I})+}$, $\mathbf{u}_r^{(\mathrm{I})-}$, $\mathbf{u}_r^{(\mathrm{II})+}$, $\mathbf{u}_r^{(\mathrm{II})-}$, $\mathbf{u}_b^{(\mathrm{III})+}$ and $\mathbf{u}_b^{(\mathrm{III})-}$ represents a set of wave amplitudes consisting of a principal extensional wave, a principal flexural propagating wave, and a principal decaying wave:

$$\mathbf{u}_{r,\,b}^{(j)\pm} = \left[\hat{w}_1^{(j)\pm} \quad \hat{u}_2^{(j)\pm} \quad \hat{u}_3^{(j)\pm}\right]. \tag{2.47}$$

In addition, the waves represented by a plain arrow in Figure 2.6 relate to waves incident on the discontinuity, while the dashed arrows are transmitted or reflected waves.

To obtain a general method, the wave incident on the joint along the first portion, which can be a straight beam or a circular bar, is assumed to be either predominantly flexural, longitudinal or decaying in nature. The presence of the joint ensures that part of this wave is reflected back along the same portion and the remainder is transmitted into the other portions. This partial reflection is also accompanied by mode conversion, so that the incident wave can generate flexural, longitudinal and decaying wave components in each of the three portions.

Assembly of the equilibrium and continuity expressions at the joint yields a system of simultaneous equations that can be solved to provide values for the required

transmission coefficients for each wave type. The transmission matrix $\mathbf{T}_{\text{ring/beam}}$ contains the transmission coefficients from any wave type, in any portion to any resulting wave after transmission or reflection. For example, in the case presented in Figure 2.6, the equilibrium and continuity equations can be derived as follows. By suppressing the temporal terms in the wave solutions (2.11) and (2.21), the transverse displacements $u_r^{(\mathrm{I})}$, $u_r^{(\mathrm{II})}$ and $u_b^{(\mathrm{III})}$; the tangential displacements $w_r^{(\mathrm{I})}$, $w_r^{(\mathrm{II})}$ and $w_b^{(\mathrm{III})}$; and the rotations of cross-section $\psi_r^{(\mathrm{I})}$, $\psi_r^{(\mathrm{II})}$ and $\psi_b^{(\mathrm{III})}$ at the ring portion (I) (left), the ring portion (II) (right) and the beam portion (III), respectively, can be expressed in terms of wave amplitudes.

By considering input waves coming from the ring portion (I) only, the displacements and slopes involved are:

Ring portion (I):

$$\begin{aligned} u_r^{(\mathrm{I})}(s) = {} & X_1\hat{w}_1^{(\mathrm{I})+}e^{-\mathrm{i}k_1 s} + \hat{u}_2^{(\mathrm{I})+}e^{-\mathrm{i}k_2 s} + \hat{u}_3^{(\mathrm{I})+}e^{-\mathrm{i}k_3 s} \\ & - X_1\hat{w}_1^{(\mathrm{I})-}e^{\mathrm{i}k_1 s} + \hat{u}_2^{(\mathrm{I})-}e^{\mathrm{i}k_2 s} + \hat{u}_3^{(\mathrm{I})-}e^{\mathrm{i}k_3 s}, \end{aligned} \tag{2.48}$$

$$\begin{aligned} w_r^{(\mathrm{I})}(s) = {} & \hat{w}_1^{(\mathrm{I})+}e^{-\mathrm{i}k_1 s} + \frac{1}{X_2}\hat{u}_2^{(\mathrm{I})+}e^{-\mathrm{i}k_2 s} + \frac{1}{X_3}\hat{u}_3^{(\mathrm{I})+}e^{-\mathrm{i}k_3 s} \\ & + \hat{w}_1^{(\mathrm{I})-}e^{\mathrm{i}k_1 s} - \frac{1}{X_2}\hat{u}_2^{(\mathrm{I})-}e^{\mathrm{i}k_2 s} - \frac{1}{X_3}\hat{u}_3^{(\mathrm{I})-}e^{\mathrm{i}k_3 s}, \end{aligned} \tag{2.49}$$

$$\psi_r^{(\mathrm{I})}(s) = \frac{\partial u_r^{(\mathrm{I})}(s)}{\partial s} + \frac{w_r^{(\mathrm{I})}(s)}{R}. \tag{2.50}$$

Ring portion (II):

$$u_r^{(\mathrm{II})}(s) = X_1\hat{w}_1^{(\mathrm{II})+}e^{-\mathrm{i}k_1 s} + \hat{u}_2^{(\mathrm{II})+}e^{-\mathrm{i}k_2 s} + \hat{u}_3^{(\mathrm{II})+}e^{-\mathrm{i}k_3 s}, \tag{2.51}$$

$$w_r^{(\mathrm{II})}(s) = \hat{w}_1^{(\mathrm{II})+}e^{-\mathrm{i}k_1 s} + \frac{1}{X_2}\hat{u}_2^{(\mathrm{II})+}e^{-\mathrm{i}k_2 s} + \frac{1}{X_3}\hat{u}_3^{(\mathrm{II})+}e^{-\mathrm{i}k_3 s}, \tag{2.52}$$

$$\psi_r^{(\mathrm{II})}(s) = \frac{\partial u_r^{(\mathrm{II})}(s)}{\partial s} + \frac{w_r^{(\mathrm{II})}(s)}{R}. \tag{2.53}$$

Beam portion (III):

$$u_b^{(\mathrm{III})}(z) = \hat{u}_2^{(\mathrm{III})+}e^{-\mathrm{i}k_{Fy} z} + \hat{u}_3^{(\mathrm{III})+}e^{-k_{Fy} z}, \tag{2.54}$$

$$w_b^{(\mathrm{III})}(z) = \hat{w}_1^{(\mathrm{III})+}e^{-\mathrm{i}k_L z}, \tag{2.55}$$

$$\psi_b^{(\mathrm{III})}(z) = \frac{\partial u_b^{(\mathrm{III})}(z)}{\partial z}. \tag{2.56}$$

Incident waves coming from the ring portion (II) and the beam portion (III) need also to be considered.

Assuming that the joint is located at $s = 0$ (or $z = 0$), displacement and slope continuity ensures that:

$$u_r^{(\mathrm{I})} + \frac{d_j}{2}\psi_r^{(\mathrm{I})} = u_r^{(\mathrm{II})} - \frac{d_j}{2}\psi_r^{(\mathrm{II})}, \tag{2.57}$$

$$w_r^{(\mathrm{I})} = w_r^{(\mathrm{II})}, \tag{2.58}$$

$$\psi_r^{(\mathrm{I})} = \psi_r^{(\mathrm{II})}, \tag{2.59}$$

$$u_r^{(\mathrm{I})} + \frac{d_j}{2}\psi_r^{(\mathrm{I})} = -w_b^{(\mathrm{III})}\sin\alpha + \left(u_b^{(\mathrm{III})} - \frac{d_j}{2}\psi_b^{(\mathrm{III})}\right)\cos\alpha, \tag{2.60}$$

$$w_r^{(\mathrm{I})} = w_b^{(\mathrm{III})}\cos\alpha + \left(u_b^{(\mathrm{III})} - \frac{d_j}{2}\psi_b^{(\mathrm{III})}\right)\sin\alpha, \tag{2.61}$$

$$\psi_r^{(\mathrm{I})} = \psi_b^{(\mathrm{III})}, \tag{2.62}$$

where d_j is the diameter of the cylindrical rigid joint. The tensile forces $T_r^{(\mathrm{I})}$, $T_r^{(\mathrm{II})}$ and $T_b^{(\mathrm{III})}$; shear forces $S_r^{(\mathrm{I})}$, $S_r^{(\mathrm{II})}$ and $S_b^{(\mathrm{III})}$; bending moments $M_r^{(\mathrm{I})}$, $M_r^{(\mathrm{II})}$ and $M_b^{(\mathrm{III})}$ of the ring portion (I) (left), the ring portion (II) (right) and the beam portion (III), respectively, evaluated at the joint at $s = 0$ (or $z = 0$) are related by the equations:

$$-S_r^{(\mathrm{I})} + S_r^{(\mathrm{II})} - T_b^{(\mathrm{III})}\sin\alpha + S_b^{(\mathrm{III})}\cos\alpha = m_j\frac{\partial^2}{\partial t^2}\left(u_r^{(\mathrm{I})} + \frac{d_j}{2}\psi_r^{(\mathrm{I})}\right), \tag{2.63}$$

$$-T_r^{(\mathrm{I})} + T_r^{(\mathrm{II})} + T_b^{(\mathrm{III})}\cos\alpha + S_b^{(\mathrm{III})}\sin\alpha = m_j\frac{\partial^2}{\partial t^2}w_r^{(\mathrm{I})}, \tag{2.64}$$

$$-M_r^{(\mathrm{I})} + M_r^{(\mathrm{II})} + M_b^{(\mathrm{III})} + \frac{d_j}{2}\left(S_r^{(\mathrm{I})} + S_r^{(\mathrm{II})} + S_b^{(\mathrm{III})}\right) = I_{y_j}\frac{\partial^2}{\partial t^2}\psi_r^{(\mathrm{I})}, \tag{2.65}$$

where m_j is the mass of the joint, and I_{y_j} is its moment of inertia along the y-axis (perpendicular to the plane of the ring). The transmission coefficients $\hat{u}_j/\hat{u}_i$ from an incident wave $\hat{u}_i$ to a reflected or transmitted wave $\hat{u}_j$ ($\hat{w}_1^{(\mathrm{I})-}/\hat{w}_1^{(\mathrm{I})+}$, $\hat{u}_2^{(\mathrm{I})-}/\hat{w}_1^{(\mathrm{I})+}$, $\hat{u}_3^{(\mathrm{I})-}/\hat{w}_1^{(\mathrm{I})+}$, etc ...) can be obtained by solving the above equations. Considering incident waves from all three portions and solving the resulting $[9 \times 9]$ system of equations gives a $[9 \times 9]$ matrix $\mathbf{T}_{\text{ring/beam}}$ that contains all the transmission coefficients such that:

$$\mathbf{a}_{\text{transmitted}} = \mathbf{T}_{\text{ring/beam}}\,\mathbf{a}_{\text{incident}}, \tag{2.66}$$

with:

$$\mathbf{T}_{\text{ring/beam}_{[9\times9]}} = \begin{bmatrix} \mathbf{\Pi}^{(\text{I})\rightarrow(\text{II})} & \mathbf{B}^{(\text{II})-} & \mathbf{\Pi}^{(\text{III})\rightarrow(\text{II})} \\ \mathbf{B}^{(\text{I})+} & \mathbf{\Pi}^{(\text{II})\rightarrow(\text{I})} & \mathbf{\Pi}^{(\text{III})\rightarrow(\text{I})} \\ \mathbf{\Pi}^{(\text{I})\rightarrow(\text{III})} & \mathbf{\Pi}^{(\text{II})\rightarrow(\text{III})} & \mathbf{B}^{(\text{III})-} \end{bmatrix}, \tag{2.67}$$

$\mathbf{a}_{\text{transmitted}_{[9\times1]}} = \begin{bmatrix} \mathbf{u}_r^{(\text{II})+} & \mathbf{u}_r^{(\text{I})-} & \mathbf{u}_b^{(\text{III})+} \end{bmatrix}^{\text{T}}$ and $\mathbf{a}_{\text{incident}_{[9\times1]}} = \begin{bmatrix} \mathbf{u}_r^{(\text{I})+} & \mathbf{u}_r^{(\text{II})-} & \mathbf{u}_b^{(\text{III})-} \end{bmatrix}^{\text{T}}$. Each $\mathbf{u}_{r,b}^{(j)\pm}$ is defined as in Equation (2.47) and the matrices contained in $\mathbf{T}_{\text{ring/beam}}$ are presented in Section 2.3.2.

When $\alpha = 90°$, certain aspects of the matrix $\mathbf{T}_{\text{ring/beam}}$ display symmetric characteristics. For example, the transmission coefficient from an extensional wave in the left ring portion to an extensional wave in the right ring portion is the same as in reverse (*i.e.* $\hat{w}_1^{(\text{II})+}/\hat{w}_1^{(\text{I})+} = \hat{w}_1^{(\text{I})-}/\hat{w}_1^{(\text{II})-}$). More generally, when $\alpha = 90°$, the following symmetric relationship can be seen between the magnitudes of the transmission coefficients: $\left|\mathbf{\Pi}^{(\text{I})\rightarrow(\text{II})}\right| = \left|\mathbf{\Pi}^{(\text{II})\rightarrow(\text{I})}\right|$, $\left|\mathbf{\Pi}^{(\text{III})\rightarrow(\text{I})}\right| = \left|\mathbf{\Pi}^{(\text{III})\rightarrow(\text{II})}\right|$, $\left|\mathbf{\Pi}^{(\text{I})\rightarrow(\text{III})}\right| = \left|\mathbf{\Pi}^{(\text{II})\rightarrow(\text{III})}\right|$ and $\left|\mathbf{B}^{(\text{I})+}\right| = \left|\mathbf{B}^{(\text{II})-}\right|$. All notations are defined in Section 2.3.2. The absolute values are needed so that the direction of propagation (positive or negative s direction) is not taken into account.

2.4.2 Transmission at an abrupt change in direction

To obtain the transmission coefficients for two beams joined at an angle without using a rigid joint mass element (see Figure 2.7), Equations (2.57)-(2.65) can be used. Note that the angles α in Figures 2.6 and 2.7) are defined in the opposite direction. The terms referring to ring portion (II) and the terms involving the coefficients X_i, which represent the coupling between radial and tangential displacements in a ring, are suppressed. A $[6 \times 6]$ system of equations that models force and displacement continuity at the junction is obtained:

$$u_b^{(\text{I})} = w_b^{(\text{II})} \sin\alpha + u_b^{(\text{II})} \cos\alpha, \tag{2.68}$$

$$w_b^{(\text{I})} = w_b^{(\text{II})} \cos\alpha - u_b^{(\text{II})} \sin\alpha, \tag{2.69}$$

$$\frac{\partial u_b^{(\text{I})}}{\partial x} = \frac{\partial u_b^{(\text{II})}}{\partial x}, \tag{2.70}$$

$$S_b^{(\mathrm{I})} = T_b^{(\mathrm{II})} \sin\alpha + S_b^{(\mathrm{II})} \cos\alpha, \tag{2.71}$$

$$T_b^{(\mathrm{I})} = T_b^{(\mathrm{II})} \cos\alpha - S_b^{(\mathrm{II})} \sin\alpha, \tag{2.72}$$

$$M_b^{(\mathrm{I})} = M_b^{(\mathrm{II})}. \tag{2.73}$$

By considering an incident set of waves $\mathbf{a}_{\mathrm{incident}_{[6\times1]}} = \begin{bmatrix} \mathbf{u}_b^{(\mathrm{I})+} & \mathbf{u}_b^{(\mathrm{II})-} \end{bmatrix}^{\mathrm{T}}$ containing an extensional wave, a propagating wave and a decaying wave travelling in the positive z-direction of (I) and negative z-direction of (II), and a transmitted/reflected set of waves $\mathbf{a}_{\mathrm{created}_{[6\times1]}} = \begin{bmatrix} \mathbf{u}_b^{(\mathrm{II})+} & \mathbf{u}_b^{(\mathrm{I})-} \end{bmatrix}^{\mathrm{T}}$, the equations that give the transmission coefficients matrix $\mathbf{T}_{\mathrm{abrupt\,angle}}$ such that $\mathbf{a}_{\mathrm{created}} = \mathbf{T}_{\mathrm{abrupt\,angle}}\, \mathbf{a}_{\mathrm{incident}}$ can be expressed as:

$$\begin{aligned} &\begin{bmatrix} \cos\alpha & -\sin\alpha & -\sin\alpha & -1 & 0 & 0 \\ \sin\alpha & \cos\alpha & \cos\alpha & 0 & -1 & -1 \\ 0 & \mathrm{i} & 1 & 0 & \mathrm{i} & 1 \\ \mathrm{i}\cos\alpha & -\mathrm{i}\sqrt{\Omega}\sin\alpha & \sqrt{\Omega}\sin\alpha & \mathrm{i} & 0 & 0 \\ \mathrm{i}\sin\alpha & \mathrm{i}\sqrt{\Omega}\cos\alpha & -\sqrt{\Omega}\cos\alpha & 0 & \mathrm{i}\sqrt{\Omega} & -\sqrt{\Omega} \\ 0 & -1 & 1 & 0 & 1 & -1 \end{bmatrix} \cdot \mathbf{T}_{\mathrm{abrupt\,angle}} \\ &= \begin{bmatrix} 1 & 0 & 0 & -\cos\alpha & \sin\alpha & \sin\alpha \\ 0 & 1 & 1 & -\sin\alpha & -\cos\alpha & -\cos\alpha \\ 0 & \mathrm{i} & 1 & 0 & \mathrm{i} & 1 \\ \mathrm{i} & 0 & 0 & \mathrm{i}\cos\alpha & -\mathrm{i}\sqrt{\Omega}\sin\alpha & \sqrt{\Omega}\sin\alpha \\ 0 & \mathrm{i}\sqrt{\Omega} & -\sqrt{\Omega} & \mathrm{i}\sin\alpha & \mathrm{i}\sqrt{\Omega}\cos\alpha & -\sqrt{\Omega}\cos\alpha \\ 0 & -1 & 1 & 0 & 1 & -1 \end{bmatrix}, \end{aligned} \tag{2.74}$$

with $\Omega = \omega\sqrt{\dfrac{I\rho}{EA}}$ and $\mathbf{T}_{\mathrm{abrupt\,angle}} = \begin{bmatrix} \mathbf{\Pi}^{(\mathrm{I})\to(\mathrm{II})} & \mathbf{B}^{(\mathrm{II})-} \\ \mathbf{B}^{(\mathrm{I})+} & \mathbf{\Pi}^{(\mathrm{II})\to(\mathrm{I})} \end{bmatrix}$ (see also the corresponding notation in Section 2.3.2).

Again, from the symmetry of the system, one can get the relationship: $\left|\mathbf{\Pi}^{(\mathrm{I})\to(\mathrm{II})}\right| = \left|\mathbf{\Pi}^{(\mathrm{II})\to(\mathrm{I})}\right|$ and $\left|\mathbf{B}^{(\mathrm{I})+}\right| = \left|\mathbf{B}^{(\mathrm{II})-}\right|$.

2.4.3 Wave reflection at common boundaries

The well-known reflection coefficients of waves in a beam at common boundaries such as clamped, free or pinned ends are derived in [54, 55]. Using the same notation as before, if an incident set of wave with amplitudes $\mathbf{a}_{\text{incident}}$, defined as

$$\mathbf{a}_{\text{incident}} = \left[\mathbf{u}_b^+\right]^{\text{T}} = \begin{bmatrix} \hat{w}_1^+ & \hat{u}_2^+ & \hat{u}_3^+ \end{bmatrix}^{\text{T}}, \tag{2.75}$$

impinges on a boundary, it produces a set of reflected waves $\mathbf{a}_{\text{reflected}}$, defined as

$$\mathbf{a}_{\text{reflected}} = \left[\mathbf{u}_b^-\right]^{\text{T}} = \begin{bmatrix} \hat{w}_1^- & \hat{u}_2^- & \hat{u}_3^- \end{bmatrix}^{\text{T}}, \tag{2.76}$$

such that $\mathbf{a}_{\text{reflected}} = \mathbf{T}_{\text{boundary}}\, \mathbf{a}_{\text{incident}}$. The transmission coefficient matrix is found using equations governing the boundary condition. For common boundary conditions (clamped, pinned and free), the transmission coefficient matrices are given by:

$$\mathbf{T}_{\text{clamped}} = \begin{bmatrix} -1 & 0 & 0 \\ 0 & -\text{i} & -1-\text{i} \\ 0 & -1+\text{i} & \text{i} \end{bmatrix}, \tag{2.77}$$

$$\mathbf{T}_{\text{pinned}} = \begin{bmatrix} -1 & 0 & 0 \\ 0 & -1 & 0 \\ 0 & 0 & -1 \end{bmatrix}, \tag{2.78}$$

$$\mathbf{T}_{\text{free}} = \begin{bmatrix} 1 & 0 & 0 \\ 0 & -\text{i} & 1+\text{i} \\ 0 & 1-\text{i} & \text{i} \end{bmatrix}. \tag{2.79}$$

2.5 Validation of the ray tracing method for simple structures

This section presents the application of the ray tracing method to the free and forced response of simple structures. A perfect ring and a beam under various

boundary conditions are studied. The objective is to validate the method for simple structures and illustrate its implementation. In Chapter 3, the ray tracing method will be applied to the complete ring-based rate sensor presented in Figure 2.1.

2.5.1 Free response of a perfect ring

It is straightforward to obtain an analytical expression for the natural frequencies of a perfect ring using the ray tracing approach. In Equation (2.32), six wave amplitudes are considered (three travelling in each direction), the transmission matrix $\mathbf{T}$ is set equal to the identity matrix as there are no joints to interrupt the waves travelling around the ring, and the diagonal dispersion matrix $\mathbf{D}$ contains the terms $e^{-\mathrm{i}2\pi R k_i}$ ($i = 1, 2, 3$). Solving Equation (2.32) analytically gives wavenumber solutions of the form $k_n = \dfrac{n}{R}$ ($n = 0, 1, 2, \ldots$). By substituting the k_n values into the dispersion relation (2.8) and solving, it can be shown that the natural frequencies are given by:

$$\omega_n^{\pm} = \sqrt{\frac{E}{2\rho R^2}\Phi(n)\left(1 \pm \sqrt{1 - \frac{\Psi(n)}{\Big(\Phi(n)\Big)^2}}\right)}, \tag{2.80}$$

with $n = 0, 1, 2, \ldots$, $\Phi(n) = \left(\dfrac{I}{AR^2}n^2 + 1\right)\Big(n^2 + 1\Big)$ and $\Psi(n) = \dfrac{4I}{AR^2}n^2\Big(n^2 - 1\Big)^2$.

For each value of n, two frequencies are obtained, one representing mainly extensional vibration and one representing mainly flexural vibration. These natural frequencies are identical to those given in [74], which are derived from the natural frequencies of cylindrical shells. With the assumption that the thickness of the ring is much smaller than the radius of the centreline, and for small n, Equation (2.80) can be simplified to the standard expressions for extensional and flexural natural frequencies in rings given in [9].

2.5.2 Forced response of a beam structure

In order to validate the developed ray tracing method for studying the forced responses of structures (see Section 2.3.3), some simple systems are investigated. A

simultaneous combination of the applied forces and torques T_{ext}, S_{ext} and M_{ext} can also be performed easily with the ray tracing method, but is not presented here as the main objective is to demonstrate the validity of the ray tracing method and to illustrate its application to simple structures.

Longitudinal force at the free end of a clamped-free beam

The system studied is shown in Figure 2.8(a). The beam has length L and is under clamped-free boundary conditions. The ray tracing method considers waves leaving all discontinuities. One of them is defined by the applied point force and it splits the beam into two components (I) and (II). The length of component (I) is equal to L (total length of the beam) and the length of component (II) is 0 as the force is applied at the end of the beam. In this study, only longitudinal vibrations are considered. The amplitudes corresponding to flexural vibrations are not taken into account in the wave amplitude vector $\mathbf{a}$, and this vector is defined here as:

$$\mathbf{a} = \begin{bmatrix} \hat{w}_1^{(\mathrm{I})+} & \hat{w}_1^{(\mathrm{I})-} & \hat{w}_1^{(\mathrm{II})+} & \hat{w}_1^{(\mathrm{II})-} \end{bmatrix}^{\mathrm{T}}. \tag{2.81}$$

The initial wave amplitude vector contains terms that consider the applied force (derived in Section 2.3.3), and is defined as:

$$\mathbf{a}_0 = \frac{T_{\text{ext}}}{2EAk_L} \begin{bmatrix} 0 & -\mathrm{i} & -\mathrm{i} & 0 \end{bmatrix}^{\mathrm{T}}. \tag{2.82}$$

The transmission and propagation matrices ($\mathbf{T}$ and $\mathbf{D}$) are defined as:

$$\mathbf{T} = \begin{bmatrix} 0 & T_{\text{clamped}} & 0 & 0 \\ 0 & 0 & 0 & 1 \\ 1 & 0 & 0 & 0 \\ 0 & 0 & T_{\text{free}} & 0 \end{bmatrix}, \tag{2.83}$$

$$\mathbf{D} = \begin{bmatrix} e^{-\mathrm{i}k_L L} & 0 & 0 & 0 \\ 0 & e^{-\mathrm{i}k_L L} & 0 & 0 \\ 0 & 0 & 1 & 0 \\ 0 & 0 & 0 & 1 \end{bmatrix}, \tag{2.84}$$

where T_{clamped} and T_{free} are defined in Section 2.4.3 and are respectively equal to -1 and 1 for longitudinal vibration. To respect the displacement continuity, a transmission coefficient equal to unity is used at the point force.

Solving Equation (2.30) with the particular values of $\mathbf{a}$, $\mathbf{a}_0$, $\mathbf{T}$ and $\mathbf{D}$ defined in Equations (2.81)-(2.84) gives the wave amplitudes $\hat{u}_1^{(\mathrm{I})+}$ and $\hat{u}_1^{(\mathrm{I})-}$ that can be substituted into Equation (2.21a) to give the longitudinal displacement in the beam. The subscript (I) is omitted as there is, in reality, only a single component in the system and the temporal term is also suppressed for simplification. This displacement models the steady-state motion of the beam and simplifies to:

$$u(z) = \frac{T_{\text{ext}} \sin(k_L z)}{EAk_L \cos(k_L L)}. \tag{2.85}$$

This standard result can also be obtained by considering the steady-state displacement in the beam to have the form [17]:

$$u(z) = \beta_1 \sin(k_L z) + \beta_2 \cos(k_L z), \tag{2.86}$$

where β_1 and β_2 are constants that can be derived from the application of the boundary conditions. The conditions $u(0) = 0$ and $T(L) = EAk_L\beta_1 \cos(k_L L) = T_{\text{ext}}$ give $\beta_1 = T_{\text{ext}}/EAk_L \cos(k_L L)$ and $\beta_2 = 0$. Substituting these values of β_1 and β_2 in Equation (2.86) gives exactly the same expression as Equation (2.85).

From this very simple example, the ray tracing method has been validated, but it is difficult to see its advantage as it appears relatively complicated to model the forced vibrations of the beam whereas a simple expression such as Equation (2.86) can easily give the required displacement. However the power of the method can be better understood when flexural vibrations are studied, and these are analysed next.

Lateral force at the mid-point of a pinned-pinned beam

Consider a pinned-pinned beam under the action of a transverse point force applied at its mid-point, as illustrated in Figure 2.8(b). For this system, the wave amplitude vector $\mathbf{a}$, the initial wave amplitude vector $\mathbf{a}_0$, the transmission matrix $\mathbf{T}$ and the dispersion matrix $\mathbf{D}$ are defined as:

$$\mathbf{a} = \begin{bmatrix} \hat{u}_2^{(\mathrm{I})+} & \hat{u}_3^{(\mathrm{I})+} & \hat{u}_2^{(\mathrm{I})-} & \hat{u}_3^{(\mathrm{I})-} & \hat{u}_2^{(\mathrm{II})+} & \hat{u}_3^{(\mathrm{II})+} & \hat{u}_2^{(\mathrm{II})-} & \hat{u}_3^{(\mathrm{II})-} \end{bmatrix}^{\mathrm{T}}, \tag{2.87}$$

$$\mathbf{a}_0 = \frac{S_{\mathrm{ext}}}{4EIk_{Fy}^3} \begin{bmatrix} 0 & 0 & -\mathrm{i} & -1 & -\mathrm{i} & -1 & 0 & 0 \end{bmatrix}^{\mathrm{T}}, \tag{2.88}$$

$$\mathbf{T}_{[8\times8]} = \begin{bmatrix} \mathbf{0} & \mathbf{T}_{\mathrm{pinned}} & \mathbf{0} & \mathbf{0} \\ \mathbf{0} & \mathbf{0} & \mathbf{0} & \mathbf{I} \\ \mathbf{I} & \mathbf{0} & \mathbf{0} & \mathbf{0} \\ \mathbf{0} & \mathbf{0} & \mathbf{T}_{\mathrm{pinned}} & \mathbf{0} \end{bmatrix}, \tag{2.89}$$

$$\mathbf{D}_{[8\times8]} = \begin{bmatrix} \mathbf{\Delta}_{L^{(\mathrm{I})}} & \mathbf{0} & \mathbf{0} & \mathbf{0} \\ \mathbf{0} & \mathbf{\Delta}_{L^{(\mathrm{I})}} & \mathbf{0} & \mathbf{0} \\ \mathbf{0} & \mathbf{0} & \mathbf{\Delta}_{L^{(\mathrm{II})}} & \mathbf{0} \\ \mathbf{0} & \mathbf{0} & \mathbf{0} & \mathbf{\Delta}_{L^{(\mathrm{II})}} \end{bmatrix}, \tag{2.90}$$

where $\mathbf{T}_{\mathrm{pinned}} = \begin{bmatrix} -1 & 0 \\ 0 & -1 \end{bmatrix}$ for flexural vibrations (defined in Section 2.4.3), and $\mathbf{\Delta}_{L^{(\mathrm{I})}} = \mathbf{\Delta}_{L^{(\mathrm{II})}} = \begin{bmatrix} e^{-\mathrm{i}k_{Fy}\frac{L}{2}} & 0 \\ 0 & e^{-k_{Fy}\frac{L}{2}} \end{bmatrix}$.

By solving Equation (2.30) with appropriate values of $\mathbf{a}$, $\mathbf{a}_0$, $\mathbf{T}$ and $\mathbf{D}$, and by using the displacement definition (2.21b) for each of the components, one can derive the flexural displacement $w(z)$ to be:

$$\text{when } 0 \le z \le \frac{L}{2} \qquad w(z) = \left(\frac{\sin(k_{Fy}z)}{\cos(k_{Fy}\frac{L}{2})} - \frac{\sinh(k_{Fy}z)}{\cosh(k_{Fy}\frac{L}{2})} \right) \frac{S_{\mathrm{ext}}}{4EIk_{Fy}^3}, \tag{2.91a}$$

$$\text{when } \frac{L}{2} \le z \le L \qquad w(z) = \left(\frac{\sin(k_{Fy}(L-z))}{\cos(k_{Fy}\frac{L}{2})} - \frac{\sinh(k_{Fy}(L-z))}{\cosh(k_{Fy}\frac{L}{2})} \right) \frac{S_{\mathrm{ext}}}{4EIk_{Fy}^3}. \tag{2.91b}$$

Using a modal approach, it can be shown (*e.g.* [75]) that the displacement $w(z)$ of a pinned-pinned beam under harmonic excitation applied at its middle point can be expressed as:

$$w(z) = \frac{2S_{\text{ext}}L^3}{EI\pi^4} \sum_{n=1,3,5,\cdots}^{\infty} (-1)^{\frac{n-1}{2}} \frac{\sin\left(\frac{n\pi z}{L}\right)}{n^4 - \beta^4}, \tag{2.92}$$

where

$$\beta = \frac{\omega L^2}{\pi^2}\sqrt{\frac{\rho A}{EI}}. \tag{2.93}$$

Figure 2.9 shows results obtained using the ray tracing method (Equations (2.91)) and by the modal approach (Equation (2.92)) for a pinned-pinned beam under harmonic excitation. It shows the flexural displacement as a function of the position z on the beam at a particular excitation frequency. When n is suitably large, the modal approach and ray tracing method are in excellent agreement.

Lateral force at the free end of a clamped-free beam

Consider a clamped-free beam under the action of a lateral force at its free end as illustrated in Figure 2.8(c). The ray tracing method allows the possibility of finding an exact analytical expression for the displacement. Its derivation is a combination of the two previous cases studied. $\mathbf{a}$ and $\mathbf{a}_0$ are defined as in Equations (2.87) and (2.88); $\mathbf{T}$ and $\mathbf{D}$ are such that:

$$\mathbf{T}_{[8\times8]} = \begin{bmatrix} \mathbf{0} & \mathbf{T}_{\text{clamped}} & \mathbf{0} & \mathbf{0} \\ \mathbf{0} & \mathbf{0} & \mathbf{0} & \mathbf{I} \\ \mathbf{I} & \mathbf{0} & \mathbf{0} & \mathbf{0} \\ \mathbf{0} & \mathbf{0} & \mathbf{T}_{\text{free}} & \mathbf{0} \end{bmatrix}, \tag{2.94}$$

$$\mathbf{D}_{[8\times8]} = \begin{bmatrix} \mathbf{\Delta}_L & \mathbf{0} & \mathbf{0} & \mathbf{0} \\ \mathbf{0} & \mathbf{\Delta}_L & \mathbf{0} & \mathbf{0} \\ \mathbf{0} & \mathbf{0} & \mathbf{I} & \mathbf{0} \\ \mathbf{0} & \mathbf{0} & \mathbf{0} & \mathbf{I} \end{bmatrix}, \tag{2.95}$$

where $\mathbf{T}_{\text{clamped}} = \begin{bmatrix} -\mathrm{i} & -1-\mathrm{i} \\ -1+\mathrm{i} & \mathrm{i} \end{bmatrix}$ and $\mathbf{T}_{\text{free}} = \begin{bmatrix} -\mathrm{i} & 1+\mathrm{i} \\ 1-\mathrm{i} & \mathrm{i} \end{bmatrix}$ for flexural vibrations (defined in Section 2.4.3), and $\mathbf{\Delta}_L = \begin{bmatrix} e^{-\mathrm{i}k_{Fy}L} & 0 \\ 0 & e^{-k_{Fy}L} \end{bmatrix}$.

Solving Equation (2.30) with appropriate values of $\mathbf{a}$, $\mathbf{a}_0$, $\mathbf{T}$ and $\mathbf{D}$, one can derive an exact analytical solution for the displacement in the beam:

$$w(z) = \frac{S_{\text{ext}}}{2EIk_{Fy}^3} \frac{\Phi\, e^{\mathrm{i}k_{Fy}z} - \Theta\, e^{-\mathrm{i}k_{Fy}z} + \Gamma\, e^{k_{Fy}z} - \Psi\, e^{-k_{Fy}z}}{\Delta}, \tag{2.96}$$

where:

$$\begin{aligned}
\Phi &= A\left(1+\mathrm{i}+2\mathrm{i}AB+(\mathrm{i}-1)B^2\right), \\
\Theta &= (\mathrm{i}-1)A+(\mathrm{i}+1)AB^2+2\mathrm{i}B, \\
\Gamma &= B\left(1+\mathrm{i}-(\mathrm{i}-1)A^2+2AB\right), \\
\Psi &= (1-\mathrm{i})B+(1+\mathrm{i})A^2B+2A, \\
\Delta &= 1+A^2+4AB+A^2B^2+B^2, \\
A &= e^{-\mathrm{i}k_{Fy}L}, \\
B &= e^{-k_{Fy}L}.
\end{aligned}$$

It can be seen from Equation (2.96) that natural frequencies of the beam (flexural modes only) occur when $\Delta = 0$, *i.e.*:

$$1 + e^{-2\mathrm{i}k_{Fy}L} + 4\, e^{-\mathrm{i}k_{Fy}L}\, e^{-k_{Fy}L} + e^{-2\mathrm{i}k_{Fy}L}\, e^{-2k_{Fy}L} + e^{-2k_{Fy}L} = 0. \tag{2.97}$$

This is the usual expression from which the natural frequencies of a clamped-free beam can be obtained [17, 65, 75].

Figure 2.10 shows the frequency response function of the beam at a particular position (z_0) obtained using the ray tracing method, Equation (2.96), and the FE method. The displacement is taken at the position $z_0 = \frac{3.2}{8}L$ so that all the modes have a distinct contribution. Both methods agree very well for the low order modes and a slight difference appears for higher modes, which can be expected as shear

deformation is neglected in the wave approach.

2.6 Conclusion

In this chapter, a systematic approach based on wave propagation has been presented to study the free and forced vibration of ring/beam structures. The approach relies on defining the displacement in each component composing the entire structure as a sum of waves propagating and decaying in each direction. The coupling between radial and tangential vibration in a curved beam has been investigated and taken into account in the ray tracing process. The ray tracing method has been found to yield accurate predictions for the natural frequencies and forced response of waveguide structures such as rings and beams. The method will be applied in Chapter 3 to a ring-based rate sensor structure. A distinctive feature of this kind of structure is its cyclic symmetry. An efficient use of this property within the ray tracing method will be presented in Chapter 3.

In the wave approach presented here, the motions at the discontinuities are described by the transmission coefficient matrices, which include the effects of decaying wave components. The transmission matrices are derived from displacement continuity and force equilibrium conditions at the discontinuity. The proposed wave approach is exact, and with the availability of propagation and transmission matrices, the vibration analysis is systematic and concise. Furthermore, it will be shown in Chapter 3 that the analysis of structures, composed of several waveguide components, can be simplified by using a substructuring method that models the substructure as particular transmission coefficients between inputs and outputs.

By comparing the results obtained using the ray tracing method and conventional modal or FEA approaches, free and forced vibration analyses using the wave approach were validated for some simple structures such as perfect rings and beams under different boundary conditions and excitation types. The ray tracing approach is expected to be very efficient compared to the FE methods that are computationally expensive, if different meshes need to be generated. The method presented here

was illustrated for simple examples, and it was shown that exact analytical expression for the steady state displacement of straight beams under various boundary conditions and loads can be obtained.

In Chapter 4, the interaction of the resonator with its support will be assessed. The wave approach presented here is an efficient way to model the vibrational energy flow from the resonator towards its support. Using the ray tracing method, the stress sources that are responsible for support losses, the energy stored in the resonator, and the associated quality factor can be calculated easily.

The approach presented in this chapter focuses on in-plane vibration but can be adapted easily to out-of-plane motions. The three-dimensional motion of ring/beam structures can be defined by a longitudinal (along the centreline) displacement, two flexural displacements (perpendicular to the centreline in mutually orthogonal directions) and a torsional component representing twisting of the cross-section. The extension of the ray tracing method to out-of-plane vibrations is the focus of Chapter 6.

Figures

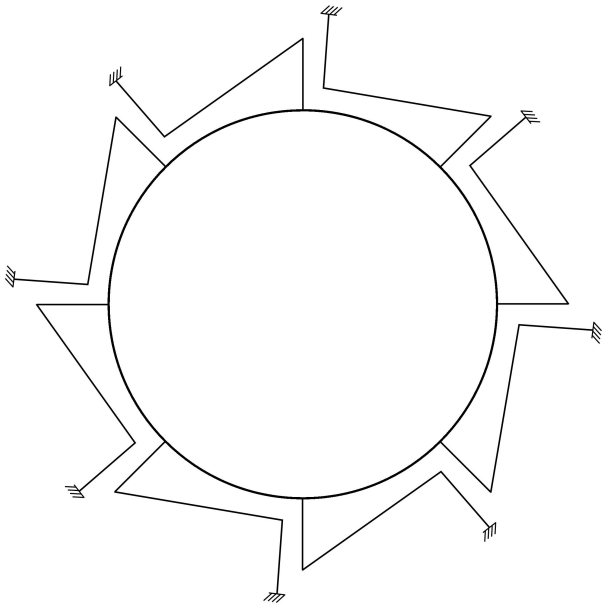

Figure 2.1: Schematic representation of a ring-based rate sensor composed of a ring and eight folded legs.

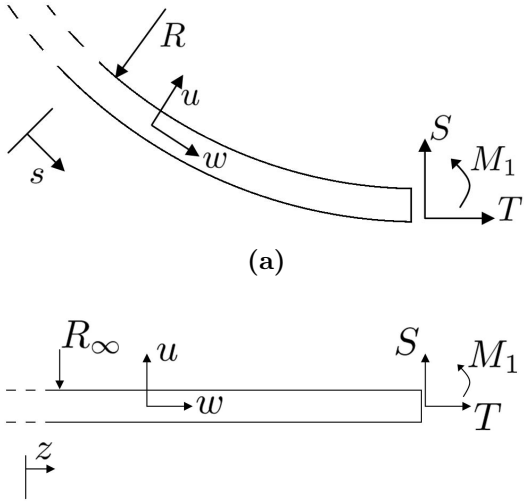

Figure 2.2: (a) curved and (b) straight beams: notation and signs conventions.

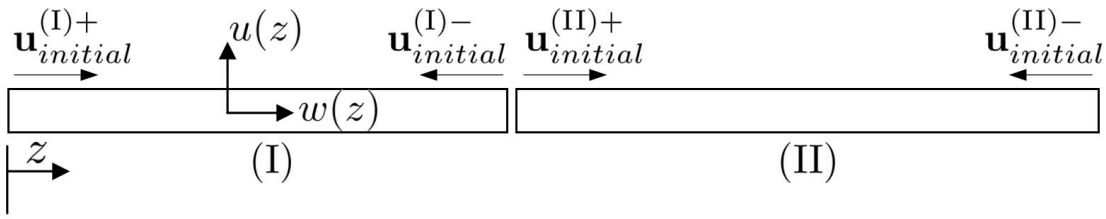

Figure 2.3: Initial wave amplitudes considered for the ray tracing method in a two beams component system.

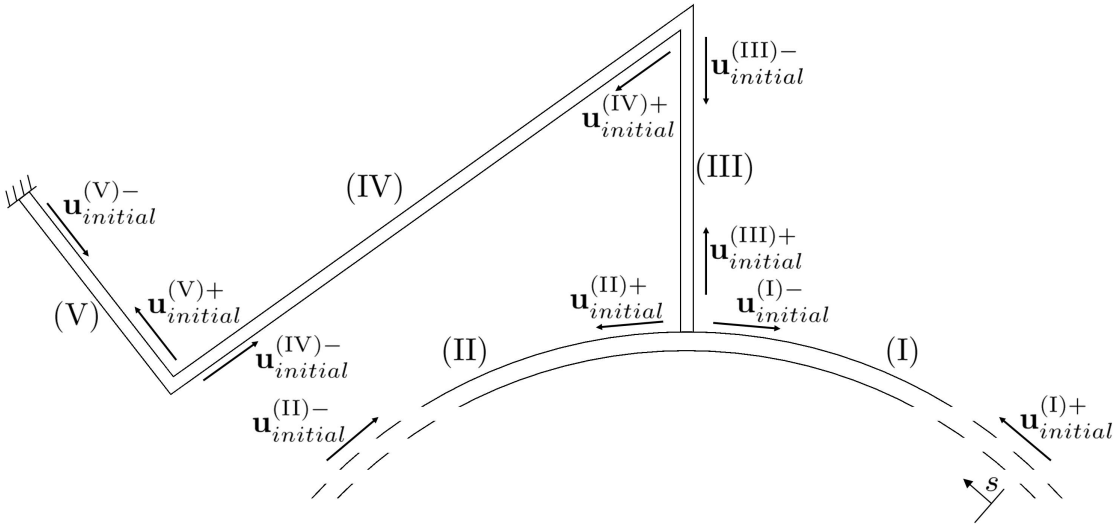

Figure 2.4: Initial wave amplitudes considered for the ray tracing method in one portion of the ring-based resonator.

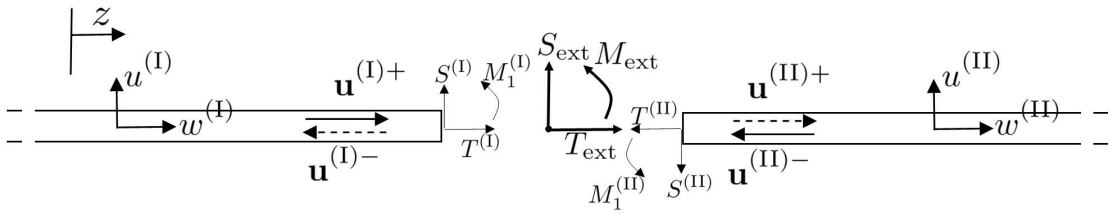

Figure 2.5: Wave amplitudes impinging and leaving the discontinuity created by the application of a point force.

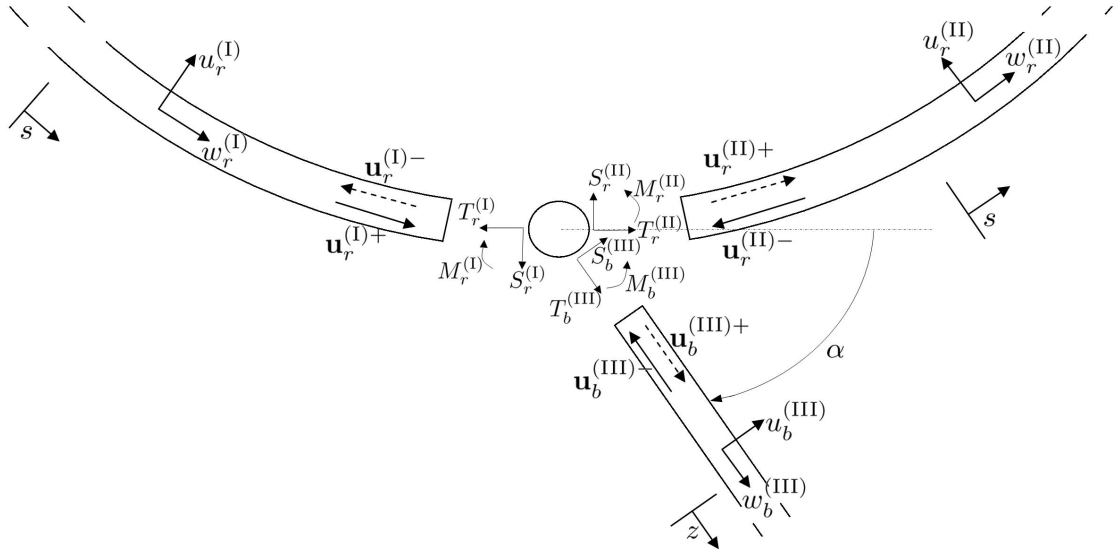

Figure 2.6: Transmission between a ring and an attached beam.

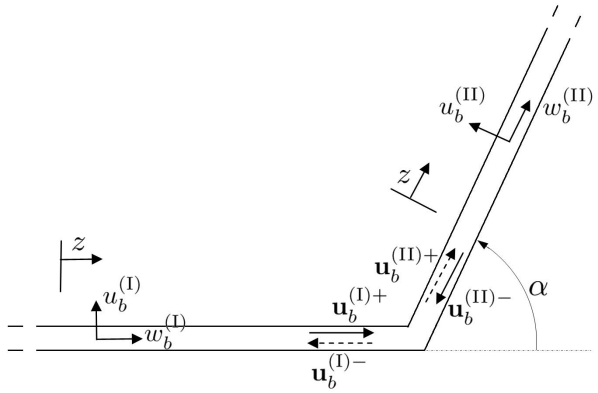

Figure 2.7: Transmission through an abrupt change in direction in beams.

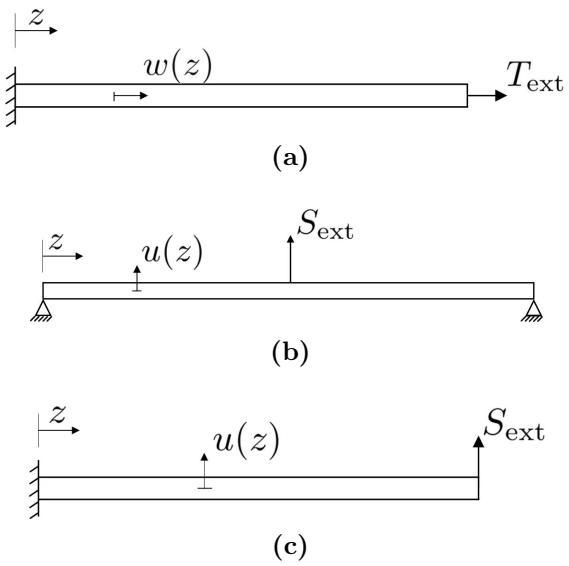

Figure 2.8: Different cases studied for the validation of the ray tracing method for modelling forced response of beams; (a) longitudinal force at the free end of a clamped-free beam, (b) flexural force at the mid-point of a pinned-pinned beam, (c) flexural force at the free end of a clamped-free beam.

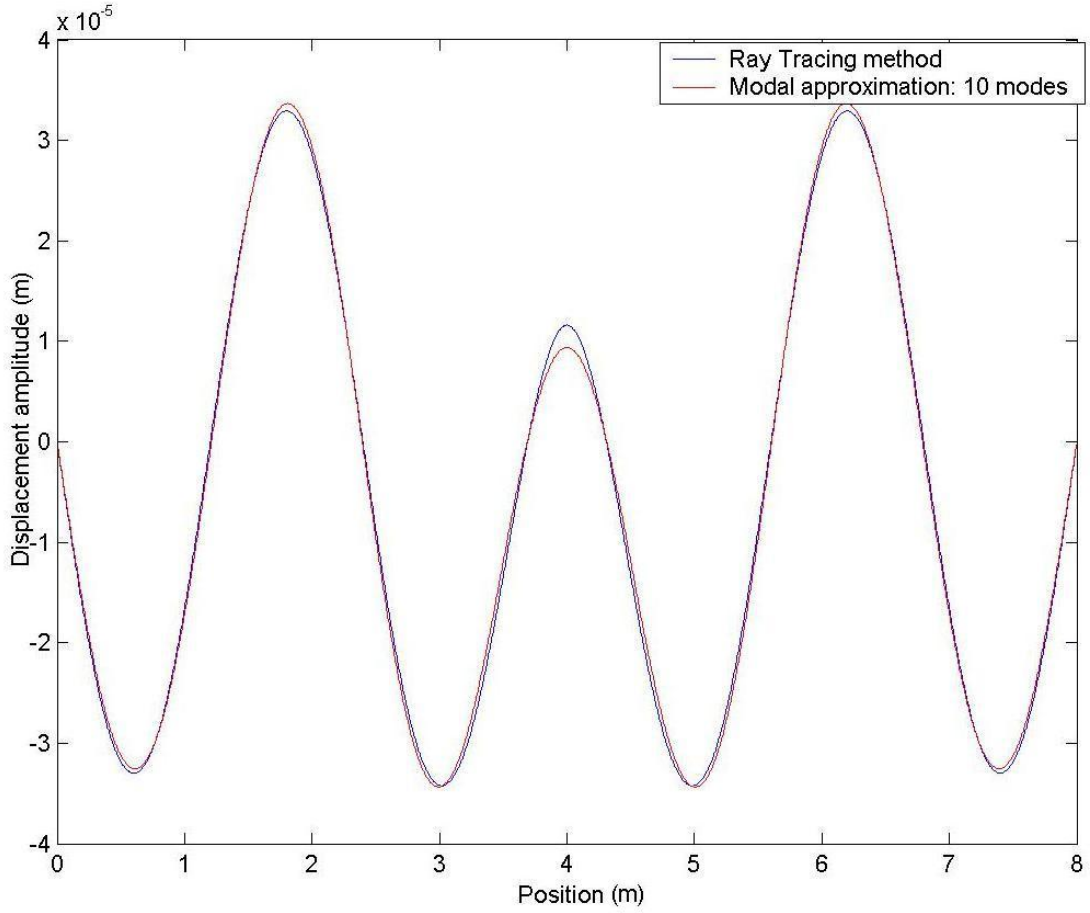

Figure 2.9: Flexural displacement of a pinned-pinned beam under force excitation at its mid-point. With $\rho = 1950\,\mathrm{kg.m^{-3}}$, $E = 2 \cdot 10^{11}\,\mathrm{Pa}$, $L = 8\,\mathrm{m}$, in-plane beam width $= 0.1\,\mathrm{m}$, out-of-plane beam thickness $= 0.5\,\mathrm{m}$, excitation frequency $\omega = 320\,\mathrm{Hz}$ and excitation amplitude $S_{\mathrm{ext}} = 10\,\mathrm{kN}$. Ten modes are considered in the modal approach.

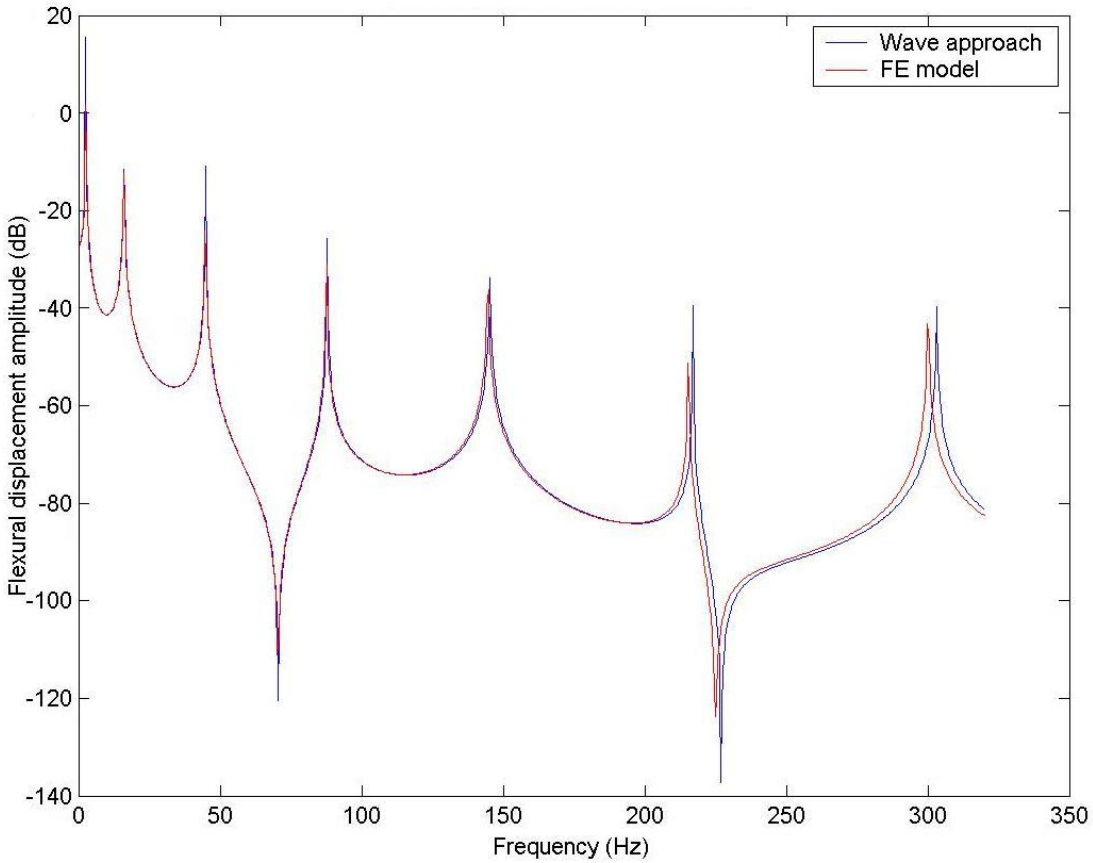

Figure 2.10: Frequency response function of a clamped-free beam under force excitation at its free end. Material properties and beam dimensions are given in Figure 2.9. The displacement is taken at $z_0 = \frac{3.2}{8}L$. The excitation force has an amplitude $S_{\text{ext}} = 10\,\text{kN}$. The FE model contains 120×2 quadratic elements.

Chapter 3

Model simplifications for symmetric structures

3.1 Introduction

Chapter 2 has presented a wave approach, called the ray tracing method, to model the free and forced vibrations of structures composed of several waveguide components. This approach is based on the propagation and transmission of waves and on the detailed knowledge of transmission/reflection coefficient matrices at discontinuities. It is theoretically possible to model any kind of network with the ray tracing approach. However, practical structures are usually more complex than the simple cases studied in Chapter 2, and it can become difficult to use an entire, non-simplified, model to analyse the structure. Some simplifications from symmetry or periodicity properties may exist that would allow the analysis to be greatly reduced.

If a structure possesses the same discontinuity several times, the associated transmission coefficients need only to be calculated once. If a structure presents one or more axes of symmetry, one can simplify the model by considering only one part of the structure. For this case, the axis of symmetry can be modelled using appropriate boundary conditions (sliding conditions, for example) which lead to transmission

coefficients at the axes of symmetry, and the ray tracing method can be applied in the same way as described in Chapter 2.

Many engineering structures are designed to be composed of identically constructed cell units that are connected end to end to form a spatially periodic array. Such structures are known as periodic structures and they consist of identical substructures, or sectors. Due to their periodic nature, these structures exhibit unique dynamic characteristics that make them act as mechanical filters for wave propagation. As a result, waves can propagate along the periodic structure only within specific frequency bands and wave propagation can be completely blocked within other frequency bands. The spectral width and location of these bands are fixed for periodic structures. It seems that the theory of periodic structures was originally developed for solid state applications [76]. The atomic lattices of pure crystals constitute perfect periodic structures, but these are lumped parameter systems with discrete masses (the atoms) interconnected by the inter-atomic elastic forces. In engineering applications, the mass and elasticity of structural members are continuous, and constitute periodic structures when arranged in regular chains. The theory of periodic structures was extended, in the early 1970's, to the design of mechanical structures [55, 77, 78]. It has been the subject of many investigations since then (*e.g.* [79–84]) and extensively applied to a wide variety of structures, such as spring-mass systems, periodic beams, stiffened plates, ribbed shells, and space structures. Free wave propagation in infinite long periodic structures is usually discussed in terms of the complex propagation constant μ. The corresponding vibration frequencies are found by imposing constraints on the finite element equations of motion of a single sector. The constraints impose that the displacement vectors on the right- and left-hand boundaries of a sector have a ratio of e^{μ}. A thorough review of wave propagation in continuous periodic structures to analyse free and forced vibration can be found in [85]. In infinite periodic structures, the evanescent terms corresponding to the presence of boundaries are not an issue in the analysis and a direct relationship can be found between the displacement of one sector and one of its neighbours. However, in a real application the presence of boundaries complicates the analysis. In Section 3.2, a different point of view is presented. A finite chain of identical sectors is modelled using a recursive form as

a function of the characteristics of a single sector. The external boundaries can then be added to the system by using the classic ray tracing method presented in Chapter 2.

Many engineering structures have cylindrical form. In some cases, such as certain pipes, chimneys, or pressure vessels, the structures are axisymmetric, and there is a considerable range of techniques available for analysing these, taking full advantage of the axisymmetric nature. Another type of symmetry is cyclic symmetry which occurs when a rotational structure is made of repetitive sectors. Thomas [86] modelled cyclically periodic structures consisting of N finite identical sectors forming a closed ring. A structure is said to have cyclic symmetry if the geometry at any radial and axial position, defined at some angle θ, is identical at angle $(\theta + 2\pi/\kappa)$, where κ is an integer smaller than N. It follows that once the geometry has been defined over a sector from θ to $\theta + 2\pi/\kappa$, the remainder of the structure can be generated by repeatedly applying the geometry over $2\pi/N$. The property of periodicity can be exploited so that the analysis of one sector gives the same information as the analysis of the entire structure [86]. However in this case, in contrast to the mirror-symmetric case, there are no direct boundary coefficients that can be associated with the cyclic symmetry. But simplifications can still be made and these are described in Section 3.3. An example of a structure, showing cyclic symmetry properties, is the ring-based rate sensor that was presented in Chapter 2. Vibrations of structures with symmetry are studied in more details here.

3.2 Structures showing periodic properties

This section presents the application of the ray tracing method to structures composed of periodic repetitive sectors. Section 3.2.1 explains a substructuring method which simplifies any system composed of several components to particular reflection and transmission coefficients matrices. Each sector is then modelled using these particular matrices. Section 3.2.2 introduces the next step for the modelling of structures that shows periodicity and presents a method to model a finite chain of identical sectors as a function of the properties of one single sector.

3.2.1 Substructuring method

A substructuring method can often be applied to simplify a system composed of several components. When an entire structure is analysed, its complexity can be reduced by using substructuring. A group of components can be modelled as a "black box", where only the input and output are of interest. The ray tracing method offers the possibility to use substructuring to model complex structural networks with simplicity. For instance, consider three straight beam components, coupled together with discontinuities, see Figure 3.1(a). The objective of substructuring is to reduce the system presented in Figure 3.1(a) to the one illustrated in Figure 3.1(b), where component (II) is not considered directly.

The idea is to find the transmission coefficients $\mathbf{\Pi}^{(\mathrm{I})\to(\mathrm{III})}$ and $\mathbf{\Pi}^{(\mathrm{III})\to(\mathrm{I})}$ that link incident waves from component (I) to transmitted waves in component (III) and waves from (III) to (I), respectively. The "reflection" coefficients $\mathbf{B}^{(\mathrm{I}-\mathrm{III})-}$ and $\mathbf{B}^{(\mathrm{III}-\mathrm{I})+}$ associated with incident waves $\mathbf{u}^{(\mathrm{I})+}$ and $\mathbf{u}^{(\mathrm{III})-}$ creating waves $\mathbf{u}^{(\mathrm{I})-}$ and $\mathbf{u}^{(\mathrm{III})+}$, respectively, also need to be considered.

First, consider an incident set of waves $\mathbf{u}^{(\mathrm{I})+}$ only. The total set of wave amplitudes $\mathbf{a}$ present in the system (incident set of waves and all the induced created set of waves) can be written as:

$$\mathbf{a}_{[15\times1]} = \begin{bmatrix} \mathbf{u}^{(\mathrm{I})+} & \mathbf{u}^{(\mathrm{I})-} & \mathbf{u}^{(\mathrm{II})+} & \mathbf{u}^{(\mathrm{II})-} & \mathbf{u}^{(\mathrm{III})+} \end{bmatrix}^{\mathrm{T}}. \tag{3.1}$$

Assume that each component of the incident set of waves has an amplitude equal to unity and that the waves in component (II) propagate and decay along a length L. Applying Equation (2.30) (see Chapter 2) to this system gives:

$$\begin{bmatrix} \mathbf{I} & \mathbf{0} & \mathbf{0} & \mathbf{0} & \mathbf{0} \\ -\mathbf{B}^{(\mathrm{I})+} & \mathbf{I} & \mathbf{0} & -\mathbf{\Pi}^{(\mathrm{II})\to(\mathrm{I})}\mathbf{\Delta}_L & \mathbf{0} \\ -\mathbf{\Pi}^{(\mathrm{I})\to(\mathrm{II})} & \mathbf{0} & \mathbf{I} & -\mathbf{B}^{(\mathrm{II})-}\mathbf{\Delta}_L & \mathbf{0} \\ \mathbf{0} & \mathbf{0} & -\mathbf{B}^{(\mathrm{II})+}\mathbf{\Delta}_L & \mathbf{I} & \mathbf{0} \\ \mathbf{0} & \mathbf{0} & -\mathbf{\Pi}^{(\mathrm{II})\to(\mathrm{III})}\mathbf{\Delta}_L & \mathbf{0} & \mathbf{I} \end{bmatrix} \begin{bmatrix} \mathbf{I} \\ \mathbf{B}^{(\mathrm{I}-\mathrm{III})-} \\ \mathbf{\Phi}_{\mathrm{intern}} \\ \mathbf{\Psi}_{\mathrm{intern}} \\ \mathbf{\Pi}^{(\mathrm{I})\to(\mathrm{III})} \end{bmatrix} = \begin{bmatrix} \mathbf{I} \\ \mathbf{0} \\ \mathbf{0} \\ \mathbf{0} \\ \mathbf{0} \end{bmatrix}, \tag{3.2}$$

where $\mathbf{B}^{(j)\pm}$, $\mathbf{\Pi}^{(i)\to(j)}$ contain respectively the reflection coefficients at the positive or negative end of component (j), and the transmission coefficients from component (i) to component (j). $\mathbf{\Delta}_L$ models the propagation and decay of waves along the length L. These matrices are defined in Equations (2.26) and (2.27) (see Chapter 2). $\mathbf{\Phi}_{\text{intern}}$ and $\mathbf{\Psi}_{\text{intern}}$ are internal matrices of the substructure and are not relevant for the current explanation.

Using Equation (3.2), it can be shown that:

$$\begin{aligned}
\mathbf{B}^{(\mathrm{I}-\mathrm{III})-} &= \mathbf{B}^{(\mathrm{I})+} + \\
&\begin{bmatrix} \mathbf{0} & -\mathbf{\Pi}^{(\mathrm{II})\to(\mathrm{I})}\mathbf{\Delta}_L & \mathbf{0} \end{bmatrix} \begin{bmatrix} \mathbf{I} & -\mathbf{B}^{(\mathrm{II})-}\mathbf{\Delta}_L & \mathbf{0} \\ -\mathbf{B}^{(\mathrm{II})+}\mathbf{\Delta}_L & \mathbf{I} & \mathbf{0} \\ -\mathbf{\Pi}^{(\mathrm{II})\to(\mathrm{III})}\mathbf{\Delta}_L & \mathbf{0} & \mathbf{I} \end{bmatrix}^{-1} \begin{bmatrix} -\mathbf{\Pi}^{(\mathrm{I})\to(\mathrm{II})} \\ \mathbf{0} \\ \mathbf{0} \end{bmatrix}, \\
\mathbf{B}^{(\mathrm{I}-\mathrm{III})-} &= \mathbf{B}^{(\mathrm{I})+} + \mathbf{\Pi}^{(\mathrm{II})\to(\mathrm{I})}\mathbf{\Delta}_L\mathbf{B}^{(\mathrm{II})+}\mathbf{\Delta}_L\Big(\mathbf{I} - \mathbf{B}^{(\mathrm{II})-}\mathbf{\Delta}_L\mathbf{B}^{(\mathrm{II})+}\mathbf{\Delta}_L\Big)^{-1}\mathbf{\Pi}^{(\mathrm{I})\to(\mathrm{II})},
\end{aligned} \tag{3.3}$$

and

$$\begin{aligned}
\mathbf{\Pi}^{(\mathrm{I})\to(\mathrm{III})} &= \\
&- \begin{bmatrix} \mathbf{0} & -\mathbf{\Pi}^{(\mathrm{II})\to(\mathrm{III})}\mathbf{\Delta}_L & \mathbf{0} \end{bmatrix} \begin{bmatrix} \mathbf{I} & \mathbf{0} & -\mathbf{\Pi}^{(\mathrm{II})\to(\mathrm{I})}\mathbf{\Delta}_L \\ \mathbf{0} & \mathbf{I} & -\mathbf{B}^{(\mathrm{II})-}\mathbf{\Delta}_L \\ \mathbf{0} & -\mathbf{B}^{(\mathrm{II})+}\mathbf{\Delta}_L & \mathbf{I} \end{bmatrix}^{-1} \begin{bmatrix} \mathbf{B}^{(\mathrm{I})+} \\ \mathbf{\Pi}^{(\mathrm{I})\to(\mathrm{II})} \\ \mathbf{0} \end{bmatrix}, \\
\mathbf{\Pi}^{(\mathrm{I})\to(\mathrm{III})} &= \mathbf{\Pi}^{(\mathrm{II})\to(\mathrm{III})}\mathbf{\Delta}_L\Big(\mathbf{I} - \mathbf{B}^{(\mathrm{II})-}\mathbf{\Delta}_L\mathbf{B}^{(\mathrm{II})+}\mathbf{\Delta}_L\Big)^{-1}\mathbf{\Pi}^{(\mathrm{I})\to(\mathrm{II})}.
\end{aligned} \tag{3.4}$$

These are the required transmission/reflection coefficients from an incident wave $\mathbf{u}^{(\mathrm{I})+}$ to a reflected set of waves $\mathbf{u}^{(\mathrm{I})-}$ in component (I) and to a transmitted set of waves $\mathbf{u}^{(\mathrm{III})+}$ in component (III).

Similarly, by considering an incident wave from component (III) only, one can get

by symmetry:

$$\mathbf{B}^{(\mathrm{III}-\mathrm{I})+} = \mathbf{B}^{(\mathrm{III})-} + \mathbf{\Pi}^{(\mathrm{II})\to(\mathrm{III})}\mathbf{\Delta}_L\mathbf{B}^{(\mathrm{II})-}\mathbf{\Delta}_L\Big(\mathbf{I} - \mathbf{B}^{(\mathrm{II})+}\mathbf{\Delta}_L\mathbf{B}^{(\mathrm{II})-}\mathbf{\Delta}_L\Big)^{-1}\mathbf{\Pi}^{(\mathrm{III})\to(\mathrm{II})}, \tag{3.5}$$

$$\mathbf{\Pi}^{(\mathrm{III})\to(\mathrm{I})} = \mathbf{\Pi}^{(\mathrm{II})\to(\mathrm{I})}\mathbf{\Delta}_L\Big(\mathbf{I} - \mathbf{B}^{(\mathrm{II})+}\mathbf{\Delta}_L\mathbf{B}^{(\mathrm{II})-}\mathbf{\Delta}_L\Big)^{-1}\mathbf{\Pi}^{(\mathrm{III})\to(\mathrm{II})}. \tag{3.6}$$

Using the transmission/reflection coefficients given in Equations (3.3)-(3.6), the entire system can be simplified to the one presented in Figure 3.1(b). A direct relationship between the input on one side of the structure to the output on the other side has been found. It simplifies greatly the analysis as the internal set of waves present in component (II) do not need to be calculated any more. The effect of the substructure component (II) can be expressed using a matrix $\mathbf{T}_{\mathrm{sub}}$ such that:

$$\mathbf{a}_{\mathrm{output}} = \mathbf{T}_{\mathrm{sub}}\,\mathbf{a}_{\mathrm{input}}, \tag{3.7}$$

or

$$\begin{bmatrix} \mathbf{u}^{(\mathrm{III})+} \\ \mathbf{u}^{(\mathrm{I})-} \end{bmatrix} = \begin{bmatrix} \mathbf{\Pi}^{(\mathrm{I})\to(\mathrm{III})} & \mathbf{B}^{(\mathrm{III}-\mathrm{I})+} \\ \mathbf{B}^{(\mathrm{I}-\mathrm{III})-} & \mathbf{\Pi}^{(\mathrm{III})\to(\mathrm{I})} \end{bmatrix} \begin{bmatrix} \mathbf{u}^{(\mathrm{I})+} \\ \mathbf{u}^{(\mathrm{III})-} \end{bmatrix}. \tag{3.8}$$

When an entire structure is composed of repetitive sectors, the substructuring method can be used to model each sector with particular transmission/reflection coefficient characteristics. Modelling the coupling of all of these sectors together in particular transmission/reflection coefficient matrices is the subject of the next section.

3.2.2 Simplifications for periodic structures

Consider a structure defined as a finite chain of N identical sectors Λ put side by side, with $N > 1$. Each sector Λ is modelled by its individual reflection coefficient matrices $\mathbf{B}_1^l$ and $\mathbf{B}_1^r$ for the reflection of waves at its left- and right-hand sides, respectively, and by its individual transmission coefficient matrices $\mathbf{\Pi}_1^{l\to r}$ and

$\mathbf{\Pi}_1^{r\to l}$ for the transmission of waves from left to right and from right to left, respectively. These matrices may be the result of a previous substructuring process, where each sector Λ may actually be composed of several components. Using similar notation, a chain of n sectors ($n = 1, \ldots, N$) is represented by the overall transmission/reflection coefficient matrices $\mathbf{B}_n^l$, $\mathbf{B}_n^r$, $\mathbf{\Pi}_n^{l\to r}$ and $\mathbf{\Pi}_n^{r\to l}$. The subscript n is the number of sectors composing the chain.

A method similar to the substructuring method explained in Section 3.2.1 can be used to model the entire chain. If a single sector is added to a chain of pre-existing $(N-1)$ sectors (see Figure 3.2), and by considering incident waves from the left hand side only, Equation (2.30) (see Chapter 2) applied to the system becomes:

$$\begin{bmatrix} \mathbf{I} & \mathbf{0} & \mathbf{0} & \mathbf{0} & \mathbf{0} \\ -\mathbf{B}_{N-1}^l & \mathbf{I} & \mathbf{0} & -\mathbf{\Pi}_{N-1}^{r\to l} & \mathbf{0} \\ -\mathbf{\Pi}_{N-1}^{l\to r} & \mathbf{0} & \mathbf{I} & -\mathbf{B}_{N-1}^r & \mathbf{0} \\ \mathbf{0} & \mathbf{0} & -\mathbf{B}_1^l & \mathbf{I} & \mathbf{0} \\ \mathbf{0} & \mathbf{0} & -\mathbf{\Pi}_1^{l\to r} & \mathbf{0} & \mathbf{I} \end{bmatrix} \begin{bmatrix} \mathbf{I} \\ \mathbf{B}_N^l \\ \mathbf{\Phi}_{\text{intern}} \\ \mathbf{\Psi}_{\text{intern}} \\ \mathbf{\Pi}_N^{l\to r} \end{bmatrix} = \begin{bmatrix} \mathbf{I} \\ \mathbf{0} \\ \mathbf{0} \\ \mathbf{0} \\ \mathbf{0} \end{bmatrix}, \tag{3.9}$$

Using Equation (3.9), the transmission/reflection coefficient matrices of the entire chain can be derived:

$$\mathbf{B}_N^l = \mathbf{B}_{N-1}^l + \mathbf{\Pi}_{N-1}^{r\to l}\mathbf{B}_1^l\left(\mathbf{I} - \mathbf{B}_{N-1}^r\mathbf{B}_1^l\right)^{-1}\mathbf{\Pi}_{N-1}^{l\to r}, \tag{3.10a}$$

$$\mathbf{\Pi}_N^{l\to r} = \mathbf{\Pi}_1^{l\to r}\left(\mathbf{I} - \mathbf{B}_{N-1}^r\mathbf{B}_1^l\right)^{-1}\mathbf{\Pi}_{N-1}^{l\to r} \tag{3.10b}$$

for incident waves from the left-hand side, and by symmetry:

$$\mathbf{B}_N^r = \mathbf{B}_1^r + \mathbf{\Pi}_1^{l\to r}\mathbf{B}_{N-1}^r\left(\mathbf{I} - \mathbf{B}_1^l\mathbf{B}_{N-1}^r\right)^{-1}\mathbf{\Pi}_1^{r\to l}, \tag{3.11a}$$

$$\mathbf{\Pi}_N^{r\to l} = \mathbf{\Pi}_{N-1}^{r\to l}\left(\mathbf{I} - \mathbf{B}_1^l\mathbf{B}_{N-1}^r\right)^{-1}\mathbf{\Pi}_1^{r\to l} \tag{3.11b}$$

for incident waves from the right-hand side.

The effect of the entire chain of N sectors can now be expressed using a matrix $\mathbf{T}_N$

such that:

$$\mathbf{a}_{\text{created}} = \mathbf{T}_N \, \mathbf{a}_{\text{incident}}, \tag{3.12}$$

or

$$\begin{bmatrix} \mathbf{u}^{(\text{II})+} \\ \mathbf{u}^{(\text{I})-} \end{bmatrix} = \begin{bmatrix} \mathbf{\Pi}_N^{l\to r} & \mathbf{B}_N^{r} \\ \mathbf{B}_N^{l} & \mathbf{\Pi}_N^{r\to l} \end{bmatrix} \begin{bmatrix} \mathbf{u}^{(\text{I})+} \\ \mathbf{u}^{(\text{II})-} \end{bmatrix}, \tag{3.13}$$

where the components (I) and (II) are on the left- and right-hand sides of the chain, see Figure 3.2. The transmission and reflection properties of the entire chain of N sectors are then expressed in a recursive form as a function of the characteristics of a chain of $(N-1)$ sectors. By calculating the relevant matrices for chains of $n = 2, 3, \ldots, (N-1)$ sectors, one can get the matrices for a chain of N sectors using Equations (3.10) and (3.11).

Specifically, for computer implementation, the use of periodicity simplifications reduces the inversion of a $[6N \times 6N]$ matrix to $2N$ inversions of a $[3 \times 3]$ matrix. This clearly reduces the computation time and analysis complexity.

In contrast to the usual work on infinite periodic structures (such as [77]), this section presented a method to study "finite" chains of sectors. The boundary conditions are added to the model in a subsequent step using the ray tracing approach. The Application of substructuring and simplifications by periodic structures methods is shown in Section 3.4.1, where the case of a finite cantilever beam with identical, uniformly-spaced point masses is studied.

3.3 Structures showing cyclic symmetry properties

The method that simplifies the analysis of cyclically symmetric (also called rotationally periodic) structures was first developed for Finite Element (FE) uses by Thomas [86, 87]. This section introduces the basis of his work and applies it to the ray tracing method. Thomas' work is an extension of the study carried out in [78]

where the structures considered were infinitely long chains of identical substructures.

3.3.1 Cyclic symmetry theory

Let us consider a rotationally periodic structure consisting of N identical sectors, each of which contains J wave amplitudes. When applying the ray tracing method, the total number of wave amplitudes in the entire structure is NJ. These wave amplitudes are ordered so that J wave amplitudes of the first sector are followed by J wave amplitudes of the second sector, and so on. The overall wave amplitude vector $\mathbf{a}$ can be written as:

$$\mathbf{a} = \begin{bmatrix} \mathbf{a}^{(1)} \\ \mathbf{a}^{(2)} \\ \mathbf{a}^{(3)} \\ \cdots \\ \mathbf{a}^{(N)} \end{bmatrix}, \tag{3.14}$$

where $\mathbf{a}^{(j)}$ is a vector of length J containing the wave amplitudes associated with the j^{th} sector. Note that the sector numbers are increasing in the positive direction of rotation.

With axisymmetric structures, it is well known that most modes of vibration occur in degenerate orthogonal pairs (see, for example, the case of a perfect ring [88]). The reason is that, if a mode has a maximum deflection at some point on the structure, it is clearly possible, because of the axisymmetric nature of the structure, to rotate the mode shape through any angle and not change the frequency of vibration. Thomas [86] showed that a similar effect occurs for rotationally periodic structures. In the ray tracing method, the mode shape is defined using the wave amplitude vector $\mathbf{a}$. Comparing the mode shape (real displacements) between two sectors is equivalent to comparing the associated wave amplitudes. For rotationally periodic structures, the possible modes shapes, and thus the associated wave amplitudes $\mathbf{a}$ fall into three classes, depending on the relationship between the shapes for individual sectors, see *e.g.* in Figure 3.3. These are:

1. Each sector has the same mode shape, or same wave amplitudes, as its neighbours. This means:

$$\mathbf{a}^{(j)} = \mathbf{a}^{(j+1)} \qquad \text{for all } j. \tag{3.15}$$

2. Each sector has the same mode shape as its neighbours, but is vibrating in antiphase with them, *i.e.*:

$$\mathbf{a}^{(j)} = -\mathbf{a}^{(j+1)} \qquad \text{for all } j. \tag{3.16}$$

   This class only exists if N is even (see later).

3. All other possible mode shapes.

It can be proved that classes 1. and 2. do not exhibit degeneracy [86]; only class 3. does and two possible orthogonal mode shapes for each natural frequency will occur in this case.

The mode shapes for class 3. require $\mathbf{a}^{(j)} \neq \mathbf{a}^{(j+1)}$ and $\mathbf{a}^{(j)} \neq -\mathbf{a}^{(j+1)}$. Since all the sectors are identical, the deflected shape $\mathbf{a}'$ can be obtained by rotating $\mathbf{a}$ through an angle commensurate with the location of the different sectors. With a complex set of wave amplitude solution $\mathbf{a}$, the vector $\mathbf{a}'$ can be expressed as:

$$\mathbf{a}' = e^{-\mathrm{i}\psi}\mathbf{a}. \tag{3.17}$$

This new vector $\mathbf{a}'$ corresponds to rotating $\mathbf{a}$ through an angle ψ. As $\mathbf{a}$ and $\mathbf{a}'$ are complex, they have a phase difference ψ. Since the application of Equation (3.17) N times leaves $\mathbf{a}$ unchanged, ψ must have the form:

$$\psi = \frac{2\pi}{N}\kappa, \tag{3.18}$$

where κ is an integer. The cyclic symmetry mode number κ indicates the number of waves around the circumference in a basic response. The deflections on any one sector can be written in terms of the deflections on any other, *i.e.*:

$$\mathbf{a}^{(j)} = e^{-\mathrm{i}\psi}\mathbf{a}^{(j+1)}, \qquad \mathbf{a}^{(j+1)} = e^{\mathrm{i}\psi}\mathbf{a}^{(j)}, \tag{3.19}$$

The values of the cyclic mode number κ used to define ψ in Equation (3.18) is considered next. For classes 1. and 2. of mode shapes considered earlier, $\psi = 0$ and $\psi = \pi$ respectively, and the corresponding values of κ are 0 and $N/2$. Clearly $N/2$ is only an integer if N is even, so class 2. modes cannot exist if N is odd. If ψ represents the angle of rotation for one sector, its possible dependent values are:

$$\psi = -\frac{2\pi}{N}\Big(\frac{N}{2} - 1\Big), \ldots, -\frac{2\pi}{N}, 0, \frac{2\pi}{N}, \ldots, \frac{2\pi}{N}\Big(\frac{N}{2} - 1\Big), \pi \tag{3.20}$$

for N even, and

$$\psi = -\frac{2\pi}{N}\Big(\frac{N-1}{2}\Big), \ldots, -\frac{2\pi}{N}, 0, \frac{2\pi}{N}, \ldots, \frac{2\pi}{N}\Big(\frac{N-1}{2}\Big) \tag{3.21}$$

for N odd. The negative values of ψ correspond to anticlockwise rotations and the positive values correspond to clockwise rotations. Since all the anticlockwise mode shapes are the orthogonal pairs of clockwise ones, they can be generated by simply taking the complex conjugates of $\mathbf{a}$ for the clockwise vectors. Furthermore, they form an orthogonal pair of mode shapes and have the same natural frequency. Therefore, two orthogonal modes exist for $\kappa = 1, 2, \ldots, N/2 - 1$ (N even) or $\kappa = 1, 2, \ldots, (N-1)/2$ (N odd), whereas the modes $\kappa = 0, N/2$ (N even) or $\kappa = 0$ (N odd) are unique. To obtain all the possible modes of vibration of the structures [86], it is necessary to find the modes corresponding to the $N/2+1$ values of ψ, *i.e.*

$$\psi = 0, \frac{2\pi}{N}, \ldots, \frac{2\pi}{N}\Big(\frac{N}{2} - 1\Big), \pi \quad \text{or} \quad \kappa = 0, 1, \ldots, \frac{N}{2} - 1, \frac{N}{2} \tag{3.22}$$

for N even, and the $(N+1)/2$ values of ψ, *i.e.*

$$\psi = 0, \frac{2\pi}{N}, \ldots, \frac{2\pi}{N}\Big(\frac{N-1}{2}\Big) \quad \text{or} \quad \kappa = 0, 1, \ldots, \frac{N-1}{2} \tag{3.23}$$

for N odd.

Figure 3.3 illustrates the three different possible classes of mode shape for a thin square vibrating structure. For this structure, the basic sector is one side and $N = 4$. The corresponding value of κ and ψ are also presented.

This section has shown how the displacement of any sector of a rotationally periodic structure can be related to the displacement of one particular sector by a phase angle ψ. For these structures, any complex mode shape of the entire structure can be expressed in terms of the deflected shape of just one sector, by using an appropriate value of ψ. There are N possible values of ψ, but only $N/2 + 1$ (N even) or $(N + 1)/2$ (N odd) represent different mode shapes. Each κ value corresponds to a κ-fold symmetric mode and needs to be examined in turn. In the following section, the rotationally periodic properties are applied in the ray tracing method.

3.3.2 Simplifications for cyclically symmetric structures

First simplification

An entire structure is analysed by considering a single "principal" sector, as illustrated in Figure 3.4(a). Artificial boundaries are introduced to model the cyclic symmetry condition. This is achieved by introducing wave amplitudes at boundaries A and B. In addition, wave amplitudes within the substructure Λ are considered.

The ray tracing method presented in Chapter 2 uses transmission coefficients to link the waves in different parts of the system together. If only one sector is modelled, there is no physical or geometrical link between boundaries A and B as they are not in direct contact. The only property that can be used is the phase change between one end and the other (see Section 3.3.1). This change of phase can be considered as a "transmission coefficient" from one end to the other, so a wave incident at one end will be "linked" to the other end by a phase change coefficient.

If the complex-valued displacement at A is u_{A}, then, from the rotationally periodic structure properties explained in Section 3.3.1, the displacement at B will be u_{B} such that $u_{\mathsf{B}} = u_{\mathsf{A}}\, e^{\mathrm{i}\frac{2\pi}{N}\kappa}$ (or $u_{\mathsf{A}} = u_{\mathsf{B}}\, e^{-\mathrm{i}\frac{2\pi}{N}\kappa}$). As the displacements are defined entirely using wave amplitudes, it follows that the waves incident on B and created at A will have an amplitude ratio of $e^{-\mathrm{i}\frac{2\pi}{N}\kappa}$; while the waves incident on A and created at B will have an amplitude ratio of $e^{\mathrm{i}\frac{2\pi}{N}\kappa}$. The difference in sign is due

to the different direction of propagation (negative s-direction – incident in A, or positive s-direction – incident in B).

To apply the ray tracing method, consider an initial set of wave amplitudes $\mathbf{a}_0$, illustrated in Figure 3.4(a), such that:

$$\mathbf{a}_{0_{[12\times1]}} = \begin{bmatrix} \mathbf{u}_{initial}^{(l)+} & \mathbf{u}_{initial}^{(l)-} & \mathbf{u}_{initial}^{(r)+} & \mathbf{u}_{initial}^{(r)-} \end{bmatrix}^{\mathrm{T}}. \tag{3.24}$$

Each wave travels along its corresponding waveguide. The waves starting on the left-hand side of the substructure or on the left boundary A will travel along $L^{(l)}$ and the ones on the right-hand side will travel along $L^{(r)}$. In this situation the dispersion matrix $\mathbf{D}$ is given by:

$$\mathbf{D}_{[12\times12]} = \begin{bmatrix} \mathbf{\Delta}_{L^{(l)}} & \mathbf{0} & \mathbf{0} & \mathbf{0} \\ \mathbf{0} & \mathbf{\Delta}_{L^{(l)}} & \mathbf{0} & \mathbf{0} \\ \mathbf{0} & \mathbf{0} & \mathbf{\Delta}_{L^{(r)}} & \mathbf{0} \\ \mathbf{0} & \mathbf{0} & \mathbf{0} & \mathbf{\Delta}_{L^{(r)}} \end{bmatrix} \tag{3.25}$$

where $\mathbf{\Delta}_{L^{(j)}} = \begin{bmatrix} e^{-\mathrm{i}k_1 L^{(j)}} & 0 & 0 \\ 0 & e^{-\mathrm{i}k_2 L^{(j)}} & 0 \\ 0 & 0 & e^{-\mathrm{i}k_3 L^{(j)}} \end{bmatrix}$, $j = l,\, r.$

The link between the left and right boundaries are given by the transmission coefficient matrix $\mathbf{T}$:

$$\mathbf{T}_{[12\times12]} = \begin{bmatrix} \mathbf{0} & \mathbf{0} & \mathbf{\Upsilon}^{-} & \mathbf{0} \\ \mathbf{B}^{(l)} & \mathbf{0} & \mathbf{0} & \mathbf{\Pi}^{(r)\to(l)} \\ \mathbf{\Pi}^{(l)\to(r)} & \mathbf{0} & \mathbf{0} & \mathbf{B}^{(r)} \\ \mathbf{0} & \mathbf{\Upsilon}^{+} & \mathbf{0} & \mathbf{0} \end{bmatrix}, \tag{3.26}$$

where $\mathbf{B}_{[3\times3]}^{(l)}$ and $\mathbf{B}_{[3\times3]}^{(r)}$ contain the reflection coefficients at the discontinuity Λ on its left and right hand sides respectively; $\mathbf{\Pi}_{[3\times3]}^{(l)\to(r)}$ and $\mathbf{\Pi}_{[3\times3]}^{(r)\to(l)}$ contain the transmission coefficients from waves incident from the left side to the right side (or from the right side to the left side, respectively). The matrices $\mathbf{\Upsilon}^{+}$ and $\mathbf{\Upsilon}^{-}$ represent the change of phase phenomenon between the cyclic symmetry boundaries in the

positive s direction and negative s direction, respectively. These are given by:

$$\boldsymbol{\Upsilon}^{+} = \begin{bmatrix} e^{\mathrm{i}\frac{2\pi}{N}\kappa} & 0 & 0 \\ 0 & e^{\mathrm{i}\frac{2\pi}{N}\kappa} & 0 \\ 0 & 0 & e^{\mathrm{i}\frac{2\pi}{N}\kappa} \end{bmatrix}, \tag{3.27a}$$

$$\boldsymbol{\Upsilon}^{-} = \begin{bmatrix} e^{-\mathrm{i}\frac{2\pi}{N}\kappa} & 0 & 0 \\ 0 & e^{-\mathrm{i}\frac{2\pi}{N}\kappa} & 0 \\ 0 & 0 & e^{-\mathrm{i}\frac{2\pi}{N}\kappa} \end{bmatrix}. \tag{3.27b}$$

Solving the fundamental equation of the ray tracing method: $|\mathbf{I} - \mathbf{TD}| = 0$, see Chapter 2 with the $\mathbf{T}$ and $\mathbf{D}$ matrices defined by Equations (3.25) and (3.26) for all κ values (see Section 3.3.1); all of the natural frequencies of the entire structure can be obtained by modelling only one of its sectors.

The advantage of modelling only one sector is that the total number of unknowns is reduced. If the substructure Λ itself contains n unknowns, then the total number of unknowns in the simplified system is $n+12$. By comparing this number with the total number of unknowns in the non-simplified system $(n+6)N$, it is clear that taking into account cyclic symmetry greatly simplifies the analysis and reduces the computation time.

Further simplification

The previous section introduced artificial boundaries A and B to take account of the cyclic symmetry. The change of phase from one end of a sector to the other end is expressed in the transmission matrix, where waves incident on symmetry boundaries are not reflected but "linked" to the other end of the sector. A further simplification can be made to the analysis, and this is presented here. For free-vibration analysis, the ray tracing method gives the relationship

$$\mathbf{a} = \mathbf{TDa}, \tag{3.28}$$

see Chapter 2, Equation (2.31). With the same structure and notation as in the previous paragraph, this gives:

$$\mathbf{a} = \begin{bmatrix} \mathbf{0} & \mathbf{0} & \boldsymbol{\Upsilon}^{-} & \mathbf{0} \\ \mathbf{B}^{(l)} & \mathbf{0} & \mathbf{0} & \boldsymbol{\Pi}^{(r)\to(l)} \\ \boldsymbol{\Pi}^{(l)\to(r)} & \mathbf{0} & \mathbf{0} & \mathbf{B}^{(r)} \\ \mathbf{0} & \boldsymbol{\Upsilon}^{+} & \mathbf{0} & \mathbf{0} \end{bmatrix} \begin{bmatrix} \boldsymbol{\Delta}_{L^{(l)}} & \mathbf{0} & \mathbf{0} & \mathbf{0} \\ \mathbf{0} & \boldsymbol{\Delta}_{L^{(l)}} & \mathbf{0} & \mathbf{0} \\ \mathbf{0} & \mathbf{0} & \boldsymbol{\Delta}_{L^{(r)}} & \mathbf{0} \\ \mathbf{0} & \mathbf{0} & \mathbf{0} & \boldsymbol{\Delta}_{L^{(r)}} \end{bmatrix} \mathbf{a}, \tag{3.29}$$

where

$$\mathbf{a} = \begin{bmatrix} \mathbf{u}^{(l)+} & \mathbf{u}^{(l)-} & \mathbf{u}^{(r)+} & \mathbf{u}^{(r)-} \end{bmatrix}^{\mathrm{T}}. \tag{3.30}$$

Expanding the second and third equations of (3.29) and re-arranging in matrix form, it can be shown that:

$$\begin{bmatrix} \mathbf{u}^{(l)-} & \mathbf{u}^{(r)+} \end{bmatrix}^{\mathrm{T}} = \begin{bmatrix} \boldsymbol{\Pi}^{(r)\to(l)} & \mathbf{B}^{(l)} \\ \mathbf{B}^{(r)} & \boldsymbol{\Pi}^{(l)\to(r)} \end{bmatrix} \begin{bmatrix} \boldsymbol{\Delta}_{L^{(r)}} \boldsymbol{\Upsilon}^{+} \boldsymbol{\Delta}_{L^{(l)}} & \mathbf{0} \\ \mathbf{0} & \boldsymbol{\Delta}_{L^{(l)}} \boldsymbol{\Upsilon}^{-} \boldsymbol{\Delta}_{L^{(r)}} \end{bmatrix} \begin{bmatrix} \mathbf{u}^{(l)-} & \mathbf{u}^{(r)+} \end{bmatrix}^{\mathrm{T}}. \tag{3.31}$$

Comparing this equation with Equation (3.28), it can be deduced that the ray tracing method can be used to model the entire structure with:

$$\mathbf{a} = \begin{bmatrix} \mathbf{u}^{(l)-} & \mathbf{u}^{(r)+} \end{bmatrix}^{\mathrm{T}}, \tag{3.32}$$

$$\mathbf{T} = \begin{bmatrix} \boldsymbol{\Pi}^{(r)\to(l)} & \mathbf{B}^{(l)} \\ \mathbf{B}^{(r)} & \boldsymbol{\Pi}^{(l)\to(r)} \end{bmatrix}, \tag{3.33}$$

$$\mathbf{D} = \begin{bmatrix} \boldsymbol{\Delta}_{L^{(r)}} \boldsymbol{\Upsilon}^{+} \boldsymbol{\Delta}_{L^{(l)}} & \mathbf{0} \\ \mathbf{0} & \boldsymbol{\Delta}_{L^{(l)}} \boldsymbol{\Upsilon}^{-} \boldsymbol{\Delta}_{L^{(r)}} \end{bmatrix}. \tag{3.34}$$

The matrix $\mathbf{D}$ can be simplified to

$$\mathbf{D} = \begin{bmatrix} \boldsymbol{\Delta}_{L^{(l)}+L^{(r)}} \boldsymbol{\Upsilon}^{+} & \mathbf{0} \\ \mathbf{0} & \boldsymbol{\Delta}_{L^{(l)}+L^{(r)}} \boldsymbol{\Upsilon}^{-} \end{bmatrix}, \tag{3.35}$$

where

$$\boldsymbol{\Delta}_{L^{(l)}+L^{(r)}}\boldsymbol{\Upsilon}^{\pm} = \begin{bmatrix} e^{\mathrm{i}\left(\pm\frac{2\pi}{N}\kappa - k_1 L_0\right)} & 0 & 0 \\ 0 & e^{\mathrm{i}\left(\pm\frac{2\pi}{N}\kappa - k_2 L_0\right)} & 0 \\ 0 & 0 & e^{\mathrm{i}\left(\pm\frac{2\pi}{N}\kappa - k_3 L_0\right)} \end{bmatrix}, \tag{3.36}$$

with $L_0 = L^{(l)} + L^{(r)}$, which represents the distance travelled along the waveguide from one substructure to its neighbour. For example, if the substructure Λ has a length $L^{(\Lambda)}$ and is placed on a ring-based system, as in Figure 3.4(a), then $L_0 = 2\pi R/N - L^{(\Lambda)}$.

From the previous derivations, the system illustrated in Figure 3.4(a) can be simplified to the one presented in Figure 3.4(b). The influence of the cyclic boundaries appears in the dispersion matrix (Equation (3.35)). The transmission coefficient matrix now contains terms on its diagonal: each wave is a function of itself (after some propagation, decay and change of phase). This simplification further reduces the number of unknown wave amplitudes: the total number of unknowns is now $n + 6$, where n is the number of unknowns present in the substructure itself.

To obtain all of the natural frequencies of the entire structure, the simplification presented above reduces the analysis of a system with $N(n+6)$ unknowns to $N/2+1$ analyses of a system with $n+6$ unknowns, when N is even; or to $(N+1)/2$ analyses of a system with $n+6$ unknowns, when N is odd. These correspond to the number of independent values of κ, see Section 3.3.1.

3.3.3 Obtaining the mode shape of the entire structure

Once the natural frequencies ω_n have been derived using Equation (3.28), the wave amplitudes of the modelled sector (with index 1) are obtained by solving $\Big[\mathbf{I} - \mathbf{T}(\omega_n)\mathbf{D}(\omega_n)\Big]\mathbf{a}_n^{(1)} = \mathbf{0}$, see Chapter 2. Here $\mathbf{a}_n^{(1)}$ contains the wave amplitudes defining the mode shape in the single "principal" sector. To obtain the mode shapes for the complete structure, the results obtained for the single sector are extended

using Equations (3.18) and (3.19). Equation (3.19) is an iterative expression that gives the mode shape of sector $(j+1)$ as a function of the mode shape of the previous sector (j). The wave amplitudes of the j^{th} sector $(j = 1, 2, \cdots, N)$ can also be expressed using those of the 1^{st} sector only with the following equation derived from Equation (3.19):

$$\mathbf{a}_n^{(j)} = e^{\mathrm{i}\frac{2\pi}{N}\kappa(j-1)}\mathbf{a}_n^{(1)}. \tag{3.37}$$

From Equation (3.37), the wave amplitudes in any sector of the structure can be calculated. The displacements corresponding to the mode shape can then by calculated using the standard equations defining the displacements as a sum of waves, see Chapter 2.

3.4 Applications

This section presents the application of the ray tracing method to analyse the free vibration of structures with periodicity and/or cyclic symmetry properties. The objective is to validate the models presented in Section 3.2 and 3.3 on simple cases first and then on the more complex case of the ring-based rate sensor.

3.4.1 Beam with identical uniformly-spaced point masses

Consider a finite cantilever beam with N identical uniformly-spaced point masses. The ray tracing approach using the periodicity simplification requires the transmission coefficient corresponding to a single sector. A sector is defined here as a beam portion of length $2L$ with a point mass in its mid-point. N identical sectors are put side by side to create a chain of N point masses uniformly separated with a distance $2L$, see Figure 3.5. The lengths $L^{(\mathrm{I})}$ and $L^{(\mathrm{II})}$ are the distance between the clamped boundary and the left side of the chain, and between the right side of the chain and the free boundary, respectively. L_{beam} is the length of the entire beam. For given lengths L_{beam}, $L^{(\mathrm{I})}$ and $L^{(\mathrm{II})}$, L is such that $L = \Big(L_{\text{beam}} - (L^{(\mathrm{I})} + L^{(\mathrm{II})})\Big)/2N$.

Using the substructuring method presented in Section 3.2.1, each sector can be modelled by its own reflection/transmission coefficient matrices. These are:

$$\mathbf{\Pi}_1^{l\to r} = \mathbf{\Delta}_L \mathbf{\Pi}_{\text{pt. mass}}^{l\to r} \mathbf{\Delta}_L, \tag{3.38a}$$

$$\mathbf{\Pi}_1^{r\to l} = \mathbf{\Delta}_L \mathbf{\Pi}_{\text{pt. mass}}^{r\to l} \mathbf{\Delta}_L, \tag{3.38b}$$

$$\mathbf{B}_1^{l} = \mathbf{\Delta}_L \mathbf{B}_{\text{pt. mass}}^{l} \mathbf{\Delta}_L, \tag{3.38c}$$

$$\mathbf{B}_1^{r} = \mathbf{\Delta}_L \mathbf{B}_{\text{pt. mass}}^{r} \mathbf{\Delta}_L. \tag{3.38d}$$

The notation is the same than the one used in Section 3.2.2. $\mathbf{\Delta}_L$ is the dispersion matrix for a straight beam of length L and is defined in Equation (2.26), see Chapter 2. $\mathbf{\Pi}_{\text{pt. mass}}^{l\to r}$ and $\mathbf{\Pi}_{\text{pt. mass}}^{r\to l}$ define the transmission coefficients from left to right and from right to left, respectively, through a point mass discontinuity. $\mathbf{B}_{\text{pt. mass}}^{l}$ and $\mathbf{B}_{\text{pt. mass}}^{r}$ contain the reflection coefficients on the left and right hand side, respectively, when waves impinge on a point mass. These four $[3 \times 3]$ matrices can be obtained using the equations presented in Chapter 2, Section 2.4.1, with the following simplifications: the rigid joint is considered to be a point mass, the third component in the transmission is neglected and curved beams models are extended to straight beams models by letting $R \to \infty$.

Equations (3.38) could also be obtained simply by intuition. These matrices contain the transmission/reflection coefficients of waves impinging and leaving a single sector composed of a beam portion of length L, a point mass and another beam portion of length L. When coming into the sector, the waves travel and decay along the length L before impinging on the point mass. They are then transmitted or reflected by the point mass by respecting the point mass own transmission/reflection characteristics. Then finally, they travel again along a length L to leave the sector. This explains the form of Equations (3.38).

Using Equations (3.10) and (3.11) with the individual sector transmission/reflection coefficients matrices defined in Equations (3.38), the transmission/reflection coefficients matrices of the overall chain of N sectors can be obtained. The entire

cantilever beam structure is then modelled by using:

$$\mathbf{T} = \begin{bmatrix} \mathbf{0} & \mathbf{T}_{\text{clamped}} & \mathbf{0} & \mathbf{0} \\ \mathbf{B}_N^l & \mathbf{0} & \mathbf{0} & \mathbf{\Pi}_N^{r\to l} \\ \mathbf{\Pi}_N^{l\to r} & \mathbf{0} & \mathbf{0} & \mathbf{B}_N^r \\ \mathbf{0} & \mathbf{0} & \mathbf{T}_{\text{free}} & \mathbf{0} \end{bmatrix}, \tag{3.39}$$

$$\mathbf{D} = \begin{bmatrix} \mathbf{\Delta}_{L^{(\text{I})}} & \mathbf{0} & \mathbf{0} & \mathbf{0} \\ \mathbf{0} & \mathbf{\Delta}_{L^{(\text{I})}} & \mathbf{0} & \mathbf{0} \\ \mathbf{0} & \mathbf{0} & \mathbf{\Delta}_{L^{(\text{II})}} & \mathbf{0} \\ \mathbf{0} & \mathbf{0} & \mathbf{0} & \mathbf{\Delta}_{L^{(\text{II})}} \end{bmatrix}. \tag{3.40}$$

Natural frequencies for particular values of N obtained with the ray tracing method using the above simplification are presented in Table 3.1. They are compared with results from a FE analysis using Euler/Bernoulli beam elements. The natural frequencies found using the two methods are in perfect agreement up to five significant figures.

3.4.2 Ring with identical uniformly-spaced point masses

Consider a ring with N identical uniformly-spaced point masses. Here, the ray tracing approach using the cyclic symmetry simplification requires the transmission coefficient corresponding to a single point mass. Calculation of the transmission coefficients for a ring with an attached mass can be obtained using the equations presented in Chapter 2, Section 2.4.1, by considering the rigid joint to have non-zero mass, zero length and zero moment of inertia. All of the matrices needed for the natural frequency analysis are [6×6] square matrices, and the wave amplitudes relate to extensional, flexural and decaying waves in both directions. For a particular cyclic mode number κ, the dispersion matrix will contain terms $e^{-\mathrm{i}\frac{2\pi}{N}\left(Rk_i \pm \kappa\right)}$ (with $i = 1, 2, 3$ and $\kappa = 0, 1, \ldots, N/2$ for N even or $\kappa = 0, 1, \ldots, (N-1)/2$ for N odd). To obtain the natural frequencies of the system for any cyclic mode number, $N/2+1$ (N even) or $(N+1)/2$ (N odd) different analyses are required, see Section 3.3.1, which correspond to the number of possible κ values.

The effect of additional masses on the natural frequencies of a ring has been investigated previously in [88]. In this work, a Rayleigh-Ritz approach was used to determine analytical expressions for the natural frequencies and natural frequency splits in terms of the orientations and magnitudes of the added masses. The assumption that the mode shapes of the imperfect ring are identical to those of a perfect ring, adopted in [88], has been shown to be reasonable provided that the degree of imperfection is sufficiently small [89]. Extending the work carried out in [88] and [89], McWilliam *et al.* [10] investigated the case of identical masses distributed uniformly around the circumference of a perfect ring. They obtained simplified analytical expressions using the Rayleigh-Ritz method for the natural frequencies and also derived frequency splitting rules, which indicate that the natural frequencies will split only when $2n/N$ is an integer, n being the mode number. n can take any integer value and is different from κ.

It is found that the natural frequencies obtained by the ray tracing method are in accordance with the natural frequency splitting rules of [10]. The frequencies of the flexural modes are illustrated in Table 3.2 for different combinations of mode number n ($= 2, 3, \ldots, 6$) and number of point masses N ($= 0, 1, \ldots, 4$). For the $N = 0$, 1, 2 and $N = 4$ cases (not $N = 3$), the angular position of the masses does not change as uniformly spaced masses are added. For any n, the corresponding natural frequencies decrease. However, changing the angular position of masses on the ring changes the mass distribution and can either increase or decrease the natural frequency, *e.g.* see $N = 2, 3$. Both analyses show very good agreement for the frequency split. However, the frequencies calculated with the two methods differ slightly due to the consideration of the Poisson's ratio in the Flügge's strain-displacement relations used to calculate the natural frequency of the original perfect ring (with $N = 0$) in [10]. The Poisson's ratio is not taken into account in the present ray tracing approach as shear deformation is neglected.

3.4.3 Regular polygons

The ray tracing method using the cyclic symmetry simplification can be applied to calculate the natural frequencies and mode shapes for the in-plane vibration of regular polygons having N sides, with each corner at a distance R from the centre. For such polygon, the external angle α between two sides is $\alpha = 2\pi/N$ and the length L_0 of one side is $L_0 = 2R\sin\dfrac{\alpha}{2}$, see Figure 3.6.

In order to apply the ray tracing method, the transmission coefficients of one corner are calculated using the analysis presented in Chapter 2, Section 2.4.2. The use of the cyclic symmetry simplification greatly reduces the number of unknowns, especially for large N. For any N, only six waves are required (extensional, flexural and decaying). Natural frequencies calculated for different numbers of sides N and cyclic mode numbers κ are compared with results from a FE analysis using Euler/Bernoulli beam elements in Table 3.3. The natural frequencies found using the two methods are in perfect agreement up to five significant figures.

These analyses were performed for a fixed distance R between the centre and one corner, and only the number of sides was varied. When the number of sides tends to infinity, it is expected that the natural frequencies of the polygon should tend to those of a perfect ring with radius R. This behaviour is illustrated in Figure 3.7 where the natural frequencies for $\kappa = 2$ and $\kappa = 3$ tend to the corresponding perfect ring natural frequencies ω_2 and ω_3 for flexural modes, which can be calculated using Equation (2.80) (see Chapter 2) and are given in Table 3.2 (with $N = 0$ and $n = 2$, 3).

3.4.4 Ring-based rate sensor

The ring-based rate sensor presented in Figure 3.8 is modelled using the cyclic symmetry simplification. The dimensions used are given in Figure 3.8(b). Only a single leg (three beam portions) is modelled. The ring is taken into account using the analysis presented in Section 3.3.2, *i.e.* waves impinging and leaving the disconti-

nuity ring/leg are still considered. Eight identical sectors are required to complete the entire structure ($N = 8$). It is assumed that the leg and ring are connected at a single point (only the centreline is modelled). The transmission coefficients for the different joints are calculated using the analysis presented in Chapter 2, Section 2.4 (*e.g.* with $\alpha = 90°$ for the ring/leg transmission). The legs are assumed to be formed with straight beams connected at abrupt changes in direction. The presence of rounded or "radiused" angles would be a more realistic model, see Figure 1.2, and it would also minimise the stress concentrations at corners. However, if one wants to model with the ray tracing method, the curved beam portion that connects the two straight beams in a rounded angle, it is not possible to use the governing equations specific for thin structures detailed in Chapter 2, Section 2.2. The radius of curvature of the curved beam is too small compared to its width to neglect shear deformation and rotary inertia. For simplification purpose, abrupt changes in direction are assumed and the direct transmission between two straight beam components is considered.

Using the ray tracing method with the cyclic symmetry simplification, the wave amplitude vector contains 24 unknowns (six waves per beam section and six waves leaving the discontinuity ring/leg along the ring), in contrast to 192 unknowns without the simplification. To obtain all of the natural frequencies of the ring-based rate sensors, five different analyses ($\kappa = 0$, 1, 2, 3, 4, see Section 3.3.1) are performed. The calculated frequencies are compared with FE predictions using Euler/Bernoulli and Timoshenko two-dimensional beam elements in Table 3.4. As in the case of regular polygons (Section 3.4.3), the converged FE solution gives natural frequencies that agree to five significant figures with the ray tracing model when Euler/Bernoulli elements are used, see Table 3.4. With Timoshenko elements, the percentage differences are less than 0.5%. This difference is due to the shear deformation being neglected in the ray tracing method, and it can be seen that the difference generally increases as the mode number increases, as expected.

From the cyclic symmetry of the system, it can be shown [86] that two orthogonal modes exist for every $\kappa = 1$, 2, 3, while the $\kappa = 0$, 4 modes are unique. Figure 3.9 presents the first mode (and its orthogonal complement) for $\kappa = 0$, 1, 2, 3, 4. The

displayed mode shapes were obtained using the ray tracing method and are similar to those given by the FE analysis. For interpretation, the first mode shape with $\kappa = 0$ corresponds to rigid body mode of a free ring rotating about its centre, while the first mode shape with $\kappa = 1$ corresponds to rigid body translation of a free ring.

The main conclusion of this study is that, subject to the assumptions that shear deformation and rotary inertia are neglected and by modelling the centreline of the ring only (two-dimensional Euler/Bernoulli beam elements), the results obtained using the ray tracing method are in excellent agreement with those obtained using the FE method but with greatly reduced computational effort.

3.5 Conclusion

In this chapter, the ray tracing method has been extended to cope efficiently with structures that are periodic. The periodicity can be modelled using a recursive form in which a chain of N sectors is characterised by the transmission and reflection characteristics of a chain of $(N-1)$ sectors. Each sector can itself be the result of a substructuring method in such a way that a sector may represent several components coupled together. The chain of identical sectors, with the use of its transmission and reflection coefficients calculated with the periodicity analysis, can be inserted into an overall bigger structure that may contain either external boundaries or other waveguide components. A cyclic symmetry simplification, based on the fact that the displacement in one sector is related to the displacement in a neighbouring sector, was also presented and proved to greatly reduce the complexity of the analysis.

Results for natural frequencies and mode shapes for periodic and cyclically symmetric structures were compared with FE analyses and showed very good agreements. The ray tracing method and its possible simplifications are then shown to be exact, rapid and efficient methods to model free vibrations of structures composed by straight and curved beam components.

Section 3.4.4 presented the free vibration analysis of a ring-based rate sensor by the ray tracing method. The objective of the thesis is to understand support losses for structures of this kind. Support loss modelling will be inspected for simple structures in Chapter 4. The ring-based rate sensor support losses and the influence of its leg design on the Q-factor will be the subject of Chapter 5. The cyclic symmetry simplification method presented here will be used thoroughly in Chapter 5 and its assets to simplifying the analysis when studying parameter changes will be shown.

While the simplest structures transmit vibrational energy by just one type of wave motion (for example flexural waves), others transmit energy in simultaneous and particular combinations of longitudinal, torsional and bi-directional flexural waves. When these different wave types encounter a discontinuity in the structure, they interact and are converted from one type into another type. This is an important notion in the wave propagation process of complex structures. In-plane vibrations consisting of flexural and longitudinal waves have been studied so far and an extension of the ray tracing method that considers bi-directional flexural and torsional waves will be the subject of Chapter 6. It will be seen that the simplifications presented within Chapter 3 for in-plane vibrations can also be applied to out-of-plane vibrations.

Figures and tables

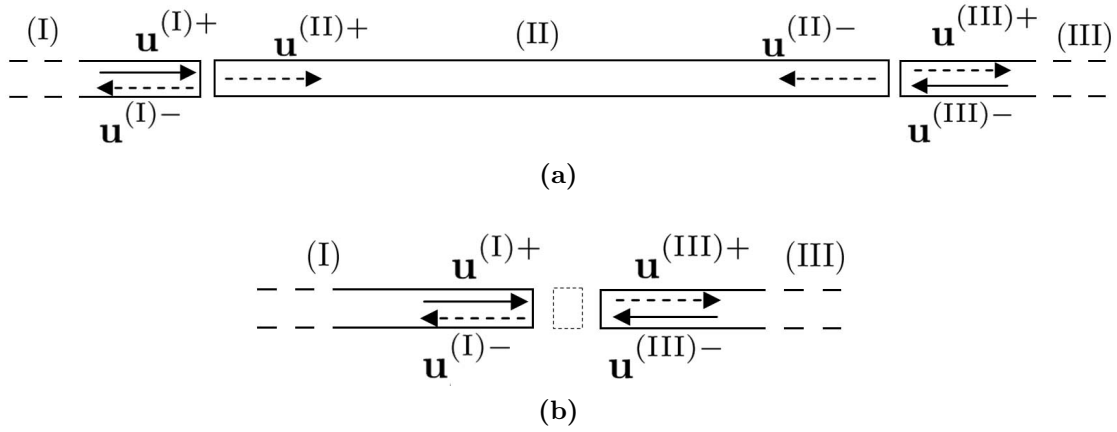

Figure 3.1: Substructuring method showing the different set of wave amplitudes considered. The system in (a) can be simplified to the system in (b).

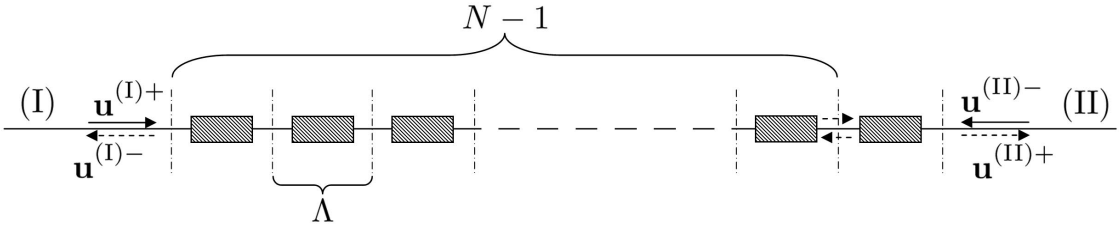

Figure 3.2: System showing periodic symmetry properties. A single sector is added to a chain of $(N-1)$ similar sectors.

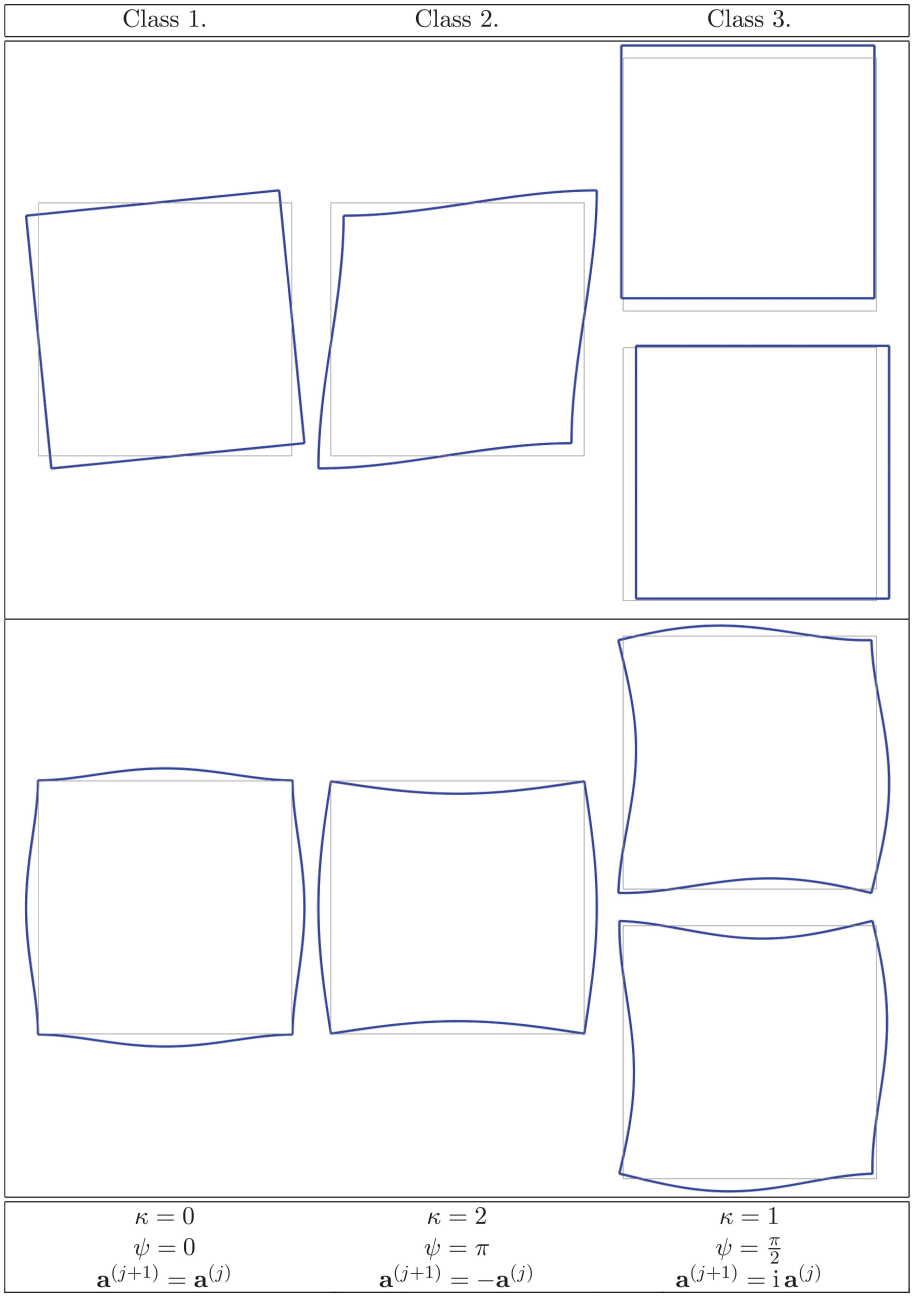

Figure 3.3: Two lowest frequency mode shapes for each class of a thin square ($N = 4$) showing the corresponding values of the different parameters.

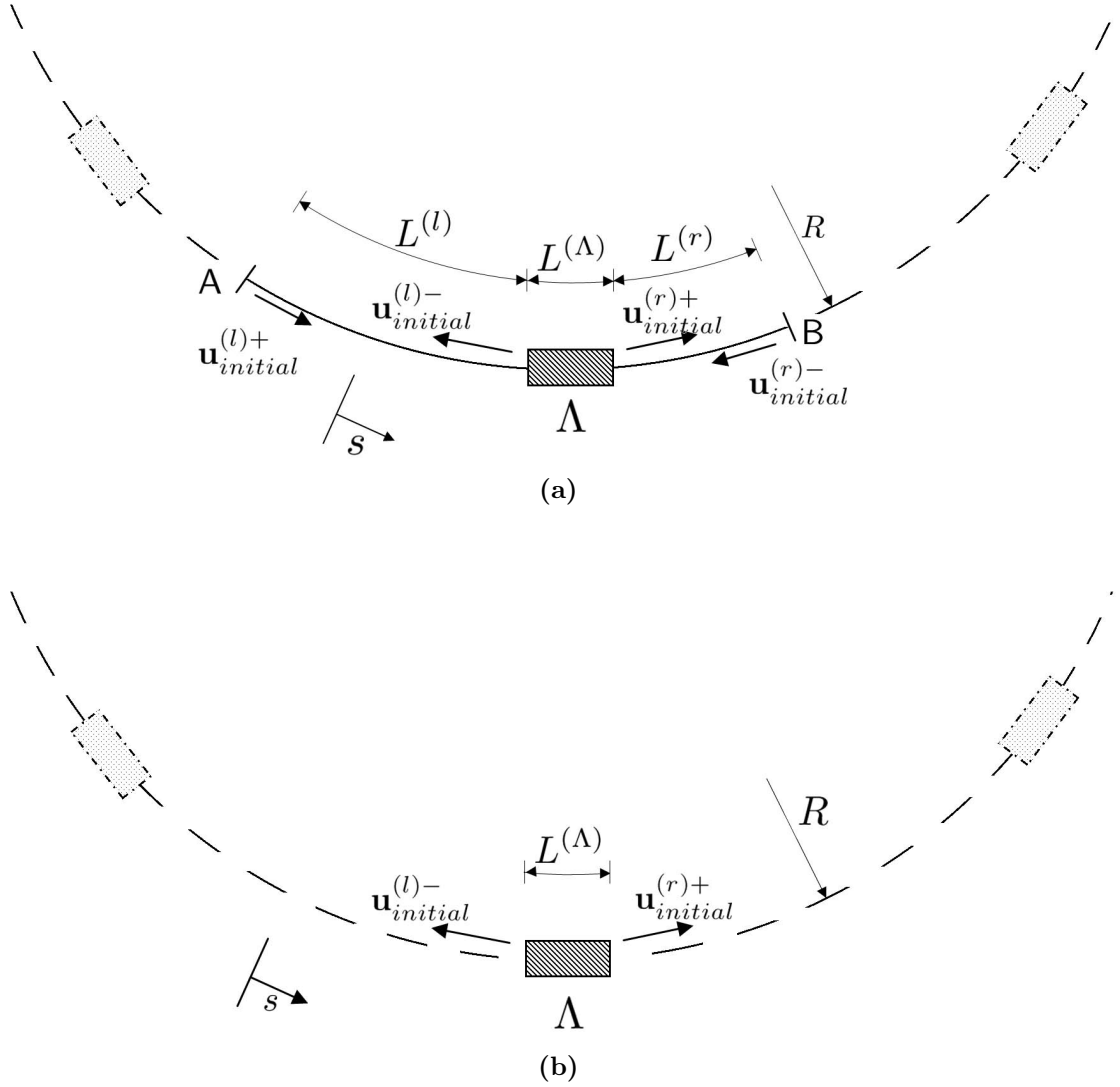

Figure 3.4: Cyclic symmetry simplifications. (a) involves four sets of wave amplitudes, whereas only two sets of wave amplitudes are considered in (b).

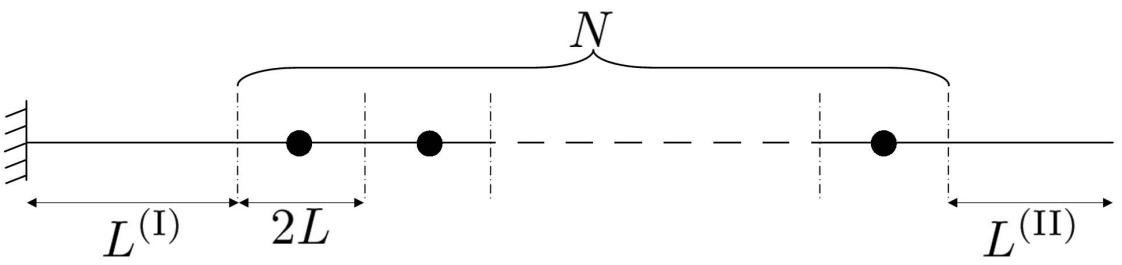

Figure 3.5: Cantilever beam with N identical, uniformly-spaced point masses.

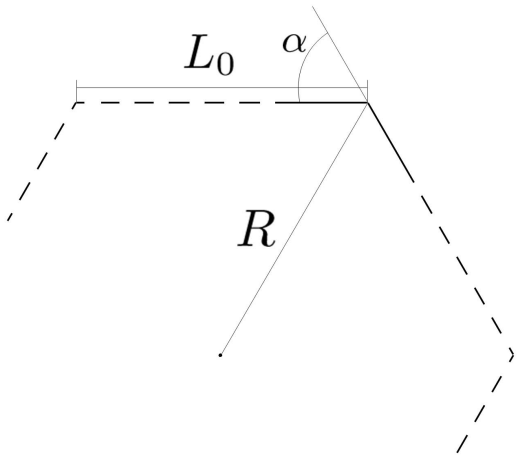

Figure 3.6: Notation used for the study of regular polygons with N sides. Note that it is not necessarily a hexagon.

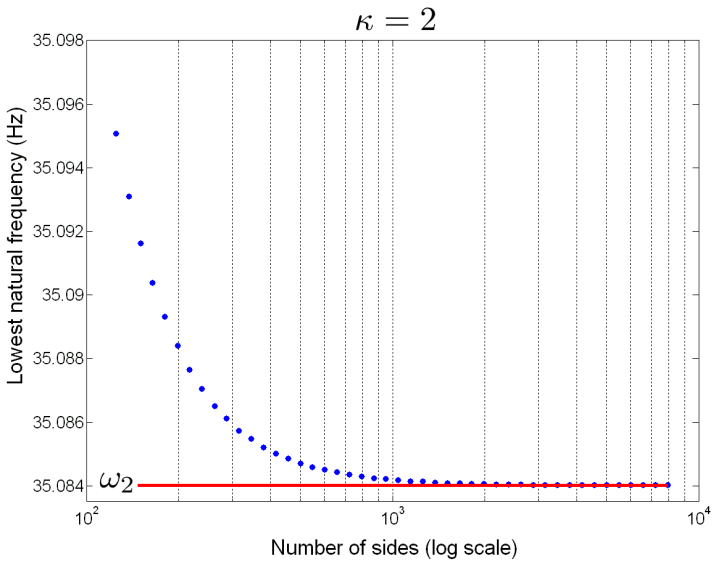

(a)

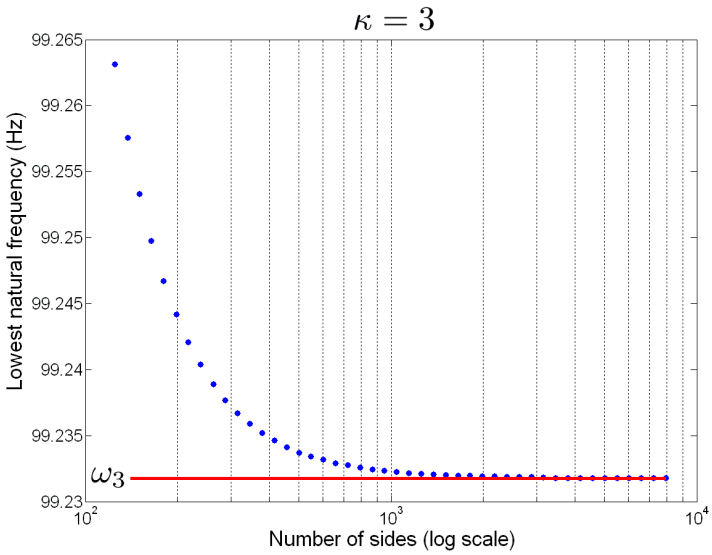

(b)

Figure 3.7: Lowest natural frequency calculated with the ray tracing method of a regular polygon with $\kappa = 2$ (a) or $\kappa = 3$ (b), function of its number of sides N. The dimensions and material properties of beams composing the polygons are the same as those used in Table 3.2. ω_2 and ω_3 are the $n = 2$ and $n = 3$ natural frequencies for flexural modes in a perfect ring, see Equation (2.80) in Chapter 2.

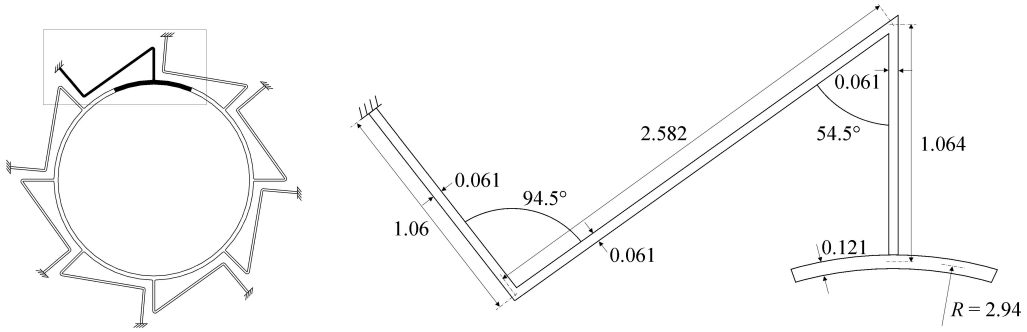

Figure 3.8: (a) Ring-based rate sensor with cyclic symmetry and its 45° principal sector. (b) Actual modelled structure and its dimensions in mm (with axial thickness = 0.1 mm).

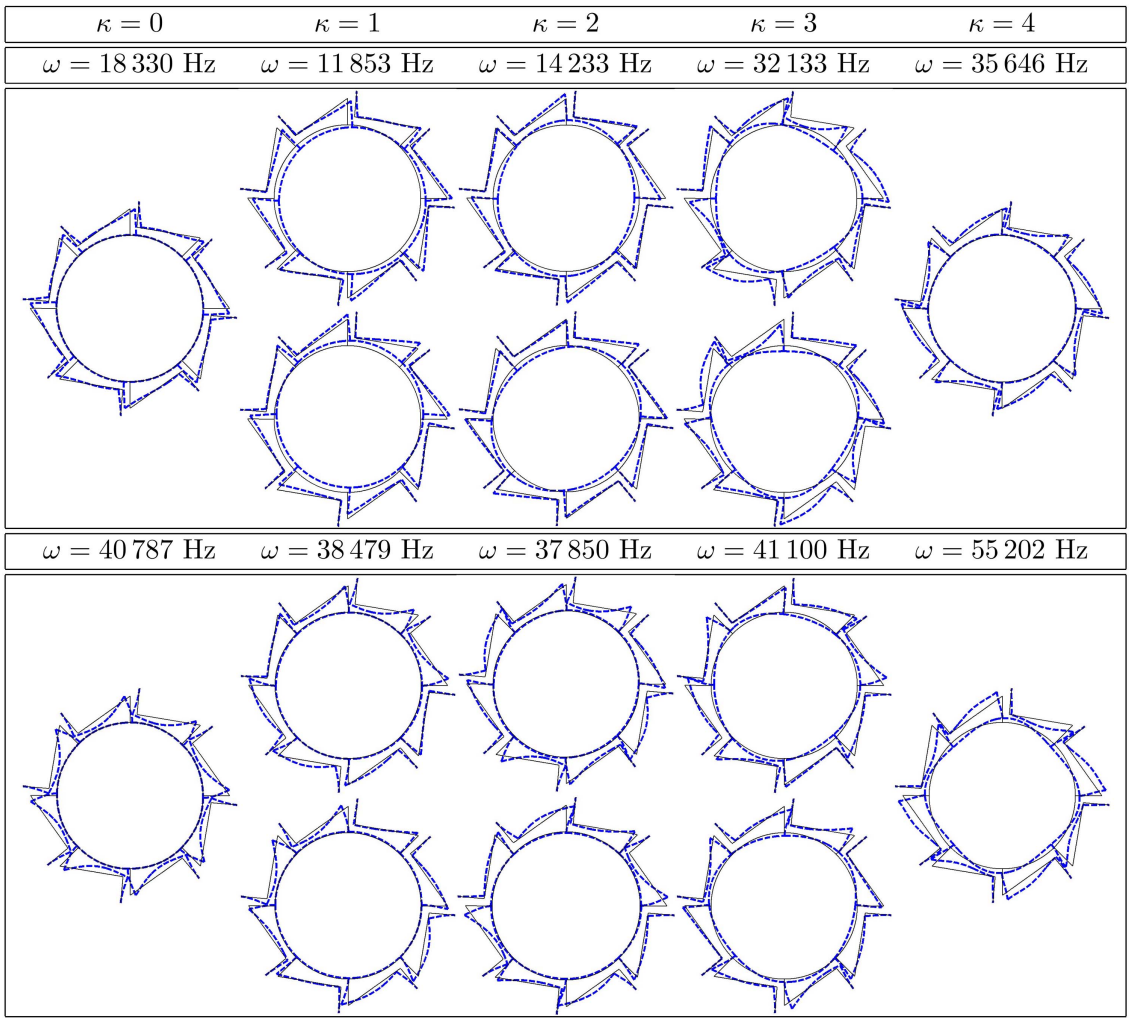

Figure 3.9: Mode shapes of the ring-based resonator for the two lowest natural frequencies of each value of κ.

Table 3.1: Natural frequencies (Hz) for a cantilever beam with N identical uniformly-spaced point masses calculated with the ray tracing ("Ray Tr.") method and a FE model (100 two-dimensional Euler/Bernoulli beams elements between each point mass). With $L_{\text{beam}} = 2\,\text{m}$, $L^{(\text{I})} = 0.2\,\text{m}$, $L^{(\text{II})} = 0.1\,\text{m}$, width $= 0.005\,\text{m}$, thickness $= 0.1\,\text{m}$, $\rho = 7850\,\text{kg/m}^3$, $E = 206 \cdot 10^9\,\text{N/m}^2$ and Poisson ratio $= 0.3$. Each additional point mass has a mass of $0.1\,\text{kg}$.

	$N = 2$		$N = 4$		$N = 7$		$N = 10$	
	Ray Tr.	FE	Ray Tr.	FE	Ray Tr.	FE	Ray Tr.	FE
$n = 1$	1.0232	1.0232	1.0106	1.0106	0.9932	0.9932	0.9767	0.9767
$n = 2$	6.4277	6.4277	6.3347	6.3347	6.2195	6.2195	6.1129	6.1129
$n = 3$	17.737	17.737	17.733	17.733	17.401	17.401	17.097	17.097
$n = 4$	35.167	35.167	34.695	34.695	34.070	34.070	33.474	33.474
$n = 5$	58.615	58.615	56.425	56.425	56.266	56.266	55.305	55.305
$n = 6$	86.468	86.468	86.446	86.446	83.954	83.954	82.602	82.602
$n = 7$	120.62	120.62	120.29	120.29	117.04	117.04	115.39	115.39

Table 3.2: Natural frequencies (Hz) splitting of the flexural modes for a perfect ring with identical uniformly-spaced masses for various combinations of mode number and added masses. With $R = 0.3\,\mathrm{m}$, radial thickness $= 0.005\,\mathrm{m}$, axial length $= 0.1\,\mathrm{m}$, $\rho = 7850\,\mathrm{kg/m^3}$, $E = 206 \cdot 10^9\,\mathrm{N/m^2}$ and Poisson ratio $= 0.3$. Each additional point mass has a mass of $0.1\,\mathrm{kg}$.

	$N=0$		$N=1$		$N=2$		$N=3$		$N=4$	
	Ray Tr.	Ref. [10]	Ray Tr.	Ref. [10]	Ray Tr.	Ref. [10]	Ray Tr.	Ref. [10]	Ray Tr.	Ref. [10]
$n=2$	35.1	36.8	34.7	36.4	34.3	36.0	34.4	36.1	33.7	35.3
	-	-	35.0	36.7	34.9	36.6	-	-	34.7	36.4
$n=3$	99.2	104.0	98.1	102.8	96.9	101.6	95.8	100.4	96.7	101.3
	-	-	99.1	103.9	99.0	103.7	98.8	103.6	-	-
$n=4$	190.3	199.5	188.0	197.0	185.7	194.6	186.6	195.5	181.2	190.0
	-	-	190.1	199.3	190.0	199.1	-	-	189.7	198.8
$n=5$	307.7	322.6	304.0	318.5	300.4	314.5	302.1	316.2	300.1	314.2
	-	-	307.5	322.4	307.4	322.2	-	-	-	-
$n=6$	451.4	473.2	446.0	467.1	440.7	461.2	435.3	455.6	430.7	450.1
	-	-	451.2	473.0	451.1	472.9	450.9	472.7	450.7	472.5

Table 3.3: Natural frequencies (Hz) for regular polygons with N sides calculated with the ray tracing method and a FE model (100 two-dimensional Euler/Bernoulli beams elements per side). Dimensions and material properties of beams composing the polygons are the same as those given in Table 3.2.

	$N=3$		$N=4$		$N=5$		$N=6$	
	Ray Tr.	FE	Ray Tr.	FE	Ray Tr.	FE	Ray Tr.	FE
$\kappa=0$	97.503	97.503	146.20	146.20	211.39	211.39	291.66	291.66
	205.84	205.84	280.16	280.16	391.69	391.69	532.57	532.57
	526.62	526.62	788.18	788.18	1134.9	1134.9	1553.1	1553.1
$\kappa=1$	70.415	70.415	126.87	126.87	203.51	203.51	299.48	299.48
	240.59	240.59	327.30	327.30	445.21	445.21	590.31	590.31
	441.31	441.31	34.353	34.353	1078.4	1078.4	1526.1	1526.1
$\kappa=2$	-	-	37.131	37.131	41.773	41.773	39.982	39.982
	-	-	64.517	64.517	123.33	123.33	213.60	213.60
	-	-	443.69	443.69	618.81	618.81	794.51	794.51
$\kappa=3$	-	-	-	-	-	-	99.841	99.841
	-	-	-	-	-	-	129.04	129.04
	-	-	-	-	-	-	973.34	973.34

Table 3.4: Natural frequencies (Hz) for the ring-based resonator calculated with the ray tracing method and a FE model (two-dimensional Euler/Bernoulli beams elements and Timoshenko (noted "T'nko") beams elements, with 0.85 as shear correction factor, of approximate length 0.01 mm). The ring dimensions are presented in Figure 3.8(b). The material properties used are $\rho = 2329\,\mathrm{kg/m^3}$, $E = 170{\cdot}10^9\,\mathrm{N/m^2}$ and the Poisson ratio is taken = 0.28.

	Ray Tracing	FE analysis		Difference %
		Euler beams	T'nko beams	Ray Tr./T'nko beams
$\kappa = 0$	18 330	18 330	18 277	0.29
	40 787	40 787	40 725	0.15
	67 320	67 320	67 028	0.43
$\kappa = 1$	11 853	11 853	11 820	0.28
	38 479	38 479	38 416	0.16
	65 971	65 971	65 697	0.42
$\kappa = 2$	14 233	14 233	14 217	0.12
	37 850	37 850	37 784	0.17
	65 520	65 520	65 253	0.41
$\kappa = 3$	32 133	32 133	32 076	0.17
	41 100	41 100	41 001	0.24
	66 135	66 135	65 871	0.40
$\kappa = 4$	35 646	35 646	35 591	0.15
	55 202	55 202	54 978	0.41
	73 110	73 110	72 830	0.38

Chapter 4

Modelling the support loss for in-plane vibrations

4.1 Introduction

The coupled resonator-substrate system is modelled to understand the interaction and energy transmission between them. Owing to the large relative size and shape complexity of the substrate, it is not possible to model the substrate in its entirety and some simplifications are made. For example, if finite elements are used, the domain of analysis needs to be truncated to a manageable size, and the effect of wave propagation into the remaining substrate is approximated as a propagation into an infinite domain. Various methods have been used to approximate infinite domains in previous works. A brief summary of these follows.

4.1.1 Analytical model

The analytical model is an extension of the work carried out by Hao *et al.* [42], which is itself based on the fundamental work of Miller and Pursey [90]. Hao *et al.* developed a theoretical approach to model the substrate and determined the

support losses in cantilevered beams and disc shaped resonators. The response of the resonant structure for in-plane vibrations was determined either from a finite element analysis or from analytical mode shape expressions. Fixed boundary conditions were assumed at the anchors of the structure. The resulting stresses at the anchors drive the substrate, which was considered to be an infinite elastic thin plate for the case of cantilever beam resonators. The displacement field in the substrate was obtained analytically by modelling its behaviour with the classic two-dimensional dynamic equations for a thin plate, subjected to the above boundary condition as stress sources. The work done by the resonator was calculated by integrating the product of shear stress at the anchor with the induced displacement in the substrate, over one cycle of vibration. This gave the loss from the system to the substrate per cycle. The ratio of total energy of the resonator, *i.e.* the energy calculated using the analytical mode shape expression for cantilever beams or using finite elements analyses for more complex resonators, to the energy lost per cycle, gave the Q-factor for the device.

This approach has its limitations. It assumes the wavelength of propagating waves to be much larger than the thickness of the vibrating structure for the two-dimensional theory to be valid. It is also unable to capture the effects of wave reflections at discontinuities in the substrate, since the substrate is modelled as a perfect semi-infinite thin plate. However, thanks to the analytical expressions of the anchor displacement found for different types of stress sources (see Section 4.2.5), calculating Q-factors for different resonators is quite straightforward. It is a very effective method in which the substrate model does not change for different resonator designs. A change of parameter in the resonator would only induce a change of the resonator model. The substrate model reduces to a simple analytical expression, and its implementation to calculate Q is numerically very efficient, which is not the case for the methods presented in subsequent sections.

An extension of this analytical model that considers different stress source conditions is presented in Section 4.2. Other methods that can model infinite domains are presented in Sections 4.3 and 4.4. The ultimate aim is to validate the use of the analytical model to calculate Q-factors by comparing results obtained from the

different methods. Once the analytical model has been validated, it will be used for the parametric study on the leg design in the entire ring-based rate sensor (see Chapter 5).

4.1.2 High-fidelity multiphysics simulations

In the approach by Park and Park [36, 37], the resonator system was partitioned into three modular subsystems consisting of the substrate, the resonator and its electrostatic actuators. Each of these was modelled independently and then integrated by matching the interface conditions. Similar to [42], this approach assumes the substrate to be a semi-infinite elastic medium. However, it is not a thin-plate in this case. The motion of the substrate was expressed as a superposition of various modes of wave propagation. The contribution of these various modes to a particular motion was obtained using a numerical scheme. The resonator response was calculated from a finite element analysis and a response receptance matrix, relating the forces and displacements at the anchor and excitation nodes, was constructed. An electro-mechanical model between the actuator nodes on the substrate and the corresponding excitation nodes on the resonant structure gave another matrix that couples two other subsystems. A response matrix relating forces and displacements corresponding to points on the substrate was constructed. The model assumed the substrate to be an infinite half-space and the displacements corresponding to a given load were obtained by adding up contributions from different wave modes. Combining the three response matrices, the matrix of the entire structure was constructed which was used to derive the stiffness and the damping matrices of the overall system and hence calculate Q.

This approach has the disadvantage that a separate response matrix needs to be calculated for the substrate every time the geometry of the resonator anchor is changed. Also the calculation of the response matrix for the substrate is computationally intensive.

4.1.3 Truncated domain FEA approaches

These finite element based methods truncate the substrate at finite dimensions and apply various boundary conditions at the edge so as to approximate the effect of infinite domains and simulate infinite boundaries. The resonator and a "finite" part of the substrate are modelled with classic finite elements, whereas special boundary elements are applied to the substrate edge.

The simplest method of infinite domain approximation is the use of damping elements. It involves placing viscous elements at the edge of the truncated domain. These elements have higher damping coefficient values than the material of the truncated domain. The propagating waves are attenuated in these elements due to higher damping characteristics. However the main drawback with this approach is that a sudden change in the material impedance induces spurious reflections at the boundary. Another disadvantage is that they are effective only for the case when the incoming wave is almost normal to the boundary. Also reflections from the outer edge are still possible if the domain containing the damping elements is not sufficiently large.

Two other methods, namely the use of a perfectly matched layer and infinite elements are possible and are studied in depth in Sections 4.3 and 4.4.

4.2 Analytical model

4.2.1 Physical modelling and main assumptions

A MEMS resonator must be attached to a foundation (or substrate). This attachment can take different forms but typically the resonator and substrate are etched in the same plane, from the same silicon wafer. The joint interface between the resonator and substrate, which is often modelled as a clamped attachment, is subjected to time-harmonic stresses that excite elastic waves in the substrate. These

waves propagate into the substrate and carry energy away from the resonator. In this way the support structure absorbs some of the vibration energy from the resonator.

For a simple cantilever beam resonator [42], the support interface is subjected to time-harmonic stresses due to shear stress only. However, in more complex resonators such as the ring-based rate sensor, the supporting legs produce both shear and normal stresses simultaneously, see Figure 4.1. In Figure 4.1, the motion of the resonator occurs in-plane only (within the plane (x, z)). Out-of-plane motion, along the y-axis direction, will be studied in Chapter 6.

It has been shown [41] that a MEMS resonator and its substrate can reasonably be analysed separately. Based on the significant dimensional difference between a typical resonator and its substrate, it can be assumed that all the energy entering the support propagates away to large distances and no energy returns to the resonator; which signifies that the elastic waves in the support will not have a significant effect on the modes of the resonator. The support is modelled as being semi-infinite, and ensures that the calculated support loss is an upper bound of the actual support loss. For the ring-based rate sensor, it is also assumed that the resonator and its substrate lie in the same plane, and have equal out-of-plane thickness h, such that all the vibrations occur in plane. Assuming that the thickness of the resonator is much smaller than the wavelength of the transverse elastic waves propagating in the support (λ_T), such that:

$$\frac{\lambda_T}{h} >> 1, \tag{4.1}$$

the substrate is modelled as a two-dimensional thin plate undergoing plane stress.

A theoretical derivation of the vibrational displacement of the substrate is possible if the stress source is uniformly distributed across the clamped interface region [90].

The main steps to analyse the support using the analytical model inspired by [42, 90] and to calculate the Q-factor of any resonator are presented in the following sections. They are summarised as follows.

- The elastic wave equations that model the behaviour of a thin-plate are ex-

pressed. They describe the displacements (in two different directions) as a function of the time and the spatial position in the plate.

- Some new operators, function of the spatial positions x and z, are introduced in the previous equations. This simplifies the equations and makes them easier to solve.

- The difficulty is now that the governing equations are still expressed as a function of x and z. A Fourier transform that removes the x dependency bypasses this issue. The equations are then solved in the wavenumber domain.

- As they are differential equations, some integration constants appear when they are solved. These constants are derived by applying appropriate boundary conditions at the anchor point on the edge of the thin-plate. These conditions express the influence of the resonator on its support.

- An inverse Fourier transform is performed to come back in the real domain. The displacement at any point of the thin-plate, induced by the applied boundary conditions, can now be found.

- The mean displacement along the x-axis and over the clamped interface region is derived in order to calculate the amount of energy lost.

- From this mean displacement and using the applied forces at the anchor point, the energy lost per cycle of vibration is expressed.

- The Q-factor that considers the quantity of energy lost through the support is finally calculated.

4.2.2 Model of the support structure

This section presents the main steps and main equations of the development of the analytical support model. A more detailed description can be found in Appendix A.

The vibration of the resonator causes elastic waves to propagate into the support. This support, as explained in Section 4.2.1, is considered as a thin-plate with equal

thickness to that of the resonator, and is modelled using a two-dimensional elastic wave theory. Starting from the three-dimensional elasticity of an isotropic solid and assuming than one dimension is much smaller than the other ones (see Appendix A), the equations governing the in-plane displacements of a thin plate can be expressed as [54]:

$$\frac{\partial^2 u}{\partial t^2} = c_L^2 \frac{\partial^2 u}{\partial x^2} + c_T^2 \frac{\partial^2 u}{\partial z^2} + \left(c_L^2 - c_T^2\right) \frac{\partial^2 w}{\partial x \partial z}, \tag{4.2}$$

$$\frac{\partial^2 w}{\partial t^2} = c_L^2 \frac{\partial^2 w}{\partial z^2} + c_T^2 \frac{\partial^2 w}{\partial x^2} + \left(c_L^2 - c_T^2\right) \frac{\partial^2 u}{\partial x \partial z}, \tag{4.3}$$

where u and w are the displacements in the support along the x- and z-axes, respectively, and c_L and c_T are the propagation velocities for longitudinal and transverse waves, respectively, given by:

$$c_L^2 = \frac{E}{\rho(1-\nu^2)}, \tag{4.4}$$

$$c_T^2 = \frac{E}{2\rho(1+\nu)}. \tag{4.5}$$

In these equations, E is the Young's modulus, ρ is the mass density and ν is the Poisson's ratio of the support material.

It is assumed that these displacements are time-dependent at frequency ω (excitation frequency) and have the form $u = \hat{u}\, e^{-\mathrm{i}\omega t}$ and $w = \hat{w}\, e^{-\mathrm{i}\omega t}$. In order to simplify Equations (4.2) and (4.3), new operators in terms of the cross-derivatives of $\hat{u}$ and $\hat{w}$ with respect to x and z are introduced:

$$\Theta = \frac{\partial \hat{u}}{\partial x} + \frac{\partial \hat{w}}{\partial z}, \tag{4.6}$$

$$\Omega = \frac{\partial \hat{w}}{\partial x} - \frac{\partial \hat{u}}{\partial z}. \tag{4.7}$$

Equations (4.2) and (4.3) can be rewritten in terms of these new operators as follows:

$$-\omega^2 \hat{u} = c_L^2 \frac{\partial \Theta}{\partial x} - c_T^2 \frac{\partial \Omega}{\partial z}, \tag{4.8}$$

$$-\omega^2 \hat{w} = c_L^2 \frac{\partial \Theta}{\partial z} + c_T^2 \frac{\partial \Omega}{\partial x}. \tag{4.9}$$

The main advantage of using Equations (4.8) and (4.9) compared to Equations (4.2) and (4.3) is that no second derivatives appear. The objective now is to solve the coupled Equations (4.2) and (4.3) in terms of Θ and Ω. To do this, they are further re-organised as:

$$c_L^2 \left(\frac{\partial^2 \Theta}{\partial x^2} + \frac{\partial^2 \Theta}{\partial z^2} \right) + \omega^2 \Theta = 0, \tag{4.10}$$

$$c_T^2 \left(\frac{\partial^2 \Omega}{\partial x^2} + \frac{\partial^2 \Omega}{\partial z^2} \right) + \omega^2 \Omega = 0. \tag{4.11}$$

Equations (4.10) and (4.11) are independent of each others and are easier to solve. To remove the double dependency in x and z, a Fourier transform, from the real domain to the wavenumber domain, is applied to this set of equations.

In the following equations, the subscript F denotes the Fourier transform and ξ is the variable of this transform, *i.e.* the Fourier transform is defined as:

$$g(\xi) = \int_{-\infty}^{+\infty} f(x)\, e^{-\mathrm{i}\xi x}\, \mathrm{d}x, \tag{4.12}$$

$$f(x) = \frac{1}{2\pi} \int_{-\infty}^{+\infty} g(\xi)\, e^{\mathrm{i}\xi x}\, \mathrm{d}\xi. \tag{4.13}$$

Applying Fourier transforms to Equations (4.10) and (4.11) gives:

$$\frac{\mathrm{d}^2 \Theta_F}{\mathrm{d}z^2} - \left(\xi^2 - \frac{\omega^2}{c_L^2} \right) \Theta_F = 0, \tag{4.14}$$

$$\frac{\mathrm{d}^2 \Omega_F}{\mathrm{d}z^2} - \left(\xi^2 - \frac{\omega^2}{c_T^2} \right) \Omega_F = 0. \tag{4.15}$$

These equations are linear second order differential equations in z and can be solved easily. The solutions to Equations (4.14) and (4.15), which remain finite when z is large, are:

$$\Theta_F = A\, e^{-\sqrt{\mathrm{L}} z}, \tag{4.16}$$

$$\Omega_F = B\, e^{-\sqrt{\mathrm{T}} z}, \tag{4.17}$$

with $\sqrt{\mathrm{L}} = \sqrt{\xi^2 - \frac{\omega^2}{c_L^2}}$ and $\sqrt{\mathrm{T}} = \sqrt{\xi^2 - \frac{\omega^2}{c_T^2}}$. A and B are constants related to the amplitude of the elastic wave and are considered next by applying boundary

conditions – related to the appropriate excitation stress sources.

4.2.3 Introducing the boundary conditions

The vibration of the support expressed in Equations (4.2) and (4.3) is generated by external stresses (shear stress τ acting parallel to the x-axis and normal stress σ acting parallel to the z-axis) given by the stress-strain relationships for a thin plate [54]:

$$\tau = \rho c_T^2 \left(\frac{\partial \hat{w}}{\partial x} + \frac{\partial \hat{u}}{\partial z} \right), \tag{4.18}$$

$$\sigma = \rho c_L^2 \frac{\partial \hat{w}}{\partial z} + \rho \left(c_L^2 - 2c_T^2 \right) \frac{\partial \hat{u}}{\partial x}. \tag{4.19}$$

Using the operators Θ and Ω defined in Equations (4.6) and (4.7) within these stress expressions, Equations (4.18) and (4.19) can be rewritten as:

$$\frac{\omega^2}{\rho c_T^4} \tau = \frac{\partial^2 \Omega}{\partial z^2} - \frac{\partial^2 \Omega}{\partial x^2} - 2r^2 \frac{\partial^2 \Theta}{\partial x \partial z}, \tag{4.20}$$

$$\frac{\omega^2}{\rho c_T^4} \sigma = -2 \frac{\partial^2 \Omega}{\partial x \partial z} - r^4 \frac{\partial^2 \Theta}{\partial z^2} + (2r^2 - r^4) \frac{\partial^2 \Theta}{\partial x^2}. \tag{4.21}$$

where r is the ratio of wave velocities: $r = c_L / c_T$.

The solutions for Ω and Θ derived earlier (Equations (4.16) and (4.17)) are in the wavenumber domain. To make use of these solutions when considering the boundary conditions, it is necessary to convert Equations (4.20) and (4.21) to the wavenumber domain. Applying the Fourier transformation to Equations (4.20) and (4.21) gives:

$$\frac{\omega^2}{\rho c_T^4} \tau_F = \frac{\mathrm{d}\Omega_F}{\mathrm{d}z^2} + \xi^2 \Omega_F - 2\mathrm{i}\xi r^2 \frac{\mathrm{d}\Theta_F}{\mathrm{d}z}, \tag{4.22}$$

$$\frac{\omega^2}{\rho c_T^4} \sigma_F = -2\mathrm{i}\xi \frac{\mathrm{d}\Omega_F}{\mathrm{d}z} - r^4 \frac{\mathrm{d}^2 \Theta_F}{\mathrm{d}z^2} - \xi^2 (2r^2 - r^4) \Theta_F. \tag{4.23}$$

In order to derive the constants A and B in Equations (4.16) and (4.17), boundary conditions are applied. These boundary conditions correspond to the stress (shear

and normal) sources on the edge of the thin plate (at $z = 0$), see Figure 4.1, induced by the vibrations of the resonator. For $\left|x\right| > b/2$, there is no stress source so $\sigma = \tau = 0$. Over the source region $\left|x\right| < b/2$, where b is the width of the clamped resonator, the boundary conditions all depend on the vibration source from the resonator. In what follows, flexural vibration and longitudinal vibration sources are considered in turn.

• Flexural vibration source

The shear stress is constant and the normal stress is linearly dependent of the x value (due to the bending moment). However, as explained in [41] or shown in Appendix A, the contribution of the normal stress to the power radiated is small and can be neglected. Hence the boundary conditions at $z = 0$ are:

$$\tau = \hat{\tau} \quad \text{for} \quad |x| < \frac{b}{2} \qquad \text{and} \qquad \tau = 0 \quad \text{for} \quad |x| > \frac{b}{2}; \tag{4.24a}$$

$$\sigma = 0 \quad \text{for all } x. \tag{4.24b}$$

$\hat{\tau}$ is the constant shear stress at the anchor point induced by flexural vibrations of the sensor.

In the wavenumber domain, Equations (4.24) give:

$$\tau_F = \frac{2\hat{\tau}}{\xi} \sin\left(\xi \frac{b}{2}\right), \tag{4.25a}$$

$$\sigma_F = 0. \tag{4.25b}$$

• Longitudinal vibration source

The shear stress is zero and the normal stress is constant over the source region. Hence at $z = 0$:

$$\tau = 0 \quad \text{for all } x; \tag{4.26a}$$

$$\sigma = \hat{\sigma} \quad \text{for} \quad |x| < \frac{b}{2} \qquad \text{and} \qquad \sigma = 0 \quad \text{for} \quad |x| > \frac{b}{2}. \tag{4.26b}$$

$\hat{\sigma}$ is the constant normal stress at the anchor point induced by longitudinal vibra-

tions of the sensor.

In the wavenumber domain, Equations (4.26) give:

$$\tau_F = 0, \tag{4.27a}$$

$$\sigma_F = \frac{2\hat{\sigma}}{\xi} \sin\left(\xi \frac{b}{2}\right). \tag{4.27b}$$

In the next subsection, Equations (4.25) and (4.27) are used to derive the constants A and B expressed in Equations (4.16) and (4.17).

4.2.4 Solution procedure

A system of two equations and two unknowns can be obtained by substituting the corresponding boundary condition (4.25) or (4.27) in Equations (4.22) and (4.23), with the solution values of Ω_F and Θ_F (given in Equations (4.16) and (4.17)), and setting $z = 0$ (at the thin plate edge). These equations are solved to calculate the constants A and B. These constants, which depend on the type of incident vibration, are used in Equations (4.16) and (4.17) to give the required longitudinal and flexural displacements in the support. For example, in the case of longitudinal vibrations of the resonator, the longitudinal displacement in the support (and in the wavenumber domain) can be expressed as:

$$\hat{w}_F = \frac{2\hat{\sigma}\sqrt{\mathrm{L}}\sin\left(\xi\frac{b}{2}\right)}{\rho c_T^2 \xi N(\xi)} \left(\left(\frac{\omega^2}{c_T^2} - 2\xi^2 \right) e^{-\sqrt{\mathrm{L}}z} + 2\xi^2 \, e^{-\sqrt{\mathrm{T}}z} \right), \tag{4.28}$$

where

$$N(\xi) = \left(\frac{\omega^2}{c_T^2} - 2\xi^2 \right)^2 - 4\xi^2 \sqrt{\mathrm{L}}\sqrt{\mathrm{T}}. \tag{4.29}$$

Similar expressions are found for flexural displacement in the support and for flexural incident vibrations.

The flexural and longitudinal displacements have been found in the wavenumber domain for two types of incident vibration (normal or shear stresses). The inverse

Fourier transform is applied to get the solutions in the real domain. Only the case of longitudinal displacement induced by longitudinal vibrations of the resonator is presented here. Similar reasoning can be done for the other cases and they can be found in Appendix A.

Applying the inverse Fourier transform to Equation (4.28) gives:

$$\hat{w} = \frac{\hat{\sigma}}{\pi\rho c_T^2}\int_{-\infty}^{\infty}\frac{\sqrt{\mathrm{L}}\sin\left(\xi\frac{b}{2}\right)}{\xi N(\xi)}\left(\left(\frac{\omega^2}{c_T^2}-2\xi^2\right)e^{-\sqrt{\mathrm{L}}z}+2\xi^2\,e^{-\sqrt{\mathrm{T}}z}\right)e^{\mathrm{i}\xi x}\,\mathrm{d}\xi. \tag{4.30}$$

For all of the different cases, the integrand will either be an odd or even function of ξ. This simplifies the integration greatly and the term in $e^{\mathrm{i}\xi x}$ becomes either $\cos(\xi x)$ or $\sin(\xi x)$. In order to further simplify expression (4.30), the following change of variable is used:

$$\gamma = \xi\frac{c_L}{\omega}. \tag{4.31}$$

Using Equation (4.31) in Equation (4.30) gives:

$$\hat{w} = \frac{2\hat{\sigma}}{\pi\rho c_T^2}\int_0^{\infty}\frac{\sqrt{\gamma^2-1}\sin\left(\mathcal{A}\gamma\right)}{\frac{\omega}{c_L}\gamma N_0(\gamma)}\Bigg(\left(r^2-2\gamma^2\right)e^{-\frac{\omega}{c_L}z\sqrt{\gamma^2-1}} +2\gamma^2\,e^{-\frac{\omega}{c_L}z\sqrt{\gamma^2-r^2}}\Bigg)\cos\left(\frac{\omega}{c_L}\gamma x\right)\mathrm{d}\gamma, \tag{4.32}$$

where $\mathcal{A} = \dfrac{b\omega}{2c_L}$ and

$$N_0(\gamma) = \left(2\gamma^2-r^2\right)^2 - 4\gamma^2\sqrt{\gamma^2-1}\sqrt{\gamma^2-r^2}. \tag{4.33}$$

The displacements at any point (x, z) in the support, induced by stresses at its free edge, can be found using Equation (4.32) (or similar).

4.2.5 Derivation of the *Q*-factor

The ultimate aim of the analysis is to determine the Q-factor of a resonator using the standard equation:

$$Q = 2\pi \frac{W}{\Delta W}, \tag{4.34}$$

where W is the total energy stored by the resonator and ΔW is the energy loss per cycle. The quantity W is independent of the support as it represents the strain (or kinetic) energy of the resonator when the system is vibrating at a natural frequency. When using the analytical support model to calculate the support losses, the total energy stored will be derived in a independent study using the ray tracing method applied to the resonator (see Chapter 2). In this chapter, we are interested in modelling the energy loss (ΔW).

The amount of energy lost per cycle from the support can be calculated explicitly as:

$$\Delta W = \frac{2\pi}{\omega} \Pi, \tag{4.35}$$

where Π is the average power transmitted from the resonator to the support. This average power is usually defined as:

$$\Pi = \frac{1}{2} \operatorname{Re} \left(\text{Force} \cdot \text{Velocity}^* \right), \tag{4.36}$$

where Re is the real part and * denotes the complex conjugate. The Force term represents the internal forces that occur at the anchor point. These forces are found by assuming that the resonator is clamped and by using the ray tracing method on the resonator itself (see Chapter 2). The Velocity term represents the mean velocity induced by the corresponding Force term over the source region (width of the resonator). This mean velocity is defined as the derivative of the mean displacement with respect to time.

From Equation (4.32) (or similar), the flexural or longitudinal displacement can be derived at any point in the support. The mean displacement $\bar{w}_{z=0}$ over the source

region is calculated by setting $z = 0$ and integrating over the resonator width, *i.e.*:

$$\bar{w}_{z=0} = \frac{1}{b}\int_{-b/2}^{b/2} \hat{w}_{z=0}\,\mathrm{d}x. \tag{4.37}$$

Substituting Equation (4.32) into Equation (4.37) and considering the parity in x of the integrand gives:

$$\bar{w}_{z=0} = \frac{br^2\hat{\sigma}}{\pi\rho c_T^2}\int_0^\infty \frac{\sqrt{\gamma^2-1}}{N_0(\gamma)}\left[\frac{\sin(\mathcal{A}\gamma)}{\mathcal{A}\gamma}\right]^2 \mathrm{d}\gamma. \tag{4.38}$$

The imaginary part of the integrand, which will contribute to support loss (see Appendix A), is non zero only for $0 < \gamma < r$. For typical resonator dimensions and corresponding natural frequencies, the term $\mathcal{A}\gamma = \dfrac{b\omega}{2c_L}\gamma$ is relatively small compared to unity for this range of γ-value. This allows Equation (4.38) to be simplified to:

$$\bar{w}_{z=0} = \frac{br^2\hat{\sigma}}{\pi\rho c_T^2}\Psi_w, \tag{4.39}$$

where

$$\Psi_w = \int_0^\infty \frac{\sqrt{\gamma^2-1}}{\left(2\gamma^2-r^2\right)^2 - 4\gamma^2\sqrt{\gamma^2-1}\sqrt{\gamma^2-r^2}}\,\mathrm{d}\gamma. \tag{4.40}$$

A similar expression can be found for the mean flexural displacement induced by shear stresses:

$$\bar{u}_{z=0} = \frac{br^2\hat{\tau}}{\pi\rho c_T^2}\Psi_u, \tag{4.41}$$

where

$$\Psi_u = \int_0^\infty \frac{\sqrt{\gamma^2-r^2}}{\left(2\gamma^2-r^2\right)^2 - 4\gamma^2\sqrt{\gamma^2-1}\sqrt{\gamma^2-r^2}}\,\mathrm{d}\gamma. \tag{4.42}$$

Using Equations (4.35), (4.36) and (4.39) (or (4.41)), the energy loss due to longitudinal vibrations ΔW_w is determined to be:

$$\Delta W_w = \frac{4(1+\nu)}{Eh(1-\nu)}\left|T\right|^2 \mathrm{Im}(\Psi_w); \tag{4.43}$$

and the energy loss due to flexural vibrations ΔW_u is:

$$\Delta W_u = \frac{4(1+\nu)}{Eh(1-\nu)}\left|S\right|^2 \mathrm{Im}(\Psi_u), \tag{4.44}$$

where T is the normal force producing the normal stress $\hat{\sigma}$ and S is the shear force producing the shear stress $\hat{\tau}$. Assuming $\nu = 0.28$, $\mathrm{Im}(\Psi_w)$ and $\mathrm{Im}(\Psi_u)$ can be calculated numerically to be:

$$\mathrm{Im}(\Psi_w) = 0.22153 \qquad \text{and} \qquad \mathrm{Im}(\Psi_u) = 0.33503. \tag{4.45}$$

The process to calculate the Q-factor of resonators can be summarised as follows:

- Assume that the resonator is clamped and use the ray tracing approach (see Chapter 2) to calculate its natural frequencies and associated mode shapes.
- From the mode shape, calculate the total energy stored W and the forces T and S at the clamped end. For example, on a simple cantilever beam resonator of length L, width b, height h and mass density ρ:

$$W = \frac{\rho bh}{2} \int_0^L \left(\frac{\partial u}{\partial t}\right)^2 + \left(\frac{\partial w}{\partial t}\right)^2 \mathrm{d}z, \tag{4.46}$$

$$S = \frac{Eb^3h}{12} \frac{\partial^3 w}{\partial z^3}_{z=z_{\text{boundary}}}, \tag{4.47}$$

$$T = Ebh \frac{\partial w}{\partial z}_{z=z_{\text{boundary}}}. \tag{4.48}$$

- Use Equations (4.43) and (4.44) to get the energy loss due to the forces T and S, and then sum the losses arising from flexural and longitudinal vibrations.
- Use Equation (4.34) to calculate the Q-factor.

4.3 Perfectly matched layer

4.3.1 Indroduction

Another approach to modelling the vibration of the resonator is to use finite element methods. The infinite boundary is modelled by adding a non-physical "sponge

layer" to dissipate waves before they reach the artificial boundary. Waves passing through the sponge layer are damped on the way to the artificial boundary, and are further damped when they are reflected back, so that most of the vibration and energy entering the layer are absorbed. To be effective, the layer must be designed so that there is no impedance mismatch to reflect waves back from the interface between the layer and the rest of the domain. A Perfectly Matched Layer (PML) is the refinement of a sponge layer. Bérenger [50] invented the perfectly matched layer for problems in electromagnetic wave propagation, and it was later re-interpreted as a complex-valued change of coordinates which could be applied to any linear wave equation. Not only do these layers rapidly attenuate waves, they also "perfectly match" the rest of the domain. As a consequence, there are no spurious reflections at the interface due to perfect impedance matching.

Bindel [38] extended this approach and implemented it in a finite element code called HiQLab [91]. HiQLab is an open-source finite element program capable of studying damping in micro-resonators. Though the program is designed with resonant MEMS in mind, the architecture is general, and can handle other types of problems. HiQLab has two user interfaces: one working with Matlab and another one standalone. The Matlab interface offers access to the full range of Matlab's numerical solvers and graphics routines. The main way to represent devices in HiQLab is to write a mesh input using the Lua programming language. The program supports elements of different kinds: linear, quadratic, cubic and brick elements for elastic problems and coupled thermoelastic problems in plane strain, plane stress, axisymmetry or three dimensions. The code also supports particular perfectly matched layer absorbing boundaries to mimic the effect of infinite domains. Modal analysis of simple structures with anchor loss and thermoelastic damping are implemented and allow energy losses to be calculated.

When a PML is used to model infinite boundaries in a finite element code, complex stiffness and mass matrices are obtained. Complex eigenvalues ω are obtained for the system of equations and the Q-factor is calculated using [38]:

$$Q = \frac{|\omega|}{2\,\mathrm{Im}(\omega)} \tag{4.49}$$

where ω is the natural frequency and Im its imaginary part.

4.3.2 Definition of the PML for a one-dimensional case

The elements in a PML use complex stretching of the coordinate axes to introduce artificial damping to the wave. This is illustrated in the following case for a one-dimensional wave propagation. Consider a longitudinal wave propagating in a homogeneous, semi-infinite rod with axial coordinate z. If the wave travels with speed c, the one-dimensional wave equation that describes this system is [54]:

$$\frac{\partial^2 w}{\partial z^2} - \frac{1}{c^2}\frac{\partial^2 w}{\partial t^2} = 0, \tag{4.50}$$

where $w(z,t)$ is the displacement. Assuming a solution of the form $w(z,t) = \hat{w}(z)\, e^{\mathrm{i}\omega t}$, the following equation is obtained:

$$\frac{\mathrm{d}^2 \hat{w}}{\mathrm{d}z^2} + k^2 \hat{w} = 0, \tag{4.51}$$

where $k = \omega/c$ is the wavenumber. This equation has a solution of the form:

$$\hat{w}(z) = a_{out}\, e^{-\mathrm{i}kz} + a_{in}\, e^{\mathrm{i}kz}, \tag{4.52}$$

where a_{out} is the magnitude of the outgoing wave travelling from the origin towards infinity, and a_{in} is the magnitude of the incoming wave travelling from infinity towards the origin.

In the PML region, the coordinate axes are stretched and the new coordinate $\tilde{z}$,

$$\tilde{z} = \int_0^z \lambda(s)\, \mathrm{d}s, \tag{4.53}$$

is used.

By definition, z and $\tilde{z}$ are differentially related:

$$\frac{\mathrm{d}\tilde{z}}{\mathrm{d}z} = \lambda(z) \qquad \text{and} \qquad \frac{\mathrm{d}}{\mathrm{d}\tilde{z}} = \frac{1}{\lambda(z)}\frac{\mathrm{d}}{\mathrm{d}z}. \tag{4.54}$$

Now suppose that the stretched coordinate $\tilde{z}$ is used as the independent variable in Equation (4.51), then Equation (4.51) becomes

$$\frac{\mathrm{d}^2\hat{w}}{\mathrm{d}\tilde{z}^2} + k^2\hat{w} = 0, \tag{4.55}$$

or in terms of z:

$$\frac{1}{\lambda}\frac{\mathrm{d}}{\mathrm{d}z}\left(\frac{1}{\lambda}\frac{\mathrm{d}\hat{w}}{\mathrm{d}z}\right) + k^2\hat{w} = 0. \tag{4.56}$$

If λ is defined as $\lambda = 1 - \mathrm{i}\sigma(s)/k$, where the choice of the PML function $\sigma(s)$ is discussed later, the new coordinate becomes:

$$\tilde{z} = z - \frac{\mathrm{i}}{k}\int_0^z \sigma(s)\,\mathrm{d}s. \tag{4.57}$$

The solution to Equation (4.55) is therefore:

$$\begin{aligned}
\hat{w} &= a_{out}\, e^{-\mathrm{i}k\left(z - \frac{\mathrm{i}}{k}\int_0^z \sigma(s)\,\mathrm{d}s\right)} + a_{in}\, e^{\mathrm{i}k\left(z - \frac{\mathrm{i}}{k}\int_0^z \sigma(s)\,\mathrm{d}s\right)}, \\
\hat{w} &= a_{out}\, e^{-\int_0^z \sigma(s)\,\mathrm{d}s}\, e^{-\mathrm{i}kz} + a_{in}\, e^{\int_0^z \sigma(s)\,\mathrm{d}s}\, e^{\mathrm{i}kz}.
\end{aligned} \tag{4.58}$$

Consider the case when σ is defined to be zero on $[0, L]$ and $\sigma(s) = \beta(s - L)$ on $[L, L_p]$, with L_p the length of the PML domain. σ corresponds here to a linear attenuation function with end magnitude $\beta(L_p - L)$; see Figure 4.2. Then for $z > L$, the outgoing wave amplitude is $a_{out}\, e^{-\beta(z-L)^2/2}$ (that decreases when z increases), and the incoming wave amplitude is $a_{in}\, e^{\beta(z-L)^2/2}$ (that decreases when z decreases). When σ is chosen such that it is zero at the boundary with the finite medium, the solution is the same for both media and hence the wave enters the PML without any reflection at the boundary. When $\sigma > 0$, the wave decays in the direction of travel. Since the outgoing wave and the incoming wave travel in opposite directions, the outgoing wave amplitude decays with increasing z, while the incoming wave amplitude decays with decreasing z.

Because waves decay so rapidly as they travel through the PML region, a good approximation to the infinite domain is obtained even if the condition $\hat{w}(L_p) = 0$ is forced for a finite length $L_p > L$. For example, with a general absorbing function

$\sigma(s)$ such that $\sigma(s) = 0$ on $[0, L]$ and $\sigma(s) > 0$ on $[L, L_p]$, suppose the displacement to satisfy $\hat{w}(0) = 1$ and $\hat{w}(L_p) = 0$. Then the boundary conditions become:

$$\begin{bmatrix} \hat{w}(0) \\ \hat{w}(L_p) \end{bmatrix} = \begin{bmatrix} 1 & 1 \\ e^{-(\eta+\mathrm{i}kL_p)} & e^{\eta+\mathrm{i}kL_p} \end{bmatrix} \begin{bmatrix} a_{out} \\ a_{in} \end{bmatrix} = \begin{bmatrix} 1 \\ 0 \end{bmatrix} \tag{4.59}$$

with

$$\eta = \int_L^{L_p} \sigma(s)\,\mathrm{d}s. \tag{4.60}$$

In the particular case of the linear function shown in Figure 4.2, $\eta = \beta\left(L_p - L\right)^2/2$. Solving Equation (4.59), the amplitudes become

$$a_{out} = \frac{1}{1 - e^{-2(\eta+\mathrm{i}kL_p)}} \qquad \text{and} \qquad a_{in} = \frac{-e^{-2(\eta+\mathrm{i}kL_p)}}{1 - e^{-2(\eta+\mathrm{i}kL_p)}} \tag{4.61}$$

To mimic the infinite domain boundary condition, one desires $a_{in} = 0$, such that there is no incoming wave. The ratio

$$r_{end} = \left|\frac{a_{in}}{a_{out}}\right| = e^{-2\eta} \tag{4.62}$$

is a measure of the quality of the boundary condition. This quantity r_{end} called the end termination coefficient [30] is the reflection that arises from a finite end termination of the PML and should be as small as possible.

From Equation (4.61), it can be seen that the end reflection coefficient is a function of the end parameter β, the wavenumber k and the length $(L_p - L)$ of the PML region. Even for small end coefficient β, the bounded-domain is a good approximation to the infinite domain solution. Increasing β decreases the reflection coefficient in the continuous case. However, in the discrete equation used in the finite element method, β must be chosen carefully. If β is too large, the wave entering the PML will decay rapidly, effectively creating a boundary layer, but if the discretisation is too coarse to resolve this decay, the numerical solution will be polluted by spurious reflections. This illustrates the complexity of finding the proper choice of PML parameters.

4.3.3 Difficulties with the convergence

To apply the method of PML for numerical approximation of the infinite boundary conditions, one must select parameters for the PML such as its length and absorbing function σ. Unless these parameters are selected properly, the performance of the PML can degrade, and the desired accuracy cannot be obtained. The main difficulty in the proper selection of PML parameters arises from the numerical discretisation of the problem. When one applies the PML method to a continuous problem defined on a finitely truncated domain, the selection of PML parameters is not too difficult, since one only has to treat the wave reflections arising from the finite termination of the PML. This is the case presented in Section 4.3.2. From Equation (4.62), it can be seen that a large η value would reduce at zero the end reflection. This η value is directly proportional to the parameter β that is set when defining the PML. However, when the PML is discretised, additional wave reflection can occur at the PML interface, leading to less accurate results. The accuracy of the method will also depend of the PML discretisation refinement.

The main objective of the PML is to minimise the incoming waves on the infinite boundary. It should theoretically completely absorb these waves and no reflection should occur. Due to the particular discretisation of the problem, some energy is reflected back. A precise analysis of the reflection was presented by Bindel [38] and Koyama [30], where the total reflection due to the PML is separated into: the end termination reflection, introduced by a finite termination of the PML; the interface reflection, introduced by the discretised PML at the PML interface; and the computed reflection, due to round-off errors in computing calculations.

Figure 4.3 presents the different domains and the mesh used when a simple beam resonator is studied. The absorbing function σ in the PML region is shown with gradually changed colour. The outside boundary of the PML region is clamped.

The different parameters that will have an effect on the Q-factor and can be modified are:

- Geometrical parameters:

  - the dimension of the PML region: L_{PML} and h_{PML}, see Figure 4.3;
  - the dimension of the "finite" support region meshed with usual finite elements: $(L_{support} - L_{PML})$ and $(h_{support} - 2h_{PML})$, see Figure 4.3;

- Meshing parameters:
  - the number of elements in the PML region;
  - the interpolation order of the elements in the PML (linear, quadratic, cubic);

- PML function properties:
  - the end value parameter β of the PML absorbing function σ;
  - the polynomial order of the PML absorbing function σ.

The works in [38] and [30] enable one to select PML parameters in a rational way. These results were used to start simulations in a sensible range of potentially good parameters. Several simulations that use different parameters values presented above are performed to check the convergence. The difficulty associated with finding the converged result makes the process quite time-consuming to obtain a single "correct" Q-value. All the results presented in Section 4.5 are obtained after the convergence study has been completed.

It is shown here that the PML method is time-consuming and the obtained results are not "exact" Q-values. Too many hypotheses and parameters have to be taken into account when calculating the Q. To complete the validation of the support model, another finite element method that uses infinite elements has been investigated, and is discussed next.

4.4 Infinite elements

4.4.1 Introduction

Infinite boundaries can be modelled using the finite element method using specific "infinite elements". First- and second-order infinite elements based on the work of Zienkiewicz *et al.* [92] for static response and of Lysmer and Kuhlemeyer [93] for dynamic response are implemented in ABAQUS^{TM} to model infinite boundaries. These infinite elements are defined over semi-infinite domains with particular decay functions that eliminate artificial wave reflections from the truncated domain of the model. These elements are used in conjunction with standard finite elements, which model the area around the resonator, with the infinite elements modelling the far-field region. Since they are semi-infinite, propagating energy is lost in these particular elements.

In this method, a steady state response is computed over a range of frequencies near the resonance. The Q-factor is then calculated from the resulting amplitude-frequency curve and defined as:

$$Q = \frac{\omega_0}{\Delta\omega}, \tag{4.63}$$

where ω_0 is the natural frequency of interest and $\Delta\omega$ is the half-power bandwidth at $-3\,\mathrm{dB}$ of the maximum amplitude, see Section 1.3.1 in Chapter 1. $\Delta\omega$ can also be interpreted as the frequency width at the points where half the maximum energy is stored in the resonator. This is the common method used in experiments to calculate Q-factors.

4.4.2 Infinite element characteristics

The infinite elements provide a theoretically non reflective boundary to the model by using special shape functions. Regular shape functions are used to model the displacement variables u while growing shape functions are used for position variables r [94].

A one-dimensional case is illustrated in Figure 4.4. The infinite element contains three nodes. The first node (node 1) is at the interface between the finite and infinite domains. Its nodal parameter is $s = -1$, and it is at a distance $r_1 = a$ from the "pole" that represents the source of propagating waves. The second node (node 2) is at a distance $r_2 = 2a$ from the pole and has a nodal parameter $s = 0$. The third node has a nodal parameter $s = 1$ and its position approaches infinity. The shape function is chosen such that:

$$r = \frac{-2s}{1-s} r_1 + \frac{1+s}{1-s} r_2. \tag{4.64}$$

This particular function gives

$$\begin{aligned} r &= r_1 && \text{at} && s = -1, \\ r &= r_2 && \text{at} && s = 0, \\ r &\to \infty && \text{as} && s \to 1. \end{aligned}$$

Hence the position coordinate approaches infinity at the outer edge of the infinite element.

The behaviour of infinite elements is based on modelling the displacement u with respect to the spatial distance r measured from the pole, such that $u \to 0$ when $r \to \infty$, and $u \to \infty$ when $r \to 0$. With standard quadratic interpolation of u with respect to s, written in terms of its values u_1 at node 1 and u_2 at node 2, the displacement is expressed as:

$$u = \frac{1}{2} s(s-1) u_1 + (1-s^2) u_2. \tag{4.65}$$

This particular displacement gives the required:

$$\begin{aligned} u &= u_1 && \text{at} && s = -1, && \\ u &= u_2 && \text{at} && s = 0, && \\ u &\to 0 && \text{as} && s \to 1 && (\text{when} \quad r \to \infty). \end{aligned}$$

Hence the displacement of the propagating wave decreases to zero as it approaches

the outer edge of the infinite element.

These elements are provided in ABAQUS™ for two-dimensional, three-dimensional and axisymmetric analyses. They are shown to work well for static and dynamic analyses. In any case, it is assumed that the response adjacent to the boundary of the infinite elements is of sufficiently small amplitude that the medium responds in a linear elastic manner. The infinite elements have to be placed sufficiently "far" from the pole. They also have to be arranged so that the dominant direction of wave propagation is orthogonal to the boundary.

4.4.3 Convergence analysis

A simple cantilever beam vibrating in-plane has been studied. Figure 4.5 shows the particular mesh applied in ABAQUS™. The beam is meshed using classical two-dimensional quadratic plane stress elements. The support is divided in two different sections: a bounded domain meshed with standard finite elements, and an infinite domain meshed using the infinite elements described in Section 4.4.2.

The infinite elements have to be numbered in a particular order in the ABAQUS™ input file. These elements can not be defined using the user interface and it makes the process time-consuming if ones wants to modify the mesh refinement or geometrical parameters. If one decides to mesh the model automatically using the ABAQUS™ user interface, then the input file has to be edited and the infinite elements node numbering changed before being inputted back into ABAQUS™. It is much simpler to directly create the mesh using a MATLAB program that defines node coordinates and node numbering in the different elements, using appropriate numbering for the particular infinite elements.

The drawback of creating a mesh manually is that it is very difficult to obtain the node coordinates of a perfectly "circular" mesh that performs better when using infinite elements. Instead, a more "rectangular" mesh is used here, see Figure 4.5. The beam width is meshed using four elements, and the element size in the support gradually increases to fill the entire bounded domain. The outer ends of the infinite

elements are placed at an approximate distance $2R$ from the pole (origin of the propagating waves – that is the beam attachment point). In order to better satisfy the fact that the propagating waves should impinge normally to the infinite elements boundary, the external edge of the support has been forced to be not totally rectangular. A polynomial interpolation is applied when defining the coordinate of the external nodes. This allows the infinite elements to have boundaries that are closer to those of a perfect circle. A perfect circle could not have been used as all the infinite elements would have shown too large distortion in size and angle. This particular polynomial approximation provides the best compromise between a circle with normally impinging waves and a model that do not contain significant mesh distortion.

The support is supposed to be infinite and a variation in the bounded domain length R (see Figure 4.5) should theoretically not influence the results for the natural frequency and Q-factor of the resonator. However, it has been found that the calculated Q-factor is actually dependent of R. It is expected that this dependency is also a function of the transverse wavelength λ of the propagating shear waves in the support. λ is defined as:

$$\lambda = \frac{1}{\omega}\sqrt{\frac{E}{2\rho(1+\nu)}}, \tag{4.66}$$

where ω is the frequency in rad/s, E the Young's modulus, ρ the mass density and ν the Poisson ratio.

For different values of R, a steady state analysis is performed in the vicinity of the expected first natural frequency. The Q-factor is then calculated using the amplitude-frequency response curve and the half-power bandwidth method presented in Section 4.4.1.

Figure 4.6 shows the calculated Q-factor for different mesh refinements and different values of R. With a very coarse mesh, the Q-value quickly diverges as R becomes large. This is probably due to the difference in size between the bounded domain and the resonator itself. It is important to notice that, for example, when $R/\lambda = 10$, the bounded domain is approximately 3000 times bigger than the beam width.

It is understandable that a coarse mesh struggles to correctly model the energy propagation and dissipation arising from a relatively small resonator. With a fine mesh, the Q-value first shows a maximum around $R/\lambda \approx 1.75$, then seems to stabilise between $3 < R/\lambda < 5$, and finally oscillates for $R/\lambda > 6$. This simple convergence test shows the complexity of calculating Q. Q is found to be highly dependent on the mesh density and on the support dimensions. However this study shows that a range of approximate Q-values can still be obtained using the infinite elements in ABAQUS^{TM}. It seems sensible to use as a maximum Q-value, the value obtained when $R/\lambda \approx 1.75$ and as an appropriate minimum Q-value, the value obtained when $R/\lambda \approx 4$. These two particular values of R/λ have been used in a parametric study presented Section 4.5.1.

4.5 Results for some simple test cases

Due to the complexity of creating meshes in the HIQLAB program and directly from MATLAB for the use of infinite elements, the difficulty to obtain a rapid converged result, and the computing cost of simulation with finite elements methods, the methods presented in Sections 4.3 and 4.4 have not been applied to the entire ring-based resonator. However, they have been applied to simple test cases in order to validate the analytical model presented in Section 4.2.

4.5.1 Cantilever beam

A simple cantilever beam (Figures 4.3 and 4.5) vibrating in its fundamental mode was studied first. For a fixed beam width, the calculated Q-factor is plotted as a function of the length/width ratio of the beam in Figure 4.7. This graph compares the results obtained using the PML method in HIQLAB, infinite elements in ABAQUS^{TM}, and the analytical model.

When applying the infinite element method, the entire mesh and its node coordinates are created using MATLAB, for each beam length. At this point, an arbitrary

value of R is used. Then, a simple frequency analysis with ABAQUS^{TM} is performed to get the first natural frequency of the system. With this frequency, appropriate R values are calculated such that $R/\lambda \approx 1.75$ or $R/\lambda \approx 4$. Using these R values, the MATLAB program is re-run and a new model created. A steady state analysis is then performed in ABAQUS^{TM} for both models ($R/\lambda \approx 1.75$ and $R/\lambda \approx 4$). This provides a sensible range of calculated Q-factors. The results obtained from these simulations are shown in Figure 4.7.

All of the curves show the same trend. It can be shown that the results display a cubic character (explained by Hao *et al.* in [42]) when the beam is made longer and/or thinner. Even though the infinite element method gives a "range" of potentially correct Q-values, it is shown that they are all in agreement. The calculated natural frequency is also presented for the analytical and PML methods in Figure 4.8. When the beam is long and thin (high length/width ratio), both methods agree perfectly for the natural frequency. This can be explained by the fact that the ray tracing method is based on thin beam theory meaning it will always be a better model for thin beams. Also, when the beam is longer, the effects that occur at the boundary beam/support become negligible compared to the beam overall vibration and a rigid-attachment is a good boundary approximation. For short beams, it is difficult to understand exactly the coupling at the beam/support boundary and the presence of high stress also degrades the finite element approximation.

In conclusion, the three methods show good agreement for Q-factor and natural frequency for a simple cantilever beam resonator. Bearing in mind that the objective is to use the analytical model to calculate the Q of the entire ring-based rate sensor, it is important to notice that the leg attached to the support will undergo flexural and longitudinal vibrations simultaneously when the ring is vibrating in its 2θ mode. This coupling between flexural and longitudinal vibrations provides a complication as the analytical model of the support uses two different expressions for shear and normal stress sources. In order to validate the model when flexural and longitudinal vibrations occur simultaneously, another test case has been studied. Again, due to the complexity of meshing and computing cost for the finite element methods, a simple model is evaluated that demonstrates coupled shear/normal stresses at its

boundary. This is considered in the next section.

4.5.2 Two-beam system

The two-beam system considered is shown in Figure 4.9. It consists of two beams at right angles to each other. Beam '1' is attached to the infinite support; beam '2' is free. The Q-factor corresponding to the first mode of vibration is studied.

For a fixed beams width, the length L_2 of beam '2' is changed. The ray tracing method is used to calculate the natural frequency of the first mode, its corresponding mode shape and shear/normal force ratio at the clamped boundary. This calculated ratio is plotted as a function of the length/width ratio of free beam '2' in Figure 4.10. This graph shows that when beam '2' is short (small length/width ratio), the shear forces are predominant at the clamped boundary. This phenomenon can easily be explained by the fact that when beam '2' is almost negligible (really short compared to the length L_1 of the attached beam '1'), the first mode of vibration of the system is similar to the fundamental mode of a cantilever beam that induces flexural vibration and shear stresses only, see Figure 4.11(a). In other words, at the shortest limit of L_2, the system behaves like a simple cantilever beam of length L_1 and only shear stresses are present in the first vibrational mode. On the other hand, when beam '2' is very long (high length/width ratio), the vibrations of the system are mainly due to beam '2' vibrating in flexure, see Figure 4.11(b). As beam '2' has most influence on the overall vibration, it will induce beam '1' to have longitudinal motion. Consequently, normal forces due to the longitudinal vibration of beam '1' become predominant at the attached end and the shear/normal force ratio tends to zero.

For the modes of interest for the entire gyroscope, it will be shown (in Chapter 5) that the shear/normal force ratio that occurs at the clamped boundary is approximately 1.5.

The lowest natural frequency calculated with the analytical model and the PML method in HiQLab is presented in Figure 4.12. As in the previous case, when the

length/width ratio is high (thin beam), the ray tracing and PML method agree very well for the calculated natural frequency. This is mainly due to the same reason explained before: the ray tracing method is based on thin beam theory and only models the centreline of the beams.

The associated Q-factor calculated is presented in Figure 4.13. For the infinite element method, the maximum Q-value, obtained when $R/\lambda \approx 1.75$, has been used. Again, all the curves show a similar trend. However, it appears in this case, which is not true for the simple cantilever beam study, that the relative Q difference increases when the length/width ratio of beam '2' is higher. In the high length/width range, normal forces are predominant at the attachment point. Thus, a possible explanation is that the analytical model does not properly quantify the loss occurring when normal stresses are predominant. An alternative explanation could be that the ray tracing method struggles to correctly model the beam joint when it is under high stresses. The thin beam theory used in the ray tracing does not consider high stress concentrations at the corner of the beam joint, as only its centreline is modelled. The complexity of a real joint could be not properly modelled with the thin beam theory.

However, a simple study has ruled out this hypothesis. The same system has been modelled in ABAQUS^{TM} using quadratic elements, similar to the ones used in HiQLab. A modal analysis in ABAQUS^{TM} gives the modal strain energy of the entire system and forces at the clamped boundary for the first mode of vibration. These clamped forces and strain energy are inputted into the analytical model of the support presented in Section 4.2, and the Q-factor is calculated. These results are illustrated in Figure 4.13. This study represents a combination between the analytical model of the support and a finite element analysis of the vibrating structure. The excellent agreement achieved indicates that the ray tracing method correctly models the vibrations, and that the difference between analytical and PML methods is only due to the support model.

In conclusion, Figure 4.13 indicates that the three different support models give the same range of Q-values and same trend when the length/width (or shear/normal

forces at the boundary) ratio is changed.

4.6 Conclusion

The objective of this chapter was to find an appropriate model for the analysis of support loss. It was intended that this model should produce accurate results in a fast and effective way such that resonator parameters can be modified without major difficulties in the support modelling.

One of the main analyses performed during the research project was to develop a ray tracing method that models vibrations of complex-shaped resonators (see Chapter 2). The support model should thus easily be adapted and coupled with this ray tracing method in order to calculate support losses. As the ray tracing method was implemented and programmed into MATLAB, a support model that fits easily into MATLAB was developed. This corresponds to the "analytical support model" presented in this chapter. The ultimate aim of this chapter was thus to validate this analytical model by using other possible methods. The other investigated methods that approximate infinite domains were the PML method and the use of infinite elements in ABAQUS^{TM}.

It has been found that the three different methods (namely the analytical model, the PML method and the use of infinite elements) give Q-values in the same range of magnitude and exhibit similar trends when a parameter is varied. This has been shown for simple (Section 4.5.1) and for more complex (Section 4.5.2) resonator vibrations.

However, the results obtained for the Q-factor, Figures 4.7 and 4.13, show that the analytical model tends to overestimate Q, or underestimate the quantity of energy lost; even though the support is considered as semi-infinite. The most plausible reason for this is in the way the resonator itself is modelled. The presence of a clamped boundary in the ray tracing method ensures that the vibrational energy stays within the resonator and is maximised. In contrast, the PML and the infinite

element methods model the resonator and its attachment. The support is therefore taken into account properly when analysing the resonator vibration. The energy that stays within the resonator and is stored is expected to be smaller. The main reason why the Q-factor is overestimated with the analytical method is therefore thought to be because the quantity of stored energy is over-evaluated. It is also very difficult to predict and model the real effect of the attachment on the resonator. Even a finite element analysis makes an important approximation in this region of high stress concentration.

It is useful to notice that finding an "exact" Q-value is not really important, but parameter trends are much more interesting. Indeed, the Q-factor is so sensitive to many factors that exact values are difficult to find. The main factors that can affect Q for support loss include: the vibration of the resonator itself, the attachment on the support, and the way the energy is supposed to leave the support. The Q-factor for typical MEMS resonator is very high, and the values obtained from experimental studies are even more approximated. External factors can affect significantly the obtained Q-factor as the quantity of energy lost through the support is very small and difficult to measure. As result, an exact value is not so relevant. On the other hand, a trend that shows the influence of some parameters on the Q-factor can be used to design more efficient resonators. It would be interesting to prove that changing a particular parameter can greatly affect the Q-factor.

From the different analyses performed in this chapter, it has been concluded that the three models all exhibit similar trends. The analytical model can thus be validated. Furthermore, it is interesting to note with this model that it is quicker to run; there are no convergence issues on its results; and, it is easy to modify some parameters in the resonator design, as the resonator and support are modelled independently. This will be the model used to calculate Q-factors of the ring-based rate sensor (see Chapter 5).

Figures

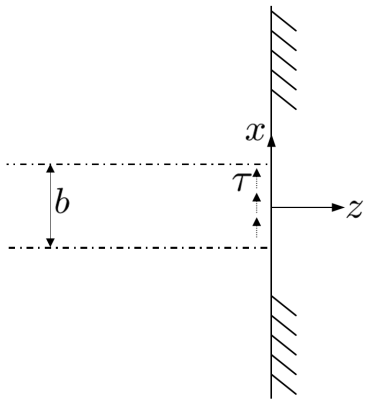

(a)

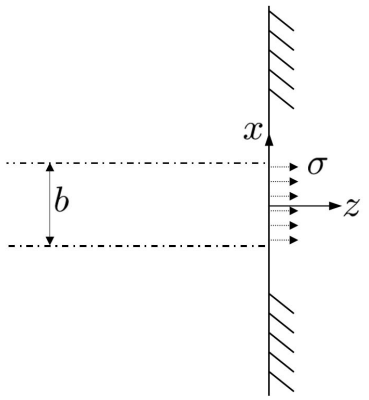

(b)

Figure 4.1: Support modelled as a semi-infinite thin plate. Excitation sources: (a) Shear stress, (b) Normal stress.

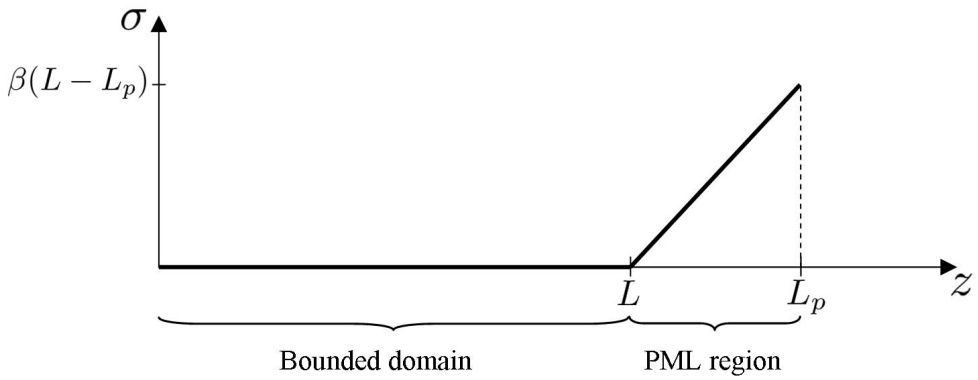

Figure 4.2: Linear attenuation function used in the PML method for a one-dimensional wave.

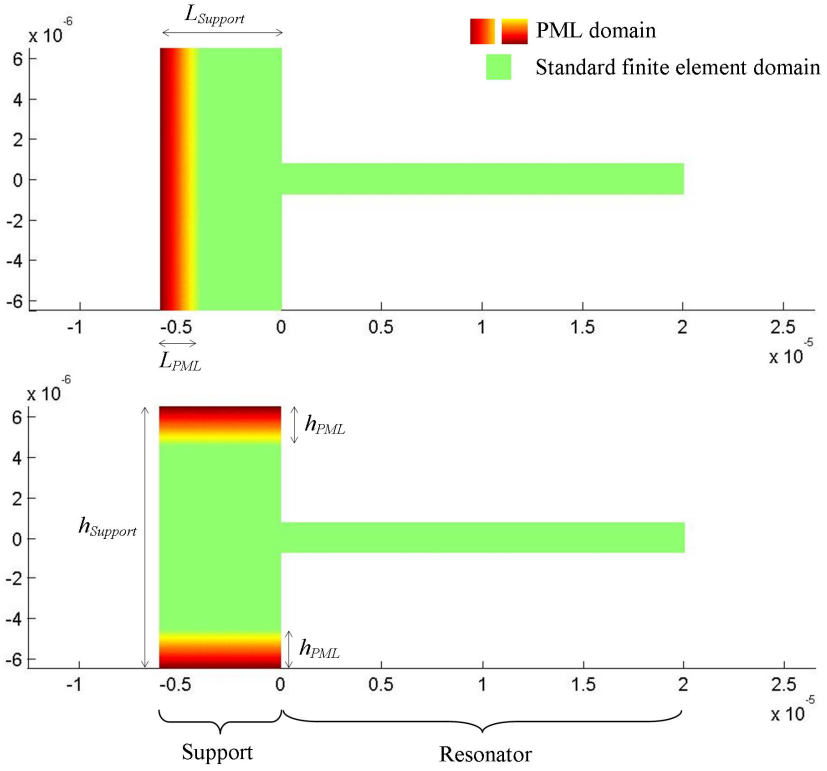

(a)

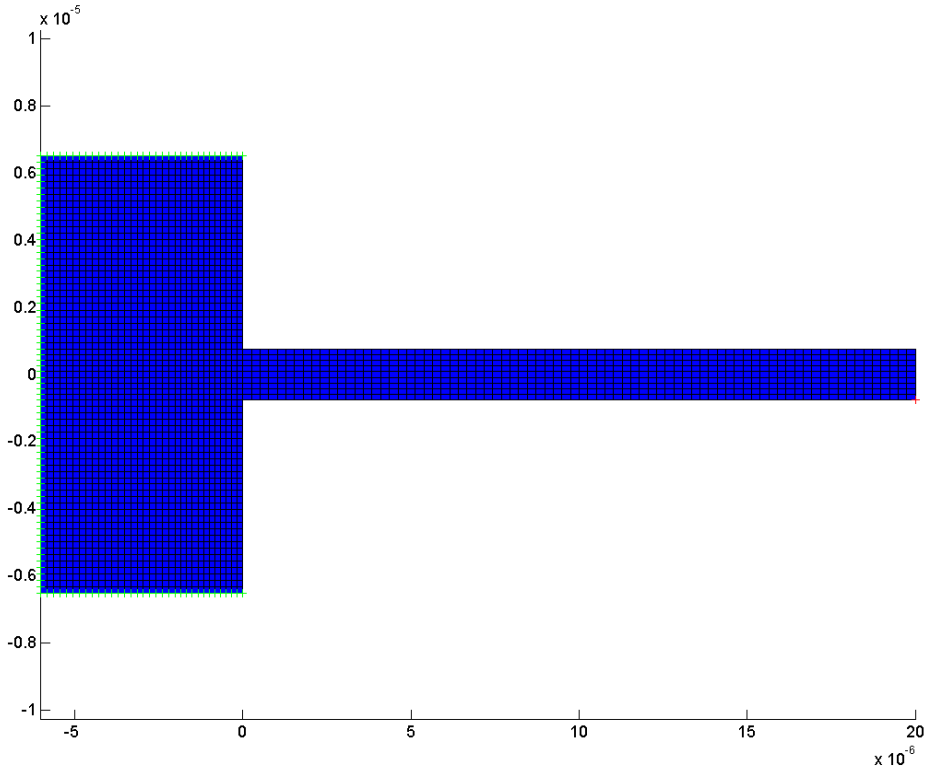

(b)

Figure 4.3: Cantilever beam system consisting of resonator, bounded support and the region; (a) Different domains; (b) Actual mesh in HiQLab and boundary conditions.

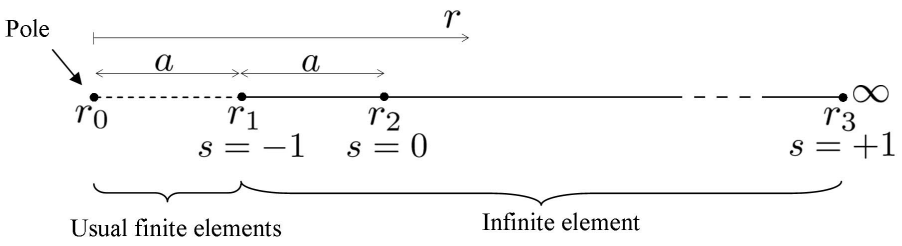

Figure 4.4: Nodal variable position for a one-dimensional infinite element in ABAQUS^{TM}.

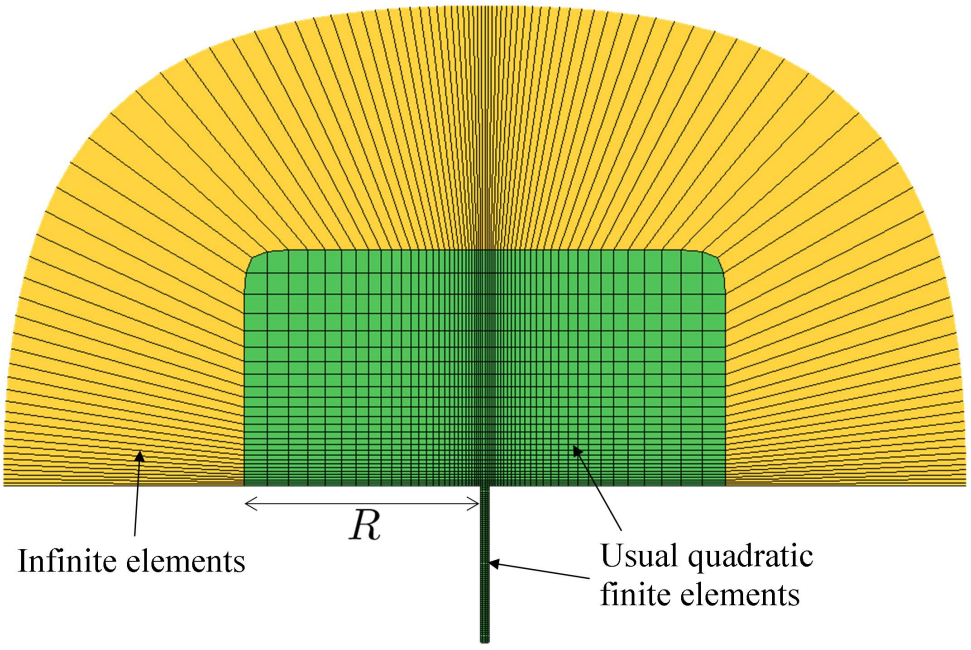

Figure 4.5: Cantilever beam system with infinite elements to model the support.

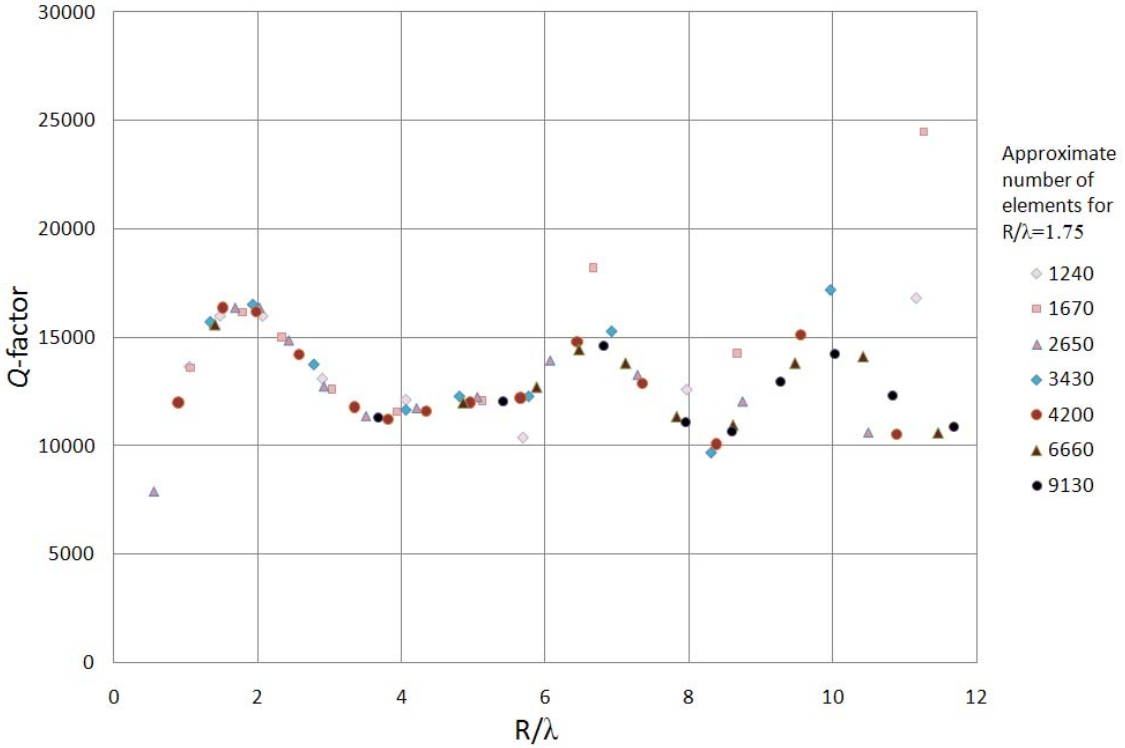

Figure 4.6: Convergence analysis. Q-factor function of R/λ calculated with different mesh densities.

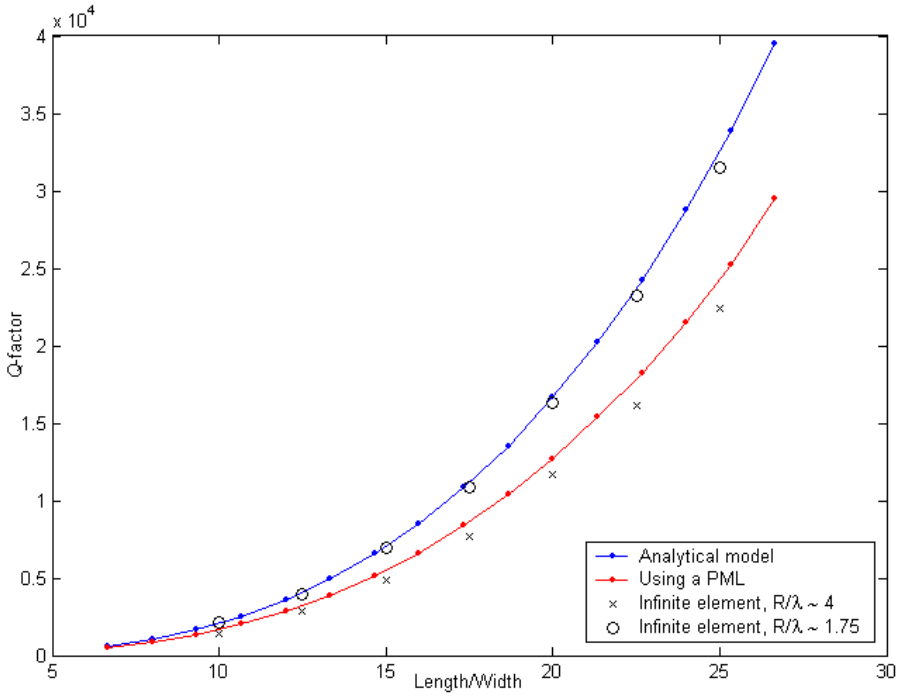

Figure 4.7: Cantilever beam case. Q-factor calculated using the three different methods as a function of the length/width ratio.

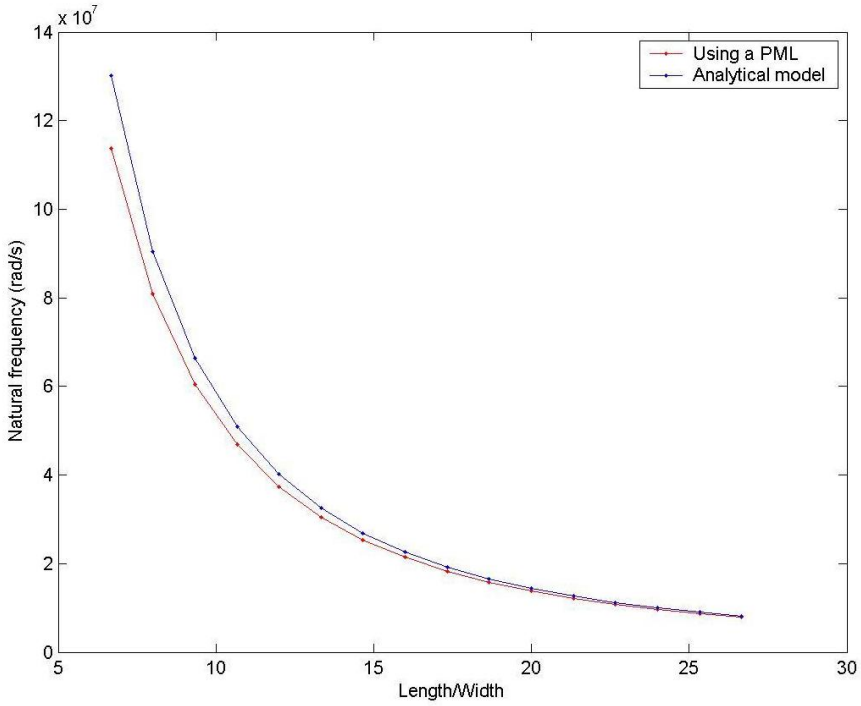

Figure 4.8: Cantilever beam case. First natural frequency calculated using different methods.

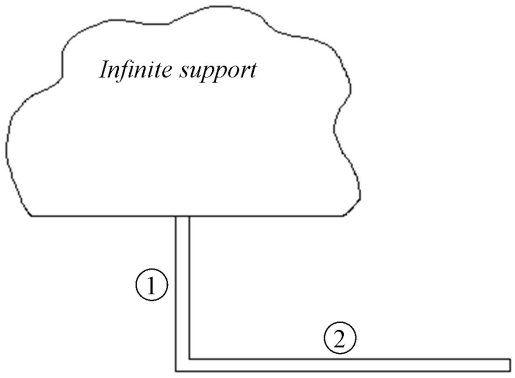

Figure 4.9: Geometry of the two-beam case.

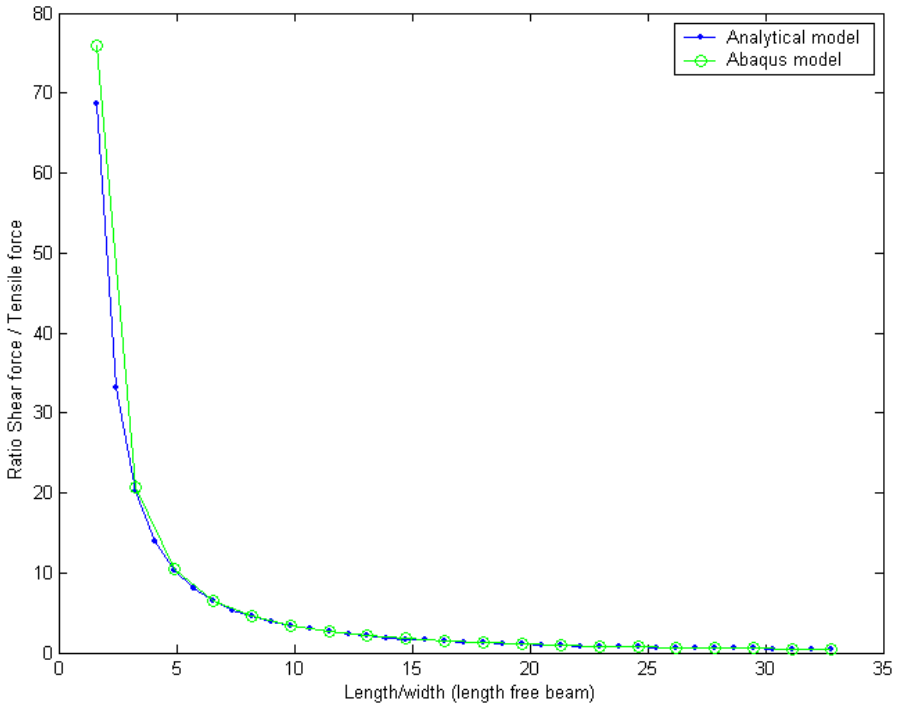

Figure 4.10: Two-beam case. Shear/normal force ratio at the attachment point between the resonator and its support.

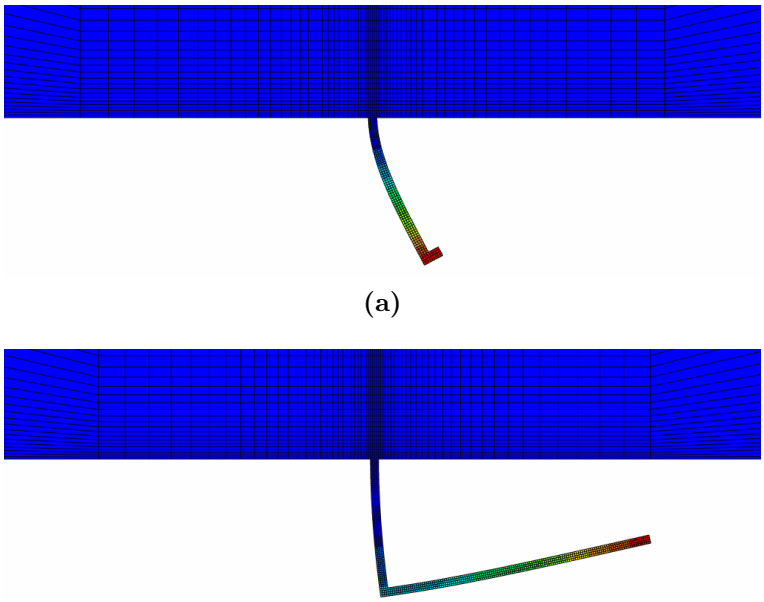

(a)

(b)

Figure 4.11: Two-beam case. Lowest frequency mode shape for the shortest (a) and longest (b) beam '2' studied.

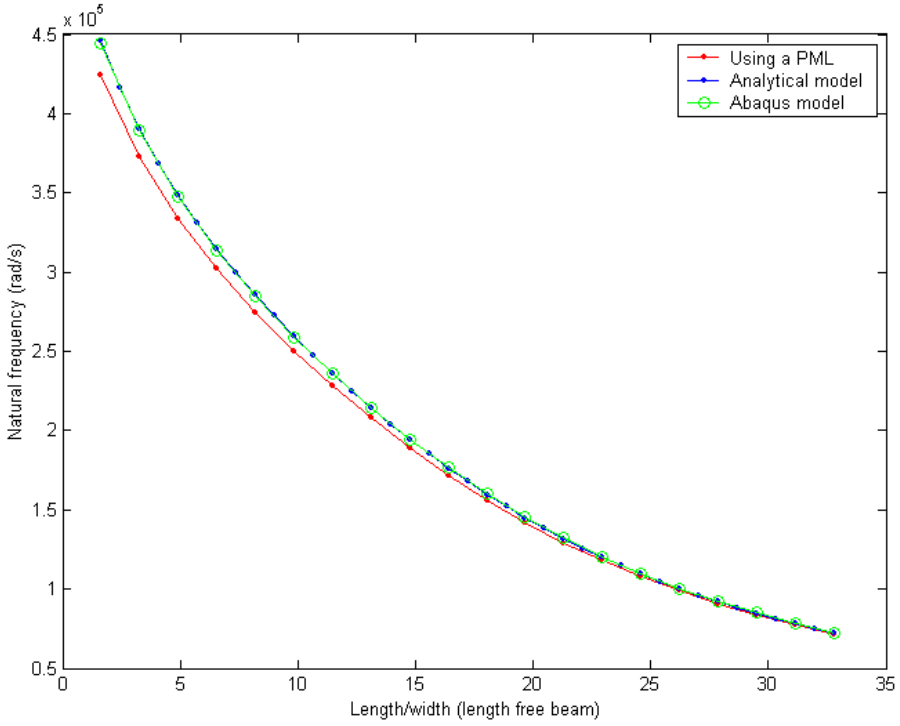

Figure 4.12: Two-beam case. First natural frequency calculated with different methods.

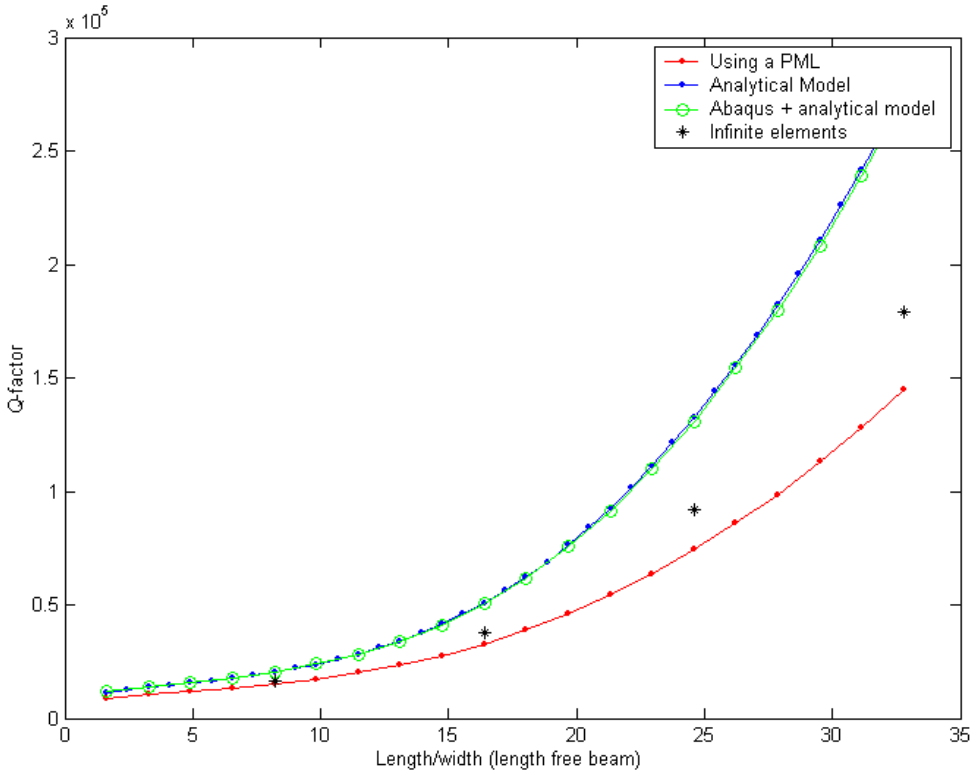

Figure 4.13: Two-beam case. Q-factor calculated using the three different methods as a function of the length/width ratio of beam '2'.

Chapter 5

Influence of leg design on the Q-factor

5.1 Introduction

Chapter 4 presented different methods for calculating the support losses in a resonator. Simple systems were investigated as it was found to be impractical to study complex-shaped resonators and their support using finite element methods. It was shown that the proposed analytical model provided a fast and efficient method to calculate support losses. Better understanding of support losses in a MEMS ring-based rate sensor is the principal aim of the thesis. Calculations of these support losses for different designs are presented in this chapter.

The main component of the ring-based resonator is a vibrating ring. It is supported on eight identical, uniformly spaced legs, see Figure 5.1. Devices like these are based on the vibration of axi-symmetric structures and are more complex than the simpler cantilever beam resonators considered previously. Their symmetric form makes them relatively immune to external vibrations. Indeed, knowing that the lowest order mode of the ring-based rate sensor, which is a translational whole ring motion with respect to the support (illustrated in Figure 3.9 in Chapter 3), occurs at a frequency superior to 5 kHz, the resonator is insensitive to environmental

vibration inputs normally experienced in aerospace and automotive applications, which usually only contain components up to about 2 kHz. Another advantage of a ring resonator is that it is possible to make use of the nodal structure of the vibration pattern to support the ring in such a way that it does not interact strongly with the support on which it is mounted. These are the main reasons why the resonator was designed with cyclic symmetry properties. The legs are designed to be as flexible as possible within the available space between the ring and its support. Engineering intuition suggests that legs composed of longer sections and smaller angles between them will be more flexible. Section 5.2 presents the calculation of support losses for the resonator with its original design and dimensions, whereas a numerical study on the leg design is presented in Section 5.3.

Another possible solution to reduce the energy lost through the support is the addition of blocking masses. Cremer *et al.* [55] gave the theoretical description of a single blocking mass for bending waves. Weisbord [95] suggested the addition of a blocking mass in a beam resonator, which compensates the moment and the force at the clamping end in a flexural mode. In a recent work, Haueis *et al.* [96] extended Weisbord's idea and described the behaviour of a beam clamped between two blocking masses. The full dynamic interaction with the clamped end was taken into consideration. Their model of a resonant beam with blocking masses was developed analytically and solved numerically using the finite element method. It was shown that the two masses reduce the vibration transmitted to the boundaries for a specific mode. In Section 5.4, blocking masses are added to a ring-based resonator. The objective is to investigate their influence on the clamping forces and the associated Q-factor variations. It is important to notice that in [96], the Q-factors are not actually calculated. The effect of the blocking masses is analysed only in terms of the clamping forces and transmission coefficients through the masses. The addition of masses also changes the energy stored in the system and this can influence the Q-factors. As a more complete study, forces, energy distributions and Q-factor variations are considered in Section 5.4.

For the ring-based resonator, the fundamental modes of interest are the 2θ modes, occurring at an angle of 45° to each other. If the resonator is perfectly cyclically

symmetric, both modes have identical frequencies. This is impossible to achieve in practice because dimensional variations and material non-uniformity may be present, and frequency splitting occurs. For improved sensor performance, it is necessary to minimise the split. The crystal symmetry of silicon helps here as this particular material does not contribute to frequency splitting. The greatest issue whilst manufacturing a product with almost no imperfections is from manufacturing tolerances, but these are minimised by the micro-machining technology used [1].

Any additional trimming requirement is satisfied by using a laser ablation to remove mass from the ring at a particular location. The subtraction from the resonator of a small mass alters both the position of the nodal points in the ring vibration and the natural frequencies. By changing the location at which the mass is removed, it is possible to adjust the position of the vibration pattern relative to the excitation force and pick-off positions so that one or other of the modes can be excited independently. It is often necessary to reduce the frequency split to the order of 0.01% to maintain strong resonant coupling between a pair of given modes. By introducing the concept of the "equivalent imperfection mass", Fox [88] showed that it is possible to consider the inverse trimming problem. His work consisted in determining the size and location of the single mass that needs to be added (or removed) from an initially imperfect ring to make the frequencies of a particular pair of modes the same. This work was later extended by Rourke *et al.* [89] who considered the problem of simultaneously trimming a number of pairs of modes of an imperfect ring. The influence of different types of random mass imperfection on the statistical distribution of the natural frequency splits was also investigated in [10].

Section 5.5 analyses support losses for imperfect ring-based resonators. Some parameters in the design of a single leg are varied so that the cyclic symmetry properties are lost. Splits in natural frequencies and associated Q-factors are presented.

5.2 Original study

5.2.1 Main steps for calculating Q

The method used throughout this chapter to calculate Q refers to the "analytical model" presented in Chapter 4. The main steps are summarised below.

- The vibrations of the system are analysed using the ray tracing method presented in Chapter 2. It is assumed that the resonator is clamped at the leg ends, and the modelling takes into account the cyclic symmetry properties of the structure (see Figure 5.1 and Chapter 3). As a consequence, only one leg (three beam portions) and one ring/beam joint transmission are modelled. To obtain the natural frequencies of the resonator, five different analyses (cyclic mode number $\kappa = 0, 1, 2, 3, 4$, see Chapter 3) are performed. For each κ, the following fundamental equation:

$$|\mathbf{I} - \mathbf{TD}| = 0, \tag{5.1}$$

  derived from the ray tracing method (see Section 2.3.1 in Chapter 2), is solved to calculate the natural frequencies of the resonator.

- The mode shapes of the principal sector are calculated using the ray tracing method with cyclic symmetry simplification. As explained in Chapter 3, the mode shapes for all sectors can be obtained from the principal sector. The mode shapes of the complete resonator are then constructed. The calculated mode shapes are used to calculate the total energy stored W and the tensile forces T and shear forces S at the clamped ends of the resonator. These quantities are then used to calculate the Q-factor, see Chapter 4. To calculate the mode shape, MATLAB actually solves an eigenvector problem and scales the calculated eigenvectors by default such that their norm is equal to '1'. In order to objectively compare results obtained for different leg configurations (see Section 5.3), it is important to find a logical way to scale the mode shape

so that all analyses use the same process. To have a better graphic visualisation, it was chosen that the maximum flexural displacement in the ring should be set equal to 0.2 mm, that corresponds to approximately a $1/10^{\text{th}}$ of the ring radius. It is important to note that the values in the eigenvector solution are "wave amplitudes" and not displacements. From the default MATLAB solution, the actual displacements (longitudinal and flexural) at any point in the resonator are first calculated. The value of maximum displacement is used. By dividing the solution vector by this value and re-constructing the actual displacements, the maximum displacement now becomes equal to 1 m. Then this mode shape is divided by 5000 ($1/5000 = 0.2 \cdot 10^{-3}$ m) and one can get the maximum displacement equal to 0.2 mm. The same scaling procedure is undergone for each mode shape presented later in this chapter so that objective results can be compared.

- The energy lost per cycle of vibration ΔW is defined as the sum of ΔW_u and ΔW_v, the energy losses from induced normal and shear stresses respectively at the clamped ends, see Chapter 4. From the axial and shear forces T and S at the clamped ends, the energy loss quantities ΔW_u and ΔW_v due respectively to longitudinal vibration (normal stress) and flexural vibration (shear stress) are derived (see Chapter 4 for a full explanation) for each particular mode. Some useful parameters are recorded during the solution analysis such as the clamped forces and the energy in each portion of the resonator in order to have a better understanding of eventual Q-variations.

- The Q-factor arising from support losses is calculated using:

$$Q = 2\pi \frac{W}{\Delta W}. \tag{5.2}$$

In order to have a maximum confidence in the MATLAB program, a few tests are run once the mode shape and energies are calculated. One example is that at a natural frequency, the total kinetic energy must be equal to the total strain energy. The symmetry properties of the transmission coefficients are also controlled.

5.2.2 Results from the original analysis

The actual dimensions of the ring-based rate sensor are presented in Table 5.1, the notation used is defined in Figure 5.2. The mode shape of the lowest modes for $\kappa = 0, 1, 2, 3, 4$ are illustrated in Chapter 3, Figure 3.9. The natural frequencies and associated Q-factor of the ten lowest modes are calculated using the method summarised above and are given in Table 5.2.

It can be seen that the Q-factor of the lowest 2θ mode (lowest mode with $\kappa = 2$) is significantly (5-10 times) higher than the other modes. For convenient comparison with results that will be presented in later sections, the deformations of the resonator for the 2θ mode are shown in Figure 5.3. The Q-factor is a measure of the energy efficiency of the resonator for particular modes. Amongst the modes considered in Table 5.2, it appears that the 2θ mode is relatively more efficient with respect to support loss; more of the energy stays within the resonator and less propagates away to the support.

To better understand this phenomenon, it is interesting to look at the strain energy contained in the different portions of the resonator for different modes. For example, in the $\kappa = 2$ mode, approximately 25% of the strain energy is contained in the legs (and 75% in the ring); whereas for the lowest $\kappa = 1$ mode, approximately 98% of the strain energy is contained in the legs, and for the lowest $\kappa = 0$ mode 99% of the energy is in the legs. It might be argued that modes for which the legs contain more of the energy will lose more energy through support loss because the legs are attached directly to the support. The main reason for these different energy ratio characteristics is whereas the $\kappa = 2$ mode is mainly a "ring mode" where the ring is the dominant deformation; the $\kappa = 0$ and $\kappa = 1$ modes are respectively a rotation of the ring about its centre and a rigid body translation of the ring, see Figure 3.9. The deformation of the ring is relatively small in these two latter mode shapes and consequently the Q-factor due to support loss is relatively small. Although this ratio of strain energy in the legs over strain energy in the ring can explain the Q-factor differences, it is also important to consider the quantity of energy loss, which is a function of the stresses at the clamped end.

The Q-factors for the 2θ and 3θ modes calculated with the developed models are approximately $1.5 \cdot 10^5$ and $8.1 \cdot 10^4$, respectively, see Table 5.2. These results can be compared with Wong's experiments and predictions [2] for thermoelastic damping in similar resonators, see Table 5.3. In his work, he measured experimentally Q-factors of approximately $9.5 \cdot 10^3$ and $1.2 \cdot 10^4$, and predicted Q-factors due to thermoelastic damping of $1.2 \cdot 10^4$ and $1.8 \cdot 10^4$, for the 2θ and 3θ modes, respectively. The measured overall Q-factor considers all damping mechanisms and is defined as in Equation (1.10). It is interesting to notice that the energy lost predicted (inverse of the Q-factor) for support loss is smaller than the difference between the energy lost by thermoelastic damping predicted by Wong and the total energy lost measured. There is therefore no inconsistency between the support loss predictions and Wong's predictions and measurements, which gives confidence in the models developed and used here.

In applications, the excited and sensed modes are usually the 2θ mode and its orthogonal companion. For clarity, only results relating to the 2θ mode are presented in the following sections as it is of primary interest.

5.3 Influence of leg dimension

In order to see the influence of different leg dimensions on the Q-factor, various parameters are varied with respect to the supporting legs. In this section, the leg dimensions are modified for all the legs so that the cyclic symmetry is maintained. The resonator is composed of eight identical sectors, each of which contains a leg (three beam portions) and a 45° ring portion. Using the cyclic symmetry simplification, only one sector is modelled in the ray tracing method.

5.3.1 Change of the leg geometry

In this section, the geometry of the leg is modified. The leg width is maintained at the original width but the beam lengths and angles between the beams that compose

the leg are changed. The beams are numbered as follows: beam '1' (length L_1) is attached to the ring, beam '2' (length L_2) connects beams '1' and '3', and beam '3' (length L_3) is clamped to the support. The angles between the beams are α between beams '1' and '2', and ϕ between beams '2' and '3'. The notation used is summarised in Figure 5.2. The original dimensions used in the previous analysis (Section 5.2.2) are shown in Table 5.1.

There are five variable parameters that define the leg geometry: L_1, L_2, L_3, α and ϕ. The geometry is constrained in the following way:

- Beam '1' and beam '3' are oriented radially (*i.e.* their centrelines pass through the centre of the ring).
- The total angle subtended by the leg, angle between beam '1' and beam '3' is equal to 40°. This ensures that the ring contains eight legs with a 5° angular separation between each.
- The point of attachment to the support is a fixed point. This means that the distance between the clamped end and the centre of the ring is constant. The reason for this is that the modifications on the legs designs are not intended to change the dimension of the silicon wafer on which the resonators are etched nor their position on the wafer.

These above constraints couple the five variable parameters together. It was decided to vary the lengths L_1 and L_3 of beams '1' and '3'. When one of these lengths varies, the other parameters (e.g. angles between them), vary accordingly. Appendix B shows how the geometric parameters have been derived from the known original dimensions. The coupling between the parameters due to the imposed constraints is also described in Appendix B.

In the models presented later, L_1 and L_3 are varied between four extreme cases, shown in Figure 5.4. For each of these extremes, and for a few values between them, the other geometric parameters needed for the ray tracing application are

calculated, see Appendix B, and the natural frequency and Q-factor are calculated following the procedure explained in Section 5.2.1.

Results for the natural frequencies for different values of L_1 are presented in Figure 5.5. They are shown as a function of L_3. The associated Q-factors are presented in Figure 5.6. Note that on these figures, the five coloured rectangles represent the four extreme cases (whose geometries are illustrated in Figure 5.4) and the original case (see Figure 5.2). The colour of each rectangle corresponds to the design illustrated with the same colour.

From Figure 5.6, it can be seen that leg designs with a longer beam '1' generally have a larger Q-factor resulting in improved performance. If at the same time, beam '3' is shortened, then the largest Q-factor is obtained. From this particular design (blue rectangle in Figures 5.5 and 5.6, and blue design in Figure 5.4), the Q-factor is approximately three times larger than for the original design. The associated mode shape is presented in Figure 5.7. The main reason for the improved Q-factor is that the leg is more flexible when beam '1' is long, *i.e.* the clamped end has less influence on the ring vibration. It can clearly be seen from the mode shape that the ring contributes in an important way to the overall energy of the resonator. It is important to recall that the Q-factor is a function of the total energy stored and the amount of energy loss. Hence a larger Q-value is obtained for designs in which the total energy stored is larger. At the same time, the natural frequencies do not change much for the variations considered. It can be seen that there is a difference of approximately 350 Hz, which is small compared to the original frequency of operation ($\approx$ 14000 Hz). It is important to control the associated change in frequency because a large variation will modify the thermoelastic loss [2].

The design with a short beam '1' and a short beam '3' (whose extreme is represented by a green rectangle in Figures 5.5 and 5.6, and green design in Figure 5.4) is inefficient compared to the original design. The Q-factor in this case is approximately 100 times smaller than the original one. Furthermore, the frequency is greatly increased with this kind of design. The mode shape of this extreme case is shown in Figure 5.8. It can be seen that for this design, the influence of the legs on the ring

vibration is significant. The ring vibration has changed significantly compared to the original case. This extreme case corresponds to the design where the legs are as straight as possible with the applied constraints. Their flexibility is greatly reduced and their participation in the overall resonator deformation is increased. From the mode shape, it is clear that the ring deformation is less important compared to the legs in the beam portion '2'. This indicates that most of the energy is contained within the legs, increasing the support losses and reducing the Q-factor.

5.3.2 Change of leg width

In this section, the geometry of the leg is maintained at the original design (see Figure 5.2 and Table 5.1). However, the in-plane width of the leg is modified. The original leg and ring widths are equal to 0.061 mm and 0.121 mm respectively. The leg width takes values between 0.03 mm and 0.105 mm. The ring width is not changed as it is intended to have a frequency of operation very close to the original 2θ frequency; and of course, changes in the ring width (the ring being the principal vibrating structure in the 2θ mode under investigation) will greatly influence the 2θ natural frequency.

Results for natural frequencies and associated Q-factors as a function of leg width are shown in Figure 5.9. From this graph, it can be seen that the 2θ frequency increases when the leg width increases, whilst the Q-factor decreases when the leg width increases. This is mainly because thin legs are more flexible in bending and constrain the ring less. This ensures that the vibration of the ring is closer to that of a ring without support, maximising the energy stored. In contrast, wide legs have a strong influence on the ring vibration and restrain its amplitude. When the width of the leg is half the original value, the Q-factor is almost 20 times larger than the original Q-factor.

To better understand the effect of these modifications, it is interesting to consider the energy distribution within the resonator as a function of the leg width. Figure 5.10 shows the percentage of energies (strain and kinetic) contained in the

different parts of the structure. The legs are divided into three beam portions, numbered from the ring to the support, as shown in Section 5.3.1. The energy corresponding to a specific portion of a leg is combined with the energies for the same portion of all other legs. This means, for instance, that the energy of beam '1' corresponds in fact to the sum of the energy of the beam portions numbered '1' for each leg. All of these energies are then divided by the total energy stored and shown as a percentage.

From Figure 5.10(a), which depicts the kinetic energy percentage for the different portions, it is clear that the ring moves less when the leg is wider. One can see that the vibrations, that are mainly present within the ring for very thin legs (approximately 75% of the kinetic energy is contained in the ring) are shifted to the legs themselves when the leg width is increased: the energy within the ring decreases by approximately 55% for the widest leg modelled. The kinetic energy percentage of beam '3' remains close to zero, as expected because beam '3' is "clamped" at its end. The fact that the percentage of kinetic energy contained within the ring decreases when the leg width increases shows that the total energy stored decreases.

It can be seen in Figure 5.10(b), which shows the strain energy percentage of the different portions, that the strain energy of the ring decreases when the leg width increases. The ring does not deform as much as for the case when the leg width is very thin. The strain energies in the leg portions increase, which can be explained because they have a larger width and also show a greater deformation. It is interesting to look at the energy of the third beam portion. As this one increases (up to 25%), it is expected that the forces at the clamped end will also increase, meaning an increase in the amount of energy lost. These explain the Q-factor decrease shown in Figure 5.9.

In the above study, the widths of all the beam portions that form the leg were modified together such that the entire leg had the same width. However, it may be interesting to investigate the consequence of independently changing the width of each beam portion. This changes the transmission coefficients at the corner of each joint. Within a beam corner, the incident and created waves do not travel in

beams of equal cross-section any more. By changing the width of the three beam portions independently, the same main conclusions discussed above are found. Legs consisting of thinner beams are more flexible, restrain the ring less and result in a higher Q-factor. On the other hand, wider beams in the legs constrain the ring vibration, contain a larger relative amount of energy (kinetic and strain) and are responsible for more energy being lost and a lower Q-factor.

In the next section, masses are added along the length of the legs, and their influence on blocking the energy flow out from the resonator studied.

5.4 Addition of blocking masses

In this whole section, masses are added to the eight legs simultaneously such that the cyclic symmetry of the ring-based resonator is maintained. Analyses of natural frequencies and mode shapes are performed using the ray tracing method, making use of cyclic symmetry simplification. From the mode shapes, the Q-factors are then calculated. The objective here is to study the influence of added masses on the natural frequencies and Q-factors of the 2θ mode. The masses are added either within a beam portion or at a corner. These two studies are discussed in the next two subsections.

5.4.1 Mass added to a beam portion within the leg

The aim of adding masses is to reduce the energy flow towards the support. It is expected that reducing the vibration amplitude within the legs may reduce this energy flow and its induced energy loss. Masses are first added within each of the three beam portions of the legs, as previously described. For simplicity it is supposed that the added masses are "point masses" added to the mid-point of each beam portion and for all legs simultaneously.

For each case (point mass in either beams '1', '2' or '3'), the natural frequencies

and associated Q-factors are calculated. The results are illustrated in Figure 5.11(a) for the natural frequencies and Figure 5.11(b) for the Q-factors. In each of these graphs, the three lines correspond to masses being added to the different beam portions. Natural frequencies and Q-factors are plotted as a function of the amount of mass added. This quantity is expressed as a percentage of the total mass of the resonator, $M_{\text{resonator}}$, defined as:

$$M_{\text{resonator}} = M_{\text{original}} + M_{\text{added}}. \tag{5.3}$$

where M_{original} and M_{added} are the original mass of the resonator (without added masses) and the total amount of added masses. M_{original} is defined as:

$$M_{\text{original}} = h\ \rho\Big(2\pi R\ b_{\text{ring}} + 8\,(L_1 + L_2 + L_3)\,b_{\text{leg}}\Big). \tag{5.4}$$

In Equation (5.4), h is the axial length of the ring and legs, ρ is the mass density, R is the ring radius, L_i $(i = 1,\ 2,\ 3)$ is the length of the beam portion i, b_{ring} and b_{leg} are the width of the ring and leg respectively. The notation is defined in Figure 5.2. The total amount of added mass M_{added} is simply defined as:

$$M_{\text{added}} = 8m, \tag{5.5}$$

where m is the value of one point mass added.

The highest mass value considered corresponds to added masses equivalent to approximately 50% of the total mass of the resonator. This is an unrealistically large value, which was only included to get a better idea of the natural frequency and Q-factor trends, and is unlikely to be implemented practically.

From Figure 5.11(a), it can be seen that in each case, adding mass reduces the natural frequency, as expected (the resonator has now a bigger mass but the stiffness is unchanged). Furthermore, if the masses are added closer to the clamped boundary, then the reduction in natural frequency is less than if the masses are added closer to the ring. Thus adding point masses to beam '1' will have a more significant effect than adding masses to beam '3'. Adding a point mass in beams '3' will not change

the natural frequency so much because beams '3' are clamped at one end and the magnitude of motion is significantly less than that of the ring in the vibration mode of interest.

Figure 5.11(b) shows Q-factors as a function of the added mass for different added mass positions. From this figure, it can be seen that adding a point mass to beams '1' increases the Q-factor whereas Q-factor decreases if masses are added to beams '2' or '3'. When point masses are added to the middle of beams '3', the Q-factor decreases by approximately 30%. This can be understood on the basis that adding point masses closer to the clamped boundary will induce further vibrations in this part of the resonator. Hence, the energy within the resonator is shifted towards the clamped boundary and more energy will tend to leave through the support.

This can be further illustrated by investigating the forces at the clamped end. Firstly, it is important to note that, with the given resonator dimensions, the energy dissipated per leg at the clamped boundary by shear stresses is approximately 10 times larger than the energy dissipated by normal stresses. Therefore, the shear force has a much more dominant influence than the normal force on the Q-factor. Figure 5.12 shows the shear force at the clamped end as a function of the added mass for different added mass positions. All three analyses were scaled in the same way, such that the maximum flexural displacement of the ring is equal to 0.2 mm. It is then possible to compare "objective" values of shear forces. From Figure 5.12, it can be seen that when masses are added to beams '2' or '3', the shear force at the clamped end increases. On the other hand, when masses are added to beams '1', it reduces the shear force. This can be directly related to Figure 5.11(b). An increase in the shear force tends to reduce the Q-factor whereas a decrease in the force increases Q.

Thus it can be concluded that adding a point mass to beams '1' increases the Q-factor. However, an increase in Q of approximately 8% results in an approximate 25% decrease in the natural frequency. A large variation in natural frequency is not desirable as it induces thermoelastic loss issues [2].

5.4.2 Mass added to a corner of the leg

Another possible location where masses can be added is at the leg corners. Each leg has three "corners". The first one, referred to as the ring joint, corresponds to the attachment between the ring and the leg. The second corner, referred to as the α joint, is between beam '1' and beam '2'. The third and last corner is the ϕ joint between beam '2' and beam '3'.

As in the previous section, masses are added to all legs simultaneously and the ray tracing method using the cyclic symmetry simplification is used to calculate the natural frequencies and mode shapes. The mode shapes are used subsequently to calculate the associated Q-factors. In contrast to the model in Section 5.4.1, adding masses at corners does not change the number of unknowns in the ray tracing analysis. The same wave amplitude unknowns are used as in the original analysis (Section 5.2.2). The only modifications in the model are the transmission coefficients calculated at the corners.

Derivation of the transmission coefficients for a ring/beam transmission and an abrupt change in direction in beams were described in Chapter 2. They were demonstrated by using a "rigid" joint at the discontinuity. For simplification purposes, it is first assumed that the rigid joint is actually a point mass, providing the same simplifications as those used in Section 5.4.1. In the second part of this section of the thesis, the addition of real masses will be modelled.

Adding point masses

Point masses were added at the three different corners and their influence on the natural frequencies and Q-factor were studied.

Figure 5.13(a) illustrates the obtained natural frequencies of the 2θ mode and Figure 5.13(b) presents the associated Q-factors. Results are shown as a function of the added masses, which take the same values as discussed in Section 5.4.1 and are

expressed as a percentage of the resonator total mass. Both of these figures show results for the different positions of added masses.

It can be seen on Figure 5.13(a) that the natural frequencies decrease when point masses are added. The closer to the ring these masses are added, the greater the reduction in natural frequencies is. This is the same result that was obtained in Section 5.4.1. Adding masses further from the ring and closer to the clamped boundary has a weaker influence on the resonator frequencies than if the masses are added to the ring.

From Figure 5.13(b), it can be seen that the Q-factors increase when masses are added to the α joints but decrease when the masses are added to the ϕ joints. Using the same argument presented in Section 5.4.1, it can be understood that if a mass is added closer to the clamped boundary, it will induce higher forces at the interface with the support and therefore reduce the Q-factor. On the other hand, if masses are added closer to the ring (at the α joints here), the energy will be confined to the vibrating ring and little energy will propagate along the leg. This creates an increase in Q-factor. However, it is difficult to understand at this point why adding masses at the ring joints (junctions ring/leg) does not affect the Q-factor greatly, or why Q does not increase significantly. An investigation to understand this phenomenon is to consider the distribution of energy along the leg. This is considered later.

Figure 5.14 shows the strain energy in the different portions of the leg as a function of the added masses. Figure 5.14(a) illustrates the strain energy in beam portion '1', Figure 5.14(b) in beam '2', and Figure 5.14(c) in beam '3'. Results are given for the different possible positions (either ring, α or ϕ joint) of added masses. As in Section 5.4.1 the numerical values are such that the maximum flexural displacement of the ring is equal to 0.2 mm. Firstly, it can be noticed that for the original design (no added masses), the strain energy contained in beam '3' is much higher than in beam '1' or '2' (almost double their value). Secondly, concerning the trends for each added masses positions, it is interesting to see that adding masses at the α or ϕ joints has the opposite effect. The energy increases in beam '1' and decreases in beams '2' and '3' with masses added at the α joints, whereas the energy decreases

in beam '1' and increases in beams '2' and '3' with masses added at the ϕ joints.

From this analysis, it can be concluded that with masses added at the α joints, the strain energy is kept within the ring and beam '1', and the amount of strain energy in beams '2' and '3' and thus its impact on the clamped boundary is reduced. On the other hand, masses added at the ϕ joints increase the energy towards the clamped end (in beams '2' and '3'). This can be related to variations in the Q-factors, illustrated in Figure 5.13(b). Increased strain energy close to the clamped boundary results in increased energy loss from the resonator and a lower Q-factor.

However, adding masses at the ring joints does not influence much the energy distribution. In this case, the strain energy for beams '1', '2' and '3' are insensitive to the added masses. This indicates that the vibration characteristics of the ring does not change significantly, which furthermore explains the insensitivity of Q when masses are added in the ring joints shown in Figure 5.13(b).

Adding real rigid masses

In all of the previous studies in Section 5.4, the masses considered were point masses. These are theoretical masses that are not physically realisable. In the following study, "real" rigid masses are added instead of point masses. These real masses have non-zero rotational inertia and non-zero size and are modelled as cylindrical rigid joints of mass m_j such that:

$$m_j = \frac{\pi \phi_j^2}{4} h \rho, \tag{5.6}$$

where ϕ_j is the diameter of the masses, h the out-of-plane depth and ρ the mass density.

Small masses are added to the different corners of the legs. Table 5.4 shows the natural frequencies and associated Q-factors calculated for the different added masses. In Table 5.4, the diameter of the joint modelling the mass is represented as an absolute value (in mm) and as a percentage of the leg width b_{leg} (defined in Table 5.1).

The corresponding mass is also presented as an absolute value (in mg) and as a percentage of the total mass of the resonator (see Equation (5.3)).

The most noteworthy result compared to the previous section is that when real masses are added to the ring joints, the natural frequencies are increased. This can be explained by the fact that the added masses are rigid and that the length of the ring which is actually vibrating is reduced. The flexing part of the ring gets smaller but the ring radius is maintained. This has the effect of increasing the natural frequency. For information, the mode shape obtained with the largest added mass modelled ($\phi_j = 0.121\,\text{mm}$) in the ring joint is presented in Figure 5.15. Figure 5.15 shows the deformed shape (with a blue dashed line) of the resonator and a closer view around one ring/leg transmission. The real masses are shown with a black line for the un-deformed shape and with a red line for the deformed shape. One can see from Figure 5.15 that the displacement continuity, imposed in the transmission coefficients calculations, is respected around the rigid joint.

Another interesting result is that in this study, the Q-factor corresponding to masses added at the α joints decreases rapidly. It is difficult to explain this phenomenon but it is probably due to the fact that the addition of real masses changes the energy distribution from one part of the leg to the other part. Seeing the influence on the Q-factor, it is thought that more energy is transmitted through this corner, increasing the energy that propagates away from the ring. This idea can be justified by investigating the energies within the ring and beam '1', which are found to decrease. In the same way, the forces (tensile and shear) at the clamped end are found to increase with the addition of masses at the α joints.

In the previous subsections, the modifications in leg design, achieved by changing their dimensions or by adding masses, were performed for all legs simultaneously. An understanding of these effects would allow design modifications to be introduced at an early stage. It is also interesting to investigate the frequency and associated Q-factor splits induced by manufacturing imperfections because these splits can have significant effect on sensor performance [97]. This topic is considered in the next subsection.

5.5 Sensitivity study by modifying one leg only

The presence of an imperfection in the resonator destroys its cyclic symmetry and this is known to create a frequency and Q-factor splits [5]. In this section, design parameters are varied in a single leg only in order to model this asymmetry and study the induced splits. To model a resonator that is not perfectly symmetric using the ray tracing method, the entire structure (without symmetry simplification) must be modelled.

In this study, one parameter was changed at a time in the range of $\pm 5\%$ of the original value. For each of the analyses, the natural frequencies of the 2θ mode are calculated (two frequencies each time there is a split). The Q-factors corresponding to each frequency are also calculated. Table 5.5 shows the results when the width of one leg is varied; Table 5.6 shows the results when the length of beam '1' in one leg is changed; and Table 5.7 shows results when the mass density of one leg is changed. When L_1 (length of beam '1') varies, it has been chosen to keep L_3 fixed and to modify the angles α, ϕ and the length L_2 according to the constraints applied in Section 5.3.1 (see also Appendix B).

From Table 5.5, it can be seen that if one leg is wider, both 2θ natural frequencies increase. This was also the case when all the legs were made wider at the same time, see Section 5.3.2 and Figure 5.9. In the same way as in Section 5.3.2, the associated Q-factors decrease when the leg is wider. It is also very interesting to note that a small frequency split (approximately 8 Hz for example) induces a split of approximately 10^4 in the Q-factor.

From Table 5.6, it appears that when the leg geometry is modified such that L_1 is longer, the calculated natural frequencies decrease. This was also the case when all leg geometries were changed simultaneously, see Section 5.3.1 and Figure 5.5. In Figure 5.5, it is clear that for a fixed value of L_3 (here imposed equal to the original dimension), the frequencies increase when L_1 increases. Concerning the Q-factor variation, while Q increases with L_1 in Section 5.3.1, here, when only one leg geometry is changed, Q either increases or decreases. As explained earlier, there

is a split in the 2θ mode frequency when the resonator is not cyclically symmetric. For each frequency, an associated Q-factor is calculated. It appears that the Q associated with one frequency (named 1^{st} in Table 5.6) decreases whereas the Q associated with the other frequency (named 2^{nd}) increases. Table 5.6 shows a larger split in the natural frequencies than Table 5.5, but a smaller split in the Q-factors.

In Table 5.7, the results illustrate the influence of a small variation in the mass density. When the mass density increases, the natural frequencies decrease, as expected. Concerning the associated Q-factors, their split is quite small (split of less than 200 in Q for a frequency split of approximately 25 Hz) and the obtained Q-factors do not vary greatly from their original value.

Increasing one leg width by 5% or one beam portion length within one leg has much more effect on the Q-factor than increasing the mass density by 5%. It shows that the geometry of the leg has more influence on Q than the material from which it is made. On the other hand, the material has more influence on the natural frequencies than the geometry.

5.6 Conclusion

The aim of this chapter was to quantify the support losses for the original ring-based resonator and for different leg designs. The results given in this chapter focused on the operating mode of the device – the 2θ mode, which shows the highest Q-factor due to support losses. Different possible designs were studied and their influence on the calculated Q-factors of the 2θ mode was analysed. It has been shown that changing the leg design can dramatically affect the associated Q-factors. Legs composed of a longer beam '1' and a shorter beam '3' show a Q-factor approximately three times higher than the original design, for a natural frequency difference that is relatively small. Thinner legs can also improve the Q-factor but in this case the change to the natural frequency is more important. The addition of masses to the ring joints, the middle of beams '1' or at the α joints increases the Q-factor, whereas Q decreases when masses are added to the middle of beam

'2' or '3' and at the ϕ joints. This clearly shows that it is better to add masses closer to the ring. This can be explained by the fact that adding masses around the ring increases the stored energy. On the other hand, adding masses closer to the clamped boundary has the opposite effect and the energy distribution is shifted towards the support.

It is well known that the presence of an imperfection in the resonator induces frequency splits. The frequency splits and associated splits in Q-factors cause practical problems in manufactured sensors. A few parameters were varied in one leg only to simulate a possible imperfection. It was seen that, in general, geometric parameter asymmetry induces greater splits than material property asymmetry. From the established support loss model, it was also shown that it is straightforward to study any possible modification in the design or the addition of imperfections at random places in the resonator.

For each analysis, different methods were used to understand the Q-variations. These included investigating the forces at the clamped end, the kinetic or strain energy distribution in the system, and the mode shape. It was sometimes impossible to explain all of the obtained results but as a general comment, it was shown that the Q-factors are a function of the clamped forces (mainly the shear force at the clamped ends for the original design) but also of the energy distribution in the resonator. It is therefore not sufficient to just minimise the clamped forces. Instead, it is necessary to consider simultaneously both clamped forces and energy contained in the resonator. The energy contained in the ring, or in the first beam portion of the leg, must be maximised, whilst the energy that propagates in the second and third beam portions of the leg must be minimised as they proved to have a strong influence on the clamped forces.

The Q-factor of the 2θ mode calculated for the original design is approximately $1.5 \cdot 10^5$. This should be compared with Q-factors arising from other energy loss mechanisms. It is well known for the current MEMS design that the main source of energy loss is thermoelastic damping. Thermoelastic damping in ring-based resonators has been analysed by Wong [2]. He predicted and experimentally measured

Q-factors of approximately 10^4 for a similar ring-based resonator to the one presented as the original design in this chapter. The predicted Q-factor for support loss is more than ten times higher than the Q-factor due to thermoelastic damping. This clearly shows that for the current design, support loss can be neglected. However, in possible future designs or by using other materials, it may be possible to minimise the energy lost by thermoelastic damping so that it becomes less significant than support loss.

Figures and tables

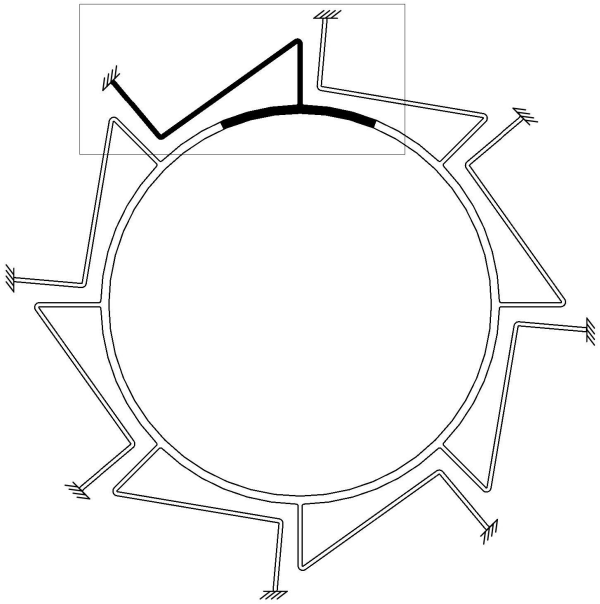

Figure 5.1: Ring-based rate sensor with cyclic symmetry and its 45° principal sector. Only this sector is actually modelled in the ray tracing analysis when the cyclic symmetry simplification is used.

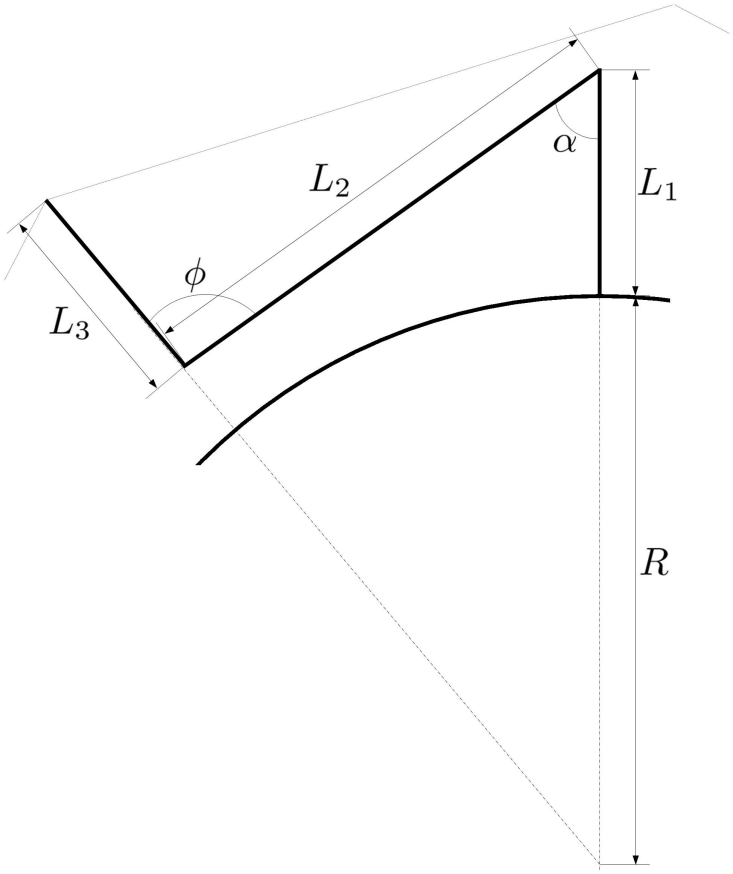

Figure 5.2: Original leg design showing the different geometric parameters that can be changed (except the radius R).

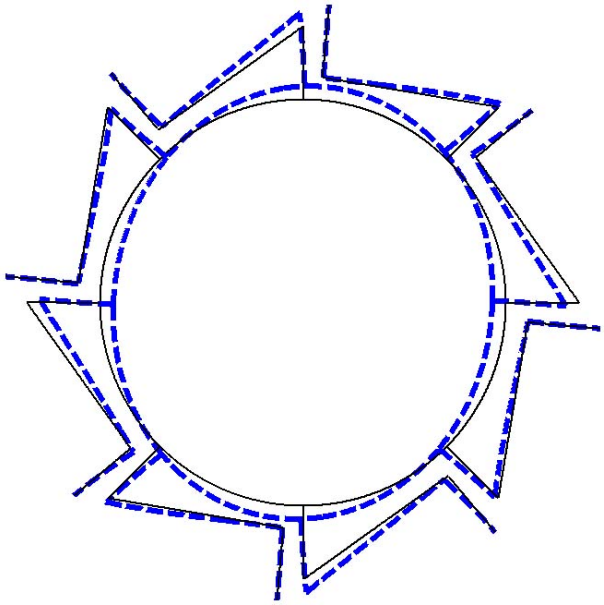

Figure 5.3: Deformed shape of the 2θ mode for the original leg design. The associated natural frequency and Q-factor are shown with a black rectangle in Figures 5.5 and 5.6.

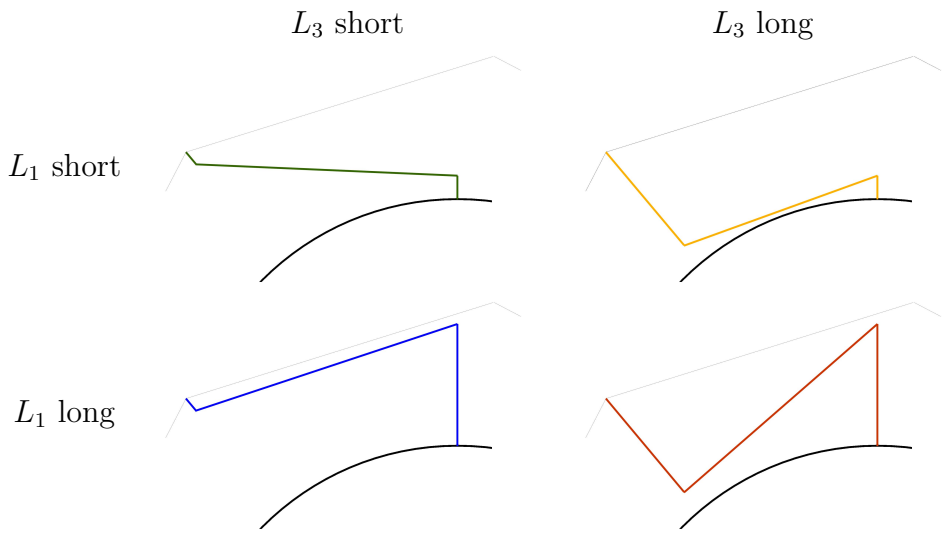

Figure 5.4: Extreme cases modelled of possible leg design. L_1 and L_3 varies between these four different cases in the analysis.

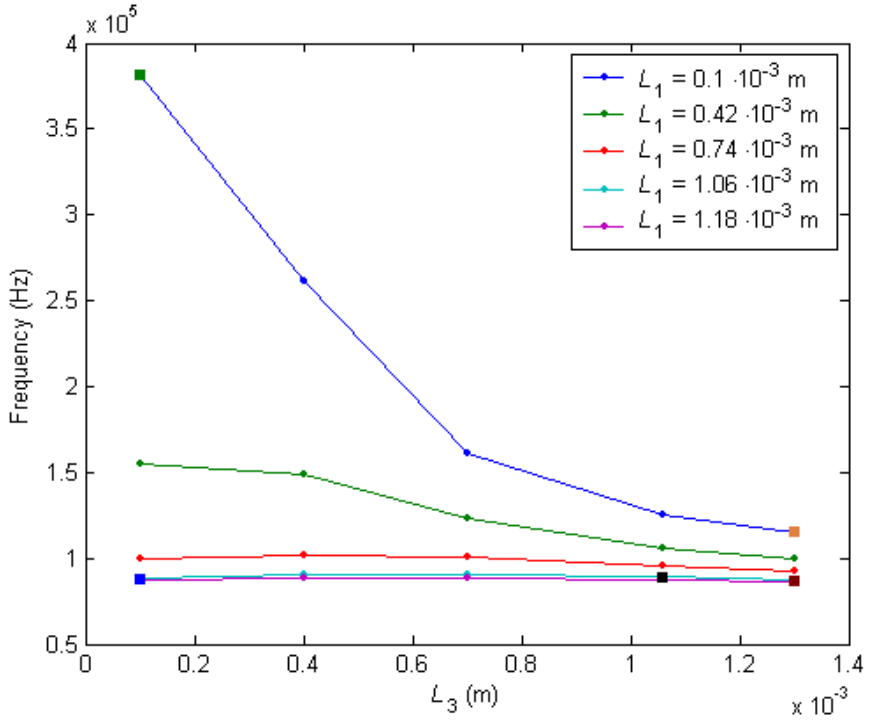

Figure 5.5: Natural frequencies (Hz) of the 2θ mode for different values of L_1 and L_3 (length of beam '1' and beam '3').

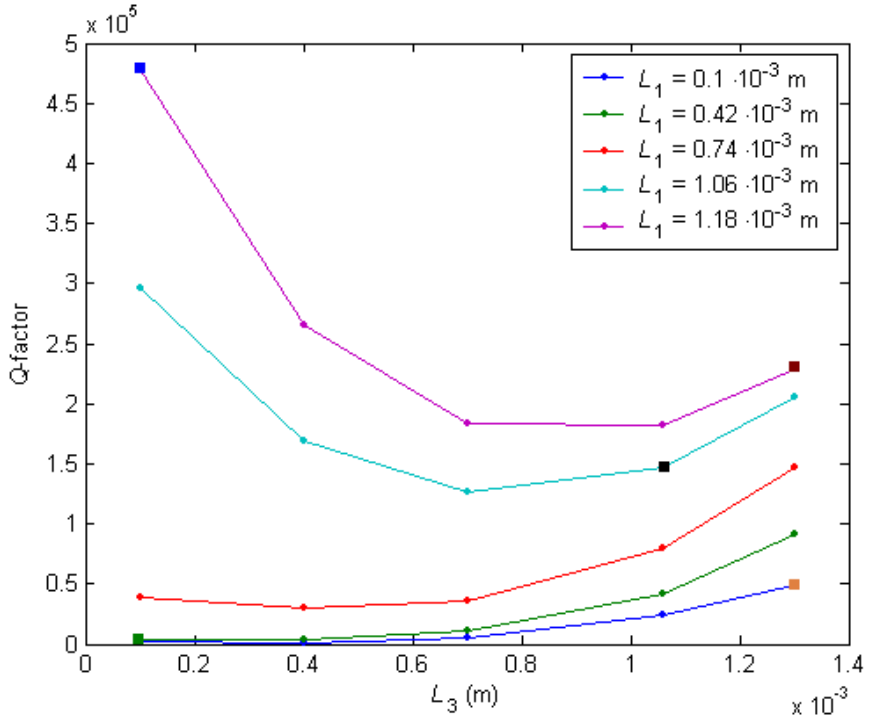

Figure 5.6: Q-factors of the 2θ mode for different values of L_1 and L_3 (length of beam '1' and beam '3').

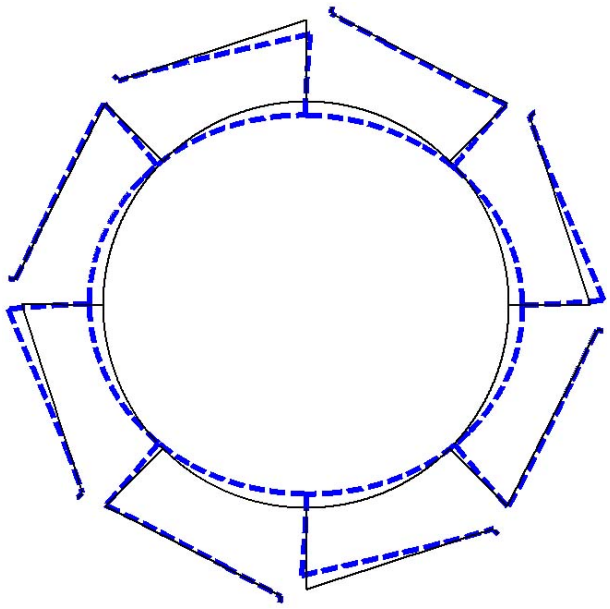

Figure 5.7: Deformed shape of the 2θ mode for a long beam '1' and a short beam '3'. This design corresponds to the 'blue' one on Figure 5.4. The associated natural frequency and Q-factor are shown with a blue rectangle in Figures 5.5 and 5.6.

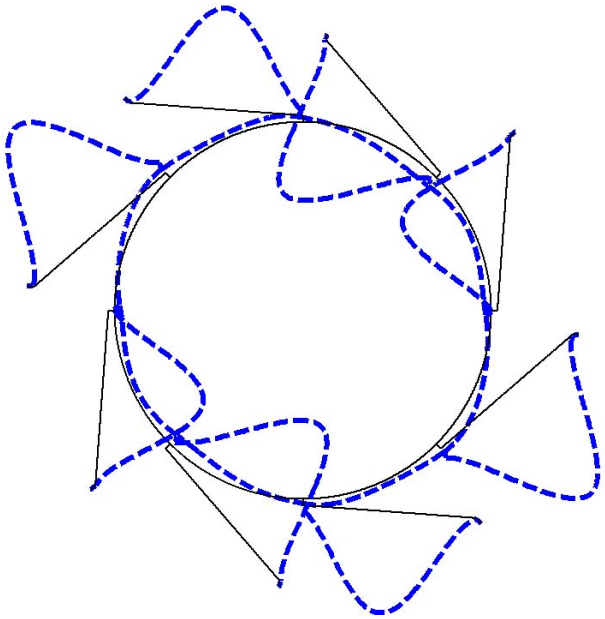

Figure 5.8: Deformed shape of the 2θ mode for a short beam '1' and a short beam '3'. This design corresponds to the 'green' one on Figure 5.4. The associated natural frequency and Q-factor are shown with a green rectangle in Figures 5.5 and 5.6.

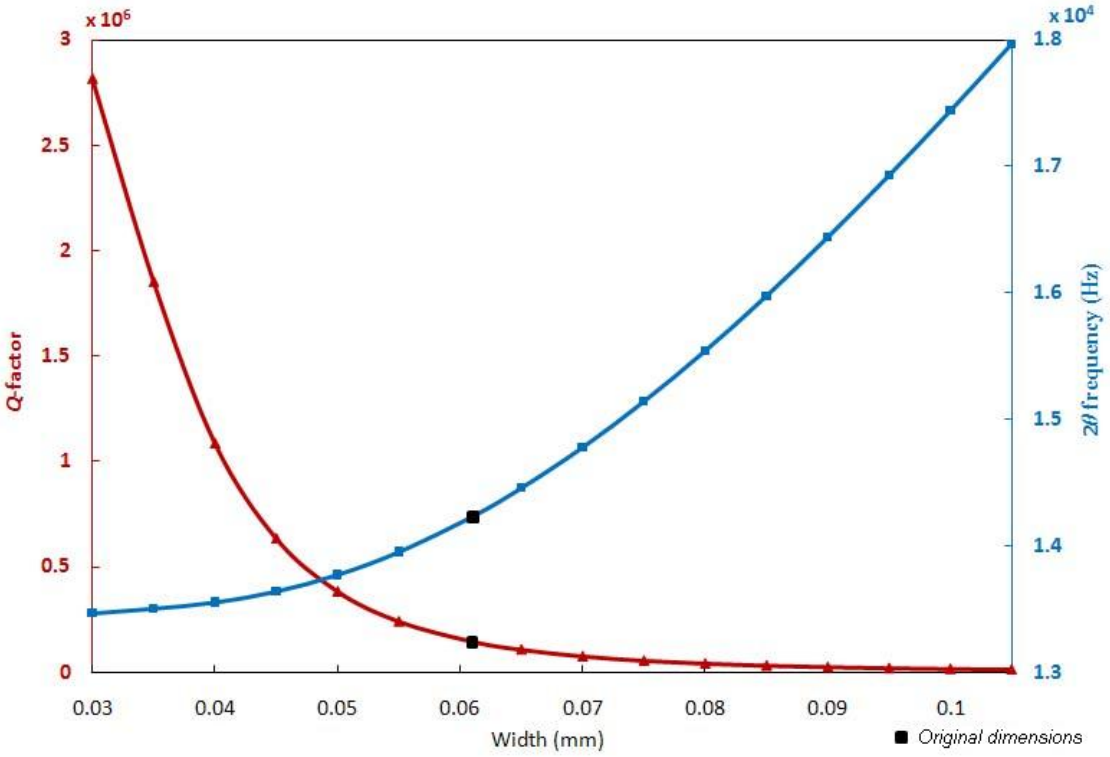

Figure 5.9: 2θ frequencies (Hz) and the associated Q-factors function of the leg width.

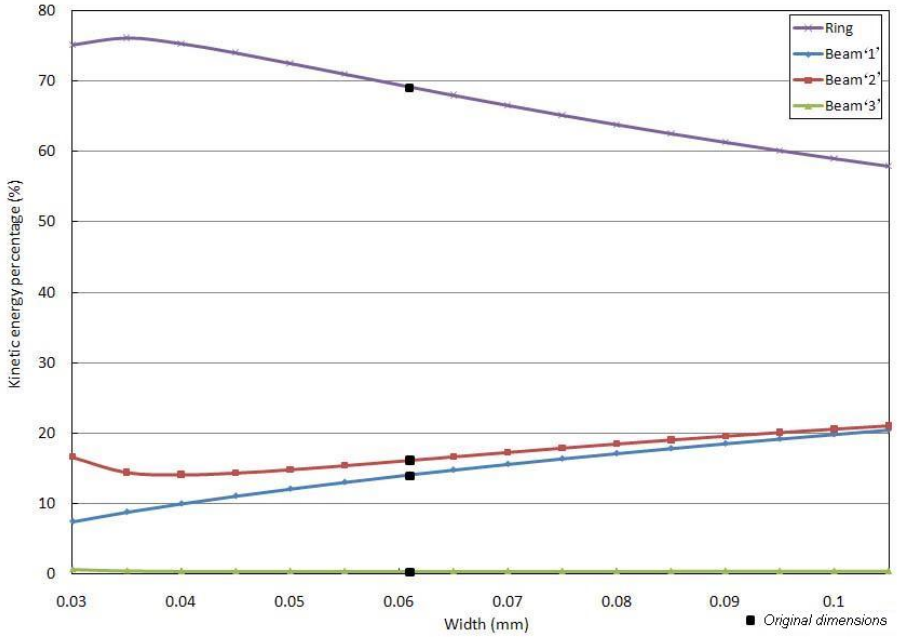

(a)

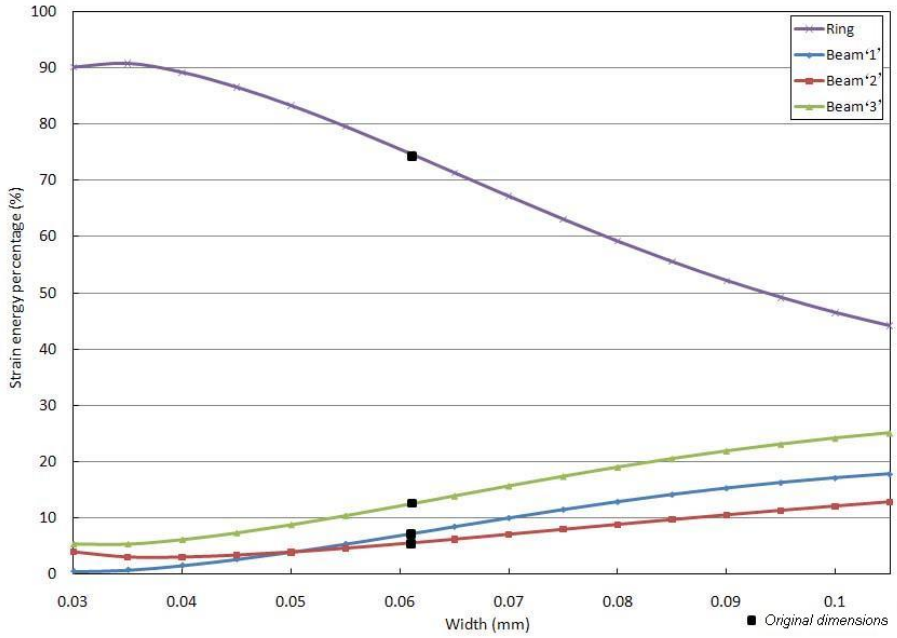

(b)

Figure 5.10: Kinetic energy (a) and strain energy (b) percentages in the different portions of the ring-based resonator, for the 2θ mode, as a function of the leg width.

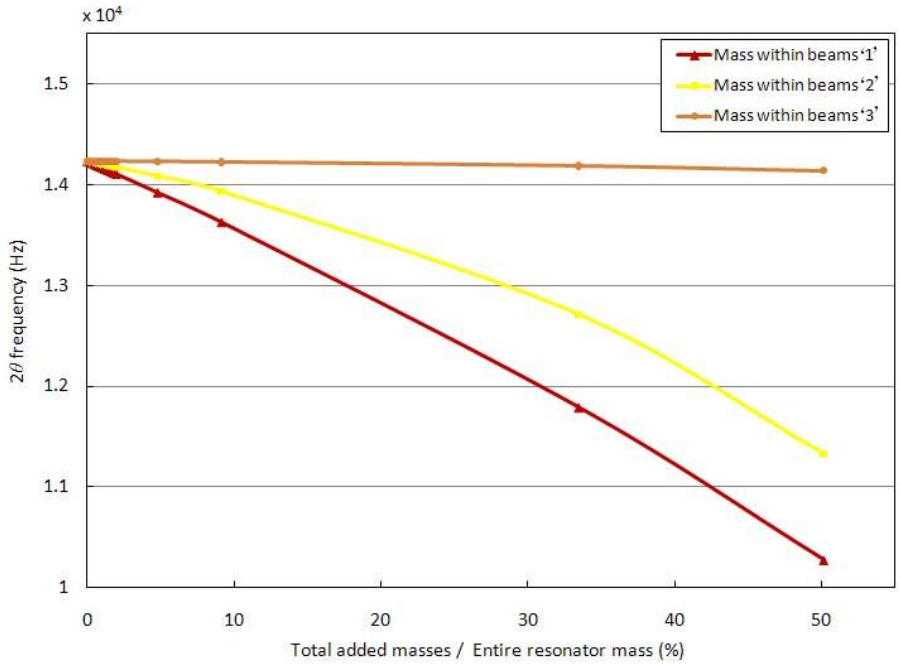

(a)

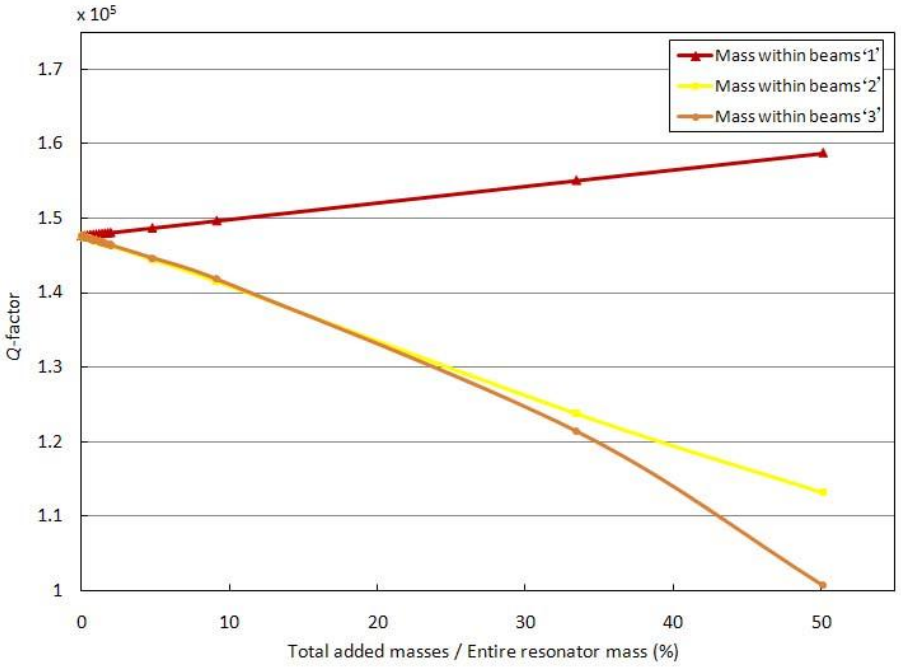

(b)

Figure 5.11: Natural frequencies (a) and the associated Q-factors (b) of the 2θ mode, as a function of the added masses. Masses are added in either beams '1', '2' or '3'.

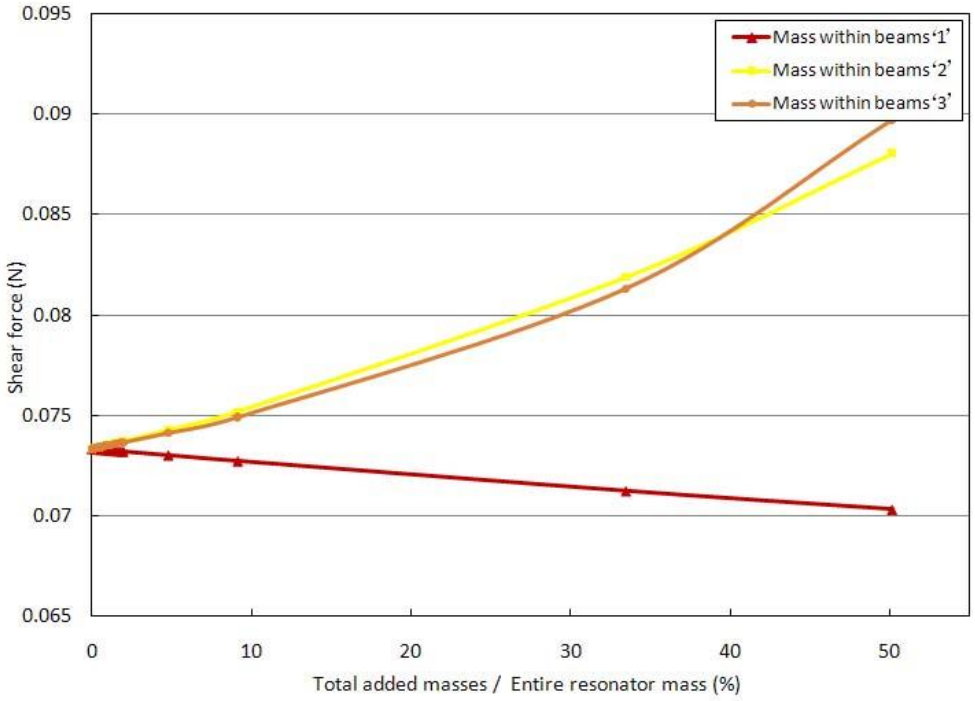

Figure 5.12: Absolute value of the shear force at a clamped end for the 2θ mode, as a function of the added masses. Masses are added in either beams '1', '2' or '3'.

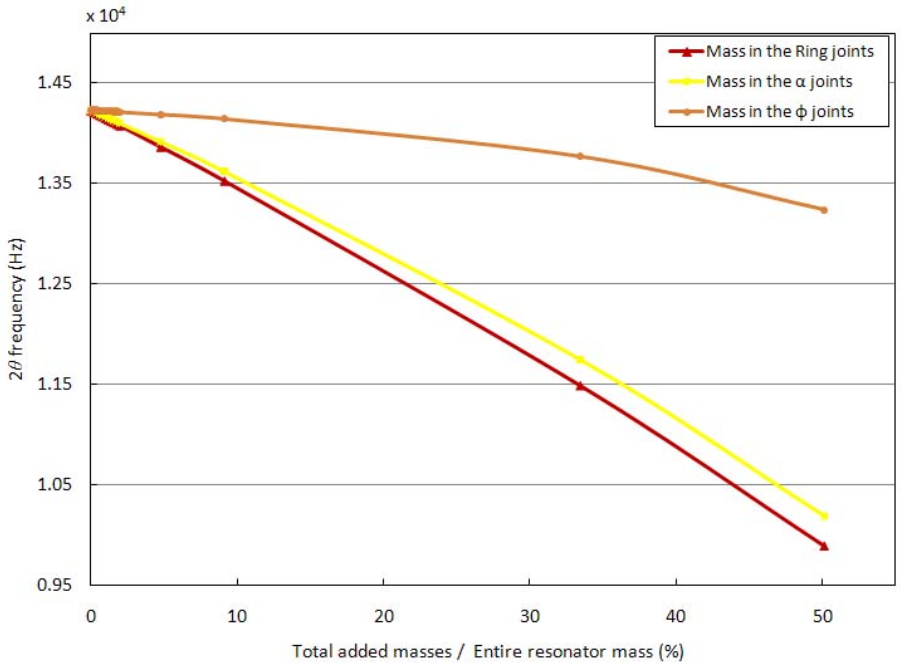

(a)

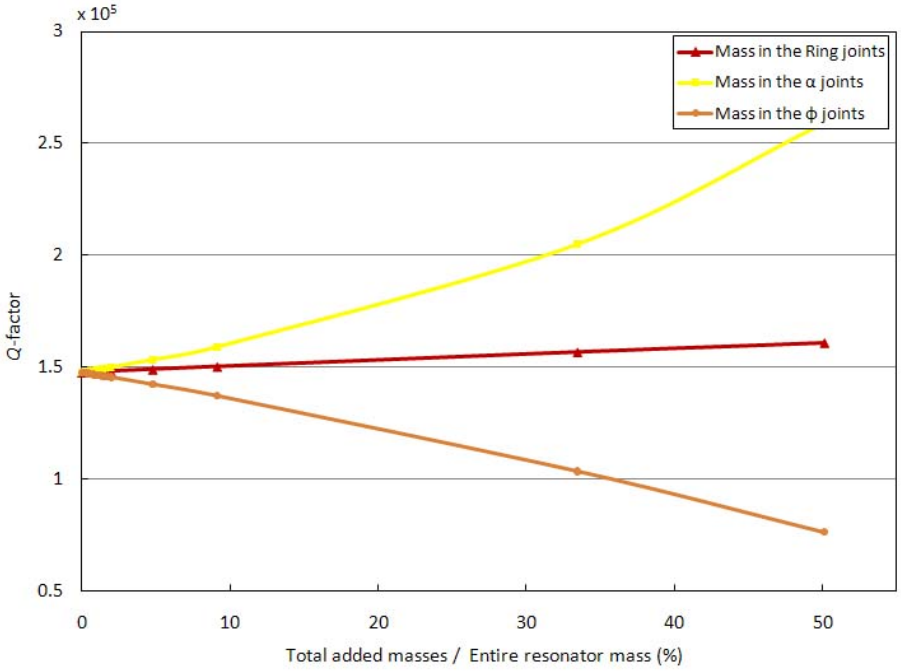

(b)

Figure 5.13: Natural frequencies (a) and the associated Q-factors (b) of the 2θ mode, as a function of the added masses. Masses are added either in the joints between the ring and the attached legs ("Ring joints"), at the first corner within the legs ("α joints"), or at the second corner within the legs ("ϕ joints").

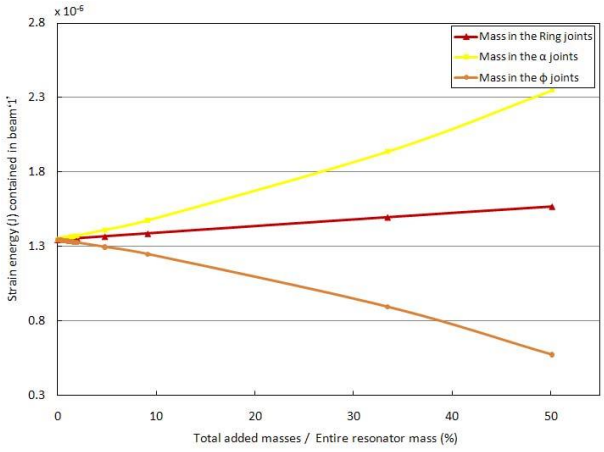

(a)

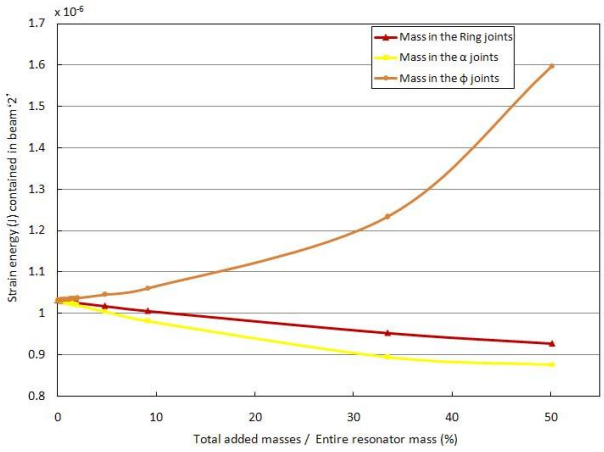

(b)

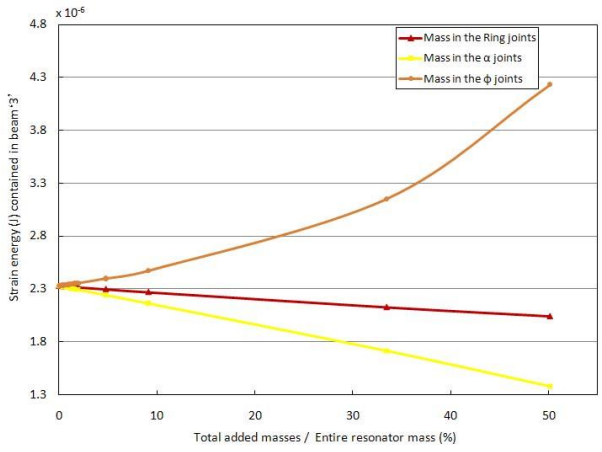

(c)

Figure 5.14: Strain energy for the 2θ mode in the beam sections '1' (a), '2' (b) and '3' (c), as a function of the added masses. The masses are added in the corners of the leg (either Ring, α or ϕ joint).

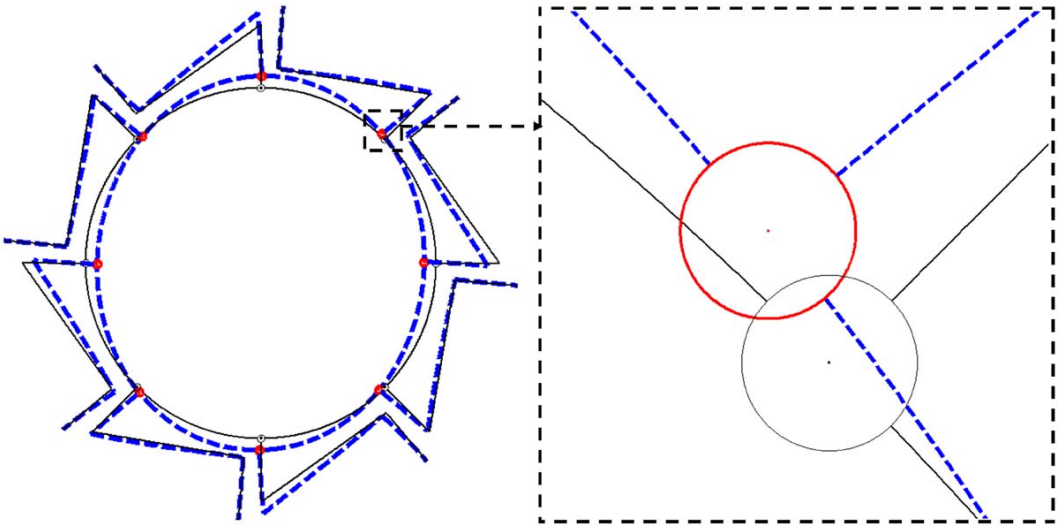

Figure 5.15: Deformed shape of the 2θ mode and zoom around one ring/leg transmission, with a rigid mass of diameter $\phi_j = 0.121\,\text{mm}$ added in the ring joints.

Table 5.1: Original dimensions of the ring-based rate sensor in mm (with axial thickness = 0.1 mm). b_{ring} and b_{leg} are the ring and leg widths; see Figure 5.2 for the other notations. The original material properties used are $\rho = 2329\,\text{kg/m}^3$, $E = 170 \cdot 10^9\,\text{N/m}^2$ and $\nu = 0.28$.

L_1	1.064
L_2	2.582
L_3	1.060
α	54.5°
ϕ	94.5°
R	2.94
b_{ring}	0.121
b_{leg}	0.061

Table 5.2: Natural frequencies (Hz) and the associated Q-factors for the ring-based rate sensor calculated using the ray tracing method and the analytical support model. The sensor dimensions and material properties are presented in Table 5.1.

	Frequency (Hz)	κ	Q-factor
	11 853	1	$2.282 \cdot 10^4$
2θ mode ⇒	14 233	2	$1.476 \cdot 10^5$
	18 330	0	$1.740 \cdot 10^4$
3θ mode ⇒	32 133	3	$8.066 \cdot 10^4$
	35 646	4	$4.528 \cdot 10^4$
	37 850	2	$4.681 \cdot 10^4$
	38 479	1	$5.655 \cdot 10^4$
	40 787	0	$9.612 \cdot 10^4$
	41 100	3	$7.744 \cdot 10^4$
	55 202	4	$4.340 \cdot 10^4$

Table 5.3: Q-factors for the 2θ and 3θ modes. Comparison between support loss predictions, thermoelastic damping predictions [2] and measurements [2].

	Damping predictions		Measurements [2]
	Support loss	Thermoelastic [2]	
2θ mode	147 600	11 731	9 455
3θ mode	80 660	17 783	12 434

Table 5.4: Natural frequencies (Hz) and the associated Q-factors of the 2θ mode, as a function of the added masses. The masses represent rigid masses. Each of them has a diameter ϕ_j and a mass m_j. Results are shown for the different possible positions of the added masses.

ϕ_j (mm)	% leg width	m_j (mg)	% total mass	Frequency (Hz)			Q-factor		
				Ring joint	α joint	ϕ joint	Ring joint	α joint	ϕ joint
0	0	0	0	14 233	14 233	14 233	147 575	147 575	147 575
0.02	32.8	$7.32 \cdot 10^{-8}$	0.07	14 415	14 257	14 237	147 655	145 811	147 138
0.04	65.6	$2.93 \cdot 10^{-7}$	0.29	14 589	14 271	14 240	147 730	144 239	146 554
0.061	100	$6.81 \cdot 10^{-7}$	0.68	14 762	14 276	14 243	147 803	142 781	145 784
0.08	131.1	$1.17 \cdot 10^{-6}$	1.16	14 908	14 272	14 243	147 865	141 623	144 950
0.1	163.9	$1.83 \cdot 10^{-6}$	1.81	15 053	14 259	14 243	147 926	140 561	143 934
0.121	198.4	$2.68 \cdot 10^{-6}$	2.62	15 193	14 234	14 241	147 985	139 609	142 718

Table 5.5: Natural frequencies (Hz) and the associated Q-factors of the 2θ mode, as a function of the change in leg width.

Leg width b_{leg} (mm)		Frequency (Hz)			Q-factor		
% change	real value	1st	2nd	Split	1st	2nd	Split
-5	0.058	14 212	14 217	5	154 343	147 571	6 772
-4	0.0586	14 216	14 220	4	153 309	147 569	5 740
-3	0.0592	14 220	14 223	3	152 117	147 569	4 547
-2	0.0598	14 224	14 226	2	150 765	147 571	3 194
-1	0.0604	14 228	14 229	1	149 251	147 573	1 678
0	0.061	14 233		0	147 575		0
1	0.0616	14 237	14 236	1	145 736	147 575	1 839
2	0.0622	14 242	14 239	3	143 738	147 574	3 836
3	0.0628	14 247	14 243	4	141 583	147 570	5 986
4	0.0634	14 253	14 247	6	139 277	147 563	8 286
5	0.0641	14 258	14 250	8	136 827	147 554	10 727

Table 5.6: Natural frequencies (Hz) and the associated Q-factors of the 2θ mode, as a function of the change in beam '1' length.

Length beam '1' L_1 (mm)		Frequency (Hz)			Q-factor		
% change	real value	1st	2nd	Split	1st	2nd	Split
-5	1.011	14 240	14 257	17	148 313	142 737	5 576
-4	1.022	14 238	14 252	14	148 170	143 795	4 375
-3	1.032	14 237	14 247	10	148 025	144 807	3 218
-2	1.043	14 235	14 242	7	147 877	145 773	2 105
-1	1.054	14 234	14 237	3	147 727	146 695	1 032
0	1.064	14 233		0	147 575		0
1	1.075	14 231	14 227	3	147 420	148 413	993
2	1.086	14 230	14 223	7	147 264	149 212	1 949
3	1.096	14 228	14 218	10	147 106	149 974	2 868
4	1.107	14 227	14 214	13	146 946	150 698	3 752
5	1.118	14 226	14 209	16	146 785	151 387	4 602

Table 5.7: Natural frequencies (Hz) and the associated Q-factors of the 2θ mode, as a function of the change in mass density.

Mass density ρ (kg/m^3)		Frequency (Hz)			Q-factor		
% change	real value	1st	2nd	Split	1st	2nd	Split
-5	2 213	14 234	14 259	25	147 640	147 718	78
-4	2 236	14 233	14 254	20	147 627	147 698	71
-3	2 259	14 233	14 248	15	147 614	147 674	59
-2	2 282	14 233	14 243	10	147 601	147 645	44
-1	2 306	14 233	14 238	5	147 588	147 612	24
0	2 329	14 233		0	147 575		0
1	2 352	14 232	14 227	5	147 561	147 533	28
2	2 376	14 232	14 222	10	147 547	147 486	61
3	2 399	14 232	14 217	15	147 534	147 436	98
4	2 422	14 232	14 212	20	147 520	147 381	139
5	2 445	14 231	14 206	25	147 506	147 321	184

Chapter 6

Support loss prediction for out-of-plane vibrations

6.1 Introduction

In Chapter 2, a wave approach was developed to study in-plane vibrations of planar structures composed of straight and curved beams. Some possible simplifications, when the structure presents symmetric aspects, were derived in Chapter 3. An analytical support model was developed in Chapter 4 and used to calculate the Q-factor for different types of resonators. The models allow support losses to be analysed efficiently for different resonator designs, see Chapter 5. All studies presented so far in this thesis considered in-plane vibrations only. This chapter will apply similar approaches for considering out-of-plane vibrations.

The single-axis rate sensors, analysed in the previous chapter, are often used in clusters of two or three to provide a multi-axis capability that many applications demand. Recent work has considered multi-axis sensors inducing in-plane and out-of-plane vibrations of the ring resonator to measure rate along two or three orthogonal axes [6, 98]. The flexural out-of-plane vibration modes of a perfect circular ring with uniform cross-section occur in degenerate pairs, with equal natural frequencies and arbitrary location [99]. Dimensional imperfections or material anisotropy

may result in a loss of degeneracy due to disturbance of the symmetry [100]. For successful operation as a rate gyroscope, the associated frequency splits must be reduced to acceptable levels using an advance form of frequency trimming [88, 89]. The single-axis sensor studied so far in this thesis relies on coupling between two in-plane modes. To achieve three-axis measurements, the coupling of in-plane vibration modes and out-of-plane vibrations mode is used [8]. This coupling arises as a direct consequence of Coriolis forces created by an external applied rate. In a freely vibrating perfect ring, with uniform cross-section and material properties distribution, the in-plane and out-of-plane motions decouple [101]. In order to study vibration analysis of multi-axis rate sensors, both in-plane and out-of-plane vibrations need to be considered. The ring-based resonator studied in this thesis is supposed to be perfectly symmetric, such that in-plane and out-of-plane modes do not interact and can be analysed separately.

The ray tracing method, based on a wave approach, presented in Chapter 2 applies exact solutions to model in-plane vibrations of structural networks. When an exact solution for a structural element is used, then the solution is valid for all frequencies and no model refinements are required as those required in the finite element method. To model vibrations in complex three-dimensional frames, each beam (straight or curved) is modelled as a single "element" and a general method for combining the individual elements is needed. Several approaches have been developed which use exact solutions; these includes the dynamic stiffness method (whose basics can be found in [67] or [66]) and the wave approach. Langley [102] has used the dynamic stiffness method to analyse power flow in general frames. Expressions for axial, torsional and flexural stiffnesses, and the associated power flow are given. Banerjee and Williams [103] have reviewed various dynamic stiffness methods. Dynamic analysis of three-dimensional frames using a wave approach has been studied by several authors. Cai and Lin [104], Young and Lin [105], and Beale and Accorsi [69] have presented a wave scattering procedure for dynamic analysis of frames and truss-type structures. Beale and Accorsi [69] developed a matrix method which includes multiple wave modes (axial, torsional and flexural) in order to calculate power flow in frame structures. The ray tracing method presented in Chapter 2 is a similar approach as it also considers the scattering and propagation

of waves. However, the ray tracing method seems more concise and easier to apply. An extension of the ray tracing method (presented in Chapter 2) to cope with out-of-plane vibration will therefore be presented in Section 6.2.

Several studies have been developed to investigate support losses of resonators, where various configurations of resonator with respect to its substrate may exist. The first one, whose modelling has been studied in depth in Chapter 4, is when the resonator is located within a substrate (usually thin) and the resonator vibrates in-plane, creating stress sources within the substrate depth, see [42]. A second possible configuration is when the resonator sits on top of a substrate, the resonator vibrates out-of-plane and stress sources act on the surface of the substrate, see [36, 39, 43]. These two configurations have been considered in a recent study [106]. A third possible configuration is when the resonator and substrate are etched from the same silicon wafer (as in the first case) but the resonator is designed to vibrate out-of-plane. Support losses for this kind of structure have previously been the subject of very little investigation. An extension of the work done by Judge *et al.* [45] who investigated the support losses of resonators for thin support structures is presented in Section 6.3. This represents a possible method to model the support losses occurring from out-of-plane motion of resonators such as the ring-based rate sensor.

By applying the method developed in Sections 6.2 and 6.3, results for the natural frequencies, mode shapes, and the associated Q-factors of the ring-based resonator vibrating out-of-plane are presented in Section 6.4.

6.2 The ray tracing method applied to out-of-plane vibrations

6.2.1 Wave propagation in straight and curved beams

This section introduces the fundamental governing equations of out-of-plane motion of curved beams with constant radius, neglecting shear deformation and rotary inertia. Torsion and out-of-plane (axial) flexure are considered. As in the case of in-plane vibrations (Chapter 2, Section 2.2), harmonic wave solution is assumed and the derivation of the corresponding wavenumbers is presented. The same approach is applied here: the governing equations of curved beams are first presented, from which one can derive the wavenumbers, and they are then simplified to the governing equations of out-of-plane vibrations of straight beams. The equations obtained are well known [65] and are used extensively in the ray tracing method presented later.

Consider a curved beam in the plane (x, z) of constant radius of curvature as shown in Figure 6.1. The curved beam is vibrating out-of-plane, in the axial y-direction. The curved beam is characterised by the radius of curvature R; the cross-sectional area A; the flexural rigidity EI_x in a normal plane; the torsional rigidity GJ (where G is the shear modulus and J is often called the torsion constant [9, 107]); and the polar moment of inertia I_{zz}. I_{zz} and J are identical for circular cross-section, but for other shapes, J must be determined by other means [65, 107]. In Figure 6.1, P is the out-of-plane shear force (along the y-axis), M_2 is the out-of-plane bending moment (rotation around x), and M_T is the twisting moment (rotation around z). v is the displacement along the y-axis, and Ω is the angular rotation of the cross-section of the beam due to torsion. The circumferential coordinate along the centreline is denoted by s.

The internal force and bending moments governing out-of-plane motion of a curved

beam are related to the displacements by the relations [65]:

$$M_2 = EI_x\left(\frac{\Omega}{R} - \frac{\partial^2 v}{\partial s^2}\right), \tag{6.1}$$

$$M_T = GJ\frac{\partial}{\partial s}\left(\Omega + \frac{v}{R}\right), \tag{6.2}$$

$$P = \frac{\partial M_2}{\partial s} + \frac{M_T}{R}. \tag{6.3}$$

For curved beams, the out-of-plane equations of motion can be expressed as [65]:

$$\frac{GJ}{R}\frac{\partial^2}{\partial s^2}\left(\Omega + \frac{v}{R}\right) + EI_x\frac{\partial^2}{\partial s^2}\left(\frac{\Omega}{R} - \frac{\partial^2 v}{\partial s^2}\right) = \rho A\frac{\partial^2 v}{\partial t^2}, \tag{6.4}$$

$$GJ\frac{\partial^2}{\partial s^2}\left(\Omega + \frac{v}{R}\right) - \frac{EI_x}{R}\left(\frac{\Omega}{R} - \frac{\partial^2 v}{\partial s^2}\right) = \rho I_{zz}\frac{\partial^2 \Omega}{\partial t^2}. \tag{6.5}$$

Equations (6.1)-(6.5) that express out-of-plane vibrations of curved beams can be simplified to vibrations of straight beams by letting $R \to \infty$. The circumferential coordinate s is changed to z for a straight linear coordinate along the beam. Thus, for a straight beam, Equations (6.1)-(6.5) become:

$$M_2 = -EI_x\frac{\partial^2 v}{\partial z^2}, \tag{6.6}$$

$$M_T = GJ\frac{\partial \Omega}{\partial z}, \tag{6.7}$$

$$P = \frac{\partial M_2}{\partial z}, \tag{6.8}$$

$$-EI_x\frac{\partial^4 v}{\partial z^4} = \rho A\frac{\partial^2 v}{\partial t^2}, \tag{6.9}$$

$$GJ\frac{\partial^2 \Omega}{\partial z^2} = \rho I_{zz}\frac{\partial^2 \Omega}{\partial t^2}. \tag{6.10}$$

In these equations, the out-of-plane flexural and angular displacements are uncoupled – in contrast to curved beam vibration.

The axial and angular displacements in straight and curved beams, satisfying Equations (6.4), (6.5), (6.9) and (6.10) are assumed to be time-harmonic waves. Using the same approach as presented in Chapter 2 concerning radial and tangential dis-

placements, it can be found that the characteristic equation for the wavenumber for out-of-plane vibrations in a curved beam is:

$$\Big(EI_xR^4GJ\Big)k_{\mathrm{o}}^6 - EI_xR^2\Big(R^2\rho\omega^2I_{zz} + 2GJ\Big)k_{\mathrm{o}}^4 \\ - GJ\Big(\rho R^2\omega^2\Big(AR^2 + I_{zz}\Big) - EI_x\Big)k_{\mathrm{o}}^2 + A\rho R^2\omega^2\Big(\rho R^2\omega^2I_{zz} - EI_x\Big) = 0. \tag{6.11}$$

In contrast, the dispersion relation for the straight beam case can be factorised and written as:

$$\left(k_{\mathrm{o}}^4 - \left(\omega\sqrt{\frac{\rho A}{EI_x}}\right)^2\right)\left(k_{\mathrm{o}}^2 - \left(\omega\sqrt{\frac{\rho I_{zz}}{GJ}}\right)^2\right) = 0. \tag{6.12}$$

The subscript "o" relates to out-of-plane vibrations. Similar to the characteristic equation (Equation (2.8)) for the wavenumber for in-plane vibration, Equation (6.11) has six complex roots $\pm k_{\mathrm{o}i}$ ($i = 1, 2, 3$) at any given frequency. Similar rules are applied to choose the appropriate wavenumbers among the six complex roots of Equation (6.11): $\mathrm{Im}(k_{\mathrm{o}i}) \leq 0$ and $\mathrm{Re}(k_{\mathrm{o}i}) > 0$. Straight and curved beams have a common limit for the wavenumbers as $R \to \infty$ or $\omega \to \infty$. Similar to in-plane vibrations, this provides a convenient way to characterise the resulting wavenumbers, *i.e.*

- The root which tends to k_T when $R \to \infty$ or $\omega \to \infty$, is related to predominantly torsional waves and is denoted here by $k_{\mathrm{o}1}$. k_T is the wavenumber of torsional waves in a straight beam and is defined from Equation (6.12) as:

$$k_T = \omega\sqrt{\frac{\rho I_{zz}}{GJ}}. \tag{6.13}$$

- The roots which tend to k_{Fx} and $-\mathrm{i}k_{Fx}$ when $R \to \infty$ or $\omega \to \infty$ are related to predominantly out-of-plane propagating far-field flexural waves and decaying near-field waves respectively. These roots will be denoted here by $k_{\mathrm{o}2}$ and $k_{\mathrm{o}3}$ respectively. k_{Fx} is the wavenumber of out-of-plane flexural waves in a

straight beam and is defined from Equation (6.12) as:

$$k_{Fx} = \sqrt{\omega\sqrt{\frac{\rho A}{EI_x}}} \tag{6.14}$$

In any curved beam section, the axial and angular displacements can be expressed as a sum of waves propagating and decaying in the right and left directions, *i.e.*:

$$v = \sum_{i=1}^{3} \left(\hat{v}_{\mathrm{o}i}^{+}\, e^{-\mathrm{i}k_{\mathrm{o}i}s} + \hat{v}_{\mathrm{o}i}^{-}\, e^{\mathrm{i}k_{\mathrm{o}i}(s-L)} \right) e^{\mathrm{i}\omega t}, \tag{6.15a}$$

$$\Omega = \sum_{i=1}^{3} \left(\hat{o}_{\mathrm{o}i}^{+}\, e^{-\mathrm{i}k_{\mathrm{o}i}s} + \hat{o}_{\mathrm{o}i}^{-}\, e^{\mathrm{i}k_{\mathrm{o}i}(s-L)} \right) e^{\mathrm{i}\omega t}, \tag{6.15b}$$

In these expressions, $\hat{v}_{\mathrm{o}i}^{+}$ and $\hat{o}_{\mathrm{o}i}^{+}$ are the complex amplitudes of the out-of-plane flexural and torsional waves travelling in the positive s direction; while $\hat{v}_{\mathrm{o}i}^{-}$ and $\hat{o}_{\mathrm{o}i}^{-}$ are the complex amplitudes of the out-of-plane flexural and torsional waves travelling in the negative s direction. As in Chapter 2, the waves travelling in the positive s direction ($\hat{v}_{\mathrm{o}i}^{+}$, $\hat{o}_{\mathrm{o}i}^{+}$) originate from the location $s = 0$, whilst the waves travelling in the negative s direction ($\hat{v}_{\mathrm{o}i}^{-}$, $\hat{o}_{\mathrm{o}i}^{-}$) originate from the location $s = L$. In applications, it is convenient to choose $s = 0$ and $s = L$ to be located at either end of the curved beam section.

The coupling between radial and tangential displacements for in-plane vibration was expressed with the characteristic ratio X_i in Chapter 2, Equation (2.12). For out-of-plane vibration, a similar coupling exists between axial and torsional displacement, and it is expressed by the ratio $X_{\mathrm{o}i}$ such that:

$$X_{\mathrm{o}i} = \frac{\hat{v}_{\mathrm{o}i}^{+}}{\hat{o}_{\mathrm{o}i}^{+}} = \frac{\hat{v}_{\mathrm{o}i}^{-}}{\hat{o}_{\mathrm{o}i}^{-}} = \frac{k_{\mathrm{o}i}R^2\Big(GJ + EI_x)}{\rho R^2 A\omega^2 - \Big(EI_x R^2 k_{\mathrm{o}i}^4 + GJk_{\mathrm{o}i}^2\Big)}. \tag{6.16}$$

The ratio $X_{\mathrm{o}i}$ relates to the ratio of the out-of-plane flexural to torsional wave amplitudes of waves travelling in the same direction that have the same wavenumber. In the same way as for in-plane vibration, non-zero values of $X_{\mathrm{o}i}$ indicate that an out-of-plane flexural wave of magnitude $\hat{v}_{\mathrm{o}i}^{+}$ ($\hat{v}_{\mathrm{o}i}^{-}$ respectively) is accompanied by a torsional wave of magnitude $X_{\mathrm{o}i}\hat{o}_{\mathrm{o}i}^{+}$ ($X_{\mathrm{o}i}\hat{o}_{\mathrm{o}i}^{-}$ respectively). Thus for the wave ampli-

tude pair ($\hat{v}_{oi}^{\pm}$, $\hat{o}_{oi}^{\pm}$) it is only necessary to determine one of the amplitudes, as the other is known implicitly from knowledge of the ratio X_{oi}. From the twelve wave amplitudes [$\hat{v}_{oi}^{\pm}$, $\hat{o}_{oi}^{\pm}$] modelling out-of-plane motion in Equations (6.15), only six are independent. As the amplitudes with subscript $i = 1$ are related to waves which are predominantly torsional, and those with subscript $i = 2$ and $i = 3$ to waves which are predominantly out-of-plane flexural (propagating and decaying respectively), the six wave amplitudes taken as primary unknowns for out-of-plane vibration are $\left[\hat{o}_1^+, \hat{v}_2^+, \hat{v}_3^+, \hat{o}_1^-, \hat{v}_2^-, \hat{v}_3^-\right]$.

In any straight beam section, the equations governing the angular Ω and out-of-plane flexural v displacements are uncoupled. The ratios expressed in Equation (6.16) become $X_{o1} = 0$ and $X_{o2} = X_{o3} = \infty$. The displacements can be described as a sum of waves travelling in the positive and negative z directions, such that [54]:

$$v = \left(\hat{v}_{o2}^+ e^{-ik_{Fx}z} + \hat{v}_{o3}^+ e^{-k_{Fx}z} + \hat{v}_{o2}^- e^{ik_{Fx}(z-L)} + \hat{v}_{o3}^- e^{k_{Fx}(z-L)}\right) e^{i\omega t}, \tag{6.17a}$$

$$\Omega = \left(\hat{o}_{o1}^+ e^{-ik_T z} + \hat{o}_{o1}^- e^{ik_T(z-L)}\right) e^{i\omega t}. \tag{6.17b}$$

In these expressions, $\hat{v}_{o2}^+$ and $\hat{v}_{o2}^-$ are the complex amplitudes of the out-of-plane flexural purely propagating waves in the positive and negative z directions respectively; $\hat{v}_{o3}^+$ and $\hat{v}_{o3}^-$ are the complex amplitudes of the out-of-plane flexural purely decaying (near field) waves in the positive and negative z directions, respectively; and, $\hat{o}_{o1}^+$ and $\hat{o}_{o1}^-$ are the complex amplitudes of the torsional waves propagating in the positive and negative z directions, respectively.

Similar to in-plane vibrations, in curved or straight beams, the axial and angular displacements are defined with six unknown wave amplitudes: three travelling in the positive direction and three in the negative direction.

6.2.2 Development of the ray tracing method for out-of-plane vibrations

The fundamentals of the ray tracing method are identical to those presented in Chapter 2. They can be summarised and extended to out-of-plane vibrations as follows.

The displacements in each component of the structure are defined as a sum of waves, see Section 6.2.1. As the waves travel from one end of a component (j) to the other, the propagating waves change phase and the decaying waves change amplitude. These effects are governed by the wavenumbers of each wave and are expressed in a diagonal matrix $\mathbf{D}$ called the dispersion matrix whose i^{th} diagonal element is defined as $D_{ii} = e^{-\mathrm{i}k_i L^{(j)}}$, where k_i is the wavenumber associated with wave i and $L^{(j)}$ is the corresponding (curved or straight) beam length. The scattering of waves at discontinuities is expressed with the matrix $\mathbf{T}$ that contains complex wave amplitude transmission/reflection coefficients, such that T_{ij} is the transmission/reflection coefficient from a wave of amplitude j to a wave of amplitude i. With six waves considered per element (torsional, out-of-plane propagating flexural and out-of-plane decaying near field waves, in each direction), the dimension of the matrices $\mathbf{T}$ and $\mathbf{D}$ is $[6n \times 6n]$, where n is the total number of elements.

If the structure is vibrating freely in an undamped mode, the ray tracing method [58] (or wave train closure principle [55]) stipulates that the wave amplitudes defining the displacement of the complete structure are the same as the wave amplitudes after the waves have performed one ray trace (*i.e.* propagated across each component and transmitted across a joint to a neighbouring element), *i.e.*:

$$\mathbf{a} = \mathbf{TDa}, \tag{6.18}$$

where $\mathbf{a}$ is a wave amplitude vector of size $6n$ that contains all the wave amplitudes considered in the system. The natural frequencies of the system can be calculated by solving:

$$|\mathbf{I} - \mathbf{TD}| = 0, \tag{6.19}$$

where $\mathbf{I}$ is the $[6n \times 6n]$ identity matrix.

The only modification when considering out-of-plane vibrations is that the overall wave amplitude vector $\mathbf{a}$ contains here amplitudes corresponding to torsional, out-of-plane flexural and out-of-plane decaying waves. It is now defined as:

$$\mathbf{a} = \left[\mathbf{u}^{(\mathrm{I})+} \quad \mathbf{u}^{(\mathrm{I})-} \quad \mathbf{u}^{(\mathrm{II})+} \quad \mathbf{u}^{(\mathrm{II})-} \quad \dots \quad \mathbf{u}^{(n)+} \quad \mathbf{u}^{(n)-}\right]^{\mathrm{T}}, \tag{6.20}$$

with

$$\mathbf{u}^{(j)\pm} = \left[\hat{o}_1^{(j)\pm} \quad \hat{v}_2^{(j)\pm} \quad \hat{v}_3^{(j)\pm}\right]. \tag{6.21}$$

Both in-plane and out-of-plane vibrations can be analysed simultaneously if the wave amplitudes defining in-plane and out-of-plane vibrations are both present in the vector $\mathbf{a}$. Consequently, the matrices $\mathbf{T}$ and $\mathbf{D}$ must also take account of the in-plane and out-of-plane propagation and scattering of waves. In this case, the dimension of the matrices becomes $[12n \times 12n]$. Solving Equation (6.19) with those particular matrices gives the natural frequencies of the system for both in-plane and out-of-plane vibrations.

6.2.3 Transmission coefficients

As seen in Section 6.2.2 or in Chapter 2, the ray tracing method requires knowledge of the transmission coefficients. They are expressed in the matrix $\mathbf{T}$ in Equations (6.18) and (6.19). In general, these transmission coefficients are calculated by considering the continuity and force equilibrium equations at each joint, with the joint being taken in isolation from the rest of the structure. It is necessary to calculate the transmission coefficients arising from each wave type impinging on a junction to all wave types in all neighbouring components. For a joint having n attached components, the force and moment equilibrium as well as displacement and slope continuity equations provide a total of $3n$ equations in terms of $3n$ unknown transmission coefficients. Solving these equations yields the transmission coefficients, which are then placed in the overall transmission matrix $\mathbf{T}$.

For common MEMS structures, such as the ring-based resonator presented extensively in the previous chapters, it is necessary to consider several discontinuities such as the transmission between a ring and an attached beam, the transmission at an abrupt change in direction (or "abrupt angle") and the reflection at boundaries. Those are studied next.

Ring/beam transmission

As the most general case, the transmission of out-of-plane vibrations between a ring and a straight beam contained in the same plane is investigated. The configuration considered is shown in Figure 6.2. As in the case of in-plane vibrations, the discontinuity is modelled as a rigid cylindrical mass. This analysis is an extension of the in-plane analysis performed in Chapter 2, Section 2.4.1.

Each set of wave amplitudes, incident or created, consists of a principal torsional wave, a principal out-of-plane flexural propagating wave, and a principal out-of-plane decaying wave:

$$\mathbf{u}_{r,\,b}^{(j)\pm} = \left[\hat{o}_1^{(j)\pm} \quad \hat{v}_2^{(j)\pm} \quad \hat{v}_3^{(j)\pm}\right]. \tag{6.22}$$

The following phenomenon appears when a wave impinges on the discontinuity. The presence of the joint ensures that part of the wave is reflected back along the same portion and the remainder is transmitted into the other portions. This partial reflection/transmission is also accompanied by mode conversion, so that the incident wave can generate out-of-plane flexural propagating, decaying and torsional wave components in each of the three portions.

The number of components considered is such that $n = 3$ (two ring portions and one beam portion). The assembly of equilibrium and continuity expressions at the joint yields a system of nine equations that can be solved simultaneously to provide the nine required transmission/reflection coefficients for each wave type. By suppressing the temporal terms in Equations (6.15) and (6.17), the axial displacements $v_r^{(\mathrm{I})}$, $v_r^{(\mathrm{II})}$ and $v_b^{(\mathrm{III})}$; the angular displacements $\Omega_r^{(\mathrm{I})}$, $\Omega_r^{(\mathrm{II})}$ and $\Omega_b^{(\mathrm{III})}$ at the ring portion (I) (left), the ring portion (II) (right) and the beam portion (III), respectively, can

be expressed in terms of wave amplitudes. The ratio $\hat{u}_j/\hat{u}_i$ of any wave amplitude over any other wave amplitude corresponds to the required transmission coefficient from an incident wave $\hat{u}_i$ to a reflected or transmitted wave $\hat{u}_j$. These ratios can be obtained by solving the following Equations (6.23)-(6.31).

Assuming that the joint is located at $s = 0$ (or $z = 0$), displacement and slope continuity for out-of-plane vibrations ensures that:

$$v_r^{(\mathrm{I})} + \frac{d_j}{2}\frac{\partial v_r^{(\mathrm{I})}}{\partial s} = v_r^{(\mathrm{II})} - \frac{d_j}{2}\frac{\partial v_r^{(\mathrm{II})}}{\partial s}, \tag{6.23}$$

$$\frac{\partial v_r^{(\mathrm{I})}}{\partial s} = \frac{\partial v_r^{(\mathrm{II})}}{\partial s}, \tag{6.24}$$

$$\Omega_r^{(\mathrm{I})} = \Omega_r^{(\mathrm{II})}, \tag{6.25}$$

$$v_r^{(\mathrm{I})} + \frac{d_j}{2}\frac{\partial v_r^{(\mathrm{I})}}{\partial s} = v_b^{(\mathrm{III})} - \frac{d_j}{2}\frac{\partial v_b^{(\mathrm{III})}}{\partial z}, \tag{6.26}$$

$$\frac{\partial v_r^{(\mathrm{I})}}{\partial s} = \frac{\partial v_b^{(\mathrm{III})}}{\partial z}\cos\alpha + \Omega_b^{(\mathrm{III})}\sin\alpha, \tag{6.27}$$

$$\Omega_r^{(\mathrm{I})} = \Omega_b^{(\mathrm{III})}\cos\alpha - \frac{\partial v_b^{(\mathrm{III})}}{\partial z}\sin\alpha, \tag{6.28}$$

where d_j is the diameter of the cylindrical rigid joint. The shear forces $P_r^{(\mathrm{I})}$, $P_r^{(\mathrm{II})}$ and $P_b^{(\mathrm{III})}$, the bending moments $M_{2_r}^{(\mathrm{I})}$, $M_{2_r}^{(\mathrm{II})}$ and $M_{2_b}^{(\mathrm{III})}$, and the twisting moments $M_{T_r}^{(\mathrm{I})}$, $M_{T_r}^{(\mathrm{II})}$ and $M_{T_b}^{(\mathrm{III})}$ of the ring portion (I) (left), the ring portion (II) (right) and the beam portion (III), respectively, evaluated at the joint at $s = 0$ (or $x = 0$) are related by the equations:

$$-P_r^{(\mathrm{I})} + P_r^{(\mathrm{II})} + P_b^{(\mathrm{III})} = m_j\frac{\partial^2}{\partial t^2}\left(v_r^{(\mathrm{I})} + \frac{d_j}{2}\frac{\partial v_r^{(\mathrm{I})}}{\partial s}\right), \tag{6.29}$$

$$\begin{aligned} -M_{2_r}^{(\mathrm{I})} + M_{2_r}^{(\mathrm{II})} + M_{2_b}^{(\mathrm{III})}\cos\alpha - M_{T_b}^{(\mathrm{III})}\sin\alpha \\ - \frac{d_j}{2}\left(P_r^{(\mathrm{I})} + P_r^{(\mathrm{II})} + P_b^{(\mathrm{III})}\right) = -I_{x_j}\frac{\partial^2}{\partial t^2}\frac{\partial v_r^{(\mathrm{I})}}{\partial s}, \end{aligned} \tag{6.30}$$

$$-M_{T_r}^{(\mathrm{I})} + M_{T_r}^{(\mathrm{II})} + M_{T_b}^{(\mathrm{III})}\cos\alpha + M_{2_b}^{(\mathrm{III})}\sin\alpha = I_{z_j}\frac{\partial^2\Omega_r^{(\mathrm{I})}}{\partial t^2}, \tag{6.31}$$

where m_j is the mass of the rigid joint, and I_{x_j} and I_{z_j} are the moments of inertia of the rigid joint along the radial (x-) and tangential (z-) axes respectively. In Figure 6.2, the forces and moments presented are those acting on the joint.

Similar to the case of in-plane vibrations, solving Equations (6.23)-(6.31) for all of the possible types of incident waves gives a $[9 \times 9]$ matrix that contains all of the required transmission coefficients for out-of-plane vibrations. This particular matrix models the scattering of waves for the ring/beam discontinuity and will be used in the assembly process of the ray tracing method.

Simplification for transmission at an abrupt change in direction

To obtain the transmission coefficients for two beams joined at an angle α without using a rigid joint mass element (see Figure 6.3), a simplification of Equations (6.23)-(6.31) can be used. Note that the angles α in Figures 6.2 and 6.3 are defined in the opposite direction. The number of components coupled together by this discontinuity is such that $n = 2$. Therefore, six equations modelling force and displacement continuity can be solved simultaneously to derive the transmission coefficients from any incident wave type to any reflected/transmitted wave type. These six equations are as follows:

$$v_b^{(\mathrm{I})} = v_b^{(\mathrm{II})}, \tag{6.32}$$

$$\frac{\partial v_b^{(\mathrm{I})}}{\partial z} = \frac{\partial v_b^{(\mathrm{II})}}{\partial z}\cos\alpha - \Omega_b^{(\mathrm{II})}\sin\alpha, \tag{6.33}$$

$$\Omega_b^{(\mathrm{I})} = \Omega_b^{(\mathrm{II})}\cos\alpha + \frac{\partial v_b^{(\mathrm{II})}}{\partial z}\sin\alpha, \tag{6.34}$$

$$P_b^{(\mathrm{I})} = P_b^{(\mathrm{II})}, \tag{6.35}$$

$$M_{2_b}^{(\mathrm{I})} = M_{2_b}^{(\mathrm{II})}\cos\alpha + M_{T_b}^{(\mathrm{II})}\sin\alpha, \tag{6.36}$$

$$M_{T_b}^{(\mathrm{I})} = M_{T_b}^{(\mathrm{II})}\cos\alpha - M_{2_b}^{(\mathrm{II})}\sin\alpha, \tag{6.37}$$

By considering an incident set of waves $\mathbf{a}_{\mathrm{incident}_{[6\times1]}} = \begin{bmatrix}\mathbf{u}_b^{(\mathrm{I})+} & \mathbf{u}_b^{(\mathrm{II})-}\end{bmatrix}^{\mathrm{T}}$ containing a torsional wave, an out-of-plane propagating flexural wave and an out-of-plane decaying wave travelling in the positive z direction of (I) and negative z direction of (II), and a transmitted/reflected set of waves $\mathbf{a}_{\mathrm{created}_{[6\times1]}} = \begin{bmatrix}\mathbf{u}_b^{(\mathrm{II})+} & \mathbf{u}_b^{(\mathrm{I})-}\end{bmatrix}^{\mathrm{T}}$, the equations that give the transmission coefficients matrix $\mathbf{T}_{\mathrm{abrupt\,angle}}$ such that

$\mathbf{a}_{\text{created}} = \mathbf{T}_{\text{abrupt angle}}\,\mathbf{a}_{\text{incident}}$ for out-of-plane vibrations can be expressed as:

$$\begin{bmatrix} 0 & -1 & -1 & 0 & 1 & 1 \\ \sin\alpha/k_{Fx} & \mathrm{i}\cos\alpha & \cos\alpha & 0 & \mathrm{i} & 1 \\ -\cos\alpha/k_{Fx} & \mathrm{i}\sin\alpha & \sin\alpha & 1/k_{Fx} & 0 & 0 \\ 0 & \mathrm{i} & -1 & 0 & \mathrm{i} & -1 \\ \delta\sin\alpha & -\cos\alpha & \cos\alpha & 0 & 1 & -1 \\ \delta\cos\alpha & \sin\alpha & -\sin\alpha & \delta & 0 & 0 \end{bmatrix} \cdot \mathbf{T}_{\text{abrupt angle}}$$
$$= \begin{bmatrix} 0 & -1 & -1 & 0 & 1 & 1 \\ 0 & \mathrm{i} & 1 & -\sin\alpha/k_{Fx} & \mathrm{i}\cos\alpha & \cos\alpha \\ -1/k_{Fx} & 0 & 0 & \cos\alpha/k_{Fx} & \mathrm{i}\sin\alpha & \sin\alpha \\ 0 & \mathrm{i} & -1 & 0 & \mathrm{i} & -1 \\ 0 & -1 & 1 & \delta\sin\alpha & \cos\alpha & -\cos\alpha \\ \delta & 0 & 0 & \delta\cos\alpha & -\sin\alpha & \sin\alpha \end{bmatrix}, \tag{6.38}$$

with $\delta = \mathrm{i}\sqrt{\dfrac{GJI_{zz}}{AEI_x}}$. From the above Equation (6.38), the matrix $\mathbf{T}_{\text{abrupt angle}}$, which contains the transmission coefficients of an abrupt angle α in straight beams for out-of-plane vibrations, can be calculated.

Wave reflection at common boundaries

For external boundaries, the number of components considered is simply $n = 1$ and the reflection coefficients are obtained by solving three equations. These equations usually model an imposed displacement, slope, or external force or torque at the boundary. For out-of-plane vibrations, if an incident set of waves with amplitudes $\mathbf{a}_{\text{incident}} = \begin{bmatrix} \hat{o}_1^+ & \hat{v}_2^+ & \hat{v}_3^+ \end{bmatrix}^{\mathrm{T}}$ impinges on a boundary, it produces a set of reflected waves $\mathbf{a}_{\text{reflected}} = \begin{bmatrix} \hat{o}_1^- & \hat{v}_2^- & \hat{v}_3^- \end{bmatrix}^{\mathrm{T}}$ such that $\mathbf{a}_{\text{reflected}} = \mathbf{T}_{\text{boundary}}\,\mathbf{a}_{\text{incident}}$. The matrices for common boundary conditions: $\mathbf{T}_{\text{clamped}}$ (for clamped boundary), $\mathbf{T}_{\text{pinned}}$ (for pinned boundary) and $\mathbf{T}_{\text{free}}$ (for free boundary) are found to be identical to those presented for in-plane vibrations (see Chapter 2, Section 2.4.3). One of the reasons for this is that these matrices are not functions of the wavenumbers or geometrical dimensions. Therefore, in-plane and out-of-plane flexural vibrations have

identical reflection coefficients. Concerning torsional vibration, its governing equations ((6.10) and (6.17b)) are similar to those of longitudinal vibrations and the constraint conditions at common boundary are identical, giving the same reflection coefficients for torsional and longitudinal waves.

6.2.4 Possible simplifications

It was shown in Chapter 3 that in-plane vibrations of a periodic structure could be modelled easily with the ray tracing method. The development presented in Section 3.2 is a general development that explains how to calculate the transmission and reflection coefficients of a chain of N sectors as a function of the transmission and reflection coefficients of one sector only. Therefore, if the coefficients of one sector account for out-of-plane vibrations, then the same method and equations (see Equations (3.10) and (3.11)) can be applied to calculate the out-of-plane transmission and reflection coefficients of the entire chain.

Thomas [86] developed a simplification for cyclically (or rotationally) symmetric structures, 360° structures that consist of N repetitive sectors, and his approach can be applied to the ray tracing method. In Chapter 3, Section 3.3, the development is explained for in-plane vibrations but similar reasoning can be applied for out-of-plane vibrations. The basic idea is that the displacements for any sector can be related to the displacements of just one particular sector by a phase angle ψ. The sectors are numbered sequentially (j) (with $j = 1, \ldots, N$), with j increasing in the positive direction of propagation.

In the context of the wave approach, the wave amplitudes $\mathbf{a}^{(j)}$ for the j^{th} sector and the wave amplitudes $\mathbf{a}^{(j+1)}$ for the $(j+1)^{\text{th}}$ sector are related as follows:

$$\mathbf{a}^{(j+1)} = e^{\mathrm{i}\psi}\mathbf{a}^{(j)}, \tag{6.39}$$

where $\psi = 2\pi\kappa/N$ and κ is the cyclic mode number, see Chapter 3. This equation presents a phase change of ψ (or $-\psi$) between one end of a sector and its other end. κ can take the following values [86]: $\kappa = 0, 1, \ldots, N/2$ (N even) or $\kappa =$

0, 1, ..., $(N-1)/2$ (N odd). Each value corresponds to a κ-fold symmetric mode and each mode must be examined independently. For out-of-plane vibrations, the wave amplitude vector $\mathbf{a}$ contains a torsional wave, an out-of-plane flexural wave and an out-of-plane decaying wave.

In the ray tracing method, only a principal sector is modelled. The phase change ψ is represented as a particular "transmission coefficient" from one end of the sector to the other, see Section 3.3.2 in Chapter 3. If the complex displacement at the left end of a sector is v, then the displacement at its right end will be $v\,e^{\mathrm{i}\psi}$. Correspondingly, if its displacement is v at its right end, then it will be $v\,e^{-\mathrm{i}\psi}$ at its left end. Thus, the waves incident on one end and the waves transmitted to the other end will have an amplitude ratio of $e^{-\mathrm{i}\psi}$ (or $e^{\mathrm{i}\psi}$). As explained in Chapter 3, this phenomenon can be expressed directly by the $\mathbf{D}$ matrix; such that with a set of wave amplitude $\mathbf{a} = \begin{bmatrix}\mathbf{u}^{(l)-} & \mathbf{u}^{(r)+}\end{bmatrix}^{\mathrm{T}}$, $\mathbf{D}$ becomes:

$$\mathbf{D} = \begin{bmatrix} \boldsymbol{\Delta}_{L_0}\boldsymbol{\Upsilon}^{+} & \mathbf{0} \\ \mathbf{0} & \boldsymbol{\Delta}_{L_0}\boldsymbol{\Upsilon}^{-} \end{bmatrix}, \tag{6.40}$$

where

$$\boldsymbol{\Delta}_{L_0}\boldsymbol{\Upsilon}^{\pm} = \begin{bmatrix} e^{\mathrm{i}\left(\pm\frac{2\pi}{N}\kappa - k_{\mathrm{o}1}L_0\right)} & 0 & 0 \\ 0 & e^{\mathrm{i}\left(\pm\frac{2\pi}{N}\kappa - k_{\mathrm{o}2}L_0\right)} & 0 \\ 0 & 0 & e^{\mathrm{i}\left(\pm\frac{2\pi}{N}\kappa - k_{\mathrm{o}3}L_0\right)} \end{bmatrix}, \tag{6.41}$$

and L_0 represents the distance travelled along the waveguide from one sector to its neighbour. For instance, if the cyclic symmetry simplification is applied to the ring-based rate sensor, L_0 is the distance along the ring between two attached legs ($L_0 = \pi R/4$).

To obtain the natural frequencies of the entire structure, Equation (6.19) must be solved. For periodic or cyclically symmetric structures, the modelling and knowledge of transmission/reflection coefficients of a single sector are most important.

In summary, out-of-plane vibration analysis using the wave approach is similar to

that used for in-plane vibration. Once the governing equations, the appropriate wavenumbers and the coupling between angular and axial displacements have been defined, the approach presented in Chapter 2 can be applied to out-of-plane vibrations. The transmission coefficients rely on different equations but their derivation depends on similar principles. The simplification for periodic or cyclically symmetric structures, developed in a general way in Chapter 3, can also be extended to analyse out-of-plane vibrations. However, a direct extension of the in-plane support model presented in Chapter 4 to cope with out-of-plane vibration is not possible as the fundamental equations governing the support assumed in-plane motion and plane stresses only.

6.3 Modelling the support losses for out-of-plane vibrations

6.3.1 Introduction

The different approaches presented in Chapter 4, namely the analytical model, and the use of perfectly matched layers (PML) or infinite elements within FE analyses, were applied to in-plane vibration only and assumed the problem to be in a plane stress configuration. In all previous studies, it was assumed that the support can be modelled as a thin plate with thickness equal to the (axial) thickness of the resonator. Knowing that the stiffness of the support in its plane is much greater than along an axis normal to its plane, it can be understood that during in-plane motion the plate constrains more the vibration of the resonator than for out-of-plane motion. It is therefore expected that the out-of-plane vibrations may induce greater support losses, and modelling these is of great interest for the design of more accurate and efficient multi-axis resonators.

When calculating support losses, knowledge of power flow from the resonator to the support is fundamental. This power flow is a direct function of the displacement of the attachment point induced by the vibrational motion of the resonator, see

Chapter 4. The admittance that links velocity and applied forces for out-of-plane vibrations, at the edge of a semi-infinite plate was first formulated by Eichler [108]. The harmonic response of the plate was analysed using Fourier transforms, which lead to explicit expressions for the plate response in integral forms. Kauffmann [109] extended Eichler's work and derived closed form integral expressions for the input power delivered by arbitrary force and moment distributions along the edge. He made a number of conjectures that were checked later by Su and Moorhouse [110]. Su and Moorhouse also solved the integrals given in [109] and offered closed form expressions that can be easily evaluated numerically with a quadrature integration method. This approach was recently used in [44, 45] to model attachment losses of a resonator in a support of finite thickness. The same method will be applied to calculate the support losses of a ring-based resonator. The main assumptions of the support model are that it must be semi-infinite in length and that the support thickness is supposed to be much smaller than the wavelength of the propagative transverse waves. It is worth mentioning at this stage that the semi-infinite thin plate model may not be realistic of actual hardware. Nevertheless, it is the best available starting point to illustrate the procedure of support loss modelling. This will be discussed in more details later. The basics of this approach are explained in Sections 6.3.2 and 6.3.3, and calculated results for the support losses for an example structure are presented in Section 6.4.2.

6.3.2 Admittance of the support

Consider a thin elastic plate of constant thickness h_p, illustrated in Figure 6.4(a), vibrating freely at an circular frequency ω. The transverse (out-of-plane) motion v satisfies the following differential equation [74]:

$$D\left(\frac{\partial^4 v}{\partial x^4} + 2\frac{\partial^4 v}{\partial x^2 \partial z^2} + \frac{\partial^4 v}{\partial z^4}\right) - \rho h_p \omega^2 v = 0, \tag{6.42}$$

where ρ is the mass density of the plate and D is its bending stiffness such that:

$$D = \frac{E h_p^3}{12(1-\nu^2)}, \tag{6.43}$$

with ν the material Poisson's ratio. If the plate is excited along its $z =$ constant edge by an externally applied bending moment per unit length $m(x)$ and an externally applied force per unit length $f(x)$, the boundary conditions can be expressed as [74, 108]:

$$-D\left(\frac{\partial^2 v}{\partial z^2} + \nu\frac{\partial^2 v}{\partial x^2}\right) = m(x), \tag{6.44a}$$

$$-D\frac{\partial}{\partial z}\left[\frac{\partial^2 v}{\partial z^2} + (2-\nu)\frac{\partial^2 v}{\partial x^2}\right] = f(x). \tag{6.44b}$$

Let us consider that the plate is excited by a transverse force P, a twisting moment M_T normal to its edge and a bending moment M_2 tangential to its edge, induced from the vibrations of the resonator, see Figure 6.4(a). It is assumed that the coupling between resonator and support takes place at a single point only, *i.e.* the point of application of these forces and moments. Also, the support is considered to be semi-infinite with excitation forces on a single point of its edge only. There are no boundaries that can reflect vibrations back to the support edge. The point mobilities from the plate at $x = 0$ and $z = 0$ (point of attachment between the resonator and support) are of interest and can be obtained by setting $f(x) = P\delta(x) - M_T\delta'(x)$ and $m(x) = M_2\delta(x)$, where δ is the Dirac function. Equations (6.44) can be solved at $x = 0$ and $z = 0$, and the following expression that links the normal angular velocity $\dot{\Omega}_n$, the tangential angular velocity $\dot{\Omega}_T$ and the transverse linear velocity $\dot{V}_y$ of the attachment point to the applied loads, can be found [110]:

$$\begin{bmatrix}\dot{\Omega}_n\\ \dot{\Omega}_t\\ \dot{V}_y\end{bmatrix} = \mathrm{i}\omega\begin{bmatrix}\Omega\\ -\partial v/\partial z\\ v\end{bmatrix} = \mathbf{Y}\begin{bmatrix}M_T\\ M_2\\ P\end{bmatrix}. \tag{6.45}$$

$\mathbf{Y}$ is the point mobility matrix and is expressed as:

$$\mathbf{Y} = \frac{1}{\sqrt{\rho h_p D}}\begin{bmatrix}y_{11}k^2 & 0 & 0\\ 0 & y_{22}k^2 & y_{23}k\\ 0 & y_{32}k & y_{33}\end{bmatrix}, \tag{6.46}$$

where k is the wavenumber of transverse motion in a plate defined as:

$$k = \sqrt{\omega\sqrt{\frac{\rho h_p}{D}}}. \tag{6.47}$$

The elements of the matrix $\mathbf{Y}$ are given as closed-form integrals in [110]. For the derivation of support losses, or power radiated into the plate, only the imaginary part of the displacements are needed (similar to the case of support loss for in-plane vibration studied in Chapter 4, Section 4.2 or in Appendix A). Therefore, only the real parts of the velocities are required and only the real parts of the components of $\mathbf{Y}$ need to be calculated. Using the expressions given in [110] and for $\nu = 0.28$, one can find the coefficients:

$$\mathrm{Re}(y_{11}) = \mathrm{Re}(y_{22}) = 0.22172 \tag{6.48}$$

$$\mathrm{Re}(y_{23}) = \mathrm{Re}(y_{32}) = -0.28546, \tag{6.49}$$

$$\mathrm{Re}(y_{33}) = 0.45735. \tag{6.50}$$

Note that Judge *et al.* [45] used the corresponding numerical values of these coefficients for $\nu = 0.3$, which were calculated in [110].

Equation (6.45) will be used to calculated the power flow into the support. This is considered in Section 6.3.3.

6.3.3 Power flow and support loss

Similar to the case of support loss for in-plane vibrations studied in Chapter 4, Section 4.2, the Q-factor can be defined as:

$$Q = 2\pi\frac{W}{\Delta W}, \tag{6.51}$$

where W is the total energy stored by the resonator and ΔW is the energy lost per cycle. ΔW is linked to the power radiated in the support by:

$$\Delta W = \frac{2\pi}{\omega}\Pi, \tag{6.52}$$

where Π is the average power transmitted to the support. It is assumed that the support is large enough compared to the resonator dimensions such that all the energy entering the support is lost and does not come back into the resonator. The power flow is a function of the forces linking the resonator with its support and is defined as (see Chapter 4, Equation (4.36)):

$$\Pi = \frac{1}{2}\,\mathrm{Re}\left(\mathrm{Force}\cdot\mathrm{Velocity}^{*}\right), \tag{6.53}$$

where Re is the real part and * denotes the complex conjugate. In Equation (6.53) the forces are multiplied by linear velocities, while the moments are multiplied by angular velocities, giving consistent units for power. Re-arranging Equations (6.51) and (6.52) gives:

$$Q = \frac{\omega W}{\Pi}. \tag{6.54}$$

From Equation (6.54), the support losses can be calculated once the total energy stored and the power flow are known. The derivation of those is considered next.

The resonator is modelled using a wave approach assuming that its attachment to its support is clamped. The ray tracing method, applied to out-of-plane vibrations, see Section 6.2, is used to calculate the natural frequencies, mode shapes, and forces and moments at the clamped end. From the mode shapes, the total energy stored W can be derived. W is the sum of the kinetic energies of each element composing the entire structure. For instance, in a straight beam of length L, illustrated in Figure 6.4(b), the kinetic energy created by out-of-plane flexure and torsion is defined as:

$$W_{\mathrm{beam}} = \frac{\rho}{2}\left(I_{zz}\int_0^L\left(\frac{\partial\Omega}{\partial t}\right)^2\mathrm{d}z + bh\int_0^L\left(\frac{\partial v}{\partial t}\right)^2\mathrm{d}z\right). \tag{6.55}$$

The power radiated into the plate can be found using Equations (6.45) and (6.53). The powers radiated Π_P due to the shear force P, Π_{M_T} due to the twisting moment M_T, and Π_{M_2} due to the bending moment M_2, when each load is taken in isolation,

are found to be:

$$\Pi_P = \sqrt{3\left(1-\nu^2\right)} y_{33} \frac{P^2}{h_p^2 \sqrt{E\rho}}, \tag{6.56}$$

$$\Pi_{M_T} = 6\left(1-\nu^2\right) y_{11} \frac{\omega M_T^2}{h_p^3 E}, \tag{6.57}$$

$$\Pi_{M_2} = 6\left(1-\nu^2\right) y_{22} \frac{\omega M_2^2}{h_p^3 E}. \tag{6.58}$$

When both bending moment M_2 and shear force P are present, the off-diagonal terms of $\mathbf{Y}$ result in an additional contribution such that the total power Π_{P+M_2} from flexural vibration is:

$$\Pi_{P+M_2} = \Pi_P + \Pi_{M_2} + \left(12\left(1-\nu^2\right)\right)^{3/4} y_{23} \frac{\sqrt{\omega} M_2 P}{\rho^{1/4} h_p^{5/2} E^{3/4}} \tag{6.59}$$

For in-plane vibrations, it was shown that the contribution of the bending moment to the support loss is negligible compared to the influence of the shear force, see Appendix A. However, for out-of-plane vibrations, the cross terms can not be neglected as for a sufficiently thin plate, the contribution to power flow from all three terms in Equation (6.59) are of similar order [45].

Substituting the values calculated by Equations (6.55) (or similar for curved beam elements) and (6.56)-(6.59) into Equation (6.54), the Q-factor can be derived for any resonator geometry. The predictions of support losses found, using this method for a cantilever beam and for a ring-based resonator, are presented in Section 6.4.2.

6.4 Applications

The ray tracing method presented in Section 6.2 is applied to different structures to obtain natural frequencies and mode shapes in the following Section 6.4.1. From this wave approach and the analysis developed in Section 6.3, support losses for out-of-plane vibrations can be calculated. The cases of a cantilever beam and a ring-based resonator are studied in Section 6.4.2.

6.4.1 Natural frequencies and mode shapes

Free response of a perfect ring

As for in-plane vibrations, it is straightforward to obtain an analytical expression for the out-of-plane natural frequencies of a perfect ring using the ray tracing method. In Equation (6.19), six wave amplitudes are considered (predominantly torsional wave, predominantly flexural wave and predominantly decaying wave, travelling in each direction). The transmission matrix $\mathbf{T}$ is set equal to the identity matrix as waves are free to travel around the ring without interruption, and the diagonal dispersion matrix $\mathbf{D}$ contains terms $e^{-\mathrm{i}2\pi R k_{\mathrm{o}i}}$ $(i = 1, 2, 3)$. Solving Equation (6.19) analytically gives wavenumber solutions of the form $k_{\mathrm{o}n} = \dfrac{n}{R}$, with $n = 0, 1, \ldots$. By substituting the $k_{\mathrm{o}n}$ values into the dispersion relation (6.11) and solving it, it can be shown that the natural frequencies for out-of-plane vibration are given by;

$$\omega_n^{\pm} = \sqrt{\frac{\Phi(n)}{2\rho I_{zz} A R^4}\left(1 \pm \sqrt{1 - \frac{\Psi(n)}{\left(\Phi(n)\right)^2}}\right)}, \tag{6.60}$$

with:

$$\Phi(n) = EI_x I_{zz} n^4 + GJ\left(I_{zz} + AR^2\right) n^2 + EI_x AR^2, \tag{6.61}$$

$$\Psi(n) = 4EI_x I_{zz} GJAR^2 n^2 \left(n^2 - 1\right)^2. \tag{6.62}$$

For each value of n, there are two natural frequencies. At ω_n^+ frequencies, the ring is essentially vibrating in torsion, analogous to the pure torsional vibration of a straight beam. At the ω_n^- frequencies, axial deflections dominate, analogous to the out-of-plane bending vibration in a straight beam. With the assumption that the radial and axial thicknesses of the ring are much smaller than the radius of the centreline, Equation (6.60) can be simplified to the standard expressions for

torsional and out-of-plane flexural natural frequencies in a ring:

$$\omega_n^+ = \omega_n^{\text{torsional}} = \sqrt{\frac{EI_x + GJn^2}{I_{zz}\rho R^2}}, \tag{6.63}$$

$$\omega_n^- = \omega_n^{\text{flexural}} = \sqrt{\frac{EI_x n^2 \left(n^2-1\right)^2}{\rho A R^4 \left(\frac{EI_x}{GJ} + n^2\right)}}. \tag{6.64}$$

For a circular cross-section, these expressions can be further simplified using $J = I_{zz} = 2I_x$ to obtain the standard expressions for torsional and flexural natural frequencies in rings with a circular cross-section [9, 75, 99].

Ring-based resonator

This section presents results for the out-of-plane natural frequencies and mode shapes of a ring-based resonator consisting of a ring supported on eight legs, as studied in the previous chapters. The approach used here is the same as that used in Chapter 3, except that out-of-plane vibrations are considered instead.

The ring-based resonator is modelled using the cyclic symmetry simplification. Only a single leg (three beam portions) is modelled. The ring is taken into account using the analysis presented in Section 6.2.4, *i.e.* waves impinging and leaving the discontinuity ring/leg are considered. It is assumed that the leg and ring are connected at a single point (only the centreline is modelled). The transmission coefficients for the ring/leg joint are calculated using the analyses presented in Section 6.2.3. The cross-sections of the ring and legs are supposed to be uniform, and the material also shows uniform distribution properties. These imply that in-plane and out-of-plane modes of the resonator are uncoupled and can be analysed separately. There is no interaction between the modes and the ray tracing method is here used to study out-of-plane motion only.

The out-of-plane motion of the resonator implies a rotation of the cross-section. Structures with non-circular cross-section will generally warp under torsion. To describe the relationship between twisting moment and rotation of the cross-section

(which is rectangular), the torsional constant J is required. This constant is calculated using the expression [65, 111]:

$$J = \frac{b^3 h}{3}\left[1 - \frac{192}{\pi^5}\frac{b}{h}\sum_{i=1,3,5,\ldots}^{\infty}\frac{1}{i^5}\tanh\left(i\pi\frac{h}{b}\right)\right], \tag{6.65}$$

where b and h ($h \geq b$) are the dimensions of the cross-section. The rotation of the cross-section predicted using the torsional constant is more accurate when the dimensions of the cross-section are close to being circular or square [101].

The ring-based resonator with original dimensions (see Figure 3.8(b)) is first analysed. Different methods are considered: the ray tracing approach, and FE models using two-dimensional Euler/Bernoulli beam elements or two-dimensional Timoshenko beam elements. The calculated frequencies are presented in Table 6.1. The mode shapes obtained with the ray tracing method for the lowest natural frequency with $\kappa = 0$, 1, 2, 3 and 4 are shown in Figures 6.5, 6.6(a) and 6.7(a). As for in-plane vibrations, the FE model meshed with Euler/Bernoulli beam elements gives excellent agreement for the natural frequencies (up to five significant figures) with the ray tracing method. With Timoshenko elements, the percentage differences, mainly due to the shear deformation being neglected in the ray tracing approach, are less than 0.4%. As the torsion of a rectangular cross-section is more difficult to predict than circular cross-section, another model has been developed. In this second model, the ring and legs have circular cross-sections. The other dimensions and material properties do not change. Again, the natural frequencies are calculated using the ray tracing method, a FE model with two-dimensional Euler/Bernoulli beam elements and another FE model with two-dimensional Timoshenko beam elements. Results are presented in Table 6.2. The percentage differences on the natural frequencies between the FE model using Timoshenko elements and the ray tracing model are slightly smaller than the ones obtained in the first analysis, with a maximum difference less than 0.25%. The most plausible reason is certainly that the analytical model for torsion of beam/ring structures with circular cross-section is more exact than the one for rectangular cross-section where warping occurs. In any case, the mode shapes obtained using the ray tracing method were similar to those given by the FE analyses.

In a practical situation, the angles that connect the straight beam elements in the legs are rounded, see Figure 1.2 in Chapter 1. So far in this thesis, it was assumed for simplicity that the beams were connected at an abrupt change in direction within the legs. A more realistic analysis is therefore performed using a more detailed finite element model. In the new FE model, a more accurate representation is used. There are curved segments connecting each straight beam component in the legs, and each attachment between the legs and the ring is also filleted to avoid stress concentrations. Also, instead of two-dimensional beam elements with two or three nodes, the structure is now meshed with twenty-noded three-dimensional brick elements. Results for the in-plane and out-of-plane natural frequencies for the 2θ and 3θ modes are shown in Table 6.3. The 2θ mode, 3θ mode respectively, corresponds to the lowest mode with $\kappa = 2$, $\kappa = 3$ respectively. They are the modes used in practical applications and are of particular interest. The out-of-plane mode shape of the 2θ and 3θ modes obtained using this FE model and the ray tracing method are presented in Figures 6.6 and 6.7. It can be seen that mode shapes obtained using the two methods are in good agreement concerning the ring vibrations. Small differences occur for the deformation of the legs. In-plane mode shapes of the ring-based resonator were illustrated in Chapter 3, Figure 3.9.

The results for the natural frequencies, comparing the ray tracing method and the realistic FE model, show good agreement with differences less than 4%. Wong [2] realised the same kind of study and presented the differences obtained between his model and a comparable FE analysis. These differences are also shown in Table 6.3. The resonator studied in [2] did not have exactly the same dimensions and material properties, but they were similar. It is especially clear that for out-of-plane vibrations, the ray tracing method is a significantly more accurate analytical/numerical model than the one developed by Wong. He used Rayleigh's quotients and an energy approach to derive an analytical model for out-of-plane vibrations of a ring-based resonator. It was an extension of the work carried out in [11] where in-plane vibrations were studied. The leg model used to estimate the out-of-plane strain energy and kinetic energy is based on the assumption that the displacement of each leg at the point of attachment to the ring is identical to that of a free ring. He also assumed that the presence of the legs does not significantly affect the mode shape

of the ring. The strain energy is calculated based on the static bending moment in the legs due to the displacement of the ring while the kinetic energy of the leg is calculated based on the static displacement shape of the leg. As can be seen in Table 6.3, his model was able to predict in-plane natural frequencies with good levels of agreement when compared against FE results. However, the agreement between out-of-plane natural frequencies predicted by FE models and those calculated analytically with its energy approach is not as good. Furthermore his assumptions are better for low modes of vibration (2θ modes) for which the legs of the resonator do not flex severely. In contrast, the ray tracing method is an exact solution, based only on the assumption that ring and leg can be modelled as a one-dimensional waveguide, and shows much better agreement with the FE model.

However, small differences still occur because the wave approach presented here neglects shear deformation and rotary inertia effects. Also, in the ray tracing method, it is assumed that the beams are connected at abrupt angle within the legs and that each leg is connected at a single point with the ring. This is expected to have only a little influence on the natural frequencies, but it may have a stronger influence on the mode shapes, and especially on the leg deformation.

6.4.2 Support loss

The method presented in Section 6.3 is applied to predict support losses for different systems. A cantilever beam resonator is studied first and then results for the support losses induced by out-of-plane vibration of a ring-based resonator are presented.

Cantilever beam

Consider a cantilever beam of length L, cross-section area $bh = A$ and flexural rigidity EI_x, that vibrates in an out-of-plane flexural motion, see Figure 6.4(b). The beam is clamped at $z = 0$ and free at $z = L$. The n^{th} mode shape can be

expressed as [65]:

$$v(z) = (\cos k_n z - \cosh k_n z) - \beta_n (\sin k_n z - \sinh k_n z), \tag{6.66}$$

where k_n is determined from $\cosh k_n L \cos k_n L = -1$ and

$$\beta_n = \frac{\cos k_n L + \cosh k_n L}{\sin k_n L + \sinh k_n L}. \tag{6.67}$$

Values of k_n are well known and can be found in any vibration textbook, such as [17, 65, 75]. For indication, $k_n L = (1.8751,\ 4.6941,\ \ldots)$ and k_n is related to the resonator frequency by $\omega_n = k_n^2 \sqrt{EI_x/\rho A}$. Substituting the mode shape definition (6.66) into Equations (6.6) and (6.8), and for $z = 0$, one gets the bending moment and shear force at the clamped end:

$$M_{2_n} = 2EI_x k_n^2, \tag{6.68}$$

$$P_n = 2EI_x \beta_n k_n^3. \tag{6.69}$$

Substituting Equation (6.66) into Equation (6.55) gives the kinetic energy W_n created by flexural vibration of the beam in its n^{th} mode such that:

$$W_n = \frac{1}{2} \rho A L \omega_n^2. \tag{6.70}$$

The power radiated into the support by flexural vibration of a cantilever beam is calculated by substituting Equations (6.68) and (6.69) into Equation (6.59). The Q-factor is then derived using Equation (6.70) in Equation (6.54). The quality factor Q_n for the n^{th} mode is found to be such that:

$$\frac{1}{Q_n} = \frac{b}{L} \left[\alpha_P \left(\frac{h}{h_p} \right)^2 + \alpha_{P+M_2} \left(\frac{h}{h_p} \right)^{5/2} + \alpha_{M_2} \left(\frac{h}{h_p} \right)^3 \right], \tag{6.71}$$

where α_P, α_{P+M_2} and α_{M_2} are functions of ν and are defined as:

$$\alpha_P = 4\sqrt{1-\nu^2}\beta_n^2\, y_{33}, \tag{6.72}$$

$$\alpha_{P+M_2} = 8\left(1-\nu^2\right)^{3/4}\beta_n\, y_{23}, \tag{6.73}$$

$$\alpha_{M_2} = 4\left(1-\nu^2\right) y_{22}. \tag{6.74}$$

The values of y_{22}, y_{23} and y_{33} were given in Section 6.3.2 for $\nu = 0.28$; these can be re-calculated for any ν-value using the expressions derived in [110]. In Equation (6.71), the first term is due only to the shear force P at the cantilever attachment, the third term is due only to the bending moment M_2, and the second term arises from the off-diagonal elements of the $\mathbf{Y}$ matrix. These coefficients can be calculated for any value of ν and mode number n. For the fundamental flexural mode of a cantilever beam ($n = 1$), and for $\nu = 0.28$, Equations (6.72)-(6.74) give: $\alpha_p = 0.946$, $\alpha_{P+M_2} = -1.577$ and $\alpha_{M_2} = 0.817$.

The coefficients α_p, α_{P+M_2} and α_{M_2} named respectively A_1, A_2 and A_3 in [45] were given for $\nu = 0.3$, such that: $A_1 = 0.95$, $A_2 = -0.65$ and $A_3 = 0.24$. However, there seems to be a mistake in the numerical values of A_2 and A_3 calculated in [45] as they do not correspond to Equations (6.73) and (6.74) which give $\alpha_{P+M_2} = -1.59$ and $\alpha_{M_2} = 0.79$ for $\nu = 0.3$. No explanation has been found on how the coefficients from [45] are different, even though they were derived from equations similar to Equations (6.66)-(6.71).

Q-factors for the fundamental out-of-plane flexural mode of vibration of a cantilever beam are calculated for beams with varying dimensions. The results can be obtained either using the analytical expression (6.71), or with a more numerical method that involves the ray tracing approach to model beam vibrations and Equations (6.54), (6.55) and (6.59) to calculate Q. As expected, and illustrated in Table 6.4, both methods agree very well as the wave approach is based on exact functions. The ratio length/width (L/b) of the beam and the ratio support thickness over resonator thickness (h_p/h) are varied. Results for Q are illustrated for $\nu = 0.28$ in Figure 6.8 as a function of L/b. One can see that the Q-factor is linearly proportional to the ratio L/b, as predicted in [41]. Also, it is important to

remark that Q is highly dependent of the support thickness. If the support becomes thicker, the Q factor increases rapidly as the support is less flexible with regards to the out-of-plane vibrations. When the flexibility of the support increases, more energy is lost by propagation of vibration, and the Q-factor decreases.

In-plane vibrations of the same cantilever beam structure were studied in Chapter 4. For in-plane vibration, the support was modelled as a thin plate with equal thickness to the resonator thickness and it was found, see Figure 4.7, that the Q-factors vary in a cubic form (as predicted in [41, 42]) approximately between 600 and 30 000 for the same L/b range ($6.7 < L/b < 26.7$). Here, when out-of-plane vibrations are considered and with $h_p/h = 1$, Q-factors vary linearly between approximately 35 and 150. One can see that the losses by propagation of in-plane vibrations into a thin plate are much smaller than the losses by propagation of out-of-plane vibrations.

Ring-based resonator

The free out-of-plane vibration analysis of a ring-based resonator was performed in Section 6.4.1. From this analysis, natural frequencies and mode shapes were obtained. To calculate the support losses using the procedure explained in Section 6.3.3, the kinetic energy, and the forces and moments at the clamped ends are required.

As cyclic symmetry simplifications are used (method explained in Section 6.2.4), the mode shapes are obtained for one single sector only. The mode shapes of all sectors are related by a change of phase, which is a function of the cyclic mode number. The corresponding displacements in each sector are complex and their absolute value is the same for all sectors. Therefore, the kinetic energy is also equal in all sectors. To calculate the clamped forces and moments, it is also possible to use the absolute value of the clamped beam displacements such that these forces and moments are equal in all sectors. The total energy lost is therefore eight (number of sectors) times the energy lost through one clamped end, and the total energy stored is also eight times the energy stored in one sector only (45° ring portion and

one entire leg). Finally, one can note that the mode shape of only one sector is actually needed to calculate support losses in a cyclic symmetric structure such as a ring-based resonator. This was also the case for in-plane vibrations.

Results for the Q-factors for the tenth lowest natural frequencies of out-of-plane vibrations are presented in Table 6.5. They were calculated with the assumption that the support and the resonator have the same axial thickness ($h_p/h = 1$), for consistency with the in-plane analysis performed in Chapter 4. It is interesting to note that these Q-factors are much smaller than those found for in-plane vibrations, see Chapter 5. This could perhaps have been expected for reasons that will be discussed in the following paragraphs. The lowest Q-factor is found for the mode with lowest natural frequency with $\kappa = 0$. This mode corresponds to translational motion of the ring along its axial direction and is illustrated in Figure 6.5(a). Most of the deformation occurs in the legs and very little deformation occurs in the ring in this mode. The energy stored is therefore relatively small, while the reactions at the boundary, which drive the substrate response, are still significant. This may at least partly explain the small Q predicted. The next smallest predicted Q-factor occurs for the lowest frequency with $\kappa = 1$. In this mode, presented in Figure 6.5(b), the ring rotates about an axis contained in the plane of the resonator. Again, little deformation occurs in the ring as it effectively undergoes rigid body rotation only. The above line of argument suggests that in order to obtain larger Q-factors, the deformation of the ring relative to that of the legs, and therefore the proportion of energy stored in the ring, should be maximised. This situation occurs for the "ring" 2θ and 3θ modes where the resonator deforms as shown in Figures 6.6 and 6.7, and it is clear from Table 6.5 that the predicted Q-factors for these modes are significantly higher.

Wong [2] made experimental measurements of Q-factors for out-of-plane vibrations of resonators with similar dimensions and material properties. He found that $Q \approx 11 \cdot 10^3$ for the 2θ mode, and $Q \approx 13 \cdot 10^3$ for the 3θ mode. These values are experimental and take account of all possible energy losses, including thermoelastic damping which was known to be the principal loss mechanism in the experimental structures. Therefore, the Q-factors due to support loss alone should be even greater

than the measured Q-factors. However, as seen in Table 6.5, the results found using the method presented in Section 6.3 are far from the measured values. A number of factors may contribute to the explanation of these discrepancies, as discussed next.

Possibly the most important factors relate to the basic assumption in the theoretical development that the actual physical support can be realistically modelled as a semi-infinite thin plate with thickness equal to that of the resonator. To examine the validity of this assumption, first see Figure 1.2 which shows a photograph and SEM photograph of a resonator structure that is essentially the same as that tested by Wong [2]. The dimensions of the silicon plate to which the resonator is directly attached are actually of the same order as the dimensions of the resonator itself (in the millimetre range). Furthermore, the plate is bonded rigidly to a pedestal glass, which is itself attached to a metal base. Hence, the support structure is finite with external boundaries that would in practice reflect some energy back into the resonator, reducing the possibility for energy to propagate away from the resonator. The assumption of semi-infinite support stipulates that the wavelength of the bending waves should be much greater than the actual size of the support. At the frequencies of the 2θ and 3θ modes, these wavelengths, in a support with thickness equal to that of the resonator, are approximately 12 mm and 8 mm, respectively. Therefore the chip is smaller than these bending wavelengths, which implies that the approximation of a semi-infinite support plate is inappropriate for the structures tested by Wong. This is clearly an issue that shows that further work is needed in the future to better model the boundary conditions.

Moreover, the out-of-plane stiffness of the real support is much greater than that of a semi-infinite plate. Indeed, as the support is of finite size, its actual end boundaries may have an important effect on the motion of the resonator/support attachment point. This effect is expected to be different for the case of out-of-plane vibration than for in-plane vibration. Because the in-plane stiffness of the plate is relatively very high, the assumption of a semi-infinite support is relatively less significant. This is because the waves attenuate "quickly" in the support and, even if the support is "short", reflections that significantly influence the attachment point motion are less likely. However, for out-of-plane vibrations, for the case where there

is relatively less stiffness in the support that constrains the vibrations, the actual dimensions of the support and the fact that it is not semi-infinite are likely to be more relevant.

Support for the general validity of the discussion given in the previous paragraph is provided by the cantilever example presented in the first part of Section 6.4.2. Reference to Figure 6.8 highlights that the predicted Q-factor depends strongly on the thickness of the support relative to that of the beam. In the cantilever example, the predicted Q-factor increases by a factor of 35, see Table 6.4, when the support/cantilever thickness ratio is increased from 1 to 10. It seems reasonable to assume that a similar trend would apply in the case of the ring resonator. The precise numerical values would of course be different, but it is interesting to note that the measured [2] and predicted (Table 6.5) Q-factors are $Q \approx 11 \cdot 10^3$ and 320 respectively for the 2θ. The ratio of these values is approximately 34, which is commensurate with the ratio of Q-factors for the cantilever when the support thickness was increased by a factor of ten.

In the ring resonator device shown in Figure 1.2, the axial thickness of the resonator silicon is of the order of 0.1 mm compared to thicknesses of approximately 2.5 mm for the supporting glass and approximately 1.5 mm for the metal base. Thus, the ratio of the thickness of the support compared to resonator is significantly greater than ten. It is therefore not unreasonable to suggest that the predicted Q-factors would be significantly higher if the support were modelled in a way that more accurately accounted for its out-of-plane stiffness characteristics. This is confirmed in Figure 6.9, which shows the Q-factors for the 2θ and 3θ modes of the ring-based resonators as a function of the support/resonator thickness. Results for the range of support thickness between 0.1 mm and 2 mm are presented. As expected, larger Q-factors are obtained if the support is considered thicker, and the values of Q-calculated here correspond to a more plausible range. However, the thicker the support is, the less the assumption of thin structure is valid. This assumption stipulates that the transverse wavelength must be much greater than the support thickness. For a frequency corresponding to the 2θ frequency, this wavelength is approximately 0.5 mm. Another support model that considers the propagation of

energy into a half-space (infinitely thick support) was presented in [45], based on the work from Miller and Pursey [90]. Given sufficient time, it would be interesting to investigate if this second model is more appropriate that the one used in this chapter. This is clearly an issue deserving further work in the future.

Another issue in the model is the rigid-attachment assumption between the resonator and its support. In the resonator vibration analysis, clamped ends are assumed with boundary conditions such that $v = 0$, $\partial v/\partial z = 0$ and $\Omega = 0$. However, as mentioned earlier, the relatively smaller stiffness of the (thin) support with regard to out-of-plane motion does not constrain the resonator as a clamped end would do. Therefore the conditions of zero displacement and rotation at the boundary should be replaced by a relationship between v, $\partial v/\partial z$, $\partial^2 v/\partial z^2$, and $\partial^3 v/\partial z^3$ determined by considering the second and third row of Equation (6.45). For torsional vibrations, the condition of zero rotation of the cross-section should be replaced by a relationship between Ω and $\partial\Omega/\partial z$ obtained with the first row of Equation (6.45). In Equation (6.45), the displacements of the attachment point are coupled to the excitation forces. For instance, instead of imposing $\Omega = 0$ as a boundary condition, one could use:

$$\Omega = \frac{1}{\mathrm{i}\omega\sqrt{\rho h_p D}} y_{11} k^2 M_T, \tag{6.75}$$

which links Ω with $\partial\Omega/\partial z$. This was performed for flexural vibration of a cantilever beam by Judge *et al.* [45]. They predicted that when the beam and support have the same thickness, an error of approximately a factor two is introduced with the rigid-attachment assumptions. This error decreases when the support thickness increases. The thicker is the support, the more it constrains the vibrations, and the closer the attachment is to being completely rigid. When the plate thickness is twice that of the cantilever beam, the error is less than 10% [45].

If one wants to apply these more realistic boundary conditions to the ring-based resonator, the reflection coefficients of waves at the boundary used in the ray tracing method need to be redefined using the new conditions obtained from Equation (6.45). Instead of imposing a rigid-attachment, a more flexible attachment could be used, which would be expected to change the Q-factor. Indeed, for a

support modelled as a thin-plate (thickness equal to the resonator thickness for instance), if the support becomes more flexible, the forces and moments at the attachment point will decrease significantly. The mode shapes of a simple cantilever beam resonator will also change significantly as they are directly linked with the boundary conditions. The energy contained in the beam is expected to decrease as this one will now deform less. The fact that energy and clamped forces decrease simultaneously explains why the Q-factor is expected to change "only" by a factor of two for the cantilever beam case. However, for the ring-based resonator case, the energy stored in the resonator in the 2θ and 3θ modes is mainly contained in the ring. Changing the boundary conditions will not affect the ring deformation so much and it is expected that the stored energy will not change too much either. But, on the other hand, the clamped forces and moments will still decrease due to the introduction of flexibility to the support. A decrease in the clamped forces will decrease the power flow into the support and therefore increase the Q-factor. The error in Q introduced by the rigid-attachment conditions for the ring-based resonator is difficult to predict. Only a numerical solution of the problem can give an approximate value of this error, but it is expected that the rigid-attachment condition tends to underestimate the Q-factors of ring-based resonators.

6.5 Conclusion

In this chapter, an extension of the ray tracing method has been developed to deal with out-of-plane vibrations, using the wave approach adopted for in-plane vibrations (see Chapters 2 and 3). The extension relies on the knowledge of out-of-plane governing equations of motion, which were derived here for curved and straight beams. Transmission coefficients, also needed in the ray tracing process, were presented for discontinuities commonly encountered in MEMS resonators. Furthermore, the previously developed simplifications for symmetrical structures were used.

Results for natural frequencies and mode shapes were presented that show very good agreement with FE models. A three-dimensional FE analysis with more realistically

modelled radiused joints between straight leg sections has also been developed for comparison. This showed that the assumptions made in the ray tracing method correctly predict the 2θ and 3θ out-of-plane modes of the resonator. Small discrepancies appear in the model of leg vibrations for these modes, mainly due to the assumption of modelling only the beam centreline in the ray tracing method. Shear deformation, rotary inertia, and stress concentration at several junctions in the resonator are neglected with the wave approach.

A possible model of support loss for out-of-plane vibrations was also presented, established on the assumption that the support can be represented as a semi-infinite thin plate with thickness equal to that of the resonator. Based on this model, the predicted Q-factors for ring-based resonators were found to be significantly smaller than experimental measurements. A number of factors that could contribute to this discrepancy were identified and discussed. These include the assumptions that the support is semi-infinite and thin. In the practical situation, the resonator and support are mounted on a chip whose dimensions, compared to the wavelengths of propagating waves, are not sufficiently large to be considered as infinite. Despite the fact that this assumption was found to be inappropriate, the method presented here offers a fundamental approach that can be easily re-formulated and refined for real applications. It is concluded that the semi-infinite thin plate assumption for the support does not realistically represent the actual tested hardware. Trends noted in the example of a ring-based resonator mounted on supports of increasing thickness could provide useful insight into the problem. An improved approach, with more realistic admittance relationship linking displacements and forces at the attachment point is required; this may be derived from theoretical analysis or experimental measurement. The investigation of approaches to model realistic support structures for the case of out-of-plane vibration is clearly a topic for further research.

Figures and tables

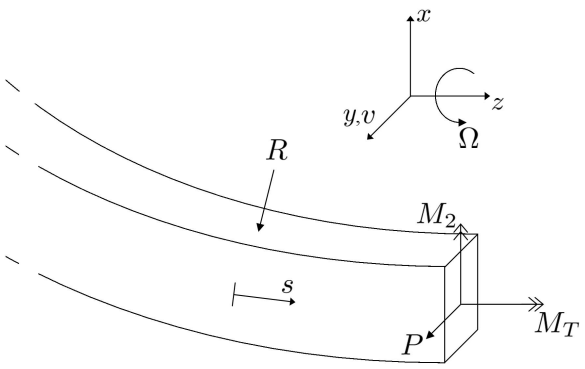

Figure 6.1: Out-of-plane vibration of a curved beam: notation and sign conventions.

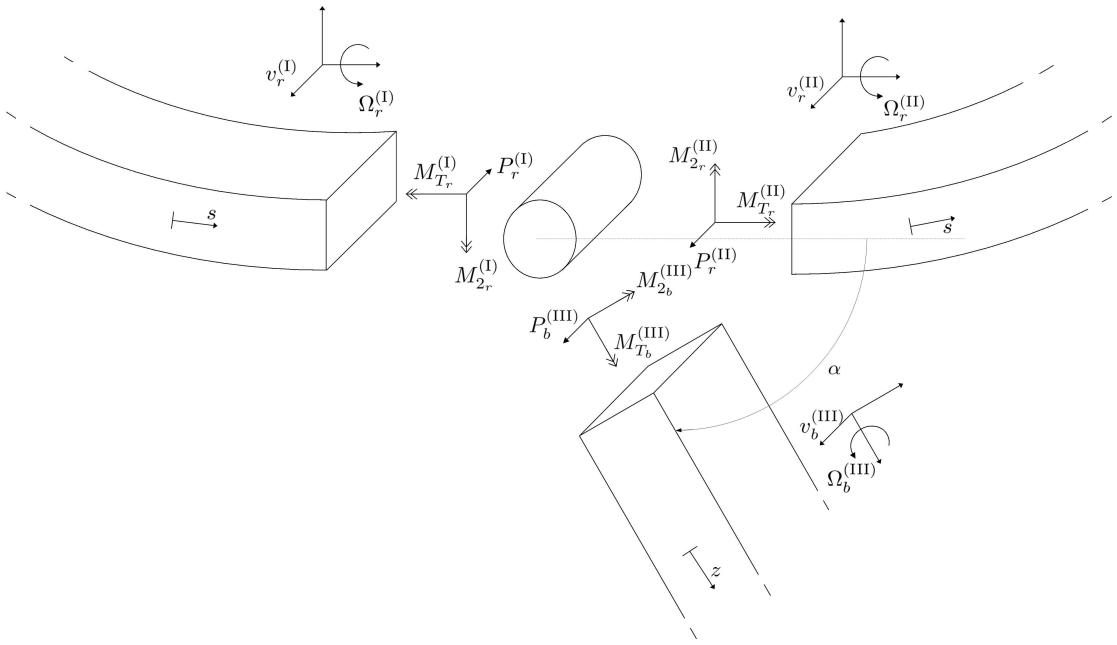

Figure 6.2: Transmission of out-of-plane vibrations between a ring and an attached beam.

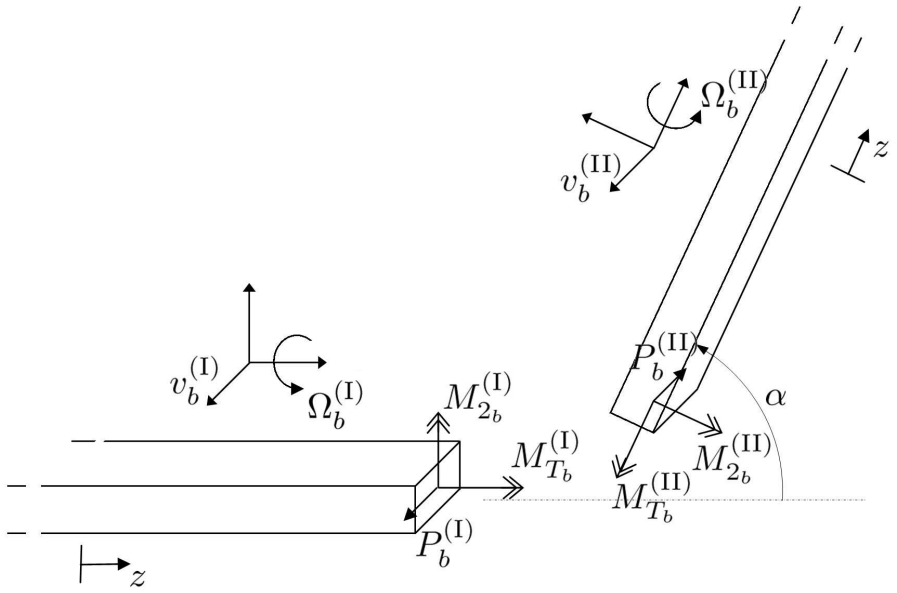

Figure 6.3: Transmission of out-of-plane vibrations through an abrupt change in direction in beams.

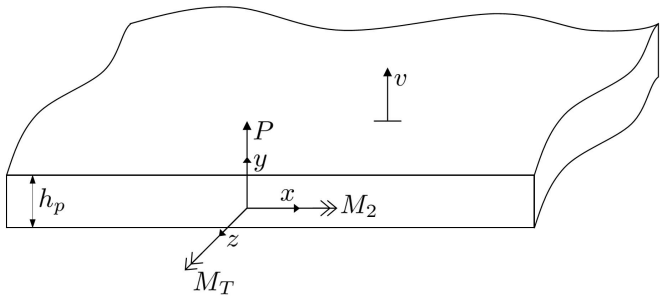

(a)

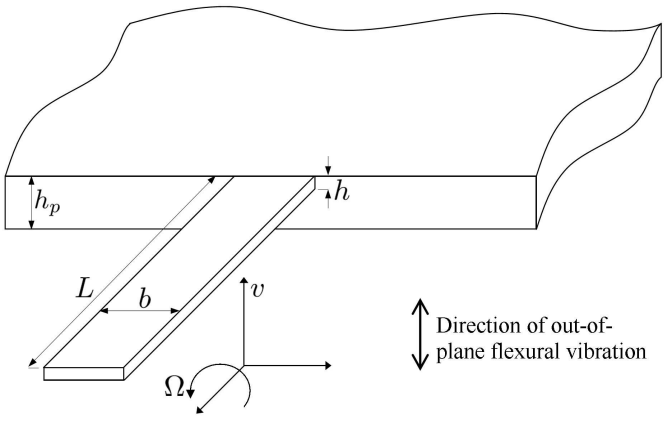

(b)

Figure 6.4: Support modelled as a semi-infinite thin plate for out-of-plane vibrations. (a) shows its excitation shear force P, bending moment M_2, twisting moment M_T, and also the axes orientation and origin. (b) presents the notation used for the cantilever beam study.

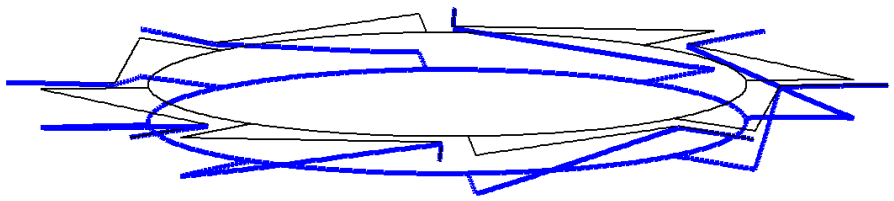

(a)

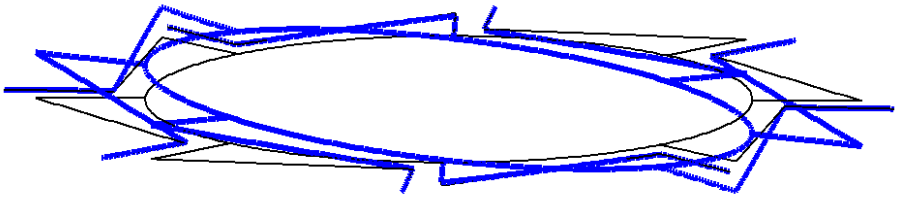

(b)

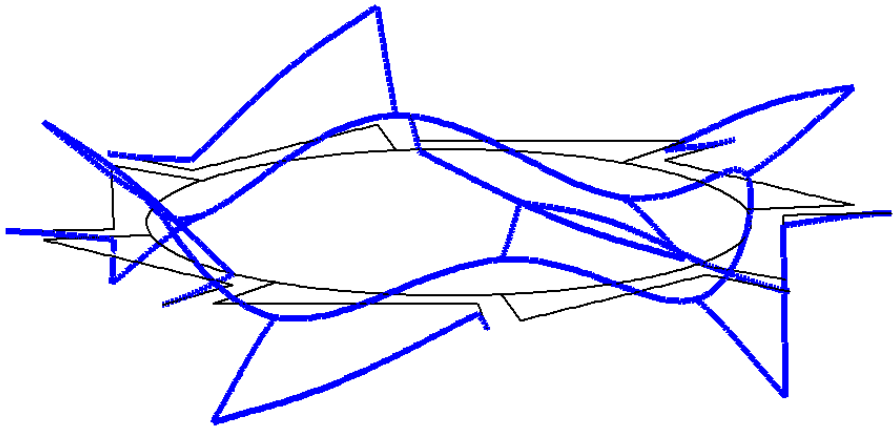

(c)

Figure 6.5: Mode shapes for out-of-plane vibrations of the ring-based resonator obtained with the ray tracing method. (a) corresponds to the lowest natural frequency with $\kappa = 0$, (b) with $\kappa = 1$, and (c) with $\kappa = 4$. The modes relate, respectively, to the natural frequencies 4 803 Hz, 5 413 Hz and 29 982 Hz given in Table 6.1.

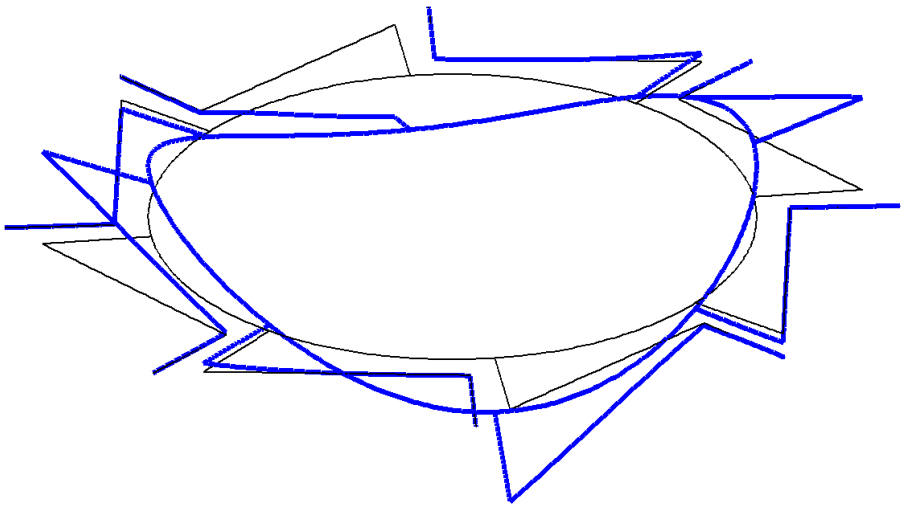

(a)

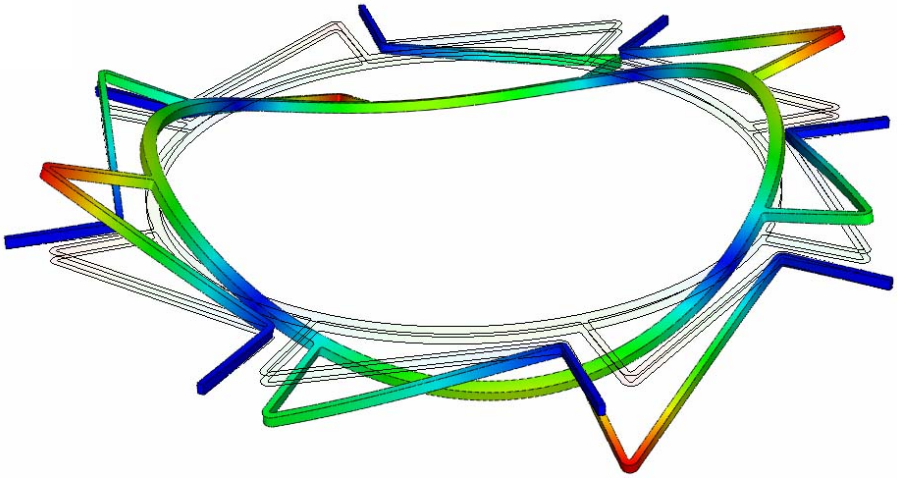

(b)

Figure 6.6: 2θ mode shape for out-of-plane vibrations of the ring-based resonator obtained with the ray tracing method (a); and, a FE model (b).

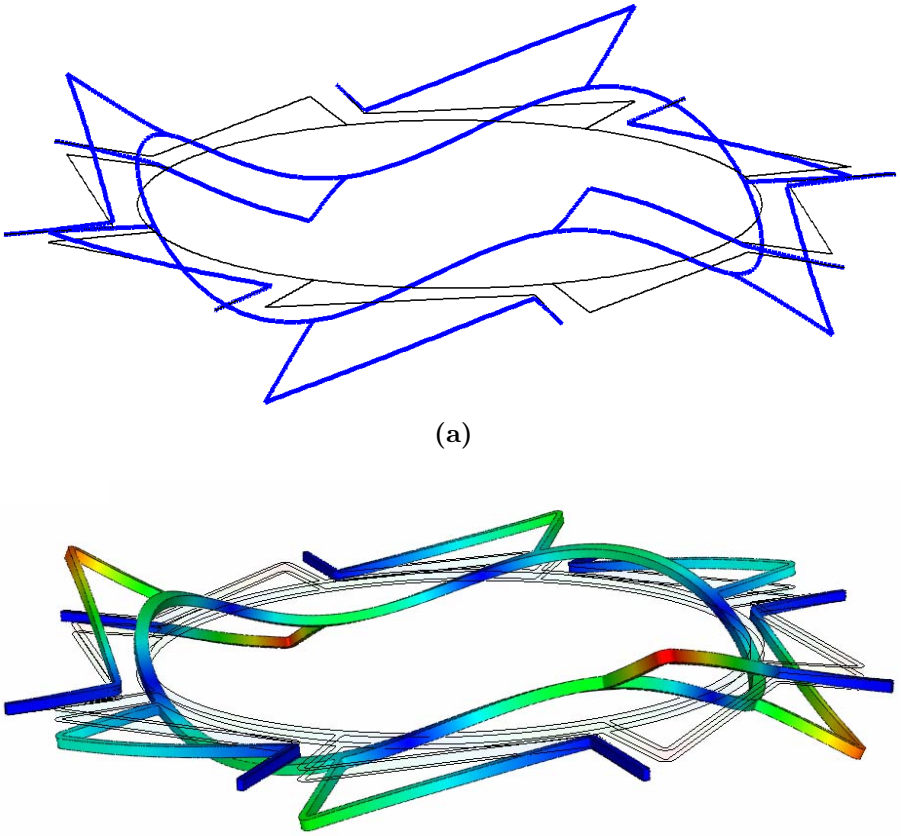

(a)

(b)

Figure 6.7: 3θ mode shape for out-of-plane vibrations of the ring-based resonator obtained with the ray tracing method (a); and, a FE model (b).

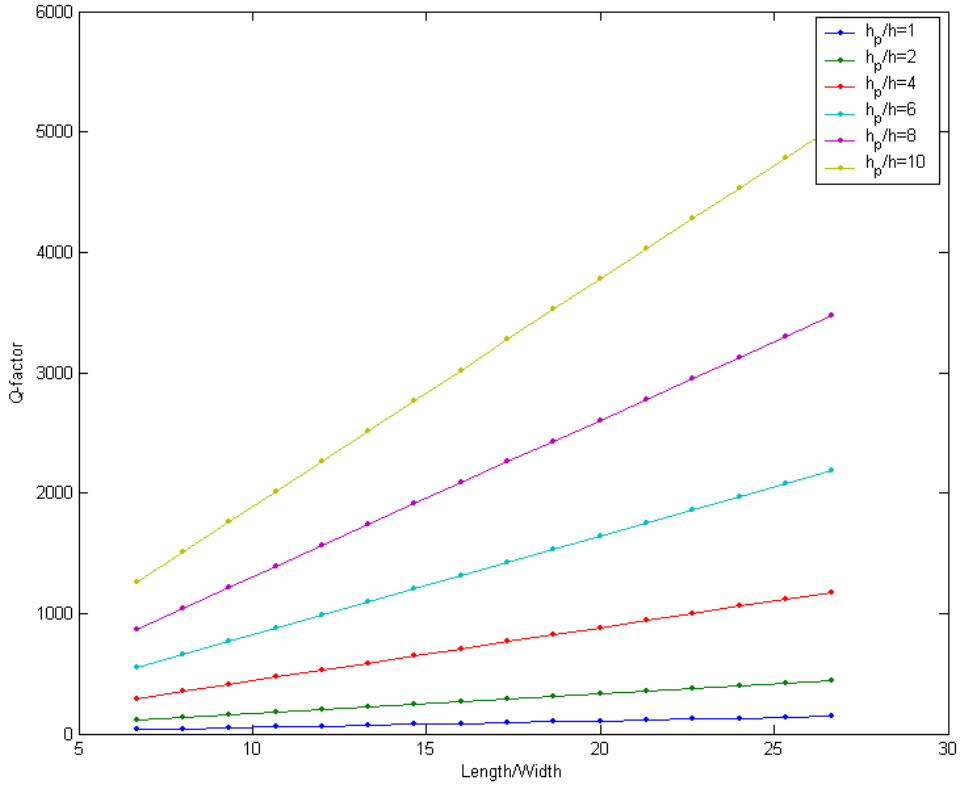

Figure 6.8: Q-factor of the fundamental out-of-plane mode of a cantilever beam, shown as a function of the length/width ratio for different support thicknesses.

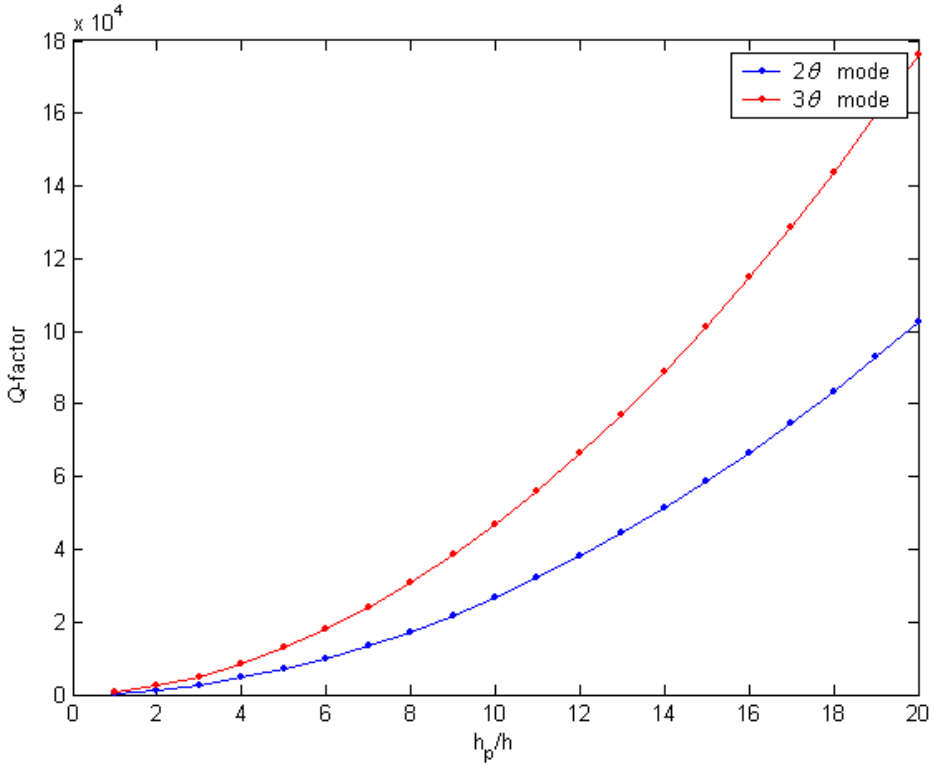

Figure 6.9: Q-factor of the 2θ and 3θ out-of-plane modes of a ring-based resonator, shown as a function of the support/resonator thickness ratio (h_p/h).

Table 6.1: Natural frequencies (Hz) for the out-of-plane vibrations of the ring-based rate sensor calculated with the ray tracing method and a FE model (two-dimensional Euler/Bernoulli beams elements and Timoshenko ("T'nko") beams elements, with 0.85 as shear correction factor, of approximate length 0.01 mm). The resonator dimensions are presented in Figure 3.8(b). The material properties used are $\rho = 2329\,\mathrm{kg/m^3}$, $E = 170 \cdot 10^9\,\mathrm{Pa}$ and $G = E/(2(1+\nu))\,\mathrm{Pa}$, with Poisson ratio $\nu = 0.28$.

	Ray Tracing	FE analysis		Difference %
		Euler beams	T'nko beams	Ray Tr./T'nko beams
$\kappa = 0$	4 803	4 803	4 800	0.05
	30 105	30 105	30 060	0.15
$\kappa = 1$	5 413	5 413	5 411	0.05
	37 266	37 266	37 193	0.20
$\kappa = 2$	10 818	10 818	10 813	0.04
	46 279	46 279	46 155	0.27
$\kappa = 3$	22 899	22 899	22 873	0.11
	52 334	52 334	52 177	0.30
$\kappa = 4$	29 982	29 982	29 928	0.18
	58 271	58 271	58 077	0.33

Table 6.2: Natural frequencies (Hz) for the out-of-plane vibrations of the ring-based rate sensor calculated with the ray tracing method and a FE model (two-dimensional Euler/Bernoulli beams elements and Timoshenko beams elements, with 0.85 as shear correction factor, of approximate length 0.01 mm). The resonator dimensions are presented in Figure 3.8(b), except that the legs and ring have now circular cross-sections with radius $r_{\text{leg}} = 4 \cdot 10^{-5}$ m and $r_{\text{ring}} = 7 \cdot 10^{-5}$ m. The material properties used are those given in Table 6.1.

	Ray Tracing	FE analysis		Difference %
		Euler beams	T'nko beams	Ray Tr./T'nko beams
$\kappa = 0$	3 720	3 720	3 718	0.04
	33 327	33 327	33 273	0.16
$\kappa = 1$	4 407	4 407	4 405	0.04
	37 120	37 120	37 046	0.20
$\kappa = 2$	12 595	12 595	12 589	0.05
	39 519	39 519	39 436	0.21
$\kappa = 3$	27 822	27 822	27 780	0.15
	42 739	42 739	42 658	0.19
$\kappa = 4$	32 826	32 826	32 759	0.20
	45 962	45 962	45 878	0.18

Table 6.3: Natural frequencies (kHz) for the 2θ and 3θ modes of vibration of the ring-based rate sensor calculated with the ray tracing method and a FE model (three-dimensional brick elements of approximate length 0.04 mm). The resonator dimensions are presented in Figure 3.8(b). The material properties used are those given in Table 6.1.

Frequency (kHz)		Ray tracing	FE model	Diff. %	Diff. % in [2]
In-plane	2θ mode	14.2	14.5	2.1	0.7
	3θ mode	32.1	32.7	1.7	6.6
Out-of-plane	2θ mode	10.8	11.2	3.4	13.7
	3θ mode	22.9	23.6	3.1	27.8

Table 6.4: Q-factor of the fundamental out-of-plane mode of a cantilever beam, calculated as a function of the length/width ratio (L/b) and for two different support thicknesses ($h_p/h = 1$ and $h_p/h = 10$). Numerical values are calculated either using Equation (6.71) or with a more numerical approach that involves the ray tracing method ("Ray Tr.").

L/b	$h_p/h = 1$		$h_p/h = 10$	
	from Eq. (6.71)	from Ray Tr.	from Eq. (6.71)	from Ray Tr.
8	42.80	42.80	1511	1511
12	64.20	64.20	2266	2266
16	85.61	85.61	3022	3022
20	107.0	107.0	3777	3777
24	128.4	128.4	4533	4533

Table 6.5: Natural frequencies (Hz) and associated Q-factors for the out-of-plane vibrations of the ring-based rate sensor. The resonator dimensions are presented in Figure 3.8(b) and material properties used are those given in Table 6.1.

	Frequency (Hz)	κ	Q-factor
	4 803	0	65
	5 413	1	74
2θ mode $\Rightarrow$	10 818	2	320
3θ mode $\Rightarrow$	22 899	3	691
	29 982	4	537
	30 105	0	725
	37 266	1	629
	46 279	2	332
	52 334	3	214
	58 271	4	139

Chapter 7

Conclusions and future work

7.1 Introduction

High accuracy sensors based on MEMS resonators are being used increasingly in different sectors, such as in the military, aerospace and automotive industries. The performance of such devices can be significantly degraded by energy losses from the resonator. Support loss is an increasingly important source of damping in MEMS resonators that has previously been the subject of relatively little research. The research reported in this thesis contributes to the understanding, modelling and quantification of this particular damping mechanism. The work presented here is thought to represent a significant improvement in predictive capability, although further work is still required. The thesis presents the development of an efficient approach to model both the transmission of vibration within a structure and quantify the energy lost to its surroundings. This chapter summarises the key models and findings of the research, and discusses possible relevant future work in this area.

7.2 Chapter reviews and conclusions

A summary of the research work performed and the detailed conclusions were presented at the end of each chapter. The main conclusions of each chapter are summarised here as follows:

1. Chapter 1 gave a general overview of the main damping mechanisms relevant to MEMS resonators, namely air damping, thermoelastic damping, intrinsic material losses and support losses. Special focus was given to support losses and support loss models available in the literature. It was shown that most of the published work uses analytical models for studying the interaction between the resonator and the support. These models used the displacement of the resonator at its anchor end to evaluate the support losses, and none of the models had been developed for complex shaped resonators. In order to create a model for a generic resonator design, from a simple cantilever beam to a more elaborate ring-based rate sensor, it was necessary to extend one of the existing methods. To achieve this, an accurate vibration analysis tool was required to predict the anchor point vibrations, and the ray tracing method was identified for this purpose. A typical characteristic of MEMS resonators is that they are designed to vibrate at specific frequencies. The ray tracing approach was deemed to be the most appropriate as it relies on exact solutions and can predict the behaviour of complex waveguide structures at particular frequencies easily. The chapter concluded with a statement of the aims and objectives of the research.

2. From the work presented in Chapter 1, it was decided to study and extend the so-called ray tracing method. Chapter 2 presented the basic method and showed how it could be applied to analyse the free and forced in-plane vibrations of structures composed of several waveguide components. This method utilises the properties of wave propagation and transmission between different components, and the phase closure principle provides a means of calculating the natural frequencies and mode shapes. Calculation of the transmission

coefficients at different discontinuities generally encountered in MEMS structures was also presented. Results for natural frequencies and mode shapes obtained using ray tracing were compared to conventional FE analyses, and were found to give perfect agreement when Euler-Bernoulli beam elements were used. The study showed that the ray tracing method is an accurate and efficient approach to model the vibrations of complex waveguide structures. It was also noted that if different structures were to be constructed for a parametric study, the ray tracing method would be much more efficient than a FE analysis which is computationally expensive when different meshes need to be generated.

3. In Chapter 3, the ray tracing approach was employed to model structures that exhibit symmetry properties. A method based on the ray tracing concept was developed that simplified the modelling when the structure being studied possessed periodic or cyclic symmetries. This was achieved by modelling the relationship between identical sectors and their neighbours. Natural frequencies and mode shapes of different symmetric structures, such as regular polygons and ring-based rate sensors, were presented. They showed very good agreement with FE analyses and/or analytical results found in the literature. The simplification methods used were shown to be very efficient for reducing the total number of unknowns in the model, reducing the complexity of the analysis and the associated computation time. From the techniques developed in Chapters 2 and 3, a tool for predicting the vibrations of ring-based resonators was developed, and this was used in subsequent chapters as a basis for calculating the associated support losses.

4. Chapter 4 focused on modelling support loss for in-plane vibrations of a resonator. The coupling between the resonator and substrate was modelled to understand and evaluate the interaction and energy transmission between them. Owing to the large relative size and complex shape of the substrate, it was not possible to model the substrate in its entirety and some simplifications were made. Different techniques for approximating the support as an infinite domain were presented. The methodology for the support loss calculation for each of these techniques was also introduced. A fully analytical method

was developed that considered separately the resonator and its support. The support was modelled using classical wave theory in a two-dimensional thin plate; whereas the resonator was modelled using the ray tracing method, or standard modal analysis. This model was then compared to two different finite elements approaches that both modelled the entire system (resonator and support). In the FE approaches, the infinite size of the support was tackled using either a Perfectly Match Layer (PML) method or infinite elements. Convergence issues were discussed for these approaches. Numerical results for each method were obtained and comparisons made for support losses of simple structures. It was shown that the results were all in the same order of magnitude and presented similar trends, validating the analytical model.

5. The analytical model for support loss developed in Chapter 4 and the vibration analysis method presented in Chapters 2 and 3 were applied to commercial MEMS ring-based resonator designs in Chapter 5. The original design was studied first and numerical values for Q-factors were obtained. In comparison to thermoelastic damping, support loss was found to be negligible. However, it was noted that future designs may significantly reduce the thermoelastic damping such that support loss may become critical. A parametric study was performed to gain a better understanding of the factors that influence support loss. Geometric parameters and material properties were varied and the associated Q-factors calculated. A design with thin, flexible legs was proposed and the analysis suggested a significant increase in Q-factors for the operating modes. The introduction of blocking masses to reduce the energy propagation away from the resonator, proved to be useful when the masses are placed in the vicinity of the ring. From the complete study, it was shown that to minimise the support loss, it is necessary to consider simultaneously both clamping forces and energy contained in the resonator. The former must be minimised, whilst the latter must generally be maximised. It was also found that for a ring-based resonator the energy distribution within the structure is important. Most of the energy must be contained in the sensor part (the ring) and not in the supporting legs which are directly attached to the substrate. This chapter provided useful recommendations for future designs with regard

to the Q-factors.

6. All of the previous models and analyses focused on in-plane vibrations, appropriate to single-axis MEMS rate sensors. However, there are many applications when it is necessary to sense rate simultaneously in two or three directions. At present, multi-axis rate sensing is achieved by using multiple single-axis rate sensors mounted orthogonally to each other. A new generation of multi-axis rate sensors is under development based on the in- and out-of-plane vibrations of rings. Chapter 6 extended the ray tracing method to study out-of-plane vibrations. A support model was introduced and developed to analyse the flexural vibrations of a semi-infinite supporting plate. The coupling between the resonator and support was achieved based on admittance characteristics. Results for the Q-factors of out-of-plane modes of ring resonators were obtained. These were found to be much smaller than expected compared to experimental measurements, indicating that the model predicted excessive levels of energy dissipation. The main reason for these discrepancies was explained, and it was concluded that the proposed model was inappropriate for practical situations. Despite this, the model presented in Chapter 6 could easily form the basis for improved modelling in real applications.

In summary, the above findings fulfilled the original aims of the research program, and the work has strengthened and improved the understanding of support loss in vibrating MEMS structures. For the first time in the study of ring rate sensors, numerical results for Q-factors that consider support loss were calculated and analysed to demonstrate its relative importance. Future designs may significantly improve the quality and performance of resonators by reducing the energy flow. The vibration transmission and support loss models developed were presented in a general way so that they can be applied to different designs of resonators. The research reported in this thesis provides significant insight into support loss mechanisms and it is believed that the development of future generation of MEMS sensors will benefit from these findings.

7.3 Suggestions for future work

The findings of this research could be extended in a number of areas. The following indicates possible topics for future work in the area of vibration transmission analysis and support loss models.

7.3.1 Vibration transmission analysis

The ray tracing method developed in this thesis is based on Euler/Bernoulli beams, and is valid for long, thin beam structures. The effect of rotary inertia and transverse shear deformation could be incorporated in the model. Mei and Mace [60] presented the basis of wave reflection and transmission in Timoshenko beams. This work could be extended to curved beams and rings, using the governing equations of motion given in [65] for instance. The inclusion of rotary inertia and shear deformation in the ray tracing method is expected to change the size and complexity of the matrices involved but the fundamentals concerning wave transmission and propagation will be similar. The resulting method would be better suited to structures composed of thicker straight and curved beams.

In the ring-based resonator model, the legs were modelled as three straight beams linked together at "sharp" cornered intersecting junctions. In practice, "radiused" corners connect the different beams. A further investigation is needed to incorporate these "radiused" corners in the analysis, as they may change the vibrational behaviour of the joint. Also, a cylindrical rigid joint was considered in the transmission coefficient calculations between a ring and an attached beam. It would be interesting to study the vibration transmission through another type of joint geometry. Ashby [59] considered other possible models for the joint between two beams.

In the out-of-plane transmission coefficients calculations, the objective was to derive the transmission coefficients at discontinuities encountered in common MEMS devices. The ring/beam transmission represented a general case that could be simpli-

fied easily to others discontinuities. However, it would be interesting to investigate the transmission between three (or more) non-planar components, the attachment between three beams in different planes for instance. The ray tracing method could then be applied to other type of structures, *e.g.* non-planar structures, and could then become an easy and efficient way to model transmission of vibration in any three-dimensional frame structures, commonly found in civil, naval or aerospace engineering structures. The wave transmission through connected structures in three dimensions has been analysed using the dynamic stiffness method [112], and application of the ray tracing method to this type of problem would be interesting. Generally, the development of the ray tracing method for non-planar structures needs further investigation. However, all of the fundamental work is presented in this thesis.

In several papers published in the literature, such as [64, 73, 113, 114], one can see that the transmission of vibration along a structure is generally linked with the transmitted energy, and the main focus of research actually concerns this energy. In the work reported in this thesis, no reference was made to the energy and power transmitted through the different joints. The reason is that the main interest was centered around the energy transmitted from the resonator, through the support attachment. As the ray tracing method is based on a travelling wave approach, the reflected/transmitted power for any discontinuity would be calculated easily. The energy transmission within the resonator has not been quantified for each particular joint and could be the focus of future investigations. By looking at each joint in isolation, it may be possible to design a geometry that is well suited to maximise the energy in the resonator.

In Chapter 3, periodic structures are modelled using a recursive formalism as a function of the characteristics of a single sector. Finite structures are considered, and the external boundaries conditions are applied in the ray tracing analysis. However, infinite periodic structures have been the subject of many investigations, see *e.g.* the review in [85]. A further investigation could use the complex propagation constant μ [85] in the ray tracing method to model infinite structures, in a similar way to that developed for cyclic symmetric structures.

7.3.2 Support loss model

In the analytical support loss model for in-plane vibrations, the resonator vibrations are first predicted using the assumption that the structure is clamped at its support. This assumption is not always fully consistent with the following step of the analysis in which the support is modelled as being excited by the applied "clamped" forces. A possible way to tackle this inconsistency is to incorporate the support model directly in the ray tracing analysis. When studying the resonator vibration, instead of being clamped at its support, the resonator could have boundary conditions that constrain the displacement and introduce energy loss directly. Basically, the standard clamped boundary could be changed to take into account the complex stiffness created by the support. The real part would restrain the displacement; whilst the imaginary part defines the damping. Using this idea, and for longitudinal motion only, one ends up trying to solve for the real and imaginary parts of Equation (4.38), presented in Chapter 4. A similar equation can be derived for flexural motion. The imaginary part of this equation was provided later in Chapter 4, but the real part is more difficult to solve, as the integrand is non-continuous. A solution procedure of this kind of integral has been performed in [90]. Once the complex stiffness boundary has been defined, the Q-factor for support loss could be found using a ray tracing analysis in combination with the half-power bandwidth approach. Further investigations are needed to analyse non-clamped and/or practical boundary conditions.

The same idea of non-rigid attachment boundary conditions was introduced for the analysis of out-of-plane vibration. In Chapter 6, the resonator was assumed to be clamped at the support, but for thin supports this assumption is not completely valid. More sophisticated boundary conditions could be developed and used in the support model to take account of the flexibility of the support.

In practical situations, the assumed thin-plate theory for the analysis of out-of-plane vibration transmission in the support is not valid. Indeed, the silicon substrate is attached to a pedestal glass, which is itself mounted on a metal base. Judge *et al.* [45] explained how a thick support could be modelled as a semi-infinite half-

space. It would be interesting to apply this model to the ring-based resonator. But of course, in practical designs, the support is neither a thin-plate or an infinitely thick support. Further work is needed to more accurately account for the out-of-plane stiffness characteristic of the support. Other models, both for in-plane and out-of-plane vibrations, that could account more precisely for the actual external boundaries of the support will be needed to make accurate predictions.

Finally, one of the most important areas for future work is to validate the present models experimentally. It is anticipated that several difficulties would be encountered. The main one being that it is impossible to measure support loss directly. Instead it is necessary to measure the overall damping using the half-power bandwidth method, taking account of all loss mechanisms [39, 42, 43, 45]. After calculating all losses, the overall loss can be compared with the experimental measurement. Several issues can be noted in the application of this method to validate the support loss model. Firstly, it assumes implicitly that the other damping predictions are correct, but it may be difficult to be sure that the predictions obtained are accurate and relevant to the specific type of resonator studied. Thermoelastic damping predictions have been investigated widely for cantilever beam resonators but the techniques may be not accurate for more complex shaped resonators. Thermoelastic damping in ring-based resonators was studied in [2] and this work provides results that can be applied with confidence.

A second problem with using experimental measurements to predict support loss is that support loss is generally not the dominant damping mechanism for the designs currently in manufacture. For instance, for the in-plane 2θ mode of the ring-based resonator, the Q-factor predicted for thermoelastic damping [2] is approximately ten times smaller than that predicted for support loss. This means that in an experimental analysis of damping performances, the contribution of support loss is small and cannot be identified precisely. In other words, it becomes very difficult to validate the support loss model using experimental results when this loss is not the dominant source of energy lost. It is suggested for future experimental work to use a structure where support loss is known to be significant, such as nano-structures or bulk resonators. To conclude, it is evident that experimental work needs to be

conducted to test the accuracy of the support loss predictions, but one must first make sure that the support loss contribution is relatively large compared to the other damping mechanisms.

References

[1] I. Hopkin. Performance and design of a silicon micromachined gyro. In *Proceedings of the DGON Symposium on Gyro Technology*, 1.0–1.10. Stuttgart, Germany, 1997.

[2] S. J. Wong. *Thermoelastic damping in MEMS ring resonators.* Ph.D. thesis, University of Nottingham, UK, 2005.

[3] N. Yasdi, F. Ayazi, and K. Najafi. Micromachined inertial sensors. In *Proceedings of the IEEE*, volume 86, 1640–1659. 1998.

[4] J. Bernstein, S. Cho, A. T. King, A. Kourepenis, P. Maciel, and M. Weinberg. A micromachined comb-drive tuning fork rate gyroscope. In *Proceedings of IEEE Workshop on the Micro Electromechanical Systems*, 143–148. Fort Lauderdale, USA, 1993.

[5] C. H. J. Fox and D. J. W. Hardie. Vibratory gyroscopic sensors. In *Proceedings of the DGON Symposium on Gyro Technology*, 13.0–13.30. Stuttgart, Germany, 1984.

[6] C. Fell, I. Hopkin, K. Townsend, and I. Sturland. A second generation silicon ring gyroscope. In *Proceedings of the DGON Symposium on Gyro Technology*, 1.0–1.14. Stuttgart, Germany, 1999.

[7] R. N. R. Elliott. *Modal identification of multi-axis vibrating MEMS rate sensors.* Ph.D. thesis, University of Nottingham, UK, 2009.

[8] R. Eley. *The dynamics of a multi-axis, vibratory rate gyroscope.* Ph.D. thesis, University of Nottingham, UK, 2000.

[9] R. D. Blevins. *Formulas for natural frequency and mode shape*. Van Nostrand Reinhold Company, New York, USA, 1979.

[10] S. McWilliam, J. Ong, and C. H. J. Fox. On the statistics of natural frequency splitting for rings with random mass imperfections. *Journal of Sound and Vibration*, **279**, 453–470, 2005.

[11] J. G. C. Ong. *Uncertainty effects on the dynamics of vibrating structure rate sensors*. Ph.D. thesis, University of Nottingham, UK, 2003.

[12] Y. Sun, D. Fang, and A. K. Soh. Thermoelastic damping in micro-beam resonators. *Journal of Solids and Structures*, **43**, 3213–3229, 2006.

[13] H. Hosaka, K. Itao, and K. Kuroda. Damping characteristics of beam-shaped micro-oscillators. *Sensors and Actuators A*, **49**, 87–95, 1995.

[14] K. Y. Yasurama, T. D. Stowe, E. M. Chow, T. Pfafman, T. W. Kenny, B. C. Stipe, and D. Rugar. Quality factors in micron- and submicron-thick cantilevers. *Journal of Microelectromechanical Systems*, **9**(1), 117–125, 2000.

[15] J. Brotz. *Damping in CMOS-MEMS Resonators*. Master's thesis, Carnegie Mellon University, USA, 2004.

[16] A. D. Nashif, D. I. G. Jones, and J. P. Henderson. *Vibration damping*. John Wiley and Sons, 1985.

[17] M. Lalanne, P. Berthier, and J. Der Hagopian. *Mechanical vibrations for engineers*. John Wiley and Sons, 1983.

[18] C. M. Harris. *Shock and Vibration Handbook*. McGraw-Hill, New York, 3rd edition, 1988.

[19] G. Stemme. Resonant silicon sensors. *Journal of Micromechanics and Microengineering*, **1**, 113–125, 1991.

[20] M. G. el Hak. *The MEMS handbook*. CRC Press, 2002.

[21] W. Ye and S. Hutcherson. Air damping of microbeam resonators in a low vacuum. In *Proceedings of* 13^{th} *International Conference on Solid-State Sensors, Actuators and Microsystems*, 772–775. Seoul, South Korea, 2005.

[22] M. I. Younis. *Modeling and Simulation of Microelectromechanical Systems in Multi-Physics Fields*. Ph.D. thesis, Virginia Polytechnic Institute and State University, USA, 2004.

[23] C. Zener. Internal friction in solids, I. Theory of internal friction in reeds. *Physical Review*, **52**, 230–235, 1937.

[24] C. Zener. Internal friction in solids, II. General theory of thermoelastic internal friction. *Physical Review*, **53**, 90–99, 1938.

[25] C. Zener, W. Otis, and R. Nuckolls. Internal friction in solids, III. Experimental demonstration of thermoelastic internal friction. *Physical Review*, **53**, 100–101, 1938.

[26] R. Lifshitz and M. L. Roukes. Thermoelastic damping in micro- and nanomechanical systems. *Physical Review B*, **61**(8), 5600–5609, 2000.

[27] A. Duwel, J. Gorman, W. M., J. Borenstein, and P. Ward. Experimental study of thermoelastic damping in MEMS gyros. *Sensors and Actuators A*, **103**, 70–75, 2003.

[28] J. P. Gorman. *Finite element model of thermoelastic damping in MEMS*. Master's thesis, Massachusetts Institute of Technology, USA, 2002.

[29] Y. B. Yi. Geometric effects on thermoelastic damping in MEMS resonators. *Journal of Sound and Vibration*, **309**, 588–599, 2008.

[30] T. Koyama. *Efficient evaluation of damping in resonant MEMS*. Ph.D. thesis, University of California, Berkeley, USA, 2008.

[31] N. Jaroensawat. *Prediction of thermoelastic dissipation in MEMS structures using a modal approach*. Ph.D. thesis, University of Nottingham, UK, 2008.

[32] P. Mohanty, D. A. Harrington, K. L. Ekinci, Y. T. Yang, M. J. Murphy, and M. L. Roukes. Intrinsic dissipation in high-frequency micromechanical resonators. *Physical Review B*, **66**(8), 085416, 2002.

[33] J. Yang, T. Ono, and M. Esashi. Energy dissipation in submicrometer thick single-crystal silicon cantilevers. *Journal of Microelectromechanical Systems*, **11**(6), 775–783, 2002.

[34] J. Yang, T. Ono, and M. Esashi. Investigating surface stress: surface loss in ultrathin single-crystal silicon cantilevers. *Journal of Vacuum Science and Technology*, **19**(2), 551–556, 2001.

[35] R. M. Langdon. Resonator sensors – a review. *Journal of Physics E: Scientific Instruments*, **18**, 103–115, 1985.

[36] Y. H. Park and K. C. Park. High-fidelity modeling of MEMS resonators – part I: Anchor loss mechanisms through substrate. *Journal of Microelectromechanical Systems*, **13**(2), 238–246, 2004.

[37] Y. H. Park and K. C. Park. High-fidelity modeling of MEMS resonators – part II: Coupled beam-substrate dynamics and validation. *Journal of Microelectromechanical Systems*, **13**(2), 248–257, 2004.

[38] D. S. Bindel and S. Govindjee. Elastic PMLs for resonator anchor loss simulation. *International Journal for Numerical Methods in Engineering*, **64**, 789–818, 2005.

[39] D. S. Bindel, E. Quévy, T. Koyoma, S. Govindjee, J. W. Demmel, and R. T. Howe. Anchor loss simulation in resonators. In *Proceedings of MEMS 2005*, 133–136. New York, USA, 2005.

[40] Y. Jimbo and K. Itao. Energy loss of a cantilever vibrator. *Journal of the Horological Institute of Japan*, **47**, 1–15, 1968.

[41] M. C. Cross and R. Lifshitz. Elastic wave transmission at an abrupt junction in a thin plate with application to heat transport and vibrations in mesoscopic systems. *Physical Review B*, **64**, 1–22, 2001.

[42] Z. Hao, A. Erbil, and F. Ayazi. An analytical model for support loss in micromachined beam resonators with in-plane flexural vibrations. *Sensors and Actuators A*, **109**, 156–164, 2003.

[43] Z. Hao and F. Ayazi. Support loss in the radial bulk-mode vibrations of centre-supported micromechanical disk resonators. *Sensors and Actuators A*, **134**, 582–593, 2007.

[44] D. M. Photiadis and J. A. Judge. Attachment losses of high Q oscillators. *Applied Physics Letters*, **85**(3), 482–484, 2004.

[45] J. A. Judge, D. M. Photiadis, J. F. Vignola, B. H. Houston, and J. Jarzynski. Attachment losses of micromechanical and nanomechanical resonators in the limits of thick and thin support structures. *Journal of Applied Physics*, **101**(1), 013521, 2007.

[46] B. Engquist and A. Majda. Absorbing boundary conditions for the numerical simulation of waves. *Mathematics of Computation*, **31**(139), 629–651, 1977.

[47] D. Givoli, I. Patlashenko, and J. B. Keller. Discrete Dirichlet-to-Neumann maps for unbounded domains. *Computer Methods in Applied Mechanics and Engineering*, **164**, 173–185, 1998.

[48] R. J. Astley. Infinite elements for wave problems: a review of current formulations and an assessment of accuracy. *International Journal for Numerical methods in Engineering*, **49**(7), 951–976, 2000.

[49] A. H. D. Cheng and D. T. Cheng. Heritage and early history of the boundary element method. *Engineering Analysis with Boundary Elements*, **29**(3), 268–302, 2005.

[50] J. P. Bérenger. A perfectly matched layer for the absorption of electromagnetic waves. *Journal of Computational Physics*, **114**, 185–200, 1994.

[51] L. Gavric and G. Pavic. A finite element method for computation of structural intensity by the normal mode approach. *Journal of Sound and Vibration*, **164**(1), 29–43, 1993.

[52] B. J. Lyon. *Statistical energy analysis of dynamic systems: theory and applications*. MIT Press, Cambridge, USA, 1975.

[53] A. J. Keane and W. G. Price. A note on the power flowing between two conservatively coupled multi-modal subsystems. *Journal of Sound and Vibration*, **144**, 185–196, 1991.

[54] K. F. Graff. *Wave Motion in Elastic Solids*. Ohio State University Press, 1975.

[55] L. Cremer, M. Heckl, and E. E. Ungar. *Structure-Borne Sound*. Springer-Verlag, Berlin, Germany, 2nd edition, 1988.

[56] B. R. Mace. Power flow between two continuous one-dimensional subsystems: a wave solution. *Journal of Sound and Vibration*, **154**, 289–319, 1992.

[57] B. R. Mace. Power flow between two coupled beams. *Journal of Sound and Vibration*, **159**, 305–325, 1992.

[58] R. S. Langley. High frequency vibration of one-dimensional systems: ray tracing, statistical energy analysis and vibration localisation, 1996. Private communication.

[59] G. T. Ashby. *Directional vibration conductivity in beam structures*. Ph.D. thesis, University of Nottingham, UK, 1998.

[60] C. Mei and B. R. Mace. Wave reflection and transmission in Timoshenko beams and wave analysis of Timoshenko beam structures. *Journal of Vibration and Acoustics, Transactions of ASME*, **127**(4), 382–394, 2005.

[61] D. J. Nefske and S. H. Sung. Power flow finite element analysis of dynamic systems: basic theory and application to beams. In *Proceedings of the Winter Annual Meeting of ASME*, 299–306. Boston, USA, 1987.

[62] J. D. Palmer. *Vibrational energy flow in structures*. Ph.D. thesis, University of Nottingham, UK, 1994.

[63] O. M. Bouthier and R. J. Bernhard. Simple models of energy flow in vibrating membranes. *Journal of Sound and Vibration*, **182**, 129–147, 1995.

[64] P. E. Cho and R. J. Bernhard. Energy flow analysis of coupled beams. *Journal of Sound and Vibration*, **211**, 593–605, 1998.

[65] S. Rao. *Vibration of Continuous Systems.* John Wiley and Sons, New Jersey, USA, 2007.

[66] R. K. Livesley. *Matrix Methods of Structural Analysis.* Pergamon Press, Oxford, UK, 2nd edition, 1975.

[67] R. L. Sack. *Matrix Structural Analysis.* PWS-Kent Publishing Company, Boston, USA, 1989.

[68] W. H. Wittrick and F. W. Williams. A general algorithm for computing natural frequencies of elastic structures. *Quaterly Journal of Mechanics and Applied Mathematics*, **24**, 781–791, 1970.

[69] L. S. Beale and M. L. Accorsi. Power flow in two- and three- dimensional frame structures. *Journal of Sound and Vibration*, **185**, 685–702, 1995.

[70] B. Kang, C. H. Riedel, and C. A. Tan. Free vibration analysis of planar curved beams by wave propagation. *Journal of Sound and Vibration*, **171**, 695–702, 2005.

[71] D. J. Mead. Waves and modes in finite beams: application of the phase-closure principle. *Journal of Sound and Vibration*, **171**, 695–702, 1994.

[72] B. R. Mace. Wave reflection and transmission in beams. *Journal of Sound and Vibration*, **97**, 237–246, 1984.

[73] S.-K. Lee, B. R. Mace, and M. J. Brennan. Wave propagation, reflection and transmission in curved beams. *Journal of Sound and Vibration*, **306**, 636–656, 2007.

[74] W. Soedl. *Vibration of shells and plates.* Marcel Dekker Inc., New York, USA, 1981.

[75] W. Weaver Jr., S. P. Timoshenko, and D. H. Young. *Vibration problems in engineering.* John Wiley and Sons, 5th edition, 1990.

[76] L. Brillouin. *Wave propagation in periodic structures.* Dover publications, New York, 2nd edition, 1953.

[77] D. J. Mead. Free wave propagation in periodically supported, infinite beams. *Journal of Sound and Vibration*, **11**(2), 181–197, 1970.

[78] R. M. Orris and M. Petyt. A finite element study of harmonic wave propagation in periodic structures. *Journal of Sound and Vibration*, **33**(2), 223–236, 1974.

[79] D. J. Mead. A general theory of harmonic wave propagation in linear periodic systems with multiple coupling. *Journal of Sound and Vibration*, **27**(2), 235–260, 1973.

[80] D. J. Mead. Wave propagation and natural modes in periodic systems: I. Mono-coupled systems. *Journal of Sound and Vibration*, **40**(1), 1–18, 1975.

[81] D. J. Mead and S. Parthan. Free wave propagation in two-dimensional periodic plates. *Journal of Sound and Vibration*, **64**(3), 325–348, 1979.

[82] D. J. Mead. A new method of analyzing wave propagation in periodic structures; Applications to periodic Timoshenko beams and stiffened plates. *Journal of Sound and Vibration*, **104**(1), 9–27, 1986.

[83] R. Langley. A variational principle for periodic structures. *Journal of Sound and Vibration*, **135**, 135–142, 1989.

[84] R. Langley. On the forced response of one-dimensional periodic structures: vibration localization by damping. *Journal of Sound and Vibration*, **178**(3), 411–428, 1994.

[85] D. J. Mead. Wave propagation in continuous periodic structures: research contributions from Southampton, 1964-1995. *Journal of Sound and Vibration*, **190**(3), 495–524, 1996.

[86] D. L. Thomas. Dynamics of rotationally periodic structures. *International Journal for Numerical Methods in Engineering*, **14**, 81–102, 1979.

[87] D. L. Thomas. Standing waves in rotationally periodic structures. *Journal of Sound and Vibration*, **37**(2), 288–290, 1974.

[88] C. H. J. Fox. A simple theory for the analysis and correction of frequency splitting in slightly imperfect rings. *Journal of Sound and Vibration*, **142**, 227–243, 1990.

[89] A. K. Rourke, S. McWilliam, and C. H. J. Fox. Multi-mode trimming of imperfect rings. *Journal of Sound and Vibration*, **248**(4), 695–724, 2001.

[90] G. F. Miller and H. Pursey. The field and radiation impedance of mechanical radiators on the free surface of a semi-infinite isotropic solid. *Proceeding of the Royal Society of London*, 521–541, 1954.

[91] D. Bindel. *HiQLab*. available online at http://www.cims.nyu.edu/∼dbindel/, accessed in Jan. 2010.

[92] O. C. Zienkiewicz, C. Emson, and P. Bettess. A novel boundary infinite element. *International Journal for Numerical Methods in Engineering*, **19**(3), 393–404, 1983.

[93] J. Lysmer and R. L. Kuhlemeyer. Finite dynamic model for infinite media. *Journal of the Engineering Mechanics division of the ASCE*, **95**(4), 859–877, 1969.

[94] Dassault Systèmes, Abaqus Online documentation. *Abaqus Theory manual*, Version 6.7, 2007.

[95] L. Weisbord. Single beam force transducer with integral mounting isolation, 1969. US Patent No: 3,470,400.

[96] M. Haueis, J. Dual, and R. Buser. A mechanical isolation of a bending resonator. *Sensors and Actuators A*, **128**, 257–264, 2006.

[97] Atlantic Inertial Systems, 2000. Private communication.

[98] C. Fox, S. McWilliam, R. Eley, and C. Fell. Development of multi-axis rate sensors based on vibrating silicon ring structures. In *Proceedings of the RTO SET Symposium on "Emerging Military Capabilities Enabled by Advances in Navigation Sensors"*, 13.1–13.12. Istanbul, Turkey, 2002.

[99] A. E. H. Love. *A treatise on the mathematical theory of elasticity*. University Press, Cambridge, UK, 4th edition, 1952.

[100] R. Eley, C. H. J. Fox, and S. McWilliam. Anisotropy effects on the vibration of circular rings made from crystalline silicon. *Journal of Sound and Vibration*, **228**(1), 11–35, 1999.

[101] P. Childamparam and A. W. Leissa. Vibrations of planar curved beams, rings and arches. *Applied Mechanics Reviews*, **46**, 467–483, 1993.

[102] R. Langley. Analysis of power flow in beams and frameworks using the direct-dynamic stiffness method. *Journal of Sound and Vibration*, **136**, 439–452, 1990.

[103] J. R. Banerjee and F. W. Williams. Coupled bending-torsional dynamic stiffness matrix for Timoshenko beam elements. *Computers and Structures*, **42**, 301–310, 1992.

[104] G. Q. Cai and Y. K. Lin. Wave propagation and scattering in structural networks. *Journal of Engineering Mechanics, American Society of Civil Engineers*, **128**, 145–162, 1991.

[105] Y. Young and Y. K. Lin. Dynamic response of truss-type structural networks: a wave propagation approach. *Journal of Sound and Vibration*, **156**, 27–45, 1992.

[106] W. Hao and Y. Xu. Vibration displacement on substrate due to time-harmonic stress sources from a micromechanical resonator. *Journal of Sound and Vibration*, **322**, 196–215, 2009.

[107] I. A. El Darwish and B. G. Johnston. Torsion of structural shapes. *Journal of the Structural Division, ASCE*, **91**, 429–453, 1965.

[108] E. Eichler. Plate-edge admittances. *Journal of Acoustical Society of America*, **36**, 344–348, 1964.

[109] C. Kauffmann. Input mobilities and power flows for edge-excited, semi-infinite plates. *Journal of Acoustical Society of America*, **103**(4), 1874–1884, 1998.

[110] J. X. Su and A. T. Moorhouse. A closed form solution for the mobility of an edge-excited, semi-infinite plate. *Journal of Acoustical Society of America*, **115**(5), 2075–2082, 2004.

[111] S. P. Timoshenko and J. N. Goodier. *Theory of elasticity*. McGraw-Hill, New York, USA, 3rd edition, 1970.

[112] R. S. Langley and P. J. Shorter. The wave transmission coefficients and coupling loss factors of point connected structures. *Journal of Acoustical Society of America*, **113**(4), 1947–1964, 2003.

[113] C. T. Hugin. A physical description of the response of coupled beams. *Journal of Sound and Vibration*, **203**(4), 563–580, 1997.

[114] G. Pavić. Numerical study of vibration damping, energy and energy flow in a beam-plate system. *Journal of Sound and Vibration*, **291**, 902–931, 2006.

Appendices

Appendix A

Analytical support model

This annexe explains the detailed derivation of the analytical model presented in Chapter 4, Section 4.2. The main equations can also be found in Chapter 4, Section 4.2, while the complete derivation is presented here, starting from three-dimensional elasticity theory. This derivation is mainly based on the work of Miller and Pursey [A.1], and Hao *et al.* [A.2]. Note that it is implicitly assumed in the following procedure that resonator and support have the same out-of-plane thickness (h).

A.1 Three dimensional model of the support

The three-dimensional elasticity of an isotropic solid is summarised by the relationship between the shear stress tensor $\mathbf{T}$ and the strain tensor $\mathbf{\Sigma}$ [A.3]:

$$T_{ij} = \lambda \Theta \delta_{ij} + 2\mu \Sigma_{ij}. \tag{A.1}$$

Here Θ is the dilatation and Σ the strain such that:

$$\Theta = \frac{\partial u_x}{\partial x} + \frac{\partial u_y}{\partial y} + \frac{\partial u_z}{\partial z}, \tag{A.2}$$

$$\Sigma_{ij} = \frac{1}{2}\left(\frac{\partial u_i}{\partial x_j} + \frac{\partial u_j}{\partial x_i}\right) - \frac{1}{3}\Theta\delta_{ij}, \tag{A.3}$$

where $\mathbf{u}(\mathbf{x})$ is the displacement vector and λ and μ are the Lamé constants.

A.2 In-plane reduction

A.2.1 Reduction

For a thin plate of thickness h in the (x, z) plane, linear elasticity theory can be separated into equations for the normal displacement $u_y(y) = v(x, z)$ of the plate and for the in-plane displacements averaged over the depth $\mathbf{u}(x, z) = (u, w)$ with $u = \langle u_x(x, y, z)\rangle_y$, and $w = \langle u_z(x, y, z)\rangle_y$, all function of just two spatial variables. This is achieved by assuming that the stresses in the direction normal to the plane, which must be zero at the nearby stress-free top and bottom surfaces, are zero everywhere.

For example, setting $T_{yy} = 0$ in Equation (A.1) gives:

$$\begin{aligned}
&T_{yy} = \lambda\Theta + 2\mu\left(\frac{\partial v}{\partial y} - \frac{1}{3}\Theta\right) = 0,\\
&\left(\lambda - \frac{2}{3}\mu\right)\left(\frac{\partial u}{\partial x} + \frac{\partial v}{\partial y} + \frac{\partial w}{\partial z}\right) + 2\mu\frac{\partial v}{\partial y} = 0,\\
&\left(\lambda + \frac{4}{3}\mu\right)\frac{\partial v}{\partial y} + \left(\lambda - \frac{2}{3}\mu\right)\left(\frac{\partial u}{\partial x} + \frac{\partial w}{\partial z}\right) = 0,\\
&\frac{\partial v}{\partial y} = -\frac{\lambda - \frac{2}{3}\mu}{\lambda + \frac{4}{3}\mu}\left(\frac{\partial u}{\partial x} + \frac{\partial w}{\partial z}\right).
\end{aligned} \tag{A.4}$$

In order to find the new two-dimensional relationship between stress and strain, Equation (A.1) is simplified using Equation (A.4). From (A.1),

$$\begin{aligned}
&T_{zz} = \lambda\Theta + 2\mu\left(\frac{\partial w}{\partial z} - \frac{1}{3}\Theta\right),\\
&T_{zz} = \left(\lambda - \frac{2}{3}\mu\right)\left(\frac{\partial u}{\partial x} + \frac{\partial v}{\partial y} + \frac{\partial w}{\partial z}\right) + 2\mu\frac{\partial w}{\partial z}.
\end{aligned} \tag{A.5}$$

Substituting Equation (A.4) into (A.5) gives:

$$
\begin{aligned}
T_{zz} &= \left(\lambda - \frac{2}{3}\mu\right)\left(1 - \frac{\lambda - \frac{2}{3}\mu}{\lambda + \frac{4}{3}\mu}\right)\left(\frac{\partial u}{\partial x} + \frac{\partial w}{\partial z}\right) + 2\mu\frac{\partial w}{\partial z}, \\
T_{zz} &= \left(\frac{2\mu\lambda - \frac{4}{3}\mu^2}{\lambda + \frac{4}{3}\mu}\right)\left(\frac{\partial u}{\partial x} + \frac{\partial w}{\partial z}\right) + 2\mu\frac{\partial w}{\partial z}, \\
T_{zz} &= \left(-\mu + \frac{\mu\left(\lambda + \frac{4}{3}\mu\right) + 2\mu\lambda - \frac{4}{3}\mu^2}{\lambda + \frac{4}{3}\mu}\right)\left(\frac{\partial u}{\partial x} + \frac{\partial w}{\partial z}\right) + 2\mu\frac{\partial w}{\partial z}, \\
T_{zz} &= \frac{3\lambda\mu}{\lambda + \frac{4}{3}\mu}\left(\frac{\partial u}{\partial x} + \frac{\partial w}{\partial z}\right) + 2\mu\left(\frac{\partial w}{\partial z} - \frac{1}{2}\left(\frac{\partial u}{\partial x} + \frac{\partial w}{\partial z}\right)\right). \qquad \text{(A.6)}
\end{aligned}
$$

The same analysis can be performed for T_{xx}. From Equation (A.6), the stress-strain relationship in two dimensions becomes:

$$T_{ij}^{(2)} = \bar{\lambda}\Theta^{(2)}\delta_{ij} + 2\bar{\mu}\Sigma_{ij}^{(2)}, \qquad \text{(A.7)}$$

where the indices i and j now only run over x and z. $\Theta^{(2)}$ and $\mathbf{\Sigma}^{(2)}$ are now the two-dimensional dilatation and shear strain tensor, defined as:

$$\Theta^{(2)} = \frac{\partial u_x}{\partial x} + \frac{\partial u_z}{\partial z}, \qquad \text{(A.8)}$$

$$\Sigma_{ij}^{(2)} = \frac{1}{2}\left(\frac{\partial u_i}{\partial x_j} + \frac{\partial u_j}{\partial x_i}\right) - \frac{1}{2}\Theta^{(2)}\delta_{ij}, \qquad \text{(A.9)}$$

and the effective two-dimensional elastic constants are:

$$\bar{\lambda} = \frac{3\lambda\mu}{\lambda + \frac{4}{3}\mu} \qquad \text{and} \qquad \bar{\mu} = \mu. \qquad \text{(A.10)}$$

A.2.2 Wave propagation velocities

The propagation velocity for longitudinal c_L and transverse c_T waves are given by [A.3]:

$$c_L^2 = \frac{\bar{\lambda} + \bar{\mu}}{\rho} \qquad \text{and} \qquad c_T^2 = \frac{\bar{\mu}}{\rho}, \qquad \text{(A.11)}$$

with ρ the mass density. Alternatively, introducing Young's modulus E and Poisson's ratio ν (with $-1 \leq \nu \leq 0.5$) we have:

$$\mu = \frac{E}{2(1+\nu)}, \tag{A.12}$$

$$\lambda = \frac{E}{3(1-2\nu)}, \tag{A.13}$$

and the propagation velocity for longitudinal waves becomes:

$$\begin{aligned}
c_L^2 &= \frac{1}{\rho}\left(\frac{3\mu\lambda}{\lambda+\frac{4}{3}\mu}+\mu\right), \\
c_L^2 &= \frac{\mu}{\rho}\left(\frac{4\lambda+\frac{4}{3}\mu}{\lambda+\frac{4}{3}\mu}\right), \\
c_L^2 &= \frac{E}{2\rho(1+\nu)}\left(\frac{\frac{4E}{3(1-2\nu)}+\frac{2E}{3(1+\nu)}}{\frac{E}{3(1-2\nu)}+\frac{2E}{3(1+\nu)}}\right), \\
c_L^2 &= \frac{E}{2\rho(1+\nu)}\left(\frac{6}{3-3\nu}\right), \\
c_L^2 &= \frac{E}{\rho(1-\nu^2)}.
\end{aligned} \tag{A.14}$$

Similarly, the propagation velocity for transverse waves can be obtained and is given by:

$$c_T^2 = \frac{E}{2\rho(1+\nu)}. \tag{A.15}$$

The longitudinal propagation velocity is larger than the transverse velocity, since ν is always less than 0.5. Therefore, the longitudinal wavelength is larger than the transverse wavelength, and hence the condition for the validity of the two-dimensional thin-plate analysis for the support region can be expressed mathematically as:

$$\frac{\lambda_T}{h} >> 1, \tag{A.16}$$

where λ_T is the transverse wavelength.

A.2.3 Elastic wave equation

The elastic waves are governed by the equation of motion [A.3]:

$$\rho\frac{\partial^2\mathbf{u}}{\partial t^2} = \nabla\mathbf{T}. \tag{A.17}$$

For direction z, Equation (A.17) gives:

$$\begin{aligned}
\rho\frac{\partial^2 w}{\partial t^2} &= \frac{\partial T_{zz}}{\partial z} + \frac{\partial T_{xz}}{\partial x},\\
\rho\frac{\partial^2 w}{\partial t^2} &= \frac{\partial}{\partial z}\left[\bar{\lambda}\left(\frac{\partial u}{\partial x}+\frac{\partial w}{\partial z}\right)+\bar{\mu}\left(2\frac{\partial w}{\partial z}-\left(\frac{\partial u}{\partial x}+\frac{\partial w}{\partial z}\right)\right)\right]+\frac{\partial}{\partial x}\left[\bar{\mu}\left(\frac{\partial w}{\partial x}+\frac{\partial u}{\partial z}\right)\right],\\
\rho\frac{\partial^2 w}{\partial t^2} &= \frac{\partial}{\partial z}\left[\left(\bar{\lambda}+\bar{\mu}\right)\frac{\partial w}{\partial z}+\left(\bar{\lambda}-\bar{\mu}\right)\frac{\partial u}{\partial x}\right]+\frac{\partial}{\partial x}\left[\bar{\mu}\left(\frac{\partial w}{\partial x}+\frac{\partial u}{\partial z}\right)\right],\\
\rho\frac{\partial^2 w}{\partial t^2} &= \left(\bar{\lambda}+\bar{\mu}\right)\frac{\partial^2 w}{\partial z^2}+\bar{\mu}\frac{\partial^2 w}{\partial x^2}+\bar{\lambda}\frac{\partial^2 u}{\partial x\partial z}.
\end{aligned} \tag{A.18}$$

Similarly, for direction x, Equation (A.17) gives:

$$\rho\frac{\partial^2 u}{\partial t^2} = \left(\bar{\lambda}+\bar{\mu}\right)\frac{\partial^2 u}{\partial x^2}+\bar{\mu}\frac{\partial^2 u}{\partial z^2}+\bar{\lambda}\frac{\partial^2 w}{\partial x\partial z}. \tag{A.19}$$

Substituting the set of Equation (A.11) into (A.18) and (A.19), the elastic wave equations governing the in-plane displacements are given by [A.3]:

$$\frac{\partial^2 u}{\partial t^2} = c_L^2\frac{\partial^2 u}{\partial x^2}+c_T^2\frac{\partial^2 u}{\partial z^2}+\left(c_L^2-c_T^2\right)\frac{\partial^2 w}{\partial x\partial z}\ , \tag{A.20}$$

$$\frac{\partial^2 w}{\partial t^2} = c_L^2\frac{\partial^2 w}{\partial z^2}+c_T^2\frac{\partial^2 w}{\partial x^2}+\left(c_L^2-c_T^2\right)\frac{\partial^2 u}{\partial x\partial z}\ . \tag{A.21}$$

A.3 Simplification and Fourier transform

A.3.1 Simplification with the introduction of new operators

By assuming that the displacements are time-dependent at frequency ω (excitation frequency) and have the form $u = \hat{u}\,e^{-\mathrm{i}\omega t}$ and $w = \hat{w}\,e^{-\mathrm{i}\omega t}$, and using the following

definition:

$$\Theta = \Theta^{(2)} = \frac{\partial \hat{u}}{\partial x} + \frac{\partial \hat{w}}{\partial z}, \tag{A.22}$$

$$\Omega = \frac{\partial \hat{w}}{\partial x} - \frac{\partial \hat{u}}{\partial z}, \tag{A.23}$$

the main equations obtained earlier can be re-written and simplified. Those are considered in turn next. Equation (A.20) becomes:

$$\begin{aligned} -\omega^2 \hat{u} &= c_L^2 \left(\frac{\partial^2 u}{\partial x^2} + \frac{\partial^2 w}{\partial x \partial z} \right) + c_T^2 \left(\frac{\partial^2 u}{\partial z^2} - \frac{\partial^2 w}{\partial x \partial z} \right), \\ -\omega^2 \hat{u} &= c_L^2 \frac{\partial \Theta}{\partial x} - c_T^2 \frac{\partial \Omega}{\partial z}. \end{aligned} \tag{A.24}$$

Equation (A.21) becomes:

$$\begin{aligned} -\omega^2 \hat{w} &= c_L^2 \left(\frac{\partial^2 w}{\partial z^2} + \frac{\partial^2 u}{\partial x \partial z} \right) + c_T^2 \left(\frac{\partial^2 w}{\partial x^2} - \frac{\partial^2 u}{\partial x \partial z} \right), \\ -\omega^2 \hat{w} &= c_L^2 \frac{\partial \Theta}{\partial z} + c_T^2 \frac{\partial \Omega}{\partial x}. \end{aligned} \tag{A.25}$$

From Equation (A.25):

$$c_L^2 = \left(-\omega^2 \hat{w} - c_T^2 \frac{\partial \Omega}{\partial x} \right) \frac{\partial z}{\partial \Theta}, \tag{A.26}$$

$$c_T^2 = \left(-\omega^2 \hat{w} - c_L^2 \frac{\partial \Theta}{\partial z} \right) \frac{\partial x}{\partial \Omega}. \tag{A.27}$$

Substituting Equation (A.27) into (A.24) gives:

$$\begin{aligned} -\omega^2 \hat{u} &= c_L^2 \frac{\partial \Theta}{\partial x} - \left(-\omega^2 \hat{w} - c_L^2 \frac{\partial \Theta}{\partial z} \right) \frac{\partial x}{\partial \Omega} \frac{\partial \Omega}{\partial z}, \\ -\omega^2 \frac{\partial \hat{u}}{\partial x} &= c_L^2 \frac{\partial^2 \Theta}{\partial x^2} + \omega^2 \frac{\partial \hat{w}}{\partial z} + c_L^2 \frac{\partial^2 \Theta}{\partial z^2}, \\ c_L^2 \left(\frac{\partial^2 \Theta}{\partial x^2} + \frac{\partial^2 \Theta}{\partial z^2} \right) &+ \omega^2 \Theta = 0. \end{aligned} \tag{A.28}$$

Substituting Equation (A.26) into (A.24) gives:

$$\begin{aligned}
-\omega^2\hat{u} &= \left(-\omega^2\hat{w} - c_T^2\frac{\partial\Omega}{\partial x}\right)\frac{\partial z}{\partial\Theta}\frac{\partial\Theta}{\partial x} - c_T^2\frac{\partial\Omega}{\partial z}, \\
-\omega^2\frac{\partial\hat{u}}{\partial z} &= -\omega^2\frac{\partial\hat{w}}{\partial x} - c_T^2\frac{\partial^2\Omega}{\partial x^2} - c_T^2\frac{\partial^2\Omega}{\partial z^2}, \\
c_T^2\left(\frac{\partial^2\Omega}{\partial x^2} + \frac{\partial^2\Omega}{\partial z^2}\right) &+ \omega^2\Omega = 0.
\end{aligned} \tag{A.29}$$

A.3.2 Introduction of the shear and normal stresses

From the stress-strain relationship (A.7), the shear stress is expressed as:

$$\begin{aligned}
\tau &= 2\bar{\mu}\left[\frac{1}{2}\left(\frac{\partial\hat{w}}{\partial x} + \frac{\partial\hat{u}}{\partial z}\right)\right], \\
\tau &= \rho c_T^2\left(\frac{\partial\hat{w}}{\partial x} + \frac{\partial\hat{u}}{\partial z}\right);
\end{aligned} \tag{A.30}$$

and the normal stress is:

$$\begin{aligned}
\sigma &= \bar{\lambda}\left(\frac{\partial\hat{u}}{\partial x} + \frac{\partial\hat{w}}{\partial z}\right) + \bar{\mu}\left(2\frac{\partial\hat{w}}{\partial z} - \left(\frac{\partial\hat{u}}{\partial x} + \frac{\partial\hat{w}}{\partial z}\right)\right), \\
\sigma &= \left(\bar{\lambda} + \bar{\mu}\right)\frac{\partial\hat{w}}{\partial z} + \left(\bar{\lambda} - \bar{\mu}\right)\frac{\partial\hat{u}}{\partial x}.
\end{aligned}$$

Knowing that:

$$\bar{\lambda} + \bar{\mu} = \rho c_L^2 \tag{A.31}$$

and

$$\bar{\lambda} - \bar{\mu} = \rho c_L^2 - 2\rho c_T^2, \tag{A.32}$$

the normal stress becomes:

$$\sigma = \rho c_L^2\frac{\partial\hat{w}}{\partial z} + \rho\left(c_L^2 - 2c_T^2\right)\frac{\partial\hat{u}}{\partial x}. \tag{A.33}$$

In order to link the operators Θ and Ω with the stresses, the particular values of $\hat{u}$ and $\hat{w}$ found from Equations (A.24) and (A.25) are incorporated into Equa-

tions (A.30) and (A.33). Equations (A.24) and (A.25) can be re-written as:

$$\hat{u} = -\frac{1}{\omega^2}\left(c_L^2\frac{\partial\Theta}{\partial x} - c_T^2\frac{\partial\Omega}{\partial z}\right), \tag{A.34}$$

$$\hat{w} = -\frac{1}{\omega^2}\left(c_L^2\frac{\partial\Theta}{\partial z} + c_T^2\frac{\partial\Omega}{\partial x}\right). \tag{A.35}$$

$$\tag{A.36}$$

Substituting the $\hat{u}$ and $\hat{w}$ values from Equations (A.34) and (A.35) into Equation (A.30) gives:

$$\begin{aligned}\tau &= -\frac{\rho c_T^2}{\omega^2}\left(c_L^2\frac{\partial^2\Theta}{\partial x\partial z} + c_T^2\frac{\partial^2\Omega}{\partial x^2} + c_L^2\frac{\partial^2\Theta}{\partial x\partial z} - c_T^2\frac{\partial^2\Omega}{\partial z^2}\right),\\ \frac{\omega^2}{\rho c_T^4}\tau &= \frac{\partial^2\Omega}{\partial z^2} - \frac{\partial^2\Omega}{\partial x^2} - 2r^2\frac{\partial^2\Theta}{\partial x\partial z}.\end{aligned} \tag{A.37}$$

where r is the ratio of wave speeds:

$$r = \frac{c_L}{c_T}. \tag{A.38}$$

Substituting the $\hat{u}$ and $\hat{w}$ values from Equations (A.34) and (A.35) into Equation (A.33) gives:

$$\begin{aligned}\sigma &= -\frac{\rho c_L^2}{\omega^2}\left(c_L^2\frac{\partial^2\Theta}{\partial z^2} + c_T^2\frac{\partial^2\Omega}{\partial x\partial z}\right) - \left(\frac{\rho c_L^2}{\omega^2} - 2\frac{\rho c_T^2}{\omega^2}\right)\left(c_L^2\frac{\partial^2\Theta}{\partial x^2} - c_T^2\frac{\partial^2\Omega}{\partial x\partial z}\right),\\ \frac{\omega^2}{\rho c_T^4}\sigma &= -r^4\frac{\partial^2\Theta}{\partial z^2} - r^2\frac{\partial^2\Omega}{\partial x\partial z} - \left(r^4\frac{\partial^2\Theta}{\partial x^2} - r^2\frac{\partial^2\Omega}{\partial x\partial z} - 2r^2\frac{\partial^2\Theta}{\partial x^2} + 2\frac{\partial^2\Omega}{\partial x\partial z}\right),\\ \frac{\omega^2}{\rho c_T^4}\sigma &= -2\frac{\partial^2\Omega}{\partial x\partial z} - r^4\frac{\partial^2\Theta}{\partial z^2} + (2r^2 - r^4)\frac{\partial^2\Theta}{\partial x^2}.\end{aligned} \tag{A.39}$$

A.3.3 Fourier Transform of the main equations

Support loss is related to the displacement in the support along the direction of the stresses. The displacements u and w are governed by two-dimensional in-plane elastic wave theory (Equations (A.20) and (A.21)). In order to remove the x variable and obtain an explicit expression from this theory, one may apply the Fourier

transform to Equations (A.24), (A.25), (A.28), (A.29), (A.37) and (A.39).

In the following equations, the subscript F denotes the Fourier transform and ξ is the variable of this transform. The Fourier transform, from the real domain to the wavenumber domain, used is defined as:

$$g(\xi) = \int_{-\infty}^{+\infty} f(x)\, e^{-\mathrm{i}\xi x}\, \mathrm{d}x, \tag{A.40}$$

$$f(x) = \frac{1}{2\pi} \int_{-\infty}^{+\infty} g(\xi)\, e^{\mathrm{i}\xi x}\, \mathrm{d}\xi. \tag{A.41}$$

The following propriety of the Fourier transform will be used:

$$\frac{\partial f(x)}{\partial x} \rightarrow \mathrm{i}\xi f_F. \tag{A.42}$$

Equations (A.24), (A.25), (A.28), (A.29), (A.37) and (A.39) become:

$$-\omega^2 \hat{u}_F = \mathrm{i}\xi c_L^2 \Theta_F - c_T^2 \frac{\mathrm{d}\Omega_F}{\mathrm{d}z}, \tag{A.43}$$

$$-\omega^2 \hat{w}_F = c_L^2 \frac{\mathrm{d}\Theta_F}{\mathrm{d}z} + \mathrm{i}\xi c_T^2 \Omega_F, \tag{A.44}$$

$$\frac{\mathrm{d}^2\Theta_F}{\mathrm{d}z^2} - \left(\xi^2 - \frac{\omega^2}{c_L^2}\right)\Theta_F = 0, \tag{A.45}$$

$$\frac{\mathrm{d}^2\Omega_F}{\mathrm{d}z^2} - \left(\xi^2 - \frac{\omega^2}{c_T^2}\right)\Omega_F = 0, \tag{A.46}$$

$$\frac{\omega^2}{\rho c_T^4}\tau_F = \frac{\mathrm{d}^2\Omega_F}{\mathrm{d}z^2} + \xi^2\Omega_F - 2\mathrm{i}\xi r^2 \frac{\mathrm{d}\Theta_F}{\mathrm{d}z}, \tag{A.47}$$

$$\frac{\omega^2}{\rho c_T^4}\sigma_F = -2\mathrm{i}\xi \frac{\mathrm{d}\Omega_F}{\mathrm{d}z} - r^4 \frac{\mathrm{d}^2\Theta_F}{\mathrm{d}z^2} - \xi^2(2r^2 - r^4)\Theta_F. \tag{A.48}$$

A.4 Solution procedure

A.4.1 Differential equation solution

Equations (A.45) and (A.46) are linear second order differential Equations in z and can be solved easily. The solutions for Equations (A.45) and (A.46) which remain

finite when z is large are:

$$\Theta_F = A\, e^{-\sqrt{\xi^2 - \frac{\omega^2}{c_L^2}}z}, \tag{A.49}$$

$$\Omega_F = B\, e^{-\sqrt{\xi^2 - \frac{\omega^2}{c_T^2}}z}, \tag{A.50}$$

A and B are constants related to the amplitude of the elastic wave and will be determined later by applying boundary conditions at the appropriate excitation stress sources. In order to simplify the notation, Equations (A.49) and (A.50) are expressed as:

$$\Theta_F = A\, e^{-\sqrt{\mathrm{L}}z} \qquad \text{with} \qquad \mathrm{L} = \xi^2 - \frac{\omega^2}{c_L^2}, \tag{A.51}$$

$$\Omega_F = B\, e^{-\sqrt{\mathrm{T}}z} \qquad \text{with} \qquad \mathrm{T} = \xi^2 - \frac{\omega^2}{c_T^2}. \tag{A.52}$$

Differentiating Equations (A.51) and (A.52) with respect to z, one gets:

$$\frac{\mathrm{d}\Theta_F}{\mathrm{d}z} = -A\sqrt{\mathrm{L}}\, e^{-\sqrt{\mathrm{L}}z}, \tag{A.53}$$

$$\frac{\mathrm{d}^2\Theta_F}{\mathrm{d}z^2} = A\mathrm{L}\, e^{-\sqrt{\mathrm{L}}z} = A\left(\xi^2 - \frac{\omega^2}{c_L^2}\right) e^{-\sqrt{\mathrm{L}}z}, \tag{A.54}$$

$$\frac{\mathrm{d}\Omega_F}{\mathrm{d}z} = -B\sqrt{\mathrm{T}}\, e^{-\sqrt{\mathrm{T}}z}, \tag{A.55}$$

$$\frac{\mathrm{d}^2\Omega_F}{\mathrm{d}z^2} = B\mathrm{T}\, e^{-\sqrt{\mathrm{T}}z} = B\left(\xi^2 - \frac{\omega^2}{c_T^2}\right) e^{-\sqrt{\mathrm{T}}z}, \tag{A.56}$$

A.4.2 Derivation of constants

The shear stress τ acting parallel to the x-axis and the normal stress σ acting parallel to the z-axis are generated by the vibration of the sensor. They are illustrated in Chapter 4, Figure 4.1. When the supposed clamped leg undergoes flexural vibration, it is firstly assumed that the support loss due to the vibrating moment is negligible compared to that incurred by the vibrating shear force. A detailed proof of this assumption is presented in Section A.8. Therefore, for flexural vibrations, only shear stresses are considered; and for longitudinal vibration, only normal stresses are considered.

To consider the most general case, let σ_F and τ_F be the value of the normal and shear stresses in the wavenumber domain at $z = 0$. Their particular value will be determined later.

Substituting Equations (A.53) and (A.56) into (A.47), and setting $z = 0$, gives:

$$\begin{aligned}
&\frac{\omega^2}{\rho c_T^4}\tau_F = B\left(\xi^2 - \frac{\omega^2}{c_T^2}\right) + \xi^2 B + 2\mathrm{i}\xi r^2 A\sqrt{\mathrm{L}},\\
&B = \frac{1}{2\xi^2 - \frac{\omega^2}{c_T^2}}\left(\frac{\omega^2}{\rho c_T^4}\tau_F - 2\mathrm{i}\xi r^2 A\sqrt{\mathrm{L}}\right).
\end{aligned} \tag{A.57}$$

Substituting Equations (A.54) and (A.55) into (A.48), and setting $z = 0$, gives:

$$\begin{aligned}
&\frac{\omega^2}{\rho c_T^4}\sigma_F = 2\mathrm{i}\xi B\sqrt{\mathrm{T}} - A\left(r^4\left(\xi^2 - \frac{\omega^2}{c_L^2}\right) + \xi^2\left(2r^2 - r^4\right)\right),\\
&A = \frac{\frac{\omega^2}{\rho c_T^4}\sigma_F}{r^2\left(\frac{\omega^2}{c_T^2} - 2\xi^2\right)} - \frac{2\mathrm{i}\xi B\sqrt{\mathrm{T}}}{r^2\left(\frac{\omega^2}{c_T^2} - 2\xi^2\right)}.
\end{aligned} \tag{A.58}$$

Substituting Equation (A.57) into (A.58) gives:

$$\begin{aligned}
A &= \frac{\frac{\omega^2}{\rho c_T^4}\sigma_F}{r^2\left(\frac{\omega^2}{c_T^2} - 2\xi^2\right)} - \frac{2\mathrm{i}\xi\sqrt{\mathrm{T}}\left(\frac{\omega^2}{\rho c_T^4}\tau_F - 2\mathrm{i}\xi r^2 A\sqrt{\mathrm{L}}\right)}{r^2\left(\frac{\omega^2}{c_T^2} - 2\xi^2\right)\left(2\xi^2 - \frac{\omega^2}{c_T^2}\right)},\\
Ar^2\left(\frac{\omega^2}{c_T^2} - 2\xi^2\right)^2 &= \frac{\omega^2}{\rho c_T^4}\left(\frac{\omega^2}{c_T^2} - 2\xi^2\right)\sigma_F + 2\mathrm{i}\xi\frac{\omega^2}{\rho c_T^4}\tau_F\sqrt{\mathrm{T}} + 4\xi^2 r^2 A\sqrt{\mathrm{L}}\sqrt{\mathrm{T}},\\
A &= \frac{\frac{\omega^2}{\rho c_T^2 c_L^2}\left(\frac{\omega^2}{c_T^2} - 2\xi^2\right)\sigma_F + 2\mathrm{i}\xi\frac{\omega^2}{\rho c_T^2 c_L^2}\tau_F\sqrt{\mathrm{T}}}{\left(\frac{\omega^2}{c_T^2} - 2\xi^2\right)^2 - 4\xi^2\sqrt{\mathrm{L}}\sqrt{\mathrm{T}}}.
\end{aligned} \tag{A.59}$$

Using the notation:

$$N(\xi) = \left(\frac{\omega^2}{c_T^2} - 2\xi^2\right)^2 - 4\xi^2\sqrt{\mathrm{L}}\sqrt{\mathrm{T}}, \tag{A.60}$$

Equation (A.59) becomes:

$$A = \frac{\omega^2\left(\frac{\omega^2}{c_T^2} - 2\xi^2\right)}{\rho c_T^2 c_L^2 N(\xi)}\sigma_F + \frac{2\mathrm{i}\xi\omega^2\sqrt{\mathrm{T}}}{\rho c_T^2 c_L^2 N(\xi)}\tau_F. \tag{A.61}$$

Substituting Equation (A.61) into (A.57) gives:

$$
\begin{aligned}
B &= \frac{1}{2\xi^2 - \frac{\omega^2}{c_T^2}} \left(\frac{\omega^2}{\rho c_T^4} \tau_F + \frac{-2\mathrm{i}\xi r^2 \omega^2 \sqrt{\mathrm{L}} \left(\frac{\omega^2}{c_T^2} - 2\xi^2 \right) \sigma_F + 4\xi^2 \omega^2 r^2 \sqrt{\mathrm{L}} \sqrt{\mathrm{T}} \tau_F}{\rho c_T^2 c_L^2 N(\xi)} \right), \\
B &= \frac{1}{2\xi^2 - \frac{\omega^2}{c_T^2}} \frac{\omega^2}{\rho c_T^4} \left[\left(\left(1 + \frac{4\xi^2 \sqrt{\mathrm{L}} \sqrt{\mathrm{T}}}{N(\xi)} \right) \tau_F \right) - \frac{2\mathrm{i}\xi \left(\frac{\omega^2}{c_T^2} - 2\xi^2 \right) \sqrt{\mathrm{L}}}{N(\xi)} \sigma_F \right], \\
B &= \frac{2\mathrm{i}\xi \omega^2 \sqrt{\mathrm{L}}}{\rho c_T^4 N(\xi)} \sigma_F + \frac{\omega^2 \left(2\xi^2 - \frac{\omega^2}{c_T^2} \right)}{\rho c_T^4 N(\xi)} \tau_F.
\end{aligned} \tag{A.62}
$$

A.4.3 Displacements arising from stress sources

• Longitudinal displacement

By substituting the values of A and B (Equations (A.61) and (A.62)) into Equation (A.44), the longitudinal displacement under the stress sources can be found:

$$
\begin{aligned}
\omega^2 \hat{w}_F &= c_L^2 A \sqrt{\mathrm{L}}\, e^{-\sqrt{\mathrm{L}} z} - \mathrm{i}\xi c_T^2 B\, e^{-\sqrt{\mathrm{T}} z}, \\
\omega^2 \hat{u}_F &= \frac{\omega^2 \left(\frac{\omega^2}{c_T^2} - 2\xi^2 \right) \sqrt{\mathrm{L}}}{\rho c_T^2 N(\xi)}\, e^{-\sqrt{\mathrm{L}} x} \sigma_F + \frac{2\mathrm{i}\xi \omega^2 \sqrt{\mathrm{L}} \sqrt{\mathrm{T}}}{\rho c_T^2 N(\xi)}\, e^{-\sqrt{\mathrm{L}} z} \tau_F \\
&\qquad + \frac{2\xi^2 \omega^2 \sqrt{\mathrm{L}}}{\rho c_T^2 N(\xi)}\, e^{-\sqrt{\mathrm{T}} z} \sigma_F - \frac{\mathrm{i}\xi \omega^2 \left(2\xi^2 - \frac{\omega^2}{c_T^2} \right)}{\rho c_T^2 N(\xi)}\, e^{-\sqrt{\mathrm{T}} z} \tau_F, \\
\hat{w}_F &= \frac{\sqrt{\mathrm{L}}}{\rho c_T^2 N(\xi)} \left(\left(\frac{\omega^2}{c_T^2} - 2\xi^2 \right) e^{-\sqrt{\mathrm{L}} z} + 2\xi^2\, e^{-\sqrt{\mathrm{T}} z} \right) \sigma_F \\
&\qquad + \frac{\mathrm{i}\xi}{\rho c_T^2 N(\xi)} \left(2\sqrt{\mathrm{L}} \sqrt{\mathrm{T}}\, e^{-\sqrt{\mathrm{L}} z} + \left(\frac{\omega^2}{c_T^2} - 2\xi^2 \right) e^{-\sqrt{\mathrm{T}} z} \right) \tau_F.
\end{aligned} \tag{A.63}
$$

• Flexural displacement

By substituting the values of A and B (Equations (A.61) and (A.62)) into Equa-

tion (A.43), the flexural displacement under the stress sources can be found:

$$\begin{aligned}
\omega^2\hat{u}_F &= -\mathrm{i}\xi c_L^2 A\, e^{-\sqrt{\mathrm{L}}z} - c_T^2 B\sqrt{\mathrm{T}}\, e^{-\sqrt{\mathrm{T}}z},\\
\omega^2\hat{u}_F &= \frac{-\mathrm{i}\xi\omega^2\left(\frac{\omega^2}{c_T^2}-2\xi^2\right)}{\rho c_T^2 N(\xi)}\, e^{-\sqrt{\mathrm{L}}z}\sigma_F + \frac{2\xi^2\omega^2\sqrt{\mathrm{T}}}{\rho c_T^2 N(\xi)}\, e^{-\sqrt{\mathrm{L}}z}\tau_F\\
&\qquad - \frac{2\mathrm{i}\xi\omega^2\sqrt{\mathrm{L}}\sqrt{\mathrm{T}}}{\rho c_T^2 N(\xi)}\, e^{-\sqrt{\mathrm{T}}z}\sigma_F - \frac{\omega^2\sqrt{\mathrm{T}}\left(2\xi^2-\frac{\omega^2}{c_T^2}\right)}{\rho c_T^2 N(\xi)}\, e^{-\sqrt{\mathrm{T}}z}\tau_F,\\
\hat{u}_F &= \frac{-\mathrm{i}\xi}{\rho c_T^2 N(\xi)}\left(\left(\frac{\omega^2}{c_T^2}-2\xi^2\right)\, e^{-\sqrt{\mathrm{L}}z} + 2\sqrt{\mathrm{L}}\sqrt{\mathrm{T}}\, e^{-\sqrt{\mathrm{T}}z}\right)\sigma_F\\
&\qquad + \frac{\sqrt{\mathrm{T}}}{\rho c_T^2 N(\xi)}\left(2\xi^2\, e^{-\sqrt{\mathrm{L}}z} + \left(\frac{\omega^2}{c_T^2}-2\xi^2\right)\, e^{-\sqrt{\mathrm{T}}z}\right)\tau_F.
\end{aligned} \tag{A.64}$$

Both displacements $\hat{w}_F$ and $\hat{u}_F$ are found to be a function of the shear and normal stresses. However, as will be shown in Section A.7, the so called "indirect" stress does not have an influence on the mean displacement. The "indirect" stress corresponds to shear stress for a longitudinal displacement and normal stress for a flexural displacement.

A.5 Inverse Fourier transform

A.5.1 Inverse Fourier transform of the displacements

The values of the shear τ_F and normal stresses σ_F are defined by assuming that the stresses are constant over the source region (width of the beam) and created by flexural and longitudinal vibrations of the sensor respectively. The effect of the bending moment occurring during flexural vibrations is neglected here. This hypothesis will be validated in Section A.8. Let us define:

$$\tau = \hat{\tau} \quad \text{for} \quad |x| < \frac{b}{2} \quad \text{and} \quad \tau = 0 \quad \text{for} \quad |x| > \frac{b}{2}; \tag{A.65}$$

$$\sigma = \hat{\sigma} \quad \text{for} \quad |x| < \frac{b}{2} \quad \text{and} \quad \sigma = 0 \quad \text{for} \quad |x| > \frac{b}{2}. \tag{A.66}$$

Therefore, the Fourier transform of τ and σ are:

$$\tau_F = \frac{2\hat{\tau}\sin\left(\xi\frac{b}{2}\right)}{\xi}, \tag{A.67}$$

$$\sigma_F = \frac{2\hat{\sigma}\sin\left(\xi\frac{b}{2}\right)}{\xi}. \tag{A.68}$$

For the flexural displacement, only shear stresses are considered (the "indirect" stress source has no effect, see Section A.7). Introducing the particular value of τ_F (Equation (A.67)) into the displacement definition (A.64) and applying the inverse Fourier transform gives:

$$\hat{u} = \frac{\hat{\tau}}{\pi\rho c_T^2}\int_{-\infty}^{\infty}\frac{\sqrt{\mathrm{T}}\sin\left(\xi\frac{b}{2}\right)}{\xi N(\xi)}\left(\left(\frac{\omega^2}{c_T^2}-2\xi^2\right)e^{-\sqrt{\mathrm{T}}z}+2\xi^2\,e^{-\sqrt{\mathrm{L}}z}\right)e^{\mathrm{i}\xi x}\,\mathrm{d}\xi \tag{A.69}$$

For the longitudinal displacement, only normal stresses are considered (the "indirect" stress source has no effect, see Section A.7). Introducing the particular value of σ_F (Equation (A.68)) into the displacement definition (A.63) and applying the inverse Fourier transform gives:

$$\hat{w} = \frac{\hat{\sigma}}{\pi\rho c_T^2}\int_{-\infty}^{\infty}\frac{\sqrt{\mathrm{L}}\sin\left(\xi\frac{b}{2}\right)}{\xi N(\xi)}\left(\left(\frac{\omega^2}{c_T^2}-2\xi^2\right)e^{-\sqrt{\mathrm{L}}z}+2\xi^2\,e^{-\sqrt{\mathrm{T}}z}\right)e^{\mathrm{i}\xi x}\,\mathrm{d}\xi \tag{A.70}$$

To simplify the integrals, a change of variable is introduced. By defining:

$$\gamma = \xi\frac{c_L}{\omega}, \qquad \xi = \gamma\frac{\omega}{c_L} \qquad \text{and} \qquad \mathrm{d}\xi = \frac{\omega}{c_L}\,\mathrm{d}\gamma, \tag{A.71}$$

one can get:

$$\sqrt{\mathrm{T}} = \sqrt{\xi^2-\frac{\omega^2}{c_T^2}} = \frac{\omega}{c_L}\sqrt{\gamma^2-r^2}, \tag{A.72}$$

$$\sqrt{\mathrm{L}} = \sqrt{\xi^2-\frac{\omega^2}{c_L^2}} = \frac{\omega}{c_L}\sqrt{\gamma^2-1}, \tag{A.73}$$

where r is defined in Equation (A.38). Therefore, from Equation (A.60):

$$N(\xi) = \left(\frac{\omega^2}{c_T^2} - r^2\right)^2 - 4\xi^2\sqrt{\mathrm{L}}\sqrt{\mathrm{T}} = \frac{\omega^4}{c_L^4} N_0(\gamma), \tag{A.74}$$

$$N_0(\gamma) = \left(2\gamma^2 - r^2\right)^2 - 4\gamma^2\sqrt{\gamma^2 - 1}\sqrt{\gamma^2 - r^2}. \tag{A.75}$$

Using Equations (A.71) to (A.75), the flexural displacement (Equation (A.69)) can be simplified to:

$$\begin{aligned}\hat{u} = \frac{\hat{\tau}}{\pi\rho c_T^2} \int_{-\infty}^{\infty} \frac{\sqrt{\gamma^2 - r^2}\sin\left(\gamma\frac{b\omega}{2c_L}\right)}{\frac{\omega}{c_L}\gamma N_0(\gamma)} \Bigg(\left(r^2 - 2\gamma^2\right) e^{-\frac{\omega}{c_L} z\sqrt{\gamma^2 - r^2}} \\ + 2\gamma^2\, e^{-\frac{\omega}{c_L} z\sqrt{\gamma^2 - 1}} \Bigg) e^{\mathrm{i}\frac{\omega}{c_L}\gamma x}\, \mathrm{d}\gamma.\end{aligned} \tag{A.76}$$

To simplify the notation, the quantity $\dfrac{b\omega}{2c_L}$ will be denoted as:

$$\mathcal{A} = \frac{b\omega}{2c_L}. \tag{A.77}$$

The flexural displacement, at $z = 0$, becomes:

$$\hat{u}_{z=0} = \frac{br^2\hat{\tau}}{2\pi\rho c_T^2} \int_{-\infty}^{\infty} \frac{\sqrt{\gamma^2 - r^2}\sin\left(\mathcal{A}\gamma\right)}{\mathcal{A}\gamma N_0(\gamma)} e^{\mathrm{i}\frac{\omega}{c_L}\gamma x}\, \mathrm{d}\gamma. \tag{A.78}$$

Considering the parity of the integrand, it can be shown that it simplifies to:

$$\hat{u}_{z=0} = \frac{br^2\hat{\tau}}{\pi\rho c_T^2} \int_{0}^{\infty} \frac{\sqrt{\gamma^2 - r^2}\sin\left(\mathcal{A}\gamma\right)}{\mathcal{A}\gamma N_0(\gamma)} \cos\left(\frac{\omega}{c_L}\gamma x\right) \mathrm{d}\gamma. \tag{A.79}$$

Using the same approach in the longitudinal displacement (Equation (A.70)), one can get at $z = 0$:

$$\hat{w}_{z=0} = \frac{br^2\hat{\sigma}}{\pi\rho c_T^2} \int_{0}^{\infty} \frac{\sqrt{\gamma^2 - 1}\sin\left(\mathcal{A}\gamma\right)}{\mathcal{A}\gamma N_0(\gamma)} \cos\left(\frac{\omega}{c_L}\gamma x\right) \mathrm{d}\gamma. \tag{A.80}$$

A.5.2 Derivation of the mean displacement over the source region

In order to calculate the energy loss and the power transmitted to the support, the mean displacement over the exciting source region (width of the sensor) is required. An integral representation for the mean flexural displacement is:

$$\bar{u}_{z=0} = \frac{1}{b}\int_{-b/2}^{b/2} \hat{u}_{z=0}\,\mathrm{d}x, \tag{A.81}$$

$$\bar{u}_{z=0} = \frac{r^2\hat{\tau}}{\pi\rho c_T^2}\int_{-b/2}^{b/2}\left[\int_0^\infty \frac{\sqrt{\gamma^2-r^2}\sin(\mathcal{A}\gamma)}{\mathcal{A}\gamma N_0(\gamma)}\cos\left(\frac{\omega}{c_L}\gamma x\right)\,\mathrm{d}\gamma\right]\mathrm{d}x. \tag{A.82}$$

Considering the parity in x of the integrand (quantity inside the brackets), this equation can be re-organised as:

$$\begin{aligned}
\bar{u}_{z=0} &= \frac{2r^2\hat{\tau}}{\pi\rho c_T^2}\int_0^\infty \frac{\sqrt{\gamma^2-r^2}\sin(\mathcal{A}\gamma)}{\mathcal{A}\gamma N_0(\gamma)}\left[\int_0^{b/2}\cos\left(\frac{\omega}{c_L}\gamma x\right)\,\mathrm{d}x\right]\mathrm{d}\gamma,\\
\bar{u}_{z=0} &= \frac{2r^2\hat{\tau}}{\pi\rho c_T^2}\int_0^\infty \frac{\sqrt{\gamma^2-r^2}\sin(\mathcal{A}\gamma)}{\mathcal{A}\gamma N_0(\gamma)}\left[\frac{\sin(\mathcal{A}\gamma)}{\mathcal{A}\gamma}\right]\mathrm{d}\gamma,\\
\bar{u}_{z=0} &= \frac{br^2\hat{\tau}}{\pi\rho c_T^2}\int_0^\infty \frac{\sqrt{\gamma^2-r^2}}{N_0(\gamma)}\left[\frac{\sin(\mathcal{A}\gamma)}{\mathcal{A}\gamma}\right]^2\mathrm{d}\gamma.
\end{aligned} \tag{A.83}$$

The imaginary part of the integrand of Equation (A.83), which will contribute to support loss (see Section A.6), is non zero for $0 < \gamma < r$. With usual resonator dimensions and corresponding natural frequencies, the term $\mathcal{A}\gamma = \frac{b\omega}{2c_L}\gamma$ is relatively small compared to 1 for this range of γ-value, which allows Equation (A.83) to be simplified to:

$$\bar{u}_{z=0} = \frac{br^2\hat{\tau}}{\pi\rho c_T^2}\Psi_u, \tag{A.84}$$

with

$$\Psi_u = \int_0^\infty \frac{\sqrt{\gamma^2-r^2}}{\left(2\gamma^2-r^2\right)^2 - 4\gamma^2\sqrt{\gamma^2-1}\sqrt{\gamma^2-r^2}}\,\mathrm{d}\gamma. \tag{A.85}$$

Equation (A.84) is the average displacement along the x-axis and over the source region induced by the stress τ. The same approach can be used to get the average longitudinal displacement along the z-axis and over the source region induced by

the stress σ:

$$\bar{w}_{z=0} = \frac{br^2\hat{\sigma}}{\pi\rho c_T^2}\Psi_w, \tag{A.86}$$

with

$$\Psi_w = \int_0^\infty \frac{\sqrt{\gamma^2-1}}{\left(2\gamma^2-r^2\right)^2 - 4\gamma^2\sqrt{\gamma^2-1}\sqrt{\gamma^2-r^2}}\,\mathrm{d}\gamma. \tag{A.87}$$

A.6 Energy loss calculation

The quality factor is defined as:

$$Q = 2\pi\frac{W}{\Delta W}, \tag{A.88}$$

where ΔW denotes the energy dissipated per cycle of vibration and W denotes the maximum vibration energy stored per cycle.

Once the displacement induced by the stresses over the source region has been determined (using Equation (A.84) or (A.86)), the amount of energy loss per cycle from the support can be calculated explicitly as:

$$\Delta W = \frac{2\pi}{\omega}\Pi \tag{A.89}$$

where Π is the average power transmitted to the support, and is defined as:

$$\Pi = \frac{1}{2}\,\mathrm{Re}\left(\mathrm{Force}\cdot\mathrm{Velocity}^*\right), \tag{A.90}$$

where Re is the real part and * denotes the complex conjugate. Considering a shear force source S creating a shear stress τ and its induced flexural displacement $\bar{u}_{z=0}$; and assuming that the force and displacement are time-dependent at frequency ω,

Equation (A.90) becomes:

$$\begin{aligned}\Pi_u &= \frac{1}{2}\,\mathrm{Re}\left(S\,e^{-\mathrm{i}\omega t}\cdot\left(-\mathrm{i}\omega\bar{u}_{z=0}\,e^{-\mathrm{i}\omega t}\right)^*\right),\\ \Pi_u &= \frac{1}{2}\,\mathrm{Re}\left(S\cdot\mathrm{i}\omega\bar{u}^*_{z=0}\right),\\ \Pi_u &= \frac{\omega}{2}\Big(\,\mathrm{Re}(S)\,\mathrm{Im}(\bar{u}_{z=0}) - \,\mathrm{Im}(S)\,\mathrm{Re}(\bar{u}_{z=0})\Big).\end{aligned} \tag{A.91}$$

The displacement $\bar{u}_{z=0}$ was defined previously (in Equation (A.84)). Its real and imaginary parts are:

$$\mathrm{Re}(\bar{u}_{z=0}) = \frac{r^2}{h\pi\rho c_T^2}\Big(\,\mathrm{Re}(S)\,\mathrm{Re}(\Psi_u) - \,\mathrm{Im}(S)\,\mathrm{Im}(\Psi_u)\Big), \tag{A.92}$$

$$\mathrm{Im}(\bar{u}_{z=0}) = \frac{r^2}{h\pi\rho c_T^2}\Big(\,\mathrm{Re}(S)\,\mathrm{Im}(\Psi_u) + \,\mathrm{Im}(S)\,\mathrm{Re}(\Psi_u)\Big), \tag{A.93}$$

where $\hat{\tau} = S/bh$ has been used, h being the resonator and support thicknesses.

Therefore, the energy loss can be defined as (from Equation (A.89)):

$$\begin{aligned}\Delta W_u &= \pi\Bigg[\,\mathrm{Re}(S)\left(\frac{r^2}{h\pi\rho c_T^2}\Big(\,\mathrm{Re}(S)\,\mathrm{Im}(\Psi_u) + \,\mathrm{Im}(S)\,\mathrm{Re}(\Psi_u)\Big)\right)\\ &\qquad - \,\mathrm{Im}(S)\left(\frac{r^2}{h\pi\rho c_T^2}\Big(\,\mathrm{Re}(S)\,\mathrm{Re}(\Psi_u) - \,\mathrm{Im}(S)\,\mathrm{Im}(\Psi_u)\Big)\right)\Bigg],\\ \Delta W_u &= \frac{r^2}{h\rho c_T^2}\Big(\Big(\,\mathrm{Re}(S)\Big)^2 + \Big(\,\mathrm{Im}(S)\Big)^2\Big)\,\mathrm{Im}(\Psi_u),\\ \Delta W_u &= \frac{r^2}{h\rho c_T^2}\Big|S\Big|^2\,\mathrm{Im}(\Psi_u).\end{aligned} \tag{A.94}$$

Using the material properties, Equation (A.94) can be re-written as:

$$\Delta W_u = \frac{4(1+\nu)}{Eh(1-\nu)}\Big|S\Big|^2\,\mathrm{Im}(\Psi_u). \tag{A.95}$$

using the same approach for the normal force T (such that $\hat{\sigma} = T/bh$) and the longitudinal displacement, the energy loss from a normal stress source can be expressed as:

$$\Delta W_w = \frac{4(1+\nu)}{Eh(1-\nu)}\Big|T\Big|^2\,\mathrm{Im}(\Psi_w). \tag{A.96}$$

Equations (A.95) and (A.96) show that only the imaginary part of the integrals Ψ_u and Ψ_w are needed to calculate the amount of energy loss.

A.7 Proof 1: The indirect stress has no contribution to the mean displacement

From Equation (A.64), the flexural displacement in the wavenumber domain produced by shear and normal stresses at the boundary is expressed as:

$$\hat{u}_F = \frac{-\mathrm{i}\xi}{\rho c_T^2 N(\xi)} \left(\left(\frac{\omega^2}{c_T^2} - 2\xi^2 \right) e^{-\sqrt{\mathrm{L}}z} + 2\sqrt{\mathrm{L}}\sqrt{\mathrm{T}}\, e^{-\sqrt{\mathrm{T}}z} \right) \sigma_F + \frac{\sqrt{\mathrm{T}}}{\rho c_T^2 N(\xi)} \left(2\xi^2\, e^{-\sqrt{\mathrm{L}}z} + \left(\frac{\omega^2}{c_T^2} - 2\xi^2 \right) e^{-\sqrt{\mathrm{T}}z} \right) \tau_F. \tag{A.97}$$

The first term (function of σ_F) of this equation and the second term (function of τ_F) in Equation (A.63) will be called indirect term. The following derivation is performed for the indirect term of the flexural displacement but the same approach can be used for the indirect term of the longitudinal displacement.

Let $\hat{u}_{F\text{–in}}$ be the indirect term of the flexural displacement, such that:

$$\hat{u}_{F\text{–in}} = \frac{-\mathrm{i}\xi}{\rho c_T^2 N(\xi)} \left(\left(\frac{\omega^2}{c_T^2} - 2\xi^2 \right) e^{-\sqrt{\mathrm{L}}z} + 2\sqrt{\mathrm{L}}\sqrt{\mathrm{T}}\, e^{-\sqrt{\mathrm{T}}z} \right) \sigma_F. \tag{A.98}$$

Considering that the normal stress σ is constant over the source region, such that $\sigma = \hat{\sigma}$ for $|x| < b/2$ and $\sigma = 0$ elsewhere (see Section 4.2.3 with the effect of the bending moment taken as negligible, see Section A.8), its Fourier transform σ_F will be defined as:

$$\sigma_F = \frac{2\hat{\sigma} \sin\left(\xi \frac{b}{2}\right)}{\xi}. \tag{A.99}$$

Substituting this particular value of σ_F into Equation (A.98) and applying the

inverse Fourier transform gives:

$$\hat{u}_{\text{in}} = -\frac{\hat{\sigma}}{\pi\rho c_T^2}\int_{-\infty}^{\infty}\frac{\mathrm{i}\sin\left(\xi\frac{b}{2}\right)}{N(\xi)}\left(\left(\frac{\omega^2}{c_T^2}-2\xi^2\right)e^{-\sqrt{\mathrm{L}}z}+2\sqrt{\mathrm{L}}\sqrt{\mathrm{T}}\,e^{-\sqrt{\mathrm{T}}z}\right)e^{\mathrm{i}\xi x}\,\mathrm{d}\xi. \tag{A.100}$$

Using the change of variable defined in Equation (A.71) and the definition of $N_0(\gamma)$ from Equation (A.75), Equation (A.100) becomes:

$$\begin{aligned}\hat{u}_{\text{in}} = -\frac{\hat{\sigma}}{\pi\rho c_T^2}\int_{-\infty}^{\infty}\frac{\mathrm{i}\sin\left(\mathcal{A}\gamma\right)}{\frac{\omega}{c_L}N_0(\gamma)}\Bigg(&\left(r^2-2\gamma^2\right)e^{-\frac{\omega}{c_L}z\sqrt{\gamma^2-1}}\\&+2\sqrt{\gamma^2-1}\sqrt{\gamma^2-r^2}\,e^{-\frac{\omega}{c_L}z\sqrt{\gamma^2-r^2}}\Bigg)e^{\mathrm{i}\frac{\omega}{c_L}\gamma x}\,\mathrm{d}\gamma.\end{aligned} \tag{A.101}$$

This displacement at $z = 0$ is:

$$\hat{u}_{z=0\text{–in}} = -\frac{\hat{\sigma}}{\pi\rho c_T^2}\int_{-\infty}^{\infty}\frac{\mathrm{i}\sin\left(\mathcal{A}\gamma\right)}{\frac{\omega}{c_L}N_0(\gamma)}\left(r^2-2\gamma^2+2\sqrt{\gamma^2-1}\sqrt{\gamma^2-r^2}\right)e^{\mathrm{i}\frac{\omega}{c_L}\gamma x}\,\mathrm{d}\gamma. \tag{A.102}$$

Considering the parity of the integrand, Equation (A.102) becomes:

$$\hat{u}_{z=0\text{–in}} = \frac{2\hat{\sigma}}{\pi\rho c_T^2}\int_{0}^{\infty}\frac{\sin\left(\mathcal{A}\gamma\right)}{\frac{\omega}{c_L}N_0(\gamma)}\left(r^2-2\gamma^2+2\sqrt{\gamma^2-1}\sqrt{\gamma^2-r^2}\right)\sin\left(\frac{\omega}{c_L}\gamma x\right)\,\mathrm{d}\gamma. \tag{A.103}$$

To calculate the energy loss, the mean displacement over the source region is required, and this is defined in Equation (A.81). Here, the mean flexural displacement due to the indirect normal stress is:

$$\begin{aligned}\bar{u}_{z=0\text{–in}} = \frac{2\hat{\sigma}}{b\pi\rho c_T^2}\int_{-b/2}^{b/2}\Bigg[\int_{0}^{\infty}\frac{\sin\left(\mathcal{A}\gamma\right)}{\frac{\omega}{c_L}N_0(\gamma)}\Bigg(&r^2-2\gamma^2\\&+2\sqrt{\gamma^2-1}\sqrt{\gamma^2-r^2}\Bigg)\sin\left(\frac{\omega}{c_L}\gamma x\right)\,\mathrm{d}\gamma\Bigg]\,\mathrm{d}x.\end{aligned} \tag{A.104}$$

The integrand quantity (inside the brackets) is an odd function in x and therefore the mean displacement evaluates is zero:

$$\hat{u}_{z=0\text{–in}} = 0. \tag{A.105}$$

The same approach can be used for the longitudinal displacement created by shear stress and one gets:

$$\hat{w}_{z=0\text{–in}} = 0. \tag{A.106}$$

A.8 Proof 2: The bending moment effect is negligible

Cross and Lifshitz [A.4] explained that when a resonator is vibrating tangentially to its support, the contribution of the normal stress due to the oscillating moment to the power radiated can be neglected compared to the contribution of the shear stress. This section presents analytical/numerical proofs of their prediction. Stresses due to the bending moment at the clamped end are added into the model. Flexural vibrations of the resonator will produce a bending moment in addition to the usual shear force. This moment induces a normal stress linearly dependent on the x-value over the width of the resonator. It gives a new boundary condition for the support model, such that for $|x| < b/2$:

$$\sigma = -\frac{M}{I}x, \tag{A.107}$$

where M is the bending moment at the anchor point induced by flexural vibrations of the resonator and I is the second moment of inertia of the resonator. The Fourier transform of this normal stress σ is:

$$\sigma_F = -2\mathrm{i}\frac{M}{I\xi^2}\left(\xi\frac{b}{2}\cos\left(\xi\frac{b}{2}\right) - \sin\left(\xi\frac{b}{2}\right)\right). \tag{A.108}$$

This additional external source will have three different effects:

- it is expected to change the displacement w in the support along the z-axis as Equation (A.63) is function of σ_F, see Section A.8.1;
- it is also expected to change the displacement u in the support along the x-axis as Equation (A.64) is also a function of σ_F, see Section A.8.2;

- it is expected to induce another source of energy loss, see Section A.8.3. As presented earlier, the energy loss is defined as the product of the "force" by the corresponding "displacement". The energy loss ΔW_s, created directly by a bending moment is (similar to Equation (A.89)):

$$\Delta W_s = \frac{2\pi}{\omega}\Pi_s \tag{A.109}$$

with $\Pi_s = \frac{1}{2}\,\mathrm{Re}(M \cdot \mathrm{i}\omega \frac{\mathrm{d}\bar{u}^*}{\mathrm{d}z}_{z=0})$. Rearranging gives:

$$\Delta W_s = \pi\,\mathrm{Re}(M \cdot \mathrm{i}\frac{\mathrm{d}\bar{u}^*}{\mathrm{d}z}_{z=0}) \tag{A.110}$$

The following three sections will present each case individually and the effect of the bending moment will be derived in each case.

A.8.1 Change of w due to a bending moment

Substituting the particular value of σ_F (Equation (A.108)) into Equation (A.64)), setting $z = 0$ and applying the inverse Fourier transform gives:

$$\hat{w}_{z=0} = \frac{-\mathrm{i}M\omega^2}{I\pi\rho c_T^4}\int_{-\infty}^{\infty}\frac{\sqrt{\mathrm{L}}}{\xi^2 N(\xi)}\left(\xi\frac{b}{2}\cos\left(\xi\frac{b}{2}\right) - \sin\left(\xi\frac{b}{2}\right)\right)e^{\mathrm{i}\xi x}\,\mathrm{d}\xi. \tag{A.111}$$

Using the parity of the integrand gives:

$$\hat{w}_{z=0} = \frac{2M\omega^2}{I\pi\rho c_T^4}\int_{0}^{\infty}\frac{\sqrt{\mathrm{L}}}{\xi^2 N(\xi)}\left(\xi\frac{b}{2}\cos\left(\xi\frac{b}{2}\right) - \sin\left(\xi\frac{b}{2}\right)\right)\sin\left(\xi x\right)\,\mathrm{d}\xi \tag{A.112}$$

To calculate the energy loss, the mean displacement over the source region is used. This mean displacement, defined in Equation (A.81), is zero when applied to the displacement in the above Equation (A.112) because the integrand is an odd function of x. This means that the introduction of a bending moment does not change the mean longitudinal displacement $\bar{w}_{z=0}$.

A.8.2 Change of u due to a bending moment

Substituting the particular value of σ_F (Equation (A.108)) into Equation (A.64) and applying the inverse Fourier transform gives:

$$\hat{u} = \frac{M}{I\pi\rho c_T^2}\int_{-\infty}^{\infty} \frac{\sin\left(\xi\frac{b}{2}\right) - \xi\frac{b}{2}\cos\left(\xi\frac{b}{2}\right)}{\xi N(\xi)} \left(\left(\frac{\omega^2}{c_T^2} - 2\xi^2\right) e^{-\sqrt{\mathrm{L}}z} + 2\sqrt{\mathrm{L}}\sqrt{\mathrm{T}}\, e^{-\sqrt{\mathrm{T}}z} \right) e^{\mathrm{i}\xi x}\, \mathrm{d}\xi. \tag{A.113}$$

Using the parity of the integrand gives:

$$\hat{u} = \frac{2M}{I\pi\rho c_T^2}\int_{0}^{\infty} \frac{\sin\left(\xi\frac{b}{2}\right) - \xi\frac{b}{2}\cos\left(\xi\frac{b}{2}\right)}{\xi N(\xi)} \left(\left(\frac{\omega^2}{c_T^2} - 2\xi^2\right) e^{-\sqrt{\mathrm{L}}z} + 2\sqrt{\mathrm{L}}\sqrt{\mathrm{T}}\, e^{-\sqrt{\mathrm{T}}z} \right) \cos\left(\xi x\right)\, \mathrm{d}\xi. \tag{A.114}$$

The change of variable defined in Equation (A.71) is re-used here and the displacement becomes:

$$\hat{u} = \frac{2r^2 M}{I\pi\rho\omega^2}\int_{0}^{\infty} \frac{\sin\left(\mathcal{A}\gamma\right) - \mathcal{A}\gamma\cos\left(\mathcal{A}\gamma\right)}{\gamma N_0(\gamma)} \left(\left(r^2 - 2\gamma^2\right) e^{-\frac{\omega}{c_L}z\sqrt{\gamma^2-1}} + 2\sqrt{\gamma^2-1}\sqrt{\gamma^2-r^2}\, e^{-\frac{\omega}{c_L}z\sqrt{\gamma^2-r^2}} \right) \cos\left(\gamma\frac{\omega}{c_L}x\right)\, \mathrm{d}\gamma. \tag{A.115}$$

With the definition of the mean displacement as in Equation (A.81), it is useful to notice that:

$$\frac{1}{b}\int_{-\frac{b}{2}}^{\frac{b}{2}} \cos\left(\gamma\frac{\omega}{c_L}x\right)\, \mathrm{d}x = \frac{\sin\left(\mathcal{A}\gamma\right)}{\mathcal{A}\gamma} \tag{A.116}$$

where $\mathcal{A} = \dfrac{b\omega}{2c_L}$. The mean flexural displacement becomes (from Equation (A.115)):

$$\bar{u} = \frac{2r^2 M}{I\pi\rho\omega^2}\int_0^\infty \frac{(\sin(\mathcal{A}\gamma) - \mathcal{A}\gamma\cos(\mathcal{A}\gamma))\sin(\mathcal{A}\gamma)}{\mathcal{A}\gamma^2 N_0(\gamma)}\Bigg(\left(r^2 - 2\gamma^2\right) e^{-\frac{\omega}{c_L}z\sqrt{\gamma^2-1}} + 2\sqrt{\gamma^2-1}\sqrt{\gamma^2-r^2}\, e^{-\frac{\omega}{c_L}z\sqrt{\gamma^2-r^2}}\Bigg)\mathrm{d}\gamma. \tag{A.117}$$

For $z = 0$, Equation (A.117) becomes:

$$\bar{u}_{z=0} = \frac{2r^2 M}{I\pi\rho\omega^2}\int_0^\infty \frac{(\sin(\mathcal{A}\gamma) - \mathcal{A}\gamma\cos(\mathcal{A}\gamma))\sin(\mathcal{A}\gamma)}{\mathcal{A}\gamma^2 N_0(\gamma)}\Big(r^2 - 2\gamma^2 + 2\sqrt{\gamma^2-1}\sqrt{\gamma^2-r^2}\Big)\mathrm{d}\gamma. \tag{A.118}$$

The imaginary part of this displacement is very small (approximately 100 times smaller) compared to the one created by the shear force during flexural vibration. The change of displacement and therefore energy loss due to the bending moment in this case can thus be neglected.

A.8.3 Energy loss due to a bending moment

From Equation (A.117), it is possible to calculate the slope of the mean displacement at $z = 0$.

$$\frac{\mathrm{d}\bar{u}}{\mathrm{d}z}_{z=0} = \frac{2r^2 M}{I\pi\rho\omega^2}\int_0^\infty \frac{(\sin(\mathcal{A}\gamma) - \mathcal{A}\gamma\cos(\mathcal{A}\gamma))\sin(\mathcal{A}\gamma)}{\mathcal{A}\gamma^2 N_0(\gamma)}\Bigg(-\frac{\omega}{c_L}\sqrt{\gamma^2-1}\left(r^2-2\gamma^2\right) - 2\frac{\omega}{c_L}\sqrt{\gamma^2-r^2}\sqrt{\gamma^2-1}\sqrt{\gamma^2-r^2}\Bigg)\mathrm{d}\gamma,$$

$$\frac{\mathrm{d}\bar{u}}{\mathrm{d}z}_{z=0} = \frac{2r^2 M}{I\pi\rho\omega^2}\int_0^\infty \frac{(\sin(\mathcal{A}\gamma) - \mathcal{A}\gamma\cos(\mathcal{A}\gamma))\sin(\mathcal{A}\gamma)}{\mathcal{A}\gamma^2 N_0(\gamma)}\Bigg(-\frac{\omega}{c_L}\sqrt{\gamma^2-1}\left(r^2-2\gamma^2+2\left(\gamma^2-r^2\right)\right)\Bigg)\mathrm{d}\gamma,$$

$$\frac{\mathrm{d}\bar{u}}{\mathrm{d}z}_{z=0} = \frac{2r^4 M}{I\pi\rho\omega c_L}\int_0^\infty \frac{(\sin(\mathcal{A}\gamma) - \mathcal{A}\gamma\cos(\mathcal{A}\gamma))\sin(\mathcal{A}\gamma)}{\mathcal{A}\gamma^2 N_0(\gamma)}\sqrt{\gamma^2-1}\,\mathrm{d}\gamma. \tag{A.119}$$

The imaginary part of the integrand of Equation (A.119), which will contribute to support loss (see Section A.6), is non zero for $0 < \gamma < r$. For typical resonator dimensions and corresponding natural frequencies, the term $\mathcal{A}\gamma = \frac{b\omega}{2c_L}\gamma$ is relatively small compared to 1 for this range of γ-value, which allows the following simplification to be made:

$$\frac{(\sin(\mathcal{A}\gamma) - \mathcal{A}\gamma\cos(\mathcal{A}\gamma))\sin(\mathcal{A}\gamma)}{\mathcal{A}\gamma} \approx \frac{(\mathcal{A}\gamma)^3}{3}. \tag{A.120}$$

using Equation (A.120) to simplify Equation (A.119) gives the following value for the slope:

$$\frac{\mathrm{d}\bar{u}}{\mathrm{d}z}_{z=0} = \frac{\omega^2 M}{\pi\rho c_T^4 h}\Psi_s. \tag{A.121}$$

Where

$$\Psi_s = \int_0^\infty \frac{\gamma^2\sqrt{\gamma^2-1}}{(2\gamma^2-r^2)^2 - 4\gamma^2\sqrt{\gamma^2-1}\sqrt{\gamma^2-r^2}}\,\mathrm{d}\gamma. \tag{A.122}$$

Using Equation (A.110) and the imaginary part of Ψ_s, it can be concluded that for typical resonator dimensions, the energy loss due to the bending moment is of the order of 1000 times smaller than due to shear stress. On this basis, it can be neglected.

References

[A.1] G. F. Miller and H. Pursey. The field and radiation impedance of mechanical radiators on the free surface of a semi-infinite isotropic solid. *Proceeding of the Royal Society of London*, 521-541, 1954.

[A.2] Z. Hao, A. Erbil, and F. Ayazi. An analytical model for support loss in micromachined beam resonators with in-plane flexural vibrations. *Sensors and Actuators A*, **109**, 156-164, 2003.

[A.3] K. F. Graff. *Wave Motion in Elastic Solids*. Ohio State University Press, 1975.

[A.4] M. C. Cross and R. Lifshitz. Elastic wave transmission at an abrupt junction in a thin plate with application to heat transport and vibrations in mesoscopic systems. *Physical Review B*, **64**, 1–22, 2001.

Appendix B

Geometry constraints

The ring-based rate sensor is manufactured in silicon, bonded on a pedestal glass and then installed on an electronic card. During the design stage, its dimensions needed for manufacturing have been defined. These dimensions are presented in Table B.1, whose notations can be seen in Figure B.1.

On this figure, two simplifications have been done. First, the width of the material in the leg or in the ring is not present. In reality, these widths are given as: leg width = 0.061 mm and ring width = 0.121 mm. The angles of each corner have also been simplified and are considered as "pointed" angles (or abrupt change in direction). In reality they are rounded angles that come from manufacturing process. The ray tracing method that has been applied all along this thesis to model the sensor vibrations neglects these rounded angles and considers an abrupt change in direction between the beam centreline. It is actually only the beam and ring centrelines that are illustrated in Figure B.1.

The leg contains three beam portions. Each of them is numbered: beam '1' is the beam portion attached to the ring, beam '3' is the portion supposed clamped at the support, and beam '2' is the portion between beam '1' and '3'.

B.1 Original dimensions

From the original dimensions given in Table B.1, all the geometric parameters that are needed to apply the ray tracing method can be derived. These parameters are the lengths of each beam portion (L_1, L_2 and L_3) and the angle between them (α and ϕ).

First, it is quite straightforward to observe, from Figure B.1, that the angle α between beam '1' and beam '2' is:

$$\begin{aligned} \alpha &= 90^\circ - (\gamma + \theta)\,, \\ &= 54.5^\circ. \end{aligned} \tag{B.1}$$

The angle ϕ, between beam '2' and beam '3' is:

$$\begin{aligned} \phi &= \beta + \alpha, \\ &= 94.5^\circ. \end{aligned} \tag{B.2}$$

With these two angles and from geometry analysis, the lengths of each beam portion can be derived:

$$\begin{aligned} L_1 &= \left(\frac{R_{\text{beam 2}}}{\sin(\pi - \phi)} \cos\beta + \left(\frac{R_{\text{beam 2}}}{\sin(\pi - \phi)} \sin\beta \right) \tan(\theta + \gamma) \right) - R \\ &= \frac{R_{\text{beam 2}}}{\sin\phi} \Big(\cos\beta + \sin\beta \, \tan(\theta + \gamma) \Big) - R \\ &\approx 1.064\,\text{mm}; \end{aligned} \tag{B.3}$$

$$\begin{aligned} L_2 &= \frac{\dfrac{R_{\text{beam 2}}}{\sin(\pi - \phi)} \sin\beta}{\cos(\theta + \gamma)}, \\ &= R_{\text{beam 2}} \frac{\sin\beta}{\sin\phi \, \cos(\theta + \gamma)}, \\ &\approx 2.582\,\text{mm}; \end{aligned} \tag{B.4}$$

$$\begin{aligned} L_3 &= \frac{R_{\text{anchor}}}{\cos(\beta-\theta)} - \frac{R_{\text{beam 2}}}{\sin(\pi-\phi)}, \\ &= \frac{R_{\text{anchor}}}{\cos(\beta-\theta)} - \frac{R_{\text{beam 2}}}{\sin\phi}, \\ &\approx 1.060\,\text{mm}. \end{aligned} \tag{B.5}$$

These dimensions are the actual dimensions of the ring-based rate sensor.

B.2 Coupling between parameters

In Chapter 5, it has been decided to change the leg shape in order to see its influence on the Q-factor. From the analysis in Section B.1, it is clear that the parameters are coupled together. Changing for example the length L_1 of the beam '1', it will automatically induce some changes in L_2, α and ϕ.

In order to find equations that express this coupling, it was necessary to consider that some parameters have to remain unchanged. These parameters that are constrained are the ring radius R; the total dimension of the sensor (dimension between the centre of the ring and the clamped end: R_{anchor}); the overall angle β of the leg (between beam '1' and beam '3') and the fact that beam '1' and beam '3' are radially directed. The value of θ that was defined for design purpose is also unchanged. Therefore the values of R_{anchor}, R, β and θ are seen as given data.

From the five Equations (B.1)-(B.5), if two unknowns are fixed within the seven parameters ($R_{\text{beam 2}}$, L_1, L_2, L_3, α, ϕ, γ), the other five parameters can be determined. In Chapter 5, it has been chosen to change the values of L_1 and L_3. Therefore these two parameters are now seen as chosen and Equations (B.1)-(B.5) have to be re-arranged to find the other five parameters.

By introducing Equation (B.1) in Equation (B.2), one can easily get:

$$\phi = \beta + 90^\circ - (\gamma + \theta). \tag{B.6}$$

This new value of ϕ is introduced in Equation (B.5), and this equation is solved in respect to $R_{\text{beam 2}}$. It becomes:

$$R_{\text{beam 2}} = \left(\frac{R_{\text{anchor}}}{\cos(\beta - \theta)} - L_3\right) \sin\Big(\beta + 90° - (\gamma + \theta)\Big). \tag{B.7}$$

Equation (B.7) and Equation (B.6) are substituted in Equation (B.3). It gives:

$$\begin{aligned} L_1 &= \left(\frac{R_{\text{anchor}}}{\cos(\beta - \theta)} - L_3\right)\Big(\cos\beta + \sin\beta\, \tan(\theta + \gamma)\Big) - R, \\ &\frac{L_1 + R}{\frac{R_{\text{anchor}}}{\cos(\beta-\theta)} - L_3} - \cos\beta = \sin\beta\, \tan(\theta + \gamma), \\ \gamma &= \arctan\left(\frac{\dfrac{L_1 + R}{\frac{R_{\text{anchor}}}{\cos(\beta-\theta)} - L_3} - \cos\beta}{\sin\beta}\right) - \theta. \end{aligned} \tag{B.8}$$

Substituting this particular value of γ (Equation (B.8)) in Equation (B.7), a numerical value of $R_{\text{beam 2}}$ can be found. ϕ and α can also then be determined using respectively Equation (B.6) and Equation (B.1). L_2 is then derived from Equation (B.4).

Therefore, by choosing L_1 and L_3 and with the appropriate constraints, L_2, α and ϕ can be derived. These parameters are needed in the ray tracing method application to find natural frequencies and mode shapes.

Figures and Tables

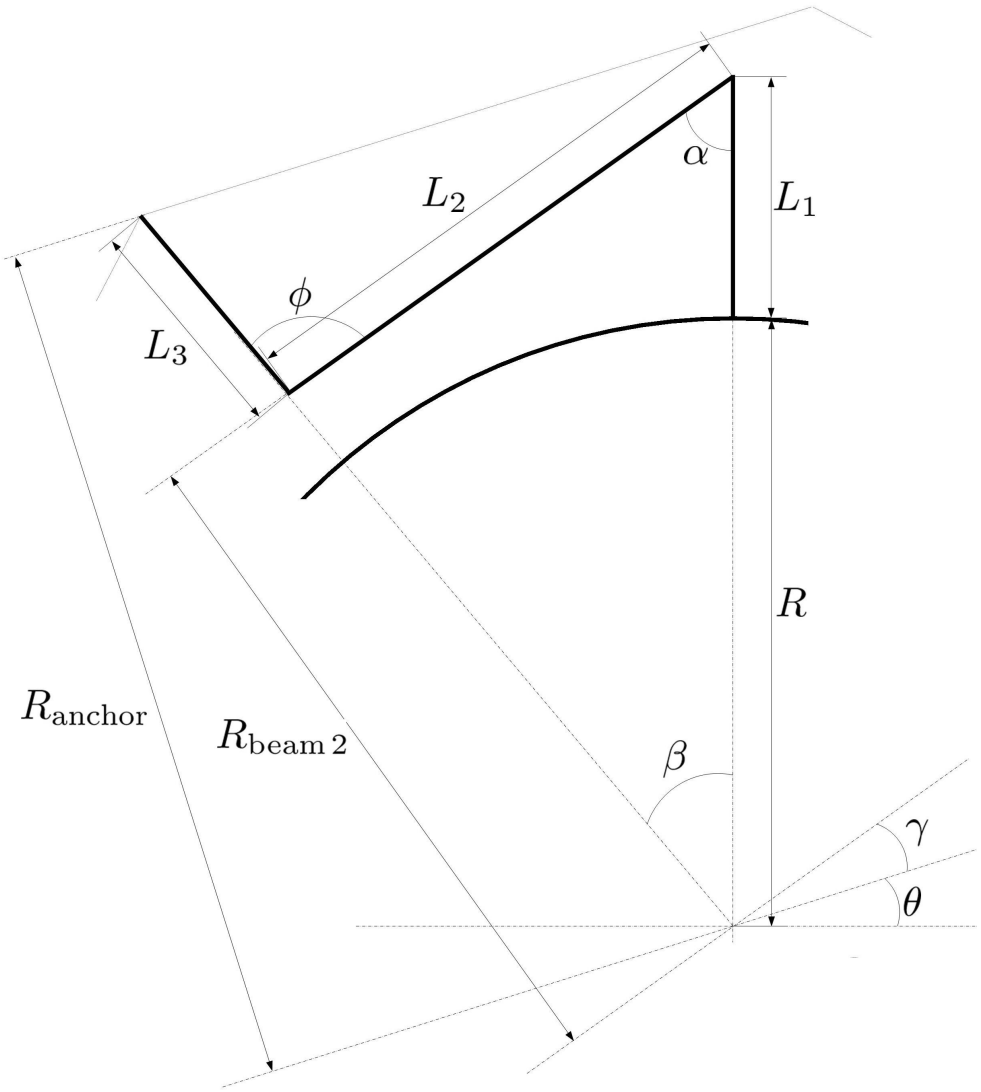

Figure B.1: Notations used on the ring-based resonator to define the different geometric parameters.

Table B.1: Actual dimensions the ring-based rate sensor given in the design process. b_{leg} and b_{ring} are the leg and ring widths. The other notations are presented in Figure B.1.

R_{anchor}	4.0005 mm
$R_{\text{beam 2}}$	3.26 mm
R	2.94 mm
β	40°
θ	17.5°
γ	18°
b_{leg}	0.061 mm
b_{ring}	0.121 mm